Characterizing and Selectively Targeting RNF20 Defects Within Colorectal Cancer Cells

by

Brent John Guppy

A Thesis submitted to the Faculty of Graduate Studies of

The University of Manitoba

In partial fulfillment of the requirements of the degree of

Doctor of Philosophy

Department of Biochemistry and Medical Genetics

University of Manitoba

Winnipeg

ABSTRACT

By 2030, the global colorectal cancer burden is projected to approximately double. This highlights the immediate need to expand our understanding of the etiological origins of colorectal cancer, so that novel therapeutic strategies can be identified and validated. The putative tumor suppressor gene *RNF20* encodes a histone H2B mono-ubiquitin ligase and has been found altered/mutated in colorectal and numerous other cancer types. Several studies suggest that RNF20, and by extension mono-ubiquitinated histone H2B (H2Bub1), play important roles in maintaining genome stability in human cells. Indeed, hypomorphic *RNF20* expression and/or function have been shown to underlie several phenotypes consistent with genome instability, making aberrant RNF20 biology a potential driver in oncogenesis.

Through an evolutionarily conserved trans-histone pathway, RNF20 and H2Bub1 have been shown to modulate downstream di-methylation events at lysines 4 (H3K4me2) and 79 (H3K79me2) of histone H3. Accordingly, understanding the biology associated with RNF20, H2Bub1, H3K4me2, and H3K79me2 is an essential preliminary step towards understanding the etiological origins of cancer-associated *RNF20* alterations and identifying a novel therapeutic strategy to selectively kill *RNF20*-deficient cancers.

In this thesis, I employ single-cell imaging, and multiple biochemical techniques to investigate the spatial and temporal patterning and characterize the biology of RNF20, H2Bub1, H3K4me2 and H3K79me2 throughout the cell cycle. In addition, I employ the CRISPR-Cas9 genome editing system to generate *RNF20*-deficient HCT116 cells. Finally, I employ synthetic lethal strategies to selectively kill RNF20-depleted cells.

In conclusion, the research chapters contained within this thesis have characterized putative drivers in cancer (Chapter 3), generated a valuable research reagent for CRISPR-Cas9

genome editing experiments (Chapter 4), and identified a novel therapeutic strategy to selectively kill certain cancer cells (Chapter 5). This thesis has increased our understanding of the etiological origins of cancer and generated novel reagents and treatments strategies that after further validation and clinical studies, could be employed to reduce morbidity and mortality rates associated with cancer.

ACKNOWLEDGEMENTS

First and foremost I would like to thank my supervisor, Dr. Kirk McManus, for providing me with guidance, support, and knowledge throughout the years. I am truly fortunate to have been a team member within the McManus lab. Kirk you are truly a science-mentor rockstar. I have enjoyed watching the lab grow over the past 6 years and look forward to the future. I would also like to thank my research committee, Drs. Mai, Davie, and Kung for providing me with valuable input and direction during my studies at the University of Manitoba. I would also like to thank the additional members of my Candidacy Examination Committee, Drs. Wigle, Ogilvie-Werbowetski, Kung, Gietz, and Murphy.

I would like to acknowledge additional individuals for technical assistance during my PhD program including Zelda Lichtensztejn, Babu Sajesh, Laura Thompson, Shannon Healy, Amy Cisyk, Aaron MacAulay, Jeff Schacter, Signe Penner-Goeke, Raghvendra Vishwakarma, Alexandra Kuzyk, Nicole Wilkinson, Laryssa Sawchuk and Nermin Moujani.

I would like to acknowledge the various agencies that have provided me funding in the form of studentships and travel awards during my tenure as a PhD student; the Mindel and Tom Olenick Research Studentship in Medicine, the Sheu L. Lee Family Scholarship in Oncology, the Manitoba Health Research Council PhD Studentship, the Dieter R. Hettig Scholarship in Cancer Biology, the *Rt. Hon.* Don Mazankowski Award for Excellence in Oncology Research, the Faculty of Graduate Studies Travel Award, the Canadian Cancer Research Alliance Conference Travel Award, and the Canadian Society for Molecular Biosciences Travel Award.

I would like to also thank those who I consider family and who have always supported my dreams; Mom, Dad, Ted, Aaron, Ryan, Christine, Craig, Camille, Mark, Jill, Sajesh, and Zelda. Thank you very much for all your support.

TABLE OF CONTENTS

LIST OF ABBREVIATIONS

%	percent
°C	degrees Celsius
3D	three-dimensional
H3K18ac	acetylated lysine 18 of histone H3
Å	Angstrom
aa	amino acid(s)
ANOVA	analysis of variance
R	arginine
ATM	ataxia telangiectasia mutated
ATP	adenosine triphosphate
ATR	ATM and Rad3-related
bp	base pair(s)
CRISPR	clustered regularly interspaced short palindromic repeats
ChIP	chromatin immunoprecipitation
CIN	chromosome instability
cm	centimeter(s)
CO_2	carbon dioxide
CRC	colorectal cancer
crRNA	small CRISPR RNA
CPTS	copper phthalocyanine 3,4',4'',4'''-tetrasulfonic acid tetrasodium salt
C-terminal	carboxy-terminal
CDK12	cyclin dependent kinase 12
Cy3	cyanin 3
DAPI	4',6-diamidino-2-phenylindole
df	degrees of freedom
H3K4me2	dimethylated K4 of histone H3
H3K79me2	dimethylated K79 of histone H3
DNA	deoxyribonucleic acid
Dot1	disrupter of telomeric silencing 1
DOT1L	Dot1-Like histone H3K79 methyltransferase
DSB	double-strand breaks
ECL	enhanced chemi-luminescence
EDTA	ethylenediaminetetraacetic acid
GFP	green fluorescent protein
FEN1	flap endonuclease 1
Gy	grey(s)
nsSNP	non-synonymous single nucleotide polymorphisms
H_0	null hypothesis
H_2SO_4	sulfuric acid
HCl	hydrochloride
HDAC	histone deacetylase(s)
h	hour(s)
HRP	horseradish peroxidase
indels	insertion and/or deletion mutations
IIF	indirect immunofluorescent

IR	ionizing radiation
K	lysine
KMT	lysine methyltransferase
KDM	lysine demethylase
kDa	kilodalton(s)
M	molar
H4K20me	monomethylated lysine 20 of histone H4
H2Bub1	monoubiquitinated K120 of histone H2B
min	minute(s)
mL	milliliters
mM	millimolar
NA	numerical aperture
NaOH	sodium hydroxide
ng	nanogram(s)
nm	nanometer(s)
nM	nanomolar
PAGE	polyacrylamide gel electrophoresis
PARP1	poly-ADP-ribose polymerase 1
PBS	phosphate buffered saline
PTEN	Phosphatase and Tensin homolog
PTM	Post-translational modification
H3S10Phos	phosphorylated serine 10 of histone H3
PI	propidium iodide
R	arginine
RAD51D	RAD51 homolog D
RAD51C	RAD51 homolog C
RAD54B	RAD54 homolog B
RNA	ribonucleic acid
RNF20	ring finger protein 20
RPM	revolutions per minute
S	serine
SAM	s-adenosyl methionine
SD	standard deviation
SDS	sodium dodecyl sulfate
SET	Su(var)3-9, Enhancer of Zeste and Trithorax
SOD1	superoxide dismutase 1
shRNA	short hairpin ribonucleic acid
siRNA	small inhibitory ribonucleic acid
sgRNA	small guide ribonucleic acid
Su(var)3-9	suppressor of variegation 3-9
SUMO	small ubiquitin-related modifier
H3K9me3	trimethylated lysine 9 of histone H3
TBS	tris buffered saline
TBST	tris buffered saline with Tween-20
Tiff	tagged image format
tracrRNA	trans-activating RNA

USP1	ubiquitin specific protease 1
USP22	ubiquitin specific protease 22
U	units
UV	ultraviolet
V	volts
v/v	volume per volume
W	watts
w/v	weight per volume
α	alpha
β	beta
γ	gamma
γ-H2AX	gamma-histone variant H2AX (phosphorylated at serine 139)
μL	micro liters
μm	microns
μM	micro molar

LIST OF TABLES

LIST OF FIGURES

USED WITH PERMISSION and CONTRIBUTION OF AUTHOR

Preface:
This thesis contains information and data published in three peer-reviewed journals in which Brent Guppy was either a primary or co-author. All journals have granted written permission to re-use published content herein.

CONTRIBUTION OF AUTHOR

1. **Guppy B.** and McManus K., Mitotic Accumulation of Di-methylated Lysine 79 of Histone H3 is Important for Maintaining Genome Integrity During Mitosis in Human Cells. *Genetics*. February 2015.
Contributions: Brent Guppy performed experiments, analyzed data, and assisted in manuscript writing.

2. Sajesh B., **Guppy B**., McManus K., Synthetic Genetic Targeting of Genome Instability in Cancer. *Cancers*. June 2013.
Contributions: Brent Guppy performed literary review and assisted in manuscript writing. Sajesh Babu performed literary review and assisted in manuscript writing.

3. Thompson L., **Guppy B.**, Sawchuk L., Davie J., McManus K., Regulation of Chromatin Structure via Histone Post-Translational Modification and the Link to Carcinogenesis. *Cancer and Metastasis Reviews*. December 2013.
Contributions: Brent Guppy performed literary review and assisted in manuscript writing. Laura Thompson performed literary review and assisted in manuscript writing. Laryssa Sawchuk assisted in manuscript writing.

Chapter 1 - INTRODUCTION

1.0.0 The Future Cancer Burden in Developed Nations

In virtually every region of the world, the number of newly diagnosed cancer cases and individuals undergoing cancer treatment will increase dramatically over the next 15 years[1]. Several economically developed countries have already evaluated and predicted the impending future impact of cancer in terms of incidence[2,3], deaths[4], prevalence[5], and costs[6]. Using a constant-rate projection model, which assumes that current cancer incidence rates remain unchanged, it is predicted that from 2008 to 2030, the total number of global cancer cases will increase by 75% and 54% among males and females, respectively[1]. For both sexes, these predicted increases are predominantly attributed to a relatively recent global surge in human population size and life expectancy[1]. Although still an important factor, modifiable cancer risk factors such as smoking, obesity, and environmental exposures play only minor roles in the future global cancer burden when compared to the greatest unmodifiable risk factor of all, age[1].

Although past, present, and future improvements in cancer prevention, diagnoses, and treatments may modulate these predictions, it remains difficult to accurately predict to what extent. It is also unlikely that a dramatic reduction in cancer incidences will be observed during this short time period. These dire yet realistic predictions highlight the immediate need to expand cancer treatment infrastructure and our understanding of the etiological origins of cancer, so that novel therapeutic strategies can be identified, validated, and implemented before the cancer burden becomes an overwhelming strain on societies throughout the world.

1.0.1 The Future Cancer Burden in Canada

By 2032 in Canada, the average number of new cancer cases is predicted to increase by 84% and 74% in males and females, respectively[7]. This represents approximately 277,200 new cases per year, which greatly exceeds the current rate of approximately 154,975 new cases per year[7]. Consistent with global predictions, the near doubling of the Canadian cancer burden by 2032 is predominantly attributed to an aging population. In 2014, ~89% of all cancers were diagnosed in Canadians over the age of 50[7]. By 2032, the number of Canadians over the age of 65 years will approximately double, and senior citizens over the age of 65 will represent one fourth of the total population[7].

Although the number of Canadian cancer cases will increase over time, the age-standardized cancer incidence rates of certain cancers are estimated to decline. These cancers predominantly include those with modifiable risk factors such as smoking, UV exposure, physical inactivity, alcohol consumption and infection (e.g. HPV, HIV, etc.)[8]. Although the decrease in certain age-standardized cancer incidence rates attest to better community education in cancer prevention, they will not meaningfully offset the projected increase in cancer incidences by 2032[7].

Taken together, the anticipated near doubling of the cancer burden by 2032 mandates immediate action in order to dampen the impending strain on cancer treatment facilities within Canada. Only through increased community education, a better understanding of the etiological origins of cancer (see Chapter 3 and Chapter 4), and novel treatment strategies (see Chapter 5), will the future Canadian cancer burden be attenuated.

1.0.2 A Focus on Colorectal Cancer in Canada

To date in Canada, colorectal cancer (CRC) is the second leading cause of cancer related deaths in men and third leading cause of cancer related death in women[7]. Currently in Canada, there are roughly 25,000 new CRC diagnoses per year and by 2032, this is expected to increase to 35,075 new CRC diagnoses per year[2]. It is estimated that 1 in every 14 males and 1 in every 16 females will develop CRC in their lifetime[7]. In 2015, it was estimated that approximately 25,000 new CRC diagnoses and 9,300 deaths were attributed to CRC[7]. Unfortunately, approximately 37% of those diagnosed with CRC will succumb to the disease within 5 years[9]. Furthermore, greater than 50% of CRC diagnoses are late stage (III and IV). Late stage diagnosis is attributed to a lack of noticeable symptoms in early stage CRCs. Unfortunately, stage IV CRCs have less than a 12% 5-year survival rate[9].

Although the number of deaths from CRC continues to rise due to an aging population, the age-standardized mortality rate for CRC is declining by 2.5% per year from 2004 to 2015 in males, and 1.8% per year from 2001 to 2015 in females[7]. These modest declines are generally thought to stem from modifiable risk factor reductions, advancements in screening coupled with early detection, and improved treatment[7]. These declines in mortality rates serve as optimistic indicators that show increased community education, a better understanding of the molecular origins of CRC (see Chapter 3 and Chapter 4), and the ability to selectively kill CRC cells (see Chapter 5), may contribute to further decreases in CRC mortalities across Canada and the world. Accordingly, novel highly effective treatment strategies must be rapidly identified, validated, and implemented to further accelerate the decline in CRC mortality rates.

1.0.3 Colorectal Cancer Diagnosis, Clinical Pathogenesis, and Treatment

Primary CRCs cancers arise within the colon and rectum and are typically sub-classified as proximal, distal, or rectal. Proximal CRCs include those arising from the cecum, ascending colon, transverse colon and splenic flexure. Distal CRCs include those arising from the descending colon and sigmoid colon. Rectal cancers include those within the rectosigmoid junction and the rectum. The large majority of CRC are adenocarcinomas and a clear progression from dysplastic epithelium to polyp to malignant cancer has been well established[10].

CRC diagnoses are typically made through colonoscopy or sigmoidoscopy which are employed to visually identify and biopsy neoplasms. Surgical resection of the cancerous segment(s) of the colon or rectum is typically indicated for stages I to III, while surgery followed by adjuvant chemotherapy is typically indicated for stages II to IV CRCs[9]. Because surgical resection is indicated for all stages, cancer genome sequencing can be performed on *ex vivo* tissues to characterize the genomic profile of the tumor. This allows the opportunity to utilize an adjuvant precision medicine approach (see Chapter 5) to target any residual cancer cells or metastatic deposits following surgery. This is particularly critical as the majority of patients that succumb to CRC typically do so as a result of complication associated with metastasis. The most common sites of metastases are the liver, lungs, and bone. Accordingly, targeted adjuvant chemotherapy may be employed to destroy metastatic deposits within these tissues, which are not typically amenable to surgery.

The heritable genetic predisposition to CRC accounts for only ~15% of all cases and include such conditions as Familial Adenomatous Polyposis or Lynch Syndrome[11]. In contrast, the majority (~85%) of CRC are sporadic, or randomly occurring in nature. Sporadic CRCs are generally believed to arise from mutations within genes that normally encode functions that are

essential to maintain genome stability[12]. The loss of genome stability, termed genome instability, is a common pathogenic event associated with many human syndromes and disease states. For example, genome instability is a characteristic of Ataxia Telangiectasia[13], Xeroderma Pigmentosa[14], Nijmegen Breakage Syndrome[15], and virtually all cancer types[16]. Sub-classifications of genome instabilities include; 1) CpG island methylator phenotype, which is most frequently associated with the epigenetic silencing of tumor suppressor or DNA repair genes due to DNA hypermethylation within promoter regions[17], 2) microsatellite instability, which is defined by an increase in the basal mutation rate and stems from defects in the DNA mismatch repair pathway[18,19], and 3) chromosome instability (CIN)[20], which is defined by an increase in the rate at which numerical and/or structural chromosome aberrations occur[11,21]. Accordingly, understanding the specific molecular drivers of CIN in CRC will allow for a further understanding of the etiological origins of CRC and thus may identify novel therapeutic targets (see *Section 1.1.0* below).

1.1.0 The Chromosome Instability Phenotype

Over a century ago, the pioneering observations of Theodor Boveri suggested that genome instability, or more specifically abnormal chromosome constitutions, are pathogenic events that drive the oncogenic process[22]. A century's worth of genetic, biochemical, cytological, and cell biological research has validated his initial observation and it is now widely accepted that the loss of genome stability contributes to the development of cancer. Surprisingly, although genome instability is associated with virtually all cancer types including both solid and liquid, the aberrant molecular origins that drive genome instability are poorly understood.

The large majorities of solid tumors such as CRC are aneuploid and exhibit CIN. As indicated above, CIN is defined as an increase in the rate at which whole chromosomes, or large parts thereof are gained or lost[12]. These large-scale genomic changes underlie cancer initiation and progression by presumably offsetting the delicate balance of oncogenes and tumor suppressor genes encoded within the altered chromosomal regions[23]. Furthermore, the ongoing genetic rearrangements conferred by CIN, underlie both intra- and inter-tumor heterogeneity. Tumor heterogeneity promotes subclonal evolution and ultimately translates into highly aggressive and multi-drug resistant cancers[23,24]. The CIN phenotype is arguably best described in CRC where it is found in approximately 85% of sporadic tumors[12]. Although there is a high correlation of CIN and CRC, the aberrant genetic alterations underlying CIN are largely unknown.

In order to conclusively detect CIN, a clonal cell CIN assay must performed. This assay evaluates changes in aneuploidy or gross chromosomal rearrangements over time (rate) and accordingly requires multiple sampling intervals[25]. Populations showing little to no change in aneuploidy or gross chromosomal rearrangements are considered stable and CIN-negative, whereas populations showing variation in aneuploidy or chromosomal rearrangements are considered CIN-positive. As one may expect, clonal cell CIN assays are labor-intensive and limited to models capable of clonal prolonged cell growth. Accordingly, the presence of aneuploidy or gross chromosomal rearrangements within a given cell population are frequently employed as a surrogate marker for CIN[11,12].

1.1.1 Numerical and Structural Chromosome Instability

The CIN phenotype can be sub-classified as numerical chromosome instability (nCIN) or structural chromosome instability (sCIN)[26]. nCIN represents an increased rate of change in whole chromosomes. nCIN, or changes in aneuploidy that are typically detected in mitotic chromosome spreads. sCIN represents an increased rate of change in gross chromosomal rearrangements, which includes translocations, deletions, duplications, and inversions. sCIN is typically detected by spectral karyotyping and/or M-banding and/or comparative genomic hybridization. Both nCIN and sCIN can be detected by single cell sequencing to assess genome-wide copy number alterations and complex karyotypes. Furthermore, conventional and high-resolution 3D imaging of telomeres in cancer cells can identify nCIN and sCIN as well as yield valuable information pertaining to prognosis, diagnosis, and treatment approaches[27-29].

1.1.2 Mechanisms of CIN

To date, several hallmarks and mechanisms that underlie aneuploidy and CIN have been identified in human cells[30,31]. Hallmarks and mechanisms of CIN include microtubule-kinetochore attachment errors, supernumerary centrosomes, chromatid cohesion defects, altered gene transcription profiles, telomere dysfunction, and aberrant epigenetic changes. Of these, microtubule-kinetochore attachment errors are the most commonly observed hallmark of CIN and are easily identified by the appearance of "lagging chromosome", which erroneously remain at the metaphase plate following the metaphase to anaphase transition during mitosis[32]. Lagging chromosomes eventually randomly partition into a daughter cell following cytokinesis and may or may not result in aneuploidy[30]. Supernumerary centrosomes are also frequently observed in many cancers and are known to underlie CIN. In one study, up to 30% of CRC cell lines

examined contained additional centrosomes[33]. Supernumerary centrosomes may cause large-scale microtubule-kinetochore attachments errors, underlies chromosome missegregation[34,35], and are positively correlated with numerical chromosomal aberrations and CIN[33]. Sister chromatid cohesion defects also underlie CIN[36-38]. Following DNA replication, sister chromatids maintain close proximity through a circular cohesin complex. During the mitotic metaphase to anaphase transition, the cohesin complex is normally released and sister chromatids are freed for segregation. Defects within the cohesin complex are generally thought to elicit premature sister chromatid separation and underlie chromosome missegregation and CIN[37-39]. Alterations in gene transcription profiles have also been shown to underlie CIN. To date, the deregulation of tumor suppressor protein p53 or the transcription factors, c-fos, c-myc, and c-jun have been shown to alter cell cycle checkpoints and lead to chromosome missegregation[40]. Telomere dysfunction also underlies CIN and is an attribute of several cancer types including prostate[41], breast[42] and colon[43]. Several chromosomal aberrations have been detected that directly result from telomere dysfunction including unbalanced translocations, dicentric chromosomes, and interstitial telomeres. At least two major telomere dysfunction mechanisms have been identified including critical telomere shortening[44,45] and telomere uncapping[46]. Unprotected telomeres can result in the formation of telomere aggregates and concomitant breakage-bridge-fusion cycles which ultimately leads to large scale genomic alterations and CIN[47,48]. Aberrant changes in certain histone post-translational modifications (PTMs) have also been shown to underlie CIN. In fact, certain histone PTMs play important roles in transcriptional regulation, DNA damage repair, telomere maintenance, chromosome compaction, and chromosome segregation.

1.1.3 The Biological Impact of Chromosome Instability

Large-scale genomic imbalances of whole chromosomes or large parts thereof more often result in cell death than transformation[49]. Accordingly, the majority of cells displaying CIN and thus aneuploidy ultimately undergo apoptosis. Aneuploidies in healthy human and mouse cells as detected by single-cell sequencing are rare, with frequencies of 0-2.7%, 3-5%, and ~5% in keratinocytes[50], brain[50,51], and liver[50], respectively. Comparatively, transformed CIN-positive cells in culture have a 20-100% aneuploidy frequency[32]. The tumor suppressor gene *TP53* plays an important role in preventing the proliferation of aneuploid cells and thus serves an important role in mitigating cellular transformation. Although the exact mechanism in unknown, chromosome segregation errors appear to trigger p53 stabilization and concomitant cell cycle arrest in G1, followed by apoptosis[32]. Not surprisingly, *TP53*-deficiencies allow aneuploid cells to proliferate and increase in karyotype complexity over successive rounds of division. Well over 50% of all human cancers are *TP53*-deficient, attesting to the importance of p53 as a guardian of the genome[52-54].

It is now clear that certain cancers preferentially gain or lose specific chromosomes in order to initiate or maintain a particular karyotypic profile (reviewed in [55]). In general it can be envisioned that chromosomes containing a greater number of oncogenes are preferentially retained, whilst chromosomes containing a greater number of tumor suppressor genes are preferentially lost. In addition, some cancers that adopt a particular malignant phenotype (e.g. metastasis, drug resistance, etc.) also retain specific karyotypic profiles that confer the requisite phenotype (e.g. mobility, invasion, drug efflux, etc.). Collectively, identifying and characterizing specific cancer driving genes will allow for a greater understanding of the etiological origins of cancer and may uncover novel therapeutic targets.

1.1.4 Therapeutic Interventions Targeting Chromosome Instability

The ability to therapeutically target CIN (or the molecular origins of CIN) may have broad clinical significance as CIN is a feature of multiple cancer types[56]. To date, several strategies have been employed to preferentially target cancer cells exhibiting CIN [23,57]. These targeting strategies can be classified as either CIN-suppressing or CIN-exacerbating. CIN-suppressing strategies attempt to attenuate or eliminate the CIN phenotype by restoring normal chromosome segregation patterns. Examples include overexpression of two microtubule-depolymerizing kinesins, MCAK and Kif2B, which stimulate kinetochore-microtubule depolymerization during mitosis to correct erroneous kinetochore-microtubule attachments and concomitant missegregation[58]. Although CIN-suppressing strategies may limit further genomic heterogeneity, they lack the ability to efficiently eliminate cancers cells with pre-existing aneuploidies. On the other hand, CIN-exacerbating strategies aim to maximize CIN to induce death by causing catastrophic increases in chromosome missegregation, chromosome rearrangement and/or DNA damage[23,59,60]. Clinical examples of CIN-exacerbating strategies include the use of taxanes in CRC. Taxanes stabilize microtubules to generate multi-polar mitotic spindles and increase kinetochore-microtubule attachment errors to ultimately cause chromosome missegregation and accelerated CIN[61]. Although the concept of this approach appears promising, taxanes failed to show clinical benefit in phase II clinical CRC trials[61]. An additional example includes the use of Poly(ADP-Ribose) Polymerase-1 inhibitors (PARP1i), which increase DNA double strand breaks (DSBs) and causes large-scale chromosome rearrangements that underlie increases in DNA mutation rates within *BRCA1/2*-deficient breast, ovarian, and CRCs[62] (discussed in *Section 1.6.4* below and Chapter 5).

1.2.0 Histone Post-Translational Modifications - Structure and Function

The fundamental repeating structure of chromatin is the nucleosome. The nucleosome is comprised of approximately 146 base pairs (bp) of DNA wrapped ~1.7 times around an octameric core particle containing two histone H2A/H2B dimers flanking a central histone $(H3/H4)_2$ tetramer[63] (Figure 1.1A). The core histones are small, highly basic nuclear proteins that share a common structure. This includes a central highly structured globular domain that is required for histone–histone and histone–DNA interactions, as well as "unstructured" carboxy-terminal and amino-terminal tails (Figure 1.1B). Although a small number of modifications can be made within the globular domains, it is the histone tails that extend out from the octameric core that generally serve as the primary substrates for residue-specific post-translational modifications (PTMs). Histones are among the most highly post-translationally modified proteins known and the substrates for at least 11 different types of PTMs including acetylation, phosphorylation, methylation, and ubiquitination[64-66]. The highly conserved amino acid sequence of histones and their propensity to accept specific PTMs is evolutionarily conserved, implying that many PTMs are essential for the maintenance of eukaryotic cell function and perturbations to certain histone PTMs may underlie various disease states including cancer.

Although the classical function of histones is DNA packaging, chromatin structure is dynamic and can undergo local or global conformational changes. These conformational changes are highly regulated by specific PTMs that render the chromatin amenable or resistant to a myriad of nuclear processes that utilize DNA/chromatin as a template, including transcription, DNA replication and repair, and chromosome compaction and segregation[67,68]. In general, chromatin imparts its regulatory effects by differentially modulating the level of DNA

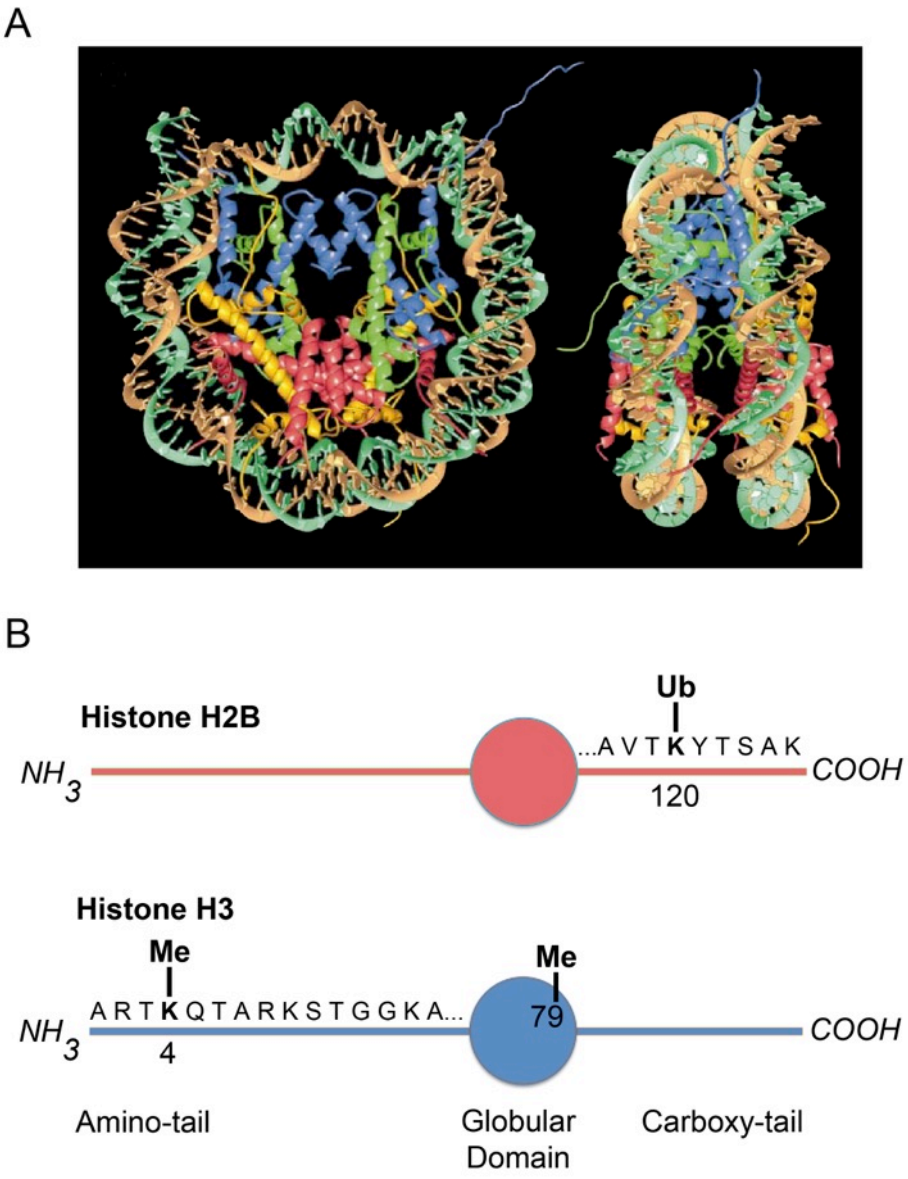

Figure 1.1: The Structure of the Nucleosome
(**A**) The crystal structure of the nucleosome core particle at the 2.8 Å resolution. DNA double helix is depicted as gold and green ribbon structure surrounding the core histones (blue: H3; green: H4; yellow: H2A; red: H2B). Unstructured 'tail' regions are shown emerging from the nucleosome ***(Adapted from Luger et al.[63], used with permission.)*** (**B**) Schematic diagram showing the amino- and carboxy-tail regions of core histones H2B (red) H3 (blue). The relevant single letter amino acid code is displayed on the histones. The numbers displayed represent specific amino acid positions. 'Ub' represents ubiquitination where lysine 120 can be unmodified or monoubiquitinated. 'Me' represents methylation where lysine 4 and 79 can be unmodified, mono-, di-, or tri-methylated. Note that the histone PTMs discussed within this thesis are identified as H2BK120 ubiquitination, H3K4 methylation, and H3K79 methylation.

compaction and thus the biochemical accessibility to DNA-binding or protein-binding effector molecules. For example, at certain stages of the cell cycle or in response to certain stimuli, chromatin can be decondensed to facilitate access to appropriate factors involved in processing the genetic information (e.g., transcription, replication, and repair). Conversely, chromatin condensation may increase to render the DNA inaccessible to certain factors, or during mitosis where maximal condensation is achieved to allow discrete packaging of the genetic material and accurate segregation to daughter cells[68]. This precise level of regulation is primarily achieved through specific histone PTMs. PTMs impact chromatin structure by virtue of the type (methylation, ubiquitination, etc.), abundance, and location of a particular PTM and the PTM's ability to structurally alter histone–histone, histone–DNA, and histone-effector protein interactions.

1.2.1 The Regulation and Abundance of Histone PTMs Impact Genome Stability

The spatial and temporal distribution of a given histone PTM is regulated by the balance of the enzymatic activities of the proteins that add ("writers") or remove ("erasers") specific histone PTMs[69]. The overall abundance of a given PTM also depends on the accessibility and activity of "writers" or "erasers" to the appropriate histone residue, as well as the availability of donor substrate itself (Table 1.1). Histone "reader" proteins interpret the histone PTM "code" to evoke specific functional and context-dependent biological outcomes. Alterations in the steady-state levels of a given PTM can be brought about through various pathogenic events (e.g., specific somatic mutations, amplifications, or deletions) that typically impact the expression, function, and/or regulation of the genes encoding the "writers" or "erasers". As a direct consequence, the steady-state level of a given histone PTM will be altered, which in turn, may impact normal

Table 1.1: Selection of Enzymes that Regulate the Abundance of Certain Histone PTMs

Histone	Residue	Mod[A]	"Writer"	Substrate	"Eraser"
H3	4	Me1	hMLL1 (KMT2A)	SAM[B]	LSD1 (KDM1A)
		Me3	hMLL2 (KMT2B)		AOF1 (KDM1B)
		Me1	hMLL3 (KMT2C)		JARID1A(RBP2)
		Me1	hMLL4 (KMT2D)		JARID1B (PLU-1)
		Me1, 3	hMLL5 (KMT2E)		JARID1C (SMCX)
		Me1, 2	hSET1A (KMT2F)		JARID1D (SMCY)
		Me3	hSET1B (KMT2G)		
		Me1	ASH1 (KMT2H)		
		Me1	NSD1 (KMT3B)		
		Me1	NSD2 (WHSC1)		
		Me1	NSD3 (WHSC1L1)		
		Me2, 3	hSETD2 (KMT3A)		
		Me1, 2, 3	SMYD1-5		
H3	79	Me	DOT1L (KMT4)	SAM	Unknown
H2B	120	Ub	RNF20/RNF40	Ubiquitin	USP22[C]

[A]Modification type; Me1, Me2, Me3: mono-, di-, tri-methylation; Ub: Ubiquitination
[B]SAM: s-adenosyl methionine
[C]USP22 is generally accepted as the predominant H2B ubiquitin specific protease

chromatin structure and function to ultimately trigger various disease states including cancer. Failure to accurately regulate chromatin condensation or decondensation can lead to increased DNA damage, aberrant gene expression, and errors in mitotic fidelity, which all contribute to genomic instability phenotypes including CIN. For example mitosis-specific increases in histone H3S10 phosphorylation[70], histone H3K9 tri-methylation[71], histone H4K20 mono-methylation[72], and histone H3K79 di-methylation[73] (see Chapter 3) have all been shown to play important roles in maintaining mitotic fidelity through a variety of pathways including chromosome condensation, chromosome segregation, and kinetochore structure. Thus alterations to the mitosis-specific levels of these PTMs, through alterations that produce hypomorphic expression and/or function in the "writer" or "eraser" enzymes that govern their abundance, may be pathogenic events associated with CIN and cancer.

1.2.2 Regulation of Chromatin Structure via Histone PTMs and the Link to Oncogenesis

It is now becoming clear that certain histone PTMs have essential roles in maintaining genome stability under normal conditions. Thus, a strong relationship exists between aberrant histone PTMs, genome instability, and oncogenesis. Indeed, research conducted over the past decade has shown that alterations in specific histone PTMs, stemming from hypomorphic expression or function of the enzymes that govern them, correlate with the development and progression of many cancer types[74]. In fact, the abundance of specific histone PTMs and histone modifying enzymes are now being explored as prognostic biomarkers for the certain cancer types such as breast cancer[75]. Consequently, it is first essential to characterize the normal roles specific histone PTMs play in maintaining genome stability before their roles in the development of cancer can be determined. Only once this information becomes available will it be possible to

devise and develop the next generation of novel therapeutic strategies that are specifically designed to exploit these aberrant epigenetic origins.

1.3.0 Histone H2B Ubiquitination

Histone ubiquitination is implicated in a number of evolutionarily conserved cellular processes including transcription[76], DNA repair[77], and genome stability[78]. The addition of the 76-amino acid ubiquitin moiety adds approximately 8.5 kDa to the overall mass of histone H2B (~13.9 kDa) and is accomplished through a three-step process that begins with an E1 ubiquitin-activating enzyme. Next, activated ubiquitin is transferred to an E2 ubiquitin-conjugating enzyme where it resides for subsequent targeting. The final step employs an E3 ubiquitin-ligase that physically targets the E2-ubiquitin complex to its cognate substrate (K123 in yeast or K120 in humans) for ubiquitin ligation. The final product is monoubiquitinated histone H2B (H2Bub1), which is formed by a covalent isopeptide linkage between the C-terminal glycine of ubiquitin and histone H2B[79]. It should be noted that histone mono-ubiquitination, unlike canonical protein poly-ubiquitination, is generally believed to not mark histones for proteolytic degradation via the 26S proteasome or subcellular targeting. As with all histone PTMs, the abundance of H2Bub1 depends on the balance between the activities of the enzymes that covalently add ubiquitin to lysine residues (RNF20, detailed in *Section 1.3.1*), those that remove it (USP22, detailed in *Section 1.3.1*), and the availability of free ubiquitin itself (see Table 1.1).

In human cells, histone ubiquitination has been predominantly observed within the C-terminal domains of H2A[80] (K119) and H2B[79] (K120) and the N-terminal domains of H2A/H2AX[81] (K13 and K15) *in vivo*. In addition, H3 and H4 have been shown to be ubiquitinated *in vivo* under UV DNA damaging conditions[82]. Although H2A, H3, and H4 can

exist in either a mono- or poly-ubiquitinated form, H2B exists predominantly in mono-ubiquitinated form (Figure 1.1B). In multicellular eukaryotes, both H2A and H2B are ubiquitinated, whereas in lower eukaryotes such as budding yeast, only H2B is capable of being ubiquitinated, which suggests it is required for highly conserved biological processes. Histone deubiquitination is generally mediated through the activities of ubiquitin-specific proteases (USPs). The role human H2Bub1 perturbations play in driving genome instability and oncogenesis has currently garnered much attention from several research groups.

1.3.1 H2Bub1, RNF20, RNF40 and their Roles in Oncogenesis

Alterations in the enzymes that regulate histone ubiquitination and deubiquitination pathways directly impact higher-order chromatin structure[83,84] (i.e., beyond the single nucleosome level). Higher-order chromatin structure influences all cellular processes that employ chromatin as a biological template. Consequently, aberrant expression or function of ubiquitin and deubiquitinating complexes may adversely impact these processes to directly affect genome stability. H2Bub1 is predominantly regulated through the enzymatic activities of the E2 ubiquitin-conjugating enzyme (UBE2A or RAD6A) and the E3 (RNF20/RNF40) ubiquitin ligase complex, and as predicted, RNAi-based silencing of these components depletes the global abundance of H2Bub1[76,85]. Therefore, altered expression of *UBE2A* and/or *RNF20/RNF40* is suggested to be a pathogenic event that contributes to the development and progression of various cancer types.

For example, gene re-sequencing efforts (detailed below) from various major cancer types including breast, prostate, and CRC have uncovered several genetic alterations in *RNF20*, *RNF40*, *UBE2A*, and *USP22*. When multiplying the frequency of gene alterations identified in

these three major cancer types by the total number of Canadians diagnosed with these cancers each year, it is estimates that approximately 14,914 Canadians may contain genetic alterations in these components. By extension, it is estimated that the same number of Canadians could potentially benefit from a therapeutic strategy designed to exploit these molecular defects (Chapter 5) (Table 1.2). Furthermore, translational studies by Shema *et al.*[76] revealed that *RNF20* promoters are hypermethylated within breast cancer tumor samples relative to controls. Additional studies have also shown that reduced *RNF20* expression levels occur in testicular germ cell carcinomas (seminomas)[77], parathyroid cancers[86], and CRC[87]. At the very least, these correlative studies suggest that altered *RNF20* expression and/or function, and presumably altered levels of H2Bub1, may be causal factors contributing to cancer development and progression.

Aberrant expression and function of the deubiquitination pathway members are also expected to affect the global abundance of H2Bub1. Multiple H2Bub1 deubiquitinating enzymes have been proposed including USP44[88], USP3[89], and USP7[90], but these appear to be cell-type and cell-context specific. On the other hand, USP22 is ubiquitously expressed and is generally accepted as the predominant H2Bub1 deubiquitinating enzyme[84,91,92]. As with *RNF20/RNF40*, a number of alterations within *USP22* (e.g., nsSNPs, amplifications, and homozygous deletions) have been identified in various cancers (Table 1.2). Recently, increases in *USP22* expression, and the resulting decrease in H2Bub1, have garnered attention as potential drivers in oncogenesis. For example, Zhang *et al.*[93] noted that USP22 levels were elevated in human breast cancer samples relative to benign and normal controls. In fact, patients with high USP22 levels had more aggressive cancers and poorer overall outcomes than patients with low USP22 levels. Furthermore, they determined that USP22 levels were positively correlated with lymph node

Table 1.2: Mutational Frequencies of Select Histone Modifying Enzymes

Gene	Histone PTM	Tumor Type	Frequency[A]	Cases[B]	Estimated Cases[C]
RNF20	H2Bub1	CRC	6%	25,100	1,506
		Breast	2%	25,200	504
		Prostate	4%	24,000	960
RNF40	H2Bub1	CRC	4%	25,100	1,004
		Breast	6%	25,200	1,512
		Prostate	3%	24,000	720
UBE2A	H2Bub1	CRC	1%	25,100	251
		Breast	1%	25,200	252
		Prostate	5%	24,000	1,200
USP22	H2Bub1	CRC	3%	25,100	753
		Breast	21%	25,200	5,292
		Prostate	4%	24,000	960
DOT1L	H3K79me2	CRC	11%	25,100	2,761
		Breast	7%	25,200	1,764
		Prostate	2%	24,000	480

[A]Estimated mutation frequency (percentage) by cancer type (data from cBIOportal.org)
[B]Estimated number of new Canadian cases by cancer type per year.
[C]Estimated number of Canadians affected by cancer type per year and predicts the number of cases that would contain alteration within the gene specified. Estimated cases is calculated by the multiplying the number of cases by the mutation frequency.

metastases, *HER2* positivity, *Ki67* expression levels and breast cancer recurrence, leading the authors to propose that USP22 may serve as a prognostic indicator of breast cancer survival[93,94]. Although not specifically evaluated, these results suggest that in addition to USP22, H2Bub1 may also have prognostic value as it reflects not only the abundance of USP22 ("eraser") but also the abundance of UBE2A ("writer") and RNF20/RNF40 ("writers").

1.3.2 H2Bub1 Promotes Tumor Suppressing Transcriptional Profiles

H2B ubiquitination is classically defined as an epigenetic mark that is associated with transcriptional activation and tumor suppression[95,96]. The covalent addition of the large ubiquitin moiety (8.5 kDa) onto the C-terminal tail of histone H2B (13.9 kDa) is expected to have a significant impact on higher-order chromatin structure and thus transcriptional regulation. Within interphase cells, the presence of nucleosomes within coding regions represents a barrier to efficient transcriptional elongation[63,97]. H2B ubiquitination is found enriched within the coding region of certain genes and disrupts higher-order chromatin structure to promote a more open and biochemically accessible chromatin fiber[76,83]. H2Bub1 is believed to disrupt 'nucleosome stacking', which is a model that proposes nucleosome 'stack together' to form close associations during chromatin condensation[98]. The addition of ubiquitin to H2B within the transcriptional start site is believed to increase gene promoters' access to transcription factors and factories, thereby enhancing transcriptional activation through increased assembly rates of transcriptional pre-initiation complexes[99,100]. Additional support for this concept came in 2003[101] when it was established that H2B ubiquitination promotes transcriptional elongation by destabilizing nucleosomes through a process that is mediated by the histone chaperone complex Facilitates Chromatin Transcription (FACT). These *in vitro* transcription studies performed on reconstituted

chromatin, revealed that RNF20-RNF40, in combination with FACT, are required for efficient and optimal transcription[101]. It is believed that the FACT complex plays a major role in promoting H2A-H2B dimer displacement when the RNA polymerase II complex is transcribing through the nucleosome. The H2A–H2B displacement appears to partially overcome the transcriptional barrier imparted by the canonical nucleosomal structure and allows for increased transcription efficiency. In agreement with the above mechanism, it was shown that FACT in the presence of H2Bub1 elicited increased transcription lengths and greater RNA polymerase II elongation rates[102]. Consistent with a role in transcriptional elongation, RNF20 is recruited to the elongating form of RNA polymerase II through an adaptor protein WAC, which is essential for transcription-associated H2B ubiquitination[103].

The information detailed above argues that altered expression and/or function of ubiquitinating or deubiquitinating complex members will offset the normal abundance of H2Bub1 and ultimately impact gene expression profiles. In fact, H2Bub1 perturbations produce gene expression profiles that promote oncogenic transformation. Shema and colleagues[76] demonstrated that *RNF20*-silencing and concomitant H2Bub1-depletion altered expression profiles of a subset of genes within HeLa cells. This not only included the down-regulation of specific tumor suppressor genes including *TP53,* but also the surprising up-regulation of several proto-oncogenes including *MYC* and *FOS*, which supports oncogenic and metastatic programs. While there have been numerous studies that can account for the transcriptional down-regulation following RNF20-silencing, the mechanism(s) that account for the unexpected increase in gene expression are just beginning to be understood[104].

In addition to modifying tumor suppressor genes and proto-oncogene expression profiles, altered *RNF20* expression also affects cell mobility and therefore may contribute to metastatic

potential. RNAi-based silencing of RNF20, and presumably diminished H2Bub1, resulted in increased cell migration, while overexpression of RNF20 significantly decreased cell mobility[76]. Finally, *RNF20*-silencing also altered the expression profiles of differentiation-associated genes, which impaired human mesenchymal stem cell differentiation[105]. Karpiuk and colleagues[105] showed that H2Bub1 levels increase during human mesenchymal stem cell differentiation, and when depleted by *RNF20*-silencing, leads to a less differentiated phenotype, thus enhancing malignant and metastatic potential. This may have important implications in a cancer-context as tumor cells deficient in H2Bub1 may fail to terminally differentiate, which may lead to aggressive high-grade cancers. Collectively, the above data strongly suggest that alterations in the enzymes that regulate the global abundance of H2Bub1 are pathogenic events that contribute to malignant transformation and metastatic potential.

1.3.3 H2Bub1 Plays a Role in DNA Damage Repair

H2Bub1 has most recently been implicated in DNA DSB repair[77,100,106,107], which is an indispensible process required to maintain genome stability. The ability of H2Bub1 to disrupt higher-order chromatin structure is required for the timely repair of DNA DSBs[107]. In fact, RNAi-based *RNF20*-silencing induced aberrant phenotypes that are associated with a defective DNA damage response, such as increased sensitivity to radiomimetic drugs and delayed repair kinetics as indicated by the persistence of γH2AX and 53BP1 foci (two surrogate markers of DNA DSBs)[107]. Furthermore, cells in which either *RNF20* or *RNF40* were independently or simultaneously silenced exhibited significant increases in DNA DSBs relative to controls, and strongly implicates H2Bub1 in DNA DSB repair[107]. Under normal conditions, DNA DSB repair requires chromatin regions surrounding the break to undergo localized decondensation that

appears to involve H2Bub1. Using a novel *in vitro* fluorescence-based assay, Fierz and colleagues[83] demonstrated that in non-DNA damaging conditions, the addition of ubiquitin to H2B disrupts higher-order chromatin structure by impairing inter-fiber interactions, thus promoting a more open and biochemically accessible chromatin fiber. Conversely, unmodified chromatin remained condensed. Efficient DNA repair is accomplished by presumably rendering chromatin more accessible to accessory DSB repair proteins through H2Bub1-mediated chromatin decondensation. Indeed, diminished recruitment of several critical members of the two DNA DSB repair pathways (i.e., non-homologous end joining and homology recombination repair) to the sites of laser-induced DNA DSBs was observed within RNF20-/RNF40-depleted cells. Failure to accurately repair DNA DSBs within critical loci has the potential to generate mutations and deletions that alter gene expression profiles and cause CIN to ultimately drive oncogenesis.

1.3.4 Rnf20/Rnf40 are Suppressors of CIN

The mouse equivalent of the human RNF20/RNF40 complex (Rnf20/Rnf40) can directly suppress CIN in mouse cells[78]. Using RNAi, Chernikova *et al.*[78] showed that Rnf20/Rnf40-depletion elicited several phenotypes consistent with CIN including increased frequencies of micronuclei formation, increased DNA content, and increased genomic rearrangements. Accordingly, these findings directly complement studies detailed above and strongly suggest that the human (RNF20/RNF40) and mouse (Rnf20/Rnf40) E3 ubiquitin ligase complexes and presumably H2Bub1, normally play essential roles in maintaining genome stability. In summary, cancer-associated alterations within *RNF20/RNF40* and concomitant H2Bub1-depletion are likely drivers in oncogenesis. Thus, H2Bub1 perturbations may represent a novel targetable

phenotype that could be exploited through genetic therapeutic strategies such as synthetic lethality (see Chapter 5).

1.3.5 The H2Bub1 Trans-Histone Pathway

The H2Bub1 trans-histone pathway describes how H2Bub1 can modulate H3K4 and H3K79 methylation levels. In 2002, Sun and Allis[108] showed in budding yeast that monoubiquitinated H2B (H2Bub1-K123, yeast equivalent to human K120) promoted H3K4 methylation by Set1-containing KMTs. The influence of H2Bub1-K123 on H3K4 was confirmed in yeast expressing non-ubiquitinatable histones where K123 was mutated to arginine (H2B-K123R). The H2B-K123R mutant phenocopied *Set1*-deletion and H3K4 methylation was ablated. This seminal finding demonstrated a unidirectional regulatory pathway where H2B monoubiquitination can play an important role in modulating subsequent histone H3 methylation at K4. Subsequent studies by Briggs *et al.*[109] expanded the H2Bub1 trans-histone pathway to include K79 of histone H3. Using similar experiments as above, H2Bub1-K123 was shown to influence H3K79 methylation, which is catalyzed by the budding yeast methyltransferase Dot1[110]. The conservation of the trans-histone pathway was later confirmed in human cells. Similar to the budding yeast, H2Bub1 was shown to modulate H3K4 and H3K79 di-methylations, which are catalyzed by human SET1-containing enzymes and human DOT1L (KMT4), respectively (Table 1.1)[111,112]. Notably, data presented within this thesis and recent studies performed by others, show that H2Bub1 is not a strict pre-requisite for H3K4 and H3K79 methylation events and thus H2Bub1-independent methylation can occur[73,113].

1.4.0 Histone H3 Methylation

As with all histone PTMs, the abundance of histone methylation is achieved through the balance of the enzymatic activities of the "writers" (i.e., lysine methyltransferases, KMTs), the "erasers" (lysine demethylases, KDMs), their accessibility to cognate substrates, and the availability of donor substrates. In general, KMTs utilize S-adenosyl methionine as the methyl donor and covalently attach methyl groups onto the ε-amino group of lysine residues that are predominantly contained within the N-terminal tails of histones H3 and H4[114-116]. Histone lysine methylation, however, is distinct from other PTMs in that it can exist in mono-, di-, and tri-methylated forms (Figure 1.2). The processive addition of methyl groups can occur, but is not an essential requirement as some KMTs have the ability to mono-, di-, or tri-methylate unmodified lysine residues[117]. Indeed, it is now well accepted that the subtle structural differences imparted by the three distinct states of lysine methylation (mono, di, tri) often confer unique biological outcomes depending on the methylation state of a particular residue[118,119].

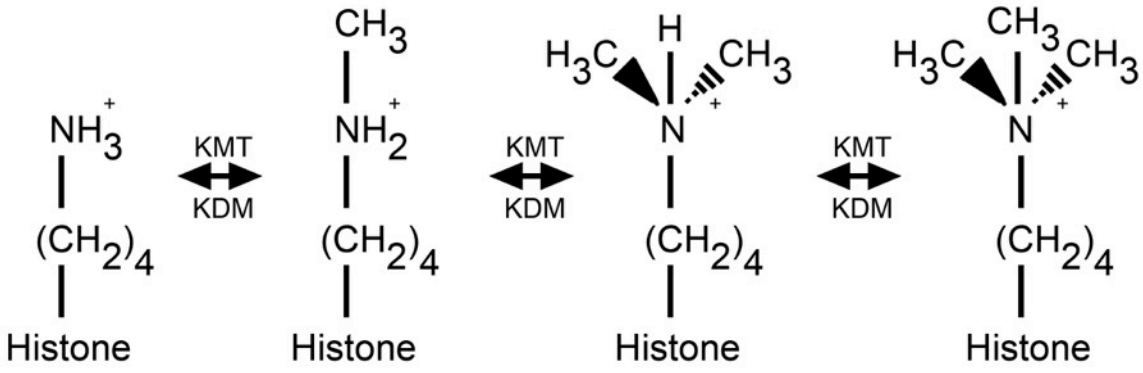

Figure 1.2: Histone Lysine Methylation
Shown here are the possible histone lysine methylation states, mono-, di-, tri-methylation, and an unmodified residue. The two classes of enzymes that catalyze forward and reverse reactions are lysine methyltransferases (KMT) and lysine demethylases (KDM), respectively. The forward reactions employ S-adenosyl methionine (SAM) as a methyl donor to the ε-amino group of the recipient lysine residue. The reverse reaction removes a methyl group from the histone. Notably, a positive charge is retained on all modification forms.

To date, two classes of KMTs have been identified. The first class known as SET-domain containing methyltransferases, contain a highly evolutionary conserved Su (var) 3-9, Enhancer-of-zest, Trithorax (SET) methyltransferase domain. KMTs from this class have been shown to target and methylate residues located on the 'unstructured' tail regions of histones H3 and H4 and include specific targets as H3K9, H3K27, H3K4, H3K36 and H3K20[120]. As indicated above, the specific histone residues modified and their methylation status will ultimately influence biological responses. For example, H3K9 can exist in many states including unmodified, acetylated, mono-methylated, di-methylated, or tri-methylated. H3K9 acetylation[121] and mono-methylation[119] are often associated with transcriptional activation, whereas H3K9 di-methylation[118] and tri-methylation[119] are frequently associated with transcriptional repression. Other examples include H3K27, which when mono-methylated[119] is associated with transcriptional activation but when di-[118] or tri-[119] methylated, is associated with strong transcriptional repression. All three H3K4 methylation states (mono, di, tri) are generally associated with transcriptional activation[121]. In addition, all three H3K36 methylation states, as well as H3K36 acetylation, are typically associated with transcriptional activation[122]. For H4K20, only mono-methylation has been identified and appears to be context dependent by either promoting transcriptional repression or activation[123].

The second class of KMT is defined by a lack of homology to the SET domain and the highly evolutionarily conserved DOT1L KMT is the only known member[124]. To date, only two DOT1L substrates have been identified, the androgen receptor (K349) and histone H3 (K79)[125]. Like all histone PTMs, the biological significance of H3K79 methylation is highly context dependent and modulated by several key factors including genomic location (mapping), state of methylation (mono-, di-, or tri-methylated), and abundance of methylation (occupancy levels).

The exact biological consequences associated with differential H3K79 methylation is an ongoing area of research and the H3K79 methylation 'code' is being gradually elucidated. Nevertheless, H3K79 methylation has been implicated in a diverse array of normal biological processes including transcription, telomere maintenance, DNA damage repair, and mitotic fidelity (detailed further in *Section 1.4.2)*[111,126,127].

1.4.1 H3K79 Methylation

Lysine residue 79 is located within the globular domain of histone H3 and can be mono-, di-, or tri-methylated by DOT1L[63,128]. To date, DOT1L is the only known H3K79 methyltransferase and *Dot1l*-deletion in mice causes a global loss of H3K79 methylation[129]. Both the PTM (H3K79 methylation) and "writer" (DOT1L) are highly conserved across multiple organisms including yeast[130], worms[131], flies[132], and humans[133], attesting to their biological importance. In addition, *Dot1l* is essential for mammalian development as germ line *Dot1l*-deletions are embryonic lethal in mice[134].

Like all histone PTMs, the biological significance of H3K79 methylation is highly context dependent and modulated by several key factors including genomic location, state of methylation (mono-, di-, or tri-methylated), abundance of methylation (occupancy levels), and cross-talk with other histone PTMs. The exact biological consequences associated with differential H3K79 methylation is an ongoing area of research and the H3K79 methylation "code" is gradually being elucidated. Nevertheless, H3K79 methylation has been implicated in a diverse array of normal biological processes including transcriptional activation, transcriptional repression, DNA repair, and chromatin dynamics[111,126,127].

Mass spectrometry and chromatin immunoprecipitation assays followed by DNA sequencing (ChIP-seq) have begun to characterize H3K79 methylation states (mono-, di-, or tri-methylated) and abundance at the global and gene-specific resolutions. Interestingly, in comparison to yeast where >90% of H3K79 residues are methylated, the global H3K79 methylation levels in mammals are substantially lower, and suggests a more refined H3K79 methylation "code" exists within higher eukaryotes[75,130]. Mass spectrometry was employed to characterize the global abundance of H3K79 methylation states across 24 asynchronously dividing human cell lines derived from both transformed and non-transformed tissues[75]. As one might predict, H3K79 methylation states were moderately variable across cell types. However, in the majority of cells, H3K79me1 was the predominant state (6-30%), H3K79me2 was the second most abundant (0.1-10%), while H3K79me3 was the least abundant (0-0.1%)[75]. The exact function of each methylation state has yet to be conclusively identified. Nevertheless, H3K79 methylation states appear to be non-random, conserved across several cell types, and strongly suggests an evolution of an H3K79-specific methylation 'code' within human cells.

At the genome-wide resolution, ChIP-Seq analysis revealed that H3K79 methylation patterns were non-random and preferentially enriched within certain DNA elements including protein coding sequences[135], miRNA coding sequences[136], enhancers, and origins of replication[137]. At the intragenic resolution, H3K79 methylation levels (mono, di, tri) peak immediately downstream from the transcriptional start site, gradually decreases throughout the first intron, and eventually attain minimal levels at downstream exons. For all three states, methylation occupancy positively correlated with gene transcription rates[138]. In other words, highly transcribed genes generally contained higher levels of H3K79 methylation within their transcribed regions, while lowly transcribed genes generally contained low levels. Although it is

not fully understood how H3K79 methylation regulates transcription, studies have shown that a subset of genes are downregulated and upregulated in *DOT1L* deleted cells, which suggests that transcription rates are at least partially modulated by H3K79 methylation[139]. On the other hand, Chapter 3 shows dynamic increases in global H3K79me2 levels that coincide with mitosis, when transcription is virtually non-existent. We further demonstrate that the loss of mitotic H3K79me2 causes a statistically significant increase in mitotic defects and aneuploidies. Accordingly, H3K79me2 may serve roles outside of transcription that are important for maintaining mitotic fidelity in human cells[73].

To date, an H3K79-specific KDM has not been identified. Nevertheless, evidence for a K79 KDM comes from studies showing dynamic changes in global H3K79 methylation levels. For example, a study using synchronized HeLa cells has shown that H3K79 methylation levels fluctuate during the cell cycle. H3K79 methylation levels decreased during S-phase, reached minimal levels during G2, and increased during mitosis[133]. Other evidence of a KDM comes from changes in H3K79 methylation during pre-implantation development in mice, where both H3K79me2 and H3K79me3 levels rapidly decrease soon after fertilization[140]. Finally, Chapter 3 presents evidence supporting mitosis-specific H3K79me2 dynamics that further suggest the existence of an H3K79-specific KDM.

1.4.2 H3K79 methylation, DOT1L (KMT4) and their Roles in Oncogenesis

Based on the above evidence, aberrant expression or function of DOT1L has the potential to adversely impact several biological processes, which ultimately could induce CIN and contribute to oncogenesis. In fact, DOT1L-depletion in either differentiated or undifferentiated embryonic stem cells resulted in aneuploidy, a hallmark of CIN[127]. H3K79 methylation is unique

in that DOT1L is the only known KMT to date. Interestingly, gene re-sequencing efforts from various major cancer types including breast, prostate, and CRC have identified several genetic alterations in DOT1L. Most notably, a sequencing study identified that approximately 11% of CRCs evaluated contained DOT1L alterations. When multiplying the frequency of DOT1L alterations identified in breast, prostate, and CRC, by the total number of Canadians diagnoses with these cancers each year, it is estimates that approximately 5,005 Canadians may contain genetic alterations in *DOT1L* (Table 1.2) and therefore could potentially benefit from a therapeutic strategy designed to exploit *DOT1L* defects[53,54,141]. Although untested, these results suggest that altered *DOT1L* expression and/or function, and presumably altered levels of H3K79 methylation, may be causal factors that contribute to cancer development and progression in various tumor types and warrant further investigations (see Chapter 3).

DOT1 was initially identified in a budding yeast screen for genes that affect telomere heterochromatinization (DNA silencing). Telomere heterochromatinization is accomplished through the recruitment and binding of the Silent Information Regulator complex (Sir complex) to proximal and distal regions of the telomere, which promote the spreading of heterochromatin to adjacent nucleosomes[142]. Interestingly, ChIP analysis in yeast revealed that *DOT1*-deletion, mutation of H3K79 to arginine (K79R), or *DOT1*-overexpression led to the mislocalization of the Sir complex and prevented efficient telomere silencing[142]. Loss of telomere silencing adversely impacts telomere structure and is associated with genome instability[143].

Studies in both yeast and mammalian cells suggest a role for DOT1/DOT1L and H3K79 methylation in the DNA damage response[144,145]. In fact, the DNA damage response protein 53BP1 interacts directly with methylated H3K79 at sites of DNA DSBs. Both DOT1L-depletion in human cells or H3K79R mutations in yeast reduced 53BP1 recruitment to sites of DNA

DSB[144,145]. Accordingly, *DOT1L* mutations may underlie a defective DNA damage response and contribute to oncogenesis. Further yeast studies also suggest a role for *DOT1* and H3K79 methylation in the cell cycle checkpoint response following DNA damage by ionizing radiation (IR). When yeast are challenged with IR under normal conditions, a G1 cell cycle arrest is evoked to allow for DNA repair to occur. Interestingly, yeast harboring inactivating *Dot1*-mutations do not arrest and continue to progress normally through the cell cycle[145]. Consequently within *Dot1*-deficient yeast cells, mutations may go unrepaired and progress through to DNA replication where they are permanently incorporated into the genome of subsequent daughter cells. Taken together, defects within the cell cycle checkpoint response allows for accumulation of mutations and is a known hallmark of cancer[146,147]. Additional evidence of the role DOT1L plays in maintaining genome stability is presented in Chapter 3 where mitotic increases in H3K79me2, mediated by DOT1L, are important for maintaining genome stability and mitotic fidelity in human cells.

1.5.0 Entering the Era of Highly-Efficient Human Genome Editing

Recent revolutionary advances in human genome editing technologies have marked the beginning of a new era of genomic research and discovery. For the first time, researchers possess the necessary tools to precisely edit the genomes of a wide variety of organisms with relative ease. Zinc finger nucleases, transcription activator-like effector nucleases, and most recently, type II Clustered Regularly Interspaced Short Palindromic Repeats (CRISPR-Cas9) represent three powerful technologies that grant researchers abilities to study specific genomic alterations in their endogenous locations. Although zinc finger nucleases and transcription activator-like

effector nucleases were the first to be identified, their use today is quickly becoming outdated as researchers favor the ease and efficiency of the CRISPR-Cas9 system.

In situ CRISPR-Cas9 genome editing represents a major leap forward over traditional approaches employed to study the biological consequences associated with cancer-associated mutations. Traditionally, these studies relied heavily on evaluating the aberrant biology associated with a particular cancer-associated mutation encoded within expression plasmids. In addition, these studies are often marred with experimental artifacts stemming from the episomal expression plasmids and the artificially strong promoters that frequently produce overexpression artifacts. Thus, a major benefit of endogenous genome editing is that the targeted loci maintain their spatial proximity with key regulatory elements including promoters, enhancers, and transcription factories. Accordingly, the CRISPR-Cas9 genome editing system holds great promise for life science research, medicine, and biotechnology.

1.5.1 Exploiting HRR and NHEJ for CRISPR-Cas9 Genome Editing

The CRISPR-Cas9 genome editing system uses a short CRISPR RNA guide strand (crRNA) and Watson-Crick RNA-DNA base pairing to bind genomic targets to generate a DNA DSB (Figure 1.3). The CRISPR-Cas9 genome editing technology requires the formation of a targeted DNA DSB as the first step in the editing process.

Understanding DNA DSB repair in human cells is an essential prerequisite to understanding CRISPR-Cas9 genome editing. DNA DSBs can be repaired through two major repair pathways, homologous recombination repair (HRR) or non-homologous end joining (NHEJ). HRR is an error-free process that employs a region of DNA homology as a template for high-fidelity repair. Homology regions can be either an endogenous homologous chromosome or

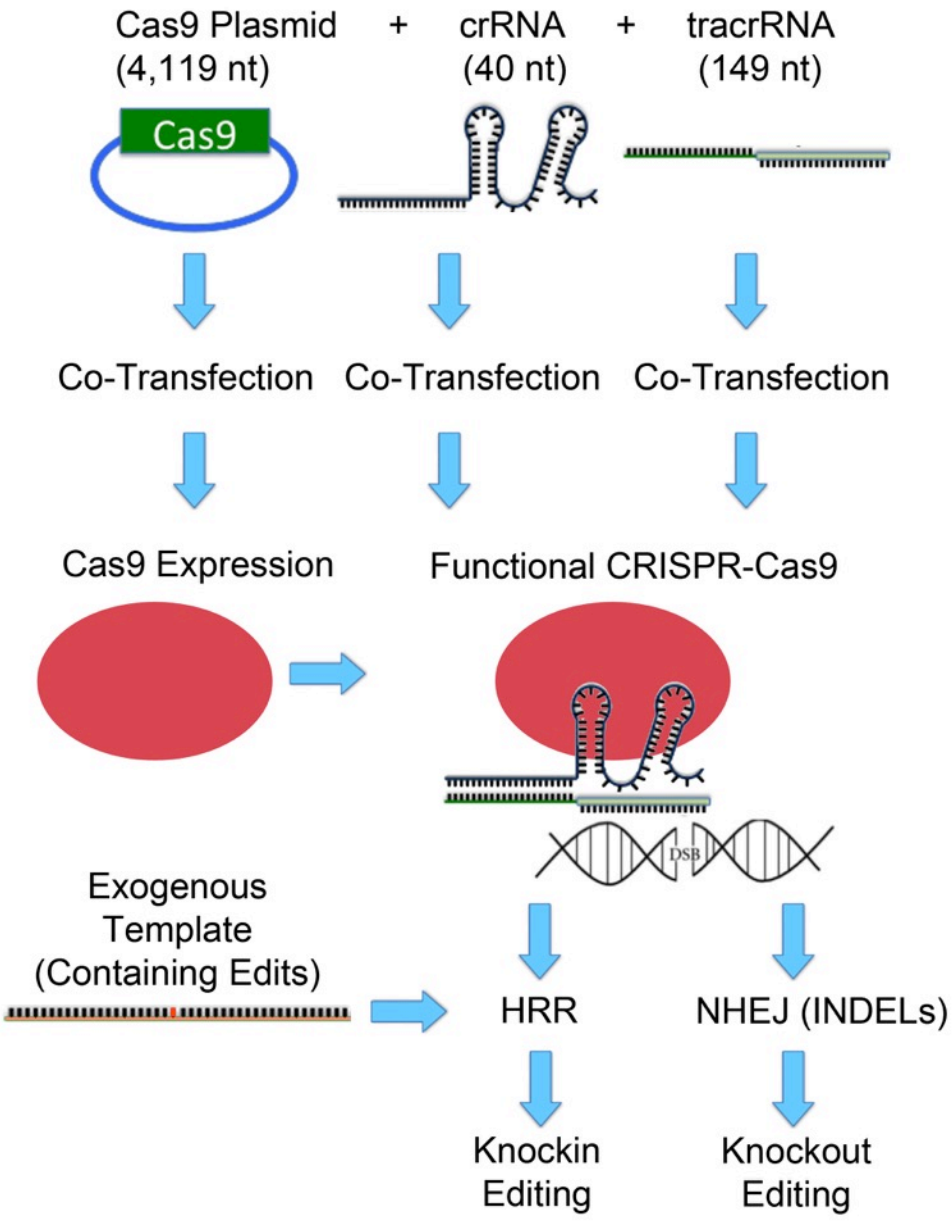

Figure 1.3: The CRISPR-Cas9 Genome Editing Approach
CRISPR-Cas9 genome editing begins with co-transfection of three essential CRISPR-Cas9 components (crRNA [small CRISPR RNA] + tracrRNA [trans-activating RNA] + Cas9 expression cassette) into target cells. Cas9 expression and assemble with crRNA and tracrRNA produce a functional CRISPR-Cas9 complex. Target DNA sequence binding causes CRISPR-Cas9 activation and the formation of a DNA DSB. DNA DSBs are repaired through either HRR or NHEJ. Various genome editing outcomes occur depending on whether HRR (knockin editing) or NHEJ (knockout editing) is employed, and if an exogenous template is provided.

an exogenously provided template containing edits that are to be incorporated into the genome. Based on this principle, HRR can be exploited to produce highly specific genome edits. First, two targeted DNA DSBs are generated at regions flanking the target locus. Next, an exogenous template containing 5' and 3' arms of homology and the specific complementary edited sequence is delivered to the break site. Arms of homology ensure the positioning of the template and HRR factors employ the template as a substrate for repair. The final step involves population screening. Following single cell sorting, PCR-based methods (e.g. surveyor assay) or antibody detection methods (e.g. Western blot, immunofluorescent imaging) are typically employed to identify clones containing appropriately edited genomes. Once identified, edited cells are often clonally expanded and cryogenically preserved for further study.

CRISPR-Cas9 edits can also involve the NHEJ pathway, which is an error-prone process that employs microhomologies present in single-stranded overhangs to direct immediate religation. Because single-stranded overhangs are not always compatible, imprecise repairs occur leading to indels (nucleotide insertions and deletions). Indels involving fewer or greater than triplet nucleotides induce frameshifts that ultimately alter the reading frame such that a premature stop codon is encountered that induces nonsense-mediated decay, a normal biological process that leads to the purposeful degradation of truncated protein. Accordingly, genetic inactivation of target genes (editing) is achieved by exploiting the error-prone nature of NHEJ and nonsense mediated decay.

1.5.2 CRISPR-Cas9 - A Historical Prospective

More than 20 years of research spanning the prokaryotic and eukaryotic kingdoms has led to the mammalian application of the CRISPR-Cas9 genome editing technology. Clustered

regularly interspaced short palindromic repeats were first discovered in the *Escherichia coli* iap gene, where a cluster of five 29 nucleotide direct repeats separated by 32 nucleotides spacers were first identified[148]. It was later discovered that over 40% of sequenced bacteria contained highly similar regular interspaced repeats[149]. In 2005, researchers determined that the 32 nucleotide spacers sequences preferentially targeted regions of the bacteriophage genome, suggesting they may play a role in bacterial adaptive immunity response against phage infection[150]. This was later confirmed in 2007, when the 32 nucleotide spacer sequence was found to function in concert with the adjacently encoded Cas9 endonuclease to cleave phage DNA[151]. By 2010, a series of successive events further elucidated the underlying CRISPR-Cas9 mechanism. First, a robust DNA-specific Cas9 endonuclease was identified in *Streptococcus thermophiles*[152]. Second, the tracrRNA molecule that plays a key role in physically scaffolding the Cas9 endonuclease to the crRNA guide strand was identified[153]. Finally, armed with this knowledge, two independent research teams in 2013 applied these key concepts to edit genes within mammalian cells[154,155]. The CRISPR-Cas9 system is arguable the greatest discovery in genome manipulation since RNA-interference and is projected to shape all facets of biomedical and biotechnology research.

1.5.3 Employing CRISPR-Cas9 to Target Mammalian Cells

CRISPR-Cas9 genome editing is a simple and straightforward process that starts with the design and synthesis of a crRNA targeting molecule. There are two main criteria for crRNA design. First, the 20 nucleotide crRNA target must immediately precede a Protospacer Adjacent Motif (PAM, a 5'-NGG sequence for the type II CRISPR-Cas9 systems)[156]. The PAM sequence is an essential consensus sequence that occurs on average every 8 bases within the human

genome and permits CRISPR-Cas9 binding, activation, and DNA cleavage. Second, the crRNA must exhibit target specificity. The question of specificity is easily addressed by online CRISPR design tools (http://crispr.mit.edu), which compare target and possible off-target sequences to estimate the likelihood of off-target binding. Only crRNA strands that are predicted to possess high specificity are selected for chemical synthesis and subsequent CRISPR-Cas9 targeting.

Typically all three essential CRISPR-Cas9 components (crRNA + tracrRNA + Cas9 expression cassette) are co-transfected into target cells. Within transfected cells, Cas9 is expressed and combined with the crRNA guide strand through tracrRNA scaffolding to form a functional complex. Once bound to target sequence, the activated CRISPR-Cas9 complex will generate a DNA DSB to initiate the genome editing process (Figure 1.3). Following a targeted DNA DSB, there are several possible outcomes; 1) DNA repair machinery employs a homologous chromosome to accomplish error-free HRR and the endogenous sequence is restored, 2) DNA repair machinery employs an exogenously provided template containing genome edits that are incorporated into the genome, 3) NHEJ is employed and the DNA DSB is accurately repaired to restore the endogenous sequence, and 4) NHEJ is employed and indels are incorporated to produce a frameshift mutation to cause genetic inactivation through nonsense-mediated decay. As expected, the potential outcomes presented above are cell cycle dependent as HRR only functions during S-phase and G2, while NHEJ can function throughout the cell cycle, but predominates in G1. Regardless of the immediate editing outcome, the final step requires identifying and isolating clones containing the desired genome edit(s). Multiple strategies are available to detect editing events including DNA sequencing, immunofluorescent labeling, and PCR-based detection assays.

Information gleaned from CRISPR-Cas9 genome editing technology will continue to impact research, medicine, and biotechnology in ways previously thought impossible. For the first time, the CRISPR-Cas9 editing system allows researchers to recapitulate complex genetically driven diseases in model organisms. Next generation sequencing has generated a wealth of data regarding the complex genomic alterations found in cancer. Understanding the functional significance of specific cancer-associated alterations and translating them into clinically relevant knowledge is the next logical step towards understanding the etiological origins of cancer.

1.6.0 Synthetic Genetic Targeting in Cancer

Many current chemotherapeutic strategies often involve the systemic administration of a drug whose cytotoxic effect is incapable of distinguishing cancerous from normal cells. Many common chemotherapeutics affect DNA replication or cellular division, and predominantly kill cancer cells based on their rapid proliferation rates relative to normal cells. As a result, adverse side effects often occur within normal cells, particularly those of the hematopoietic lineages as they frequently proliferate. Consequently, novel therapeutic strategies designed to selectively kill cancer cells while minimizing damage to healthy tissues are urgently needed.

Synthetic genetic interactions have been studied extensively in model organisms for decades and are now being explored for their therapeutic potential in human cancer contexts. Over the past decade, a growing body of evidence suggests that synthetic genetic approaches may be successful in delivering enhanced targeting and killing of cancer cells, and therefore may hold therapeutic potential for many cancers. Conceptually, these approaches seek to exploit the aberrant genetics (e.g., mutation, deletion or amplification) associated with tumor development,

and are predicted to evoke highly-specific killing of cancer cells while minimizing collateral damage within normal cells.

Synthetic genetic targeting of cancer cells represents a paradigm shift from traditional approaches and can be generally classified into two distinct categories; (1) synthetic lethal (SL) approaches that exploit the aberrant genetics associated with hypomorphic expression and/or function typically within tumor suppressor or DNA repair genes; and (2) synthetic dosage lethal approaches that exploit the aberrant genetics associated with hypermorphic expression and/or function typically within oncogenes. Although synthetic dosage lethality is an important area of research, the work presented in Chapter 5 focuses exclusively on SL approaches and thus only synthetic lethality will be detailed further below.

1.6.1 Synthetic Lethality

In 1946, Theodosius Dobzhansky, a geneticist and evolutionary biologist, first coined the term synthetic lethality to describe a lethal genetic interaction observed when two independently viable homologous chromosomes were allowed to recombine in *Drosophila pseudoobscura*[157]. Synthetic lethality is now used to describe a rare and lethal genetic interaction in which the outcome of a particular mutation or deletion is influenced by the presence of a pre-existing mutation or deletion (Figure 1.4A). However, if slowed growth rather than death is observed, a synthetic growth defect or synthetic sickness is defined. To relate these two concepts to a patient context, Synthetic Lethal (SL) strategies may result in cancer cell death or slowed growth, which could potentially translate into cancer cures or at least extend the survival and quality of life for those diagnosed with cancer. SL interactions generally occur via three basic mechanisms (Figure 1.5) that include; 1) partial ablation of two proteins contained within the same essential

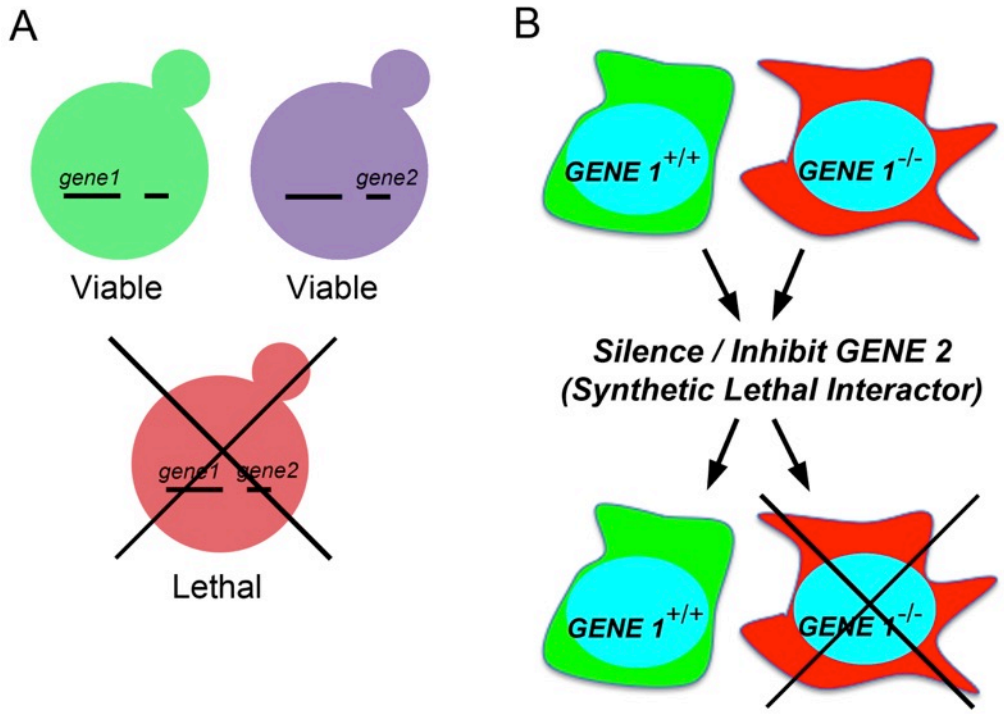

Figure 1.4: Synthetic Genetic Approaches in Yeast and Cancer
(**A**) Synthetic lethality is a rare genetic interaction that occurs when two independent and viable mutations or deletions (*gene1* [green yeast] or *gene2* [purple yeast]) result in death when combined (red yeast). (**B**) A cancer-associated hypomorphic mutation or deletion in a gene (e.g., *GENE1* is a deleted tumor suppressor or DNA repair gene) is selectively killed through a synthetic lethal approach by silencing or inhibiting the protein product encoded by *GENE2*. Green and red cells represent normal and cancerous cells, respectively.

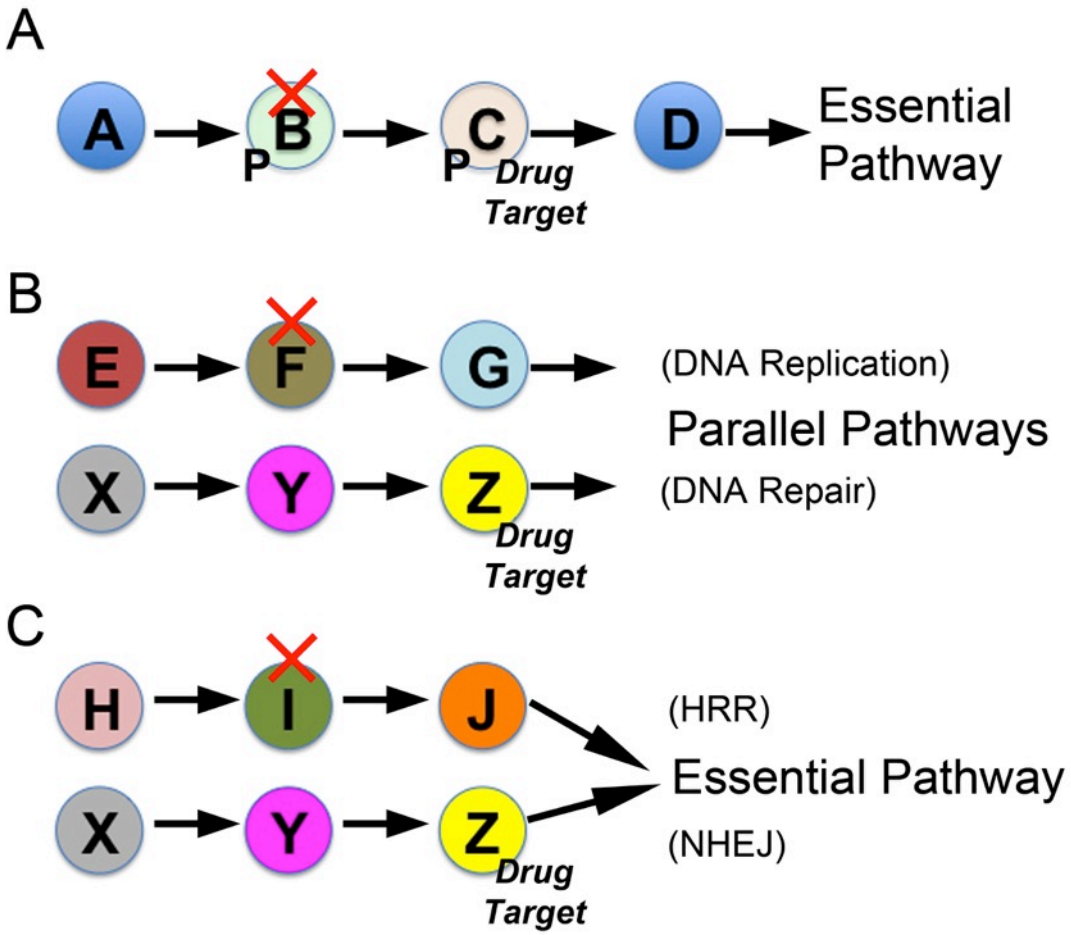

Figure 1.5: Conceptual Models of Various Synthetic Lethal Interactions
Conceptual models detailing three mechanisms that produce a SL phenotype (cell death). Circles represent genes, a red "X" identifies cancer-associated mutations or deletions, and "Drug Target" identifies candidate synthetic lethal interactors. (**A**) Partial loss of function (indicated by "P") of two gene products encoded within a single essential pathway (e.g., epistasis group), such that the pathway is no longer functional. (**B**) Ablation of two functions encoded within two distinct parallel pathways. For example, defects in DNA replication would lead to DNA errors requiring repair, and small molecule inhibitors preventing DNA repair will cause lethality. (**C**) Ablation of two functions encoded within two separate pathways that together impinge on a single essential process. For example, DNA DSBs can only be repaired through two pathways, namely HRR and NHEJ, and defects or inhibition within both pathways will induce lethality.

biological pathway, or epistasis group such that the pathway become non-functional, 2) ablation of two proteins contained within parallel pathways both of which are required for viability, and 3) ablation of two proteins within parallel pathways that together impinge on an essential biological pathway or process. This approach can be extrapolated to a cancer context (Figure 1.4B) where a somatic mutation in a gene normally required to maintain genome stability represents a sensitizing mutation that will render all subsequent progeny susceptible to attack by down-regulating or inhibiting a SL interactor[158-160].

In 1997, Hartwell and colleagues[161] suggested that cancer cells harboring somatic mutations represent genetically sensitized cells, relative to normal surrounding cells that may be susceptible to drug therapies by selectively targeting a SL interactor[162]. The development of both RNAi-based libraries and gene knockout models in a variety of model systems, coupled with significant advances in high-content and high-throughput approaches has now made it possible to screen, identify and validate SL interactors in a variety of model organisms and cancer-model systems. In fact, many researchers are now routinely employing these reagents, resources and approaches to identify novel candidate drug targets by uncovering therapeutically exploitable SL interactors of genes that are somatically mutated in cancer. In general, SL interactors have been identified through three independent, yet interrelated approaches that predominantly differ only in scale and scope. These approaches include; 1) knowledge-based direct tests, 2) cross-species candidate gene approaches, and 3) whole genome-based approaches. Chapter 5 employs a knowledge-based approach to identify a SL interaction between *RNF20* and *PARP1*, and is detailed below.

1.6.2 Therapeutically Exploiting Genome Instability

Somatic mutations[16,163] and epigenetic changes[17] underlying genomic instability are recognized as significant drivers in oncogenesis. Consequently, the genetic insults that drive cancer development are the very targets exploited through SL strategies. Extensive DNA re-sequencing efforts have identified a myriad of cancer-specific mutations, deletions, and amplifications in hundreds of candidate genes. Many of these genes are involved in biological pathways that affect genome stability including DNA repair, DNA replication, and chromosome segregation[53,54,141]. However, the exact aberrant mechanism associated with a particular insult is not required to identify an effective SL strategy, which relies on rare genetic interactions and can be identified by screening approaches if needed. Thus, SL approaches are custom-tailored to restrict their therapeutic effect(s) and killing to the specific aberrant genetic and epigenetic phenomena that occur within certain cancer cells.

Genetic changes that drive CIN are particularly attractive targets for SL targeting approaches. CIN is frequently observed in multiple tumors and positively correlated with poor patient outcome[164-166]. In general, most solid tumors arise through the accumulation of genetic defects within tumor suppressor genes and proto-oncogenes that encode loss-of-functions and gain-of-functions, respectively[167]. Proteins encoded by tumor suppressor genes such as TP53[168] and RB1[169] normally function to preserve genome stability. Under certain genotoxic stresses, these proteins generally function in the DNA damage response or by limiting cell cycle progression. Consequently, their diminished expression and/or function within cells are associated with increases in genome instability and are thus, pathogenic events in cancer development. Accordingly, targeting altered tumor suppressor or DNA repair genes that cause genome instability may be an effective way to restrict therapeutic targeting to cancer cells.

Most conventional strategies are designed to combat the gain-of-function associated with oncogenes (e.g., ERBB2[170]), and ignore tumor suppressor genes due to the inherent complexities in restoring a loss-of-function(s) mutation within a tumor cell. Synthetic genetic approaches represent an evolution from conventional strategies in that they can selectively target loss-of function(s) within tumor suppressor or DNA repair genes. This is possible because synthetic genetic approaches do not specifically target the aberrant gene *per se*, but rather exploit the defect by targeting a second unlinked gene partner (i.e., a synthetic genetic interactor). In principle, only cancer cells harboring specific defects will be susceptible to a SL attack. Normal cells which do not contain the defect, will remain unaffected. Thus identifying and characterizing synthetic genetic interactors of tumor suppressor genes is a critical step for the development of the next generation of candidate drug targets and therapeutic strategies.

1.6.3 Knowledge-Based Direct Tests to Identify Synthetic Lethal Interactors

Decades of biochemical and genetic research in many model organisms and systems coupled with the recent advancements in RNAi-based libraries and gene knockout models have significantly increased our knowledge about the biological components and processes that impact genomic stability. Many critical players within these pathways are well characterized including members involved in DNA replication, DNA repair and mitogenic signaling. Many research programs are now focused on determining how aberrant expression and/or function of these pathway components contribute to the development and progression of cancer. For example, a number of extensive gene re-sequencing efforts have been conducted in various cancers (e.g., colon, breast, lung, etc.) that have identified somatic alterations in a large number of genes that normally encode functions within pathways required to maintain genome

stability[53,54,141]. These mutations include nsSNP encoding single amino acid substitutions or premature stop codons, and gene amplifications and deletions that depending on the gene context (i.e., oncogene vs. tumor suppressor gene) may be associated with hypermorphic or hypomorphic expression and/or function, respectively. Candidate SL interactors of somatically altered tumor suppressor genes can be identified through knowledge-based approaches, which relies on fundamental knowledge about the molecular players and biological processes in which they participate. Knowledge-based tests are therefore predictions of SL interactors based on *a priori* knowledge of the molecular constituents of pathways and molecular network whose members are mutated in cancer.

1.6.4 The Prototypic Human Synthetic Lethal Interaction Between *BRCA1/2* and *PARP1*

The prototypic and perhaps best-studied example of a knowledge-based approach is the SL interaction observed between the genes *Breast Cancer 1* (*BRCA1*) or *Breast Cancer 2* (*BRCA2*) and *Poly ADP-ribose Polymerase 1* (*PARP1*). *BRCA1/2* are classically defined as breast cancer susceptibility genes but are also found somatically altered in a number of other cancers including ovarian[171], prostate[172] and CRC[53]. BRCA1/2 function in HRR, which is critical for the error-free repair of DNA DSBs[173]. PARP1 is involved in DNA single strand break repair, and traditionally functions in base excision repair[174]. Once activated following a DNA DSB, PARP1 catalyzes the cleavage of NAD+ to generate nicotinamide and negatively charged ADP-ribose. This process is repeated as PARP1 assembles a "string" of negatively charged branched-chain poly-ADP-ribose moieties to various targets including acceptor proteins, histones, DNA repair proteins, and finally itself (auto-modification)[175,176]. The single-stranded lesion when surrounded by negatively charged moieties serves as signal/docking site for the recruitment of additional DNA damage

repair proteins. PARP1 inhibition results in significant increases in unresolved single-stranded DNA breaks which can persist during DNA replication and convert to DSBs through replication drop-off events[177]. Armed with this information and the knowledge that single-strand breaks can be converted to DSBs[178], two research teams reasoned that PARP1 inhibition would ultimately increase DSBs, which would not be amenable to error-free repair within *BRCA1/2*-deficient backgrounds[179,180]. Indeed as predicted, targeted killing of the *BRCA1*/2-deficient embryonic stem cells occurred following PARP1 inhibition and/or silencing relative to *BRCA1/2*-proficient controls. The *BRCA1/2* and *PARP1* SL interaction was further substantiated in mouse models[179], thus validating PARP1 as a candidate drug target in *BRCA1/2*-deficient cancers.

The initial characterization of a SL interaction between *BRCA1/2* and *PARP1* spawned several small molecule inhibitor screens and studies to identify novel PARP1 inhibitors[181]. Many PARP1 inhibitors (e.g., Veliparib, CEP-9722, Rucaparib, E7016, BMN-673, etc.) are now being evaluated as single agents and in combinatorial approaches within a number of tumor types (see [[182]]). Olaparib (AstraZeneca; AZD-2281) is perhaps the best-known PARP1 inhibitor. Olaparib is an orally active compound that inhibits PARP1 through competitive binding with NAD+ and the first clinical report was published in 2009[183]. Early phase I clinical trials in breast cancers with *BRCA1/2*-deficiencies suggested that Olaparib was well tolerated and may exhibit a beneficial clinical response[184]. Taken together, PARP1 inhibition may represent the first highly efficient application of synthetic lethality to selectively kill *BRCA1/2*-deficient cancers in a precision medicine approach.

1.6.5 Employing Knowledge-Based Direct Tests to Identify Novel Synthetic Lethal Interactors

To expand beyond the prototypic *BRCA1/2 PARP1* example described above, a similar knowledge-based approach can be employed. There are several enzymes that function within the HRR pathway that likely exhibit hypomorphic expression and/or function in various cancer types. In fact, several cancer-associated alterations have been identified in important components of the HRR pathway including *RAD51*, *RAD54B*, and *RNF20*[52-54,171]. Accordingly, these as well as other HRR genes, may represent a repository of *PARP1* SL interactors that should be tested in human cells.

RNAi gene-silencing approaches are ideally suited for SL testing. A tumor suppressor or DNA repair gene (i.e., cancer query gene) can be downregulated to model cancer-associated alterations such as homozygous deletions, promoter hypermethylation, and nsSNPs that cause loss-of-function. Downregulating or inhibiting a candidate SL interactor through RNAi or small molecule inhibitors, respectively, and assaying for enhanced death compared to controls can identify a novel SL interaction. Beyond the caveats associated with the silencing efficacy of RNAi-based approaches and specificity concerns associated with small molecule inhibitors, there are additional factors that impact the success of a knowledge-based approach. These factors include cell- and tissue-specific gene expression profiles as well as genetic and functional redundancy within certain pathways. For example, if a candidate interactor is not normally expressed in a particular tissue, or alternatively a genetically redundant gene is expressed that functionally compensates for the candidate interactor, a lethal phenotype will not occur. Finally, the cellular contexts in which these experiments are performed such as transformed vs. immortalized cell types, or combinatorial approaches involving chemotherapeutics that induce

genotoxic stress, will undoubtedly impact gene expression profiles that may influence SL interactions. Nevertheless, this approach has been successfully applied (detailed below) and additional SL interactors continue to be identified using this approach.

1.7.0 Rationale, Hypotheses, and Aims

Cancer-associated alterations to the genes that encode histone modifying enzymes are now being identified as drivers in the oncogenic process. RNF20 is an essential H2B E3 ubiquitin ligase that functions in the HRR pathway and is altered in a variety of cancers including CRC, breast and prostate. Accordingly, I have developed the following three hypotheses regarding the study of hypomorphic RNF20 expression and/or function and its relevance to CRC. First, I hypothesize that DOT1l-depletion or -inhibition will reduce mitotic levels of H3K79me2 and cause CIN. Second, I posit that stably integrating a Cas9 expression cassette within the HCT116 genome will increase the CRISPR-Cas9 transfection and genome editing efficiency. Third, I hypothesize that *RNF20* and *PARP1* are human SL interactors and accordingly PARP1-silencing of -inhibition can selectively kill RNF20-depleted cells.

1.7.1 Chapter 3 - Mitotic Accumulation of Dimethylated Lysine 79 of Histone H3 is Important for Maintaining Genome Integrity During Mitosis in Human Cells

Recent studies have revealed that certain histone post-translational modifications exhibit dynamic and global increases in abundance that coincide with mitosis and exhibit essential roles in maintaining genomic stability. H2Bub1 is regulated by RNF20, an E3 ubiquitin ligase that is altered in many tumor types. Through an evolutionarily conserved trans-histone pathway, H2Bub1 is an essential pre-requisite for subsequent downstream di-methylation events at lysines

4 (H3K4me2) and 79 (H3K79me2) of histone H3. Although the role that RNF20 plays in tumorigenesis has garnered much attention, the downstream components of the trans-histone pathway, H3K4me2 and H3K79me2, and their potential contributions to genome stability remain largely overlooked. Accordingly, we have generated the following three experimental aims.

Aim 1: To identify and characterize the normal spatial and temporal progression pattern of RNF20, H2Bub1, and the downstream components of the H2Bub1 trans-histone pathway, H3K4me2 and H3K79me2.

Aim 2: To determine whether any of these PTMs display dynamic changes that are coincident with cell cycle progression.

Aim 3: To selectively deplete mitotic levels of H3K79me2 and evaluate CIN within a model colorectal cancer cell line (HCT116).

1.7.2 Chapter 4 - Generation and Phenotypic Characterization of an HCT116-Cas9 Expressing Cell Line

The E3 ubiquitin ligase RNF20 is an attractive molecule for detailed study as hypomorphic expression and/or function underlies genomic instability and occurs in a wide variety of cancer types. To date, studies characterizing the abnormal cell biology associated with hypomorphic *RNF20* expression have been limited to RNAi approaches, which only produce transient and/or incomplete protein depletion and may not accurately model the total loss of RNF20 predicted to occur in certain cancers. Therefore, to ultimately generate *RNF20*-deficent cells we have formulated the following three experimental aims.

Aim 1: To employ lentiviral transduction to generate stable HCT116 Cas9 expressing cell lines.

Aim 2: To phenotypically characterize HCT116-Cas9 expressing clones and identify a Cas9 expressing clone that displays similar characteristics to parental HCT116 cells.

Aim 3: To employ HCT116-Cas9 cells in combination with the CRISPR-Cas9 genome editing system to generate *RNF20*-deficient and *PPIB*-deficient cells.

1.7.3 Chapter 5 - *RNF20* and *PARP1* are Synthetic Lethal Interactors in Human Cells.

Several studies suggest that RNF20, and by extension mono-ubiquitinated histone H2B, play important roles in the DNA HRR response within human cells. Many groups have demonstrated that certain cancer cells bearing defects within the HRR pathway can be selectively killed through PARP1 depletion or inhibition. Accordingly, we have specifically generated three experimental aims to evaluate *RNF20* and *PARP1* as synthetic lethal interactors in human cells.

Aim 1: To determine if *RNF20* is SL with *PARP1*.

Aim 2: To determine whether PARP1 inhibitors can functionally substitute for siRNA and induce a SL phenotype.

Aim 3: To characterize the mechanism of cell death in *RNF20*-silenced cells following BMN673 treatment.

Chapter 2 - MATERIALS AND METHODS

2.1 Reagents

Appendix A (pg. 223) contains a list of solutions and reagents.

2.2 Cell Lines and Tissue Culture

For reference purposes, the cell lines employed in these studies are listed in Table 2.1. HeLa (human cervical carcinoma) and HCT116 cells (human colorectal carcinoma) were purchased from American Type Culture Collection (Rockville, MD). The immortalized (human telomerase) hTERT normal skin fibroblasts (hereinafter known as hTERT) were a generous gift from C. P. Case (University of Bristol, Bristol, UK). The Lenti-X 293T cells were purchased from Clontech Laboratories (Takara Bio Company, Mountain View, CA). HeLa and HCT116 cells were grown in modified McCoy's 5A media (HyClone, Logan, UT). hTERT and Lenti-X 293T cells were grown in Dulbecco's modified Eagle's media (DMEM, HyClone). All media was supplemented with 10% fetal bovine serum (FBS, Sigma-Aldrich, St. Louis, MO). Cell lines were authenticated on the basis of recovery, viability, growth, morphology, and spectral karyotyping[185]. All cells were maintained at subconfluent levels in a 37°C humidified incubator containing 5% CO_2. Cells were generally passaged every 2-3 days to maintain cell viability. In brief, cell culture media was removed by aspiration and cells were rinsed with sterile phosphate buffered saline (PBS) (Appendix A). To promote detachment from tissue culture plates, cells were incubated at room temperature for six min in the presence of trypsin (0.05% + 0.53 mM EDTA) (ThermoScientific). Trypsin was neutralized with complete media, cells were collected and pelleted via centrifugation (500×g, 21°C, 5 min, Sorvall Legend XFR; ThermoScientific), the supernatant was removed by aspiration, and the cell pellet was resuspended in sterile PBS to promote a single cell suspension.

Table 2.1: List of Cell Lines Employed

Cell Line[A]	Cat.[B]	Sex	Description	K. S.[C]	Approx. D.T[D]
HCT116	ATCC-CCL-247	Male	Epithelial Colorectal Carcinoma	Stable[F]	18 h
hTERT	C.P Case[E]	Male	Fibroblasts Foreskin Immortalized (Telomerase)	Stable	36 h
Lenti-X 293T	Clontech-632180	Female	Embryonic Kidney Transformed	Unstable	24 h
HeLa	ATCC-CCL-2	Female	Epithelial Cervical Carcinoma	Unstable	24 h

[A]Name of cell line employed in study
[B]Catalog number and supplier
[C]Karyotypic stability
[D]Approximate doubling time
[E]Cell line was a gift from C.P Case (University of Bristol, Bristol, UK)
[F] Karyotype: 45, X,-Y, der(10) dup(10)(q24;q26), t(10;16)(q24;q24), der(16) t(8;16)(q13;p13), der(18) t(17;18)(q21;p11)

2.3 Cell Synchronization and Mitotic Enrichment

A standard nocodazole arrest was employed to generate a mitotically-enriched cell population (Chapter 3). In brief, asynchronously dividing HCT116 or hTERT cells were grown in the presence of 15 nM nocodazole (Sigma-Aldrich) (Appendix A) for 14 h. Following treatment, a mitotic 'shake off' technique, which employs mechanical force to detach and collect loosely adherent mitotic cells, was used to further enrich the mitotic population. Flow cytometry (detailed below) was performed to confirm mitotic enrichment and determine the percentage of cells arrested in G_2/M relative to asynchronously dividing controls. In addition, digital imaging microscopy (detailed below) was performed on DNA-counterstained (Hoechst-33342 [300ng/mL], Sigma-Aldrich) chromatin to visually confirm cells were arrested in a prophase/prometaphase state.

2.4 Flow Cytometry

Flow cytometry was employed to confirm mitotic enrichment following nocodazole treatment as well as to evaluate changes in the cell cycle progression of DOT1L-silenced and DOT1L-inhibited cells compared to controls (Chapter 3). An overview of flow cytometry fixation, staining and analyses are detailed below.

2.4.1 Ethanol Fixation

Subconfluent and asynchronously-dividing or mitotically-enriched cells were detached, pelleted, resuspended in 10 mL ice cold PBS and transferred to a sterile 15 mL conical (Sarstedt). In order to remove residual amounts of trypsin, cell suspensions were pelleted (500×g, 21°C, 5 min, Sorvall Legend XFR), PBS was removed by aspiration and cells were resuspended

in 10 mL ice cold PBS. To determine cell concentrations, 40 µl of cell solution was combined with 40 µl of 0.2% Trypan Blue Stain (Invitrogen) and approximate cell concentrations were identified using a Cedex XS Cellular Analyzer (Roche). A volume representing approximately 2.0×10^6 cells was transferred to a 5 mL round-bottom tube (BD Falcon; VWR, Mississauga, Ontario), cells were pelleted by centrifugation (500×g, 21°C, 5 min, Sorvall Legend XFR) and PBS was removed by aspiration. To avoid cell aggregates, cells were fixed and permeablized with ice-cold 70% ethanol (Appendix A), added in a drop-wise manner, under continuous agitation. Cells were stored at 4°C for a minimum of 16 h prior to propidium iodide staining and flow cytometric analysis.

2.4.2 Propidium Iodide Staining

Following ethanol fixation, cells were pelleted (700×g, 4°C, 10 min, Sorvall Legend XFR), ethanol was removed and cells were resuspended in a 1 mL PBS solution containing 60 µM propidium iodide (Appendix A) and 25 µM RNase A (ThermoScientific) (Appendix A). Cells were protected from light and incubated at 37°C for 30 min. Finally, cells were pelleted, resuspended in 500 µl PBS and stored on ice prior to flow cytometric analysis.

2.4.3 Flow Cytometric Analysis

All cells were analyzed using a Becton Dickinson FACS Calibur cytometer (BD Cell Quest Pro Software, version 0.4.cf2b) according to standard procedures. Initial instrument setup was performed on asynchronously dividing control cells counterstained with propidium iodide. Events were gated according to standard forward scatter and side scatter parameters. Three replicates of 10,000-gated events were collected for each sample. Flow cytometry data were

imported into FlowJo (version 10.0.5) for analysis. Events representing cellular aggregates, based on standard FL2-A and FL2-W parameters, were excluded from analysis. Finally, the cell cycle analysis option contained within FlowJo was utilized to determine the percentage of cells within G0/G1, S and G2/M. Representative cell cycle histograms were generated in FlowJo and exported to Photoshop Creative Suite 5 (Adobe) for figure assembly.

2.5 Immunoblotting

In general, immunoblots were performed to identify the relative protein abundance following depletion by siRNA or shRNA approaches (Chapter 3 and 5). In addition, immunoblots were employed to identify the relative abundance of specific histone PTMs throughout the cell cycle (Chapter 3) and Cas9 expression levels (Chapter 4). The primary and secondary antibodies employed in all immunoblot assays and their working dilutions are listed in Table 2.2. Generally, loading controls included α–tubulin; unmodified histone H3; or copper phthalocyanine tetrasulfonic acid tetrasodium salt (CPTS) (Appendix A), a protein stain. For whole cell lysates (detailed below), 30 μg was loaded per well. For nuclear extracts (detailed below), 4 μg was loaded per well.

Table 2.2: List of Antibodies Employed

Epitope[A]	Cat.[B]	Species	[Immunoblot][C]	[IIF][D]	Chapter[E]
Primary Antibodies					
α-Tubulin	ab7291	Mouse	1 in 20,000	n/a	3-5
RNF20	ab32629	Rabbit	1 in 8,000	1 in 400	3-5
H2B	ab1790	Rabbit	1 in 7,000	n/a	3, 5
H2Bub1	05-1312	Mouse	1 in 10,000	1 in 200	3, 5
H3	ab10799	Mouse	1 in 6,000	n/a	3
H3K4me2	ab32356	Rabbit	1 in 10,000	1 in 400	3
H3K79me2	ab3594	Rabbit	1 in 15,000	1 in 400	3
H3S10Phos	ab14955	Mouse	n/a	1 in 2,000	3
DOT1L	ab180483	Mouse	1 in 2,000	n/a	3
Cas9	MAC133	Mouse	1 in 10,000	1 in 200	4
PPIB	ab16045	Rabbit	n/a	1 in 400	4
PARP1	ab6079	Rabbit	1 in 3,000	n/a	5
γ-H2AX	ab2893	Rabbit	n/a	1 in 1,000	5
Caspase-3 (Cleaved)	ab13847	Rabbit	n/a	1 in 1,000	5
Secondary Antibodies					
Rabbit IgG-Alexa Fluor 488	A11034	Goat	n/a	1 in 200	3-5
Mouse IgG-Cy3	A10521	Goat	n/a	1 in 200	3-5
Rabbit IgG-HRP	111-035-006	Goat	1 in 15,000	n/a	3-5
Mouse IgG-HRP	115-035-146	Goat	1 in 10,000	n/a	3-5

[A]Epitope targeted by antibody
[B]Catalog number
[C]Antibody concentration employed for immunoblot detection
[D]Antibody concentration employed for indirect immunofluorescent imaging
[E]Thesis Chapter where reagent was employed
n/a: not applicable

2.5.1 Whole Cell Lysate Preparation

In general, protein lysates were directly harvested from treated or control cells grown in 6-well tissue culture plates (BD Falcon; VWR). All protein extraction steps were performed at 4°C. Briefly, growth media was removed and cells were rinsed twice with ice-cold PBS. Tissue culture plates were equilibrated to 4°C (~5 min) prior to the addition of 300 µl/well radioimmunoprecipitation assay buffer (RIPA, Appendix A) plus protease inhibitor (cOmplete EDTA-free; Roche) (Appendix A). Following a 5 min incubation period, whole protein lysates were collected and transferred to a sterile 1.5 mL microcentrifuge tube. Samples were further disrupted by probe sonication (Branson Ultrasonics, Danbury, Connecticut, 2 sec, 50% duty cycle, output 6) and insoluble cellular debris was pelleted by table top centrifugation (13,225×g, 4°C, 1 min, Heraeus Biofuge Fresco, ThermoScientific). The protein soluble supernatant was transferred to a sterile 1.5 mL microcentrifuge tube and samples were place at -80°C for storage prior to protein quantification by bicinchoninic acid assay (ThermoScientific)(detailed below).

2.5.2 Acid-Extraction of Nuclear Proteins

Cells were detached, pelleted, washed twice in ice cold PBS, counted, and resuspended to a concentration of 10.0×10^6 cells/mL. Approximately 10.0×10^6 cells (i.e. 1 mL) were transferred to a sterile 1.5 mL microcentrifuge tube and pelleted by table top centrifugation (500×g, 4°C, 5 min). PBS was decanted and cells were lysed for 1 min in 1.0 mL ice-cold nuclei buffer (Appendix A) plus protease inhibitor (Roche). Nuclei were pelleted by table top centrifugation (3,000×g, 4°C, 2 min, Heraeus Biofuge Fresco, ThermoScientific) and the soluble cytoplasmic fraction (supernatant) was transferred to a sterile 1.5 mL microcentrifuge tube and stored at -80°C. To extract the acid-soluble nuclear proteins (predominantly histones), nuclei

were resuspended in 570 μL of de-ionized water, sulfuric acid was added to a concentration of 0.4 N, and samples were incubated at 4°C for a minimum of 1h to a maximum of 12 h. Insoluble nuclear debris was pelleted by table top centrifugation (13,225×g, 4°C, 10 min, Heraeus Biofuge Fresco, ThermoScientific) and the acid-soluble fraction (supernatant) was transferred to a sterile 1.5 mL microcentrifuge tube containing 60 μL Tris Buffer, pH 8.0 (Appendix A). The acidic solution was neutralized with 40 μL of concentrated sodium hydroxide (10N) and samples were placed at -80°C for storage prior to protein quantification by bicinchoninic acid assay (detailed below).

2.5.3 Protein Quantification via Bicinchoninic Acid Assay

Protein concentrations were quantified using a Pierce Bicinchoninic Acid Assay kit (ThermoScientific). In order to generate a standard curve, 9 samples of known concentrations were arrayed in triplicate across a 96-well plate (Corning). For unknown samples, 5 μL aliquots were deposited in triplicate into adjacent wells. The assay plate was incubated at 37°C for 45 min in the dark. Following incubation, a Cytation 3 (BioTek) high-content imager was employed to acquire 562 nm absorbance measurements for each well. Standard curves were generated by Gen5 software and unknown concentrations are calculated

2.5.4 Protein Resolution via Electrophoresis and Immunoblotting

Samples were diluted to identical concentrations and denatured for 10 min at 95°C in the presence of 5× sample loading buffer (Appendix A). All denaturing polyacrylamide Mini-Protean TGX Precast Gels were purchased from Bio-Rad (Hercules, California). Generally, larger proteins (>50 kDa) were resolved on a 7.5% precast gel and smaller proteins

(predominantly histones, <50 kDa) were resolved on a 4-20% gradient gel. Following denaturation, approximately 4 μg or 30 μg of acid-soluble or whole cell lysate was loaded in each well, respectively. Gels were electrophoresed at a constant 140 volts (Bio-Rad, Power Pac 1000) in a Mini-Protean electrophoretic tank (Bio-Rad) containing 1X Running Buffer (Appendix A) for approximately 65 min at 4°C. Proteins were electrophoretically transferred at a constant 14 volts to an activated 0.45 μm polyvinylidene fluoride (PVDF) membrane in a Trans-Blot SD Semi-Dry Transfer Cell (Bio-Rad) containing 1X transfer buffer (Appendix A), for approximately 45 min at room temperature. Protein transfer was verified by Copper phthalocyanine 3,4',4'',4'''-tetrasulfonic acid tetrasodium salt (CPTS) (Appendix A) staining, a total protein stain. Briefly, membranes were lightly agitated for 10 min in 25 mL CPTS followed by a 5 min wash in a Tris-buffered saline solution containing 0.1% Tween 20 (TBST, Appendix A). After protein transfer was confirmed, membranes were blocked with 5% non-fat milk (Appendix A) in TBST at room temperature for 1h under gentle agitation. Following blocking, membranes were sealed in a plastic film containing a primary antibody solution (antibody + TBST + 5% milk) diluted to an appropriate working concentration (Table 2.2). Membranes were incubated overnight at 4°C on an orbital shaker. The next day, membranes were washed three times with TBST (10 min each) and incubated with a secondary antibody solution (antibody + TBST + 5% milk) diluted to an appropriate working concentration (Table 2.2). Membranes were incubated for 1 h at room temperature under gentle agitation. Following secondary antibody incubation, membranes were washed as above, and incubated in 4 mL of enhanced chemiluminescent substrate (SuperSignal West Dura, ThermoScientific) for 5 min at room temperature. Finally, membranes were deposited on to a clear plastic sheet and immunoblot images were acquired using a MyECL imager equipped with a 16-bit, 4.2 megapixel,

thermoelectrically regulated (-25°C) charge-coupled device camera (ThermoScientific). Immunoblot exposure times were optimized to produce zero pixel saturation and maximum dynamic range. Images were saved as Tiff files and figures were assembled in Photoshop Creative Suite 5 (Adobe).

2.5.5 Semi-Quantitative Immunoblot Analysis

Semi-quantitative immunoblot analyses were performed in all Chapters to evaluate changes in protein abundance. Following image acquisition, Tiff images were imported into ImageJ (v1.48s) and raw mean signal intensities were measured for proteins of interest and loading controls. In addition, background signal intensities were measured for proteins of interest and loading controls. Background signal intensities were subtracted from the raw mean signal intensities to yield a background-subtracted net signal intensity that was employed for subsequent semi-quantitative calculations. To account for minor variations in protein loading, proteins of interest were normalized to their respective loading controls. Normalized values were divided by experimental controls (e.g. siGAPDH), and fold-change was calculated and annotated within immunoblot figures using Photoshop Creative Suite 5 (Adobe).

2.6 siRNA-Based Silencing

For siRNA silencing, a lipid-based transfection reagent (RNAiMAX; Invitrogen, Carlsbad, CA) was employed to deliver siRNA duplexes into HCT116 and hTERT cells. HCT116 cells were seeded in six-well plates at a density of 210,000 cells/well and permitted to grow for 24 h prior to treatment. hTERT cells were seeded in six-well plates at a density of 130,000 cells/well and permitted to grow for 24 h prior to treatment. Cells were transfected

according to the standard RNAiMAX protocol with 30 pmol of siRNA diluted in 6 μl of RNAiMAX. Cell culture media were replaced 24 h post-transfection and every 48 h thereafter. Immunoblots were preformed as described to assess changes in protein abundance following silencing. All siRNAs were purchased from Dharmacon. The following catalog numbers were employed: RNF20 LU-007027-00-0002, DOT1L LU-014900-01-0002, PARP1 LU-006656-03-0002. Sequences are property of Dharmacon.

2.7 DOT1L Inhibition

For DOT1L inhibition, cells were seeded as above and incubated with 5 μM SGC0946 (Appendix A) (Selleck Chemicals, Houston, TX) or DMSO (vehicle control). Cells were incubated with chemicals for either 2 or 48 h prior to analysis (Chapter 3).

2.8 Mitotic Chromosome Spreads

Mitotic chromosome spreads were employed to evaluate the number of chromosomes within DOT1L-silenced or -inhibited cells (Chapter 3) and HCT116-Cas9 expressing clones (Chapter 4). Following treatment, cells were detached and pelleted by centrifugation. Cell culture media was removed and cells were incubated in a 5 mL 75 mM KCl hypotonic solution (Appendix A) at room temperature for 10 min. Following hypotonic treatment, cells were chemically fixed with a 1 mL mixture of methanol and acetic acid at a ratio of 3:1. Three rounds of cell pelleting, fixative removal and fresh fixative replacement were performed. Finally, cells were resuspended in 5 mL fixative and stored at 4°C for subsequent use. To generate mitotic spreads, cell solutions were drawn into a 200 μl pipettor and dropped onto a pre-cleaned Surgipath glass slide (ThermoScientific) at a distance of approximately 0.5 m. To fix

chromosomes *in situ*, slides were desiccated on a 37°C hotplate and immediately submerged in a 50% acetic acid solution. Chromatin was stained with 0.5 μg/mL 4',6-diamidino-2-phenylindole (DAPI, Appendix A) in mounting media overnight at 4°C and slides were imaged with a 40× objective by digital imaging microscopy. Images were imported into ImageJ and a minimum of 100 mitotic chromosome spreads for each condition was manually evaluated. Chromosome counts were exported to Prism (GraphPad) and statistically significant differences in chromosome numbers were evaluated.

2.9 Mitotic Defect Analysis Based on Chromatin Morphology

HCT116 cells were grown in 96-well optically clear bottom tissue culture plates (Nunc, ThermoScientific) and treated as detailed in DOT1L silencing and DOT1L inhibition above. To easily identify mitotic cells, samples were immunolabeled with an antibody targeting phosphorylated serine 10 of histone 3 (H3S10Phos)[70]. Nine non-overlapping images/well were acquired with a Cytation 3 Imager (BioTek) equipped with a 10× long working distance air objective (UPLFLN103; NA = 0.3). Each experimental condition was repeated at least four times and a minimum of 275 mitotic cells were evaluated per treatment condition (siGAPDH, siDOT1L, DMSO, SGC0946). Mitotic defects were visually identified by aberrant chromatin morphology and included chromosome congression errors, lagging chromosomes, and anaphase bridges. The frequencies of mitotic defects were calculated and the fold-change relative to controls (siGAPDH or DMSO) are presented.

2.10 Lentiviral and Stable Cell Line Production

High-titer Edit-R Lentiviral Cas9 nuclease vectors were directly purchased from Dharmacon (Lafayette, CO) and employed in Chapter 4 to produce stable HCT116-Cas9 cell lines (detailed in results section, Chapter 4). Lentiviruses were generated and employed in Chapter 5 to produce stable HCT116-shRNA cells (detailed below).

2.10.1 pGIPZ Lentiviral shRNA Plasmid Preparations

shRNAs were purchased from Dharmacon. Catalog number RNF20 RHS4531-EG56254. Sequences are property of Dharmacon. 5 mL Luria-Bertani broth solutions containing 60 μg/mL carbenicillin (Appendix A) (Sigma Aldrich) were inoculated with a 5 μl inoculum derived from pre-existing pGIPZ shRNA glycerol stocks. Broth cultures were grown overnight at 37°C under moderate agitation. The following day, plasmids were harvested and purified using a QIAprep Spin Miniprep kit according to the manufacturers directions (Qiagen). DNA concentrations and purities were measured using a Nano-Drop spectrophotometer (ThermoScientific). DNA was stored at -20°C.

2.10.2 Lentiviral Production

For lenti-viral production, approximately 4.5×10^6 Lenti-X 293T cells were seeded into a 100mm plate and incubated at 37°C for 24 h in DMEM media containing 10% tetracycline-free FBS. The following day, cells were transfected as detailed in the Lenti-X HTX Packaging system protocol (Clontech). Briefly, 7 μl of pGIPZ shRNA DNA (1 μg/ μl) was mixed with 36 μl of Lenti-X HTX Packaging Mix 2 (Clontech) and 557 μl of Xfect reaction buffer (Clontech) in a 2 mL microcentrifuge tube. In a separate 2 mL microcentrifuge tube, 7.5 μL of Xfect polymer

(Clontech) was mixed with 592.5 μL of Xfect reaction buffer. Both tubes were agitated for 10 seconds, mixed together, and incubated at room temperature for 10 minutes to allow nanoparticle complexes to form. The transfection solution was added drop-wise to the cells and plates were incubated for 12 h at 37°C. Following transfection, cell culture media was replaced with fresh pre-warmed DMEM containing 10% tetracycline-free FBS. Cells were grown for an additional 48 h at 37°C prior to lentivirus harvesting. A commercially available lentiviral detection kit (Lenti-X GoStix, Clontech) was employed to confirm the presence of virus. Lentivirus containing media was filtered through a low protein binding 0.2 μm filter (Millipore, Billerica, MA) to remove cellular debris, transferred to a sterile 50 mL conical, and cooled to 4 °C. A commercially available Lenti-X concentrator kit (Clontech) was employed to increase lentiviral concentrations. Approximately 3 mL of Lenti-X concentrator was added to the viral solution and the mixture was incubated at 4°C for 16 h. Following incubation, lentiviruses were pelleted by centrifugation at 1,500 ×g for 45 min at 4 °C. The clarified supernatant was removed by aspiration and discarded according to biosafety standards for lentiviral containing media. The lentiviral pellet was resuspended in 1 mL sterile ice-cold PBS and stored at -80°C prior to use.

2.10.3 Lentiviral Transduction

For lentiviral transduction, approximately 50,000 HCT116 cells/well were seeded into a 24-well plate (Costar, Corning, NY) and infected the following day. Lentiviral titers were not determined. Accordingly, a 2-fold serial dilution ranging from a virus-to-media ratio of 1:2 to 1:64 was performed across 6 wells to limit the number of cells infected and increase the likelihood of a single integration event within target cells. Cell culture media was removed and 100 μl of transduction solution (serum-free media plus diluted virus) was added. Cells were

incubated at 37°C for 4 h. Following the initial transduction period, 400 μl of pre-warmed complete media was added and cells were incubated overnight. The following day, viral-containing media was disposed of according to biosafety standards and 500 μl of pre-warmed complete media was replaced. Approximately 48 h post-transduction, cell culture media was replaced with selective media (McCoy's 5A + 1 μg/mL Puromycin [Clontech]). Cells were cultured in selective media until distinct colonies were observed (~5 days). To prevent selecting cells with multiple integration events, only wells containing 10 distinct colonies or less were chosen for expansion. Cells were expanded and early passages were cryogenically preserved.

2.11 Immunofluorescent Labeling

Immunofluorescent labeling and imaging was employed in to identify changes in protein abundance and localization throughout the cell cycle (Chapter 3), Cas9 expression levels (Chapter 4), and the abundance of surrogate markers of DNA damage and Apoptosis (Chapter 5).

2.11.1 Indirect Immunofluorescent Labeling.

Asynchronous cells were seeded onto sterilized glass coverslips one day prior to analysis, such that they were ~80% confluent the following day. Cells were fixed in a 4% formaldehyde PBS solution (Appendix A) for 10 min at room temperature. Following fixation, fixative was removed and cells were rinsed twice with PBS. Cells were permeablized in a 0.5% Triton X-100 PBS solution (Appendix A) for 10 min at room temperature and rinsed twice with PBS. Coverslips were inverted onto parafilm containing 30 μL of primary antibody solution (antibody + PBS) diluted to an appropriate working concentration. Table 2.2 presents the antibodies and dilutions employed. Coverslips were incubated at room temperature overnight in a humidified

chamber to prevent desiccation. Coverslips were rinsed twice in PBS, once in a 0.1% Triton X-100 PBS solution (Appendix A), and inverted onto parafilm containing 30 μl of secondary antibody solution (antibody + PBS) diluted to 1 in 200. Coverslips were incubated at room temperature for 2 h in a humidified chamber protected from light. Coverslips were rinsed twice in PBS, once in a 0.1% Triton X-100 PBS solution, twice in PBS, inverted onto a glass slide containing ~10 μL of DAPI in mounting media, and stored at 4°C overnight protected from light. The following day, slides were rinsed with nano pure water to remove residual PBS solids prior to imaging. Several assays were performed to evaluated antibody specificity (*see 2.12 below*).

Notably, an additional antigen retrieval step was required prior to indirect immunofluorescence labeling with the H2Bub1 antibody. Briefly, cells were fixed in paraformaldehyde for 10 min, washed twice in nanopure water, permeablized with ice-cold (-20°C) acetone for 2 min, and rinsed five times with nanopure water. Cells were incubated in 2 N HCl for 15 min at room temperature prior to neutralization with two washes of 0.1 M NaBorate (pH 8.5) for 2 min each. Cells were incubated in PBS for 5 min prior to indirect immunofluorescent labeling as detailed above.

2.12 Antibody Validation - Peptide Competition and Dot Blot Assays

Antibody epitope specificities were evaluated by immunofluorescent peptide competition assays and dot blot assays. Briefly, the H2Bub1, H3K4me2, and H3K79me2 antibodies were pre-incubated at a 10-fold molar excess with specific or nonspecific peptides at 4°C for 16 hr and indirect immunofluorescent imaging was performed as described. Dot blot assays were performed by dispensing 20 ng of each peptide (controls or experimental) onto a 0.2-μm PVDF membrane. Peptide aliquots were allowed to dry and antibody specificity was determined using a

standard immunoblot blot approach. Although the above standard antibody specificity assays were performed, there remains the possibility of target epitope occlusion by a histone PTM found on a nearby residue. The H2Bub1 peptide was custom synthesized by Biomatik (Cambridge, ON, Canada), while the remaining peptides were purchased from Abcam: H2B (ab5489), H3 (ab7228), H3K4me1 (ab8895), H3K4me2 (ab7766), H3K4me3 (ab8580), H3K79me1 (ab4555), H3K79me2 (ab4556), and H3K79me3 (ab4557).

2.13 Image Acquisition

In general, two complementary digital imaging platforms were utilized, widefield high-resolution imaging and widefield high-content imaging (Chapter 3-5). High-resolution digital imaging microscopy was performed using an AxioImager.Z1 (Carl Zeiss, Toronto, ON) microscope equipped with a 12-bit gray scale AxioCam HRm charge-coupled device camera and a Z-stage motor. All images were collected with either a 40x oil-immersion plan-neofluar lens [numerical aperture (NA) = 1.3] or a 63x oil-immersion plan-apochromat lens (NA = 1.4). All three-dimensional (3D) image series were acquired at 200-nm intervals and saved as 16-bit Tiff images. High-content imaging microscopy was performed using a Cytation 3 imager (BioTek, Winooski, Vermont) equipped with a 16-bit gray scale 1.25 megapixel Sony charge-coupled device camera and a motorized stage. All images were automatically focused and collected with a 10× long working distance air lens (UPLFLN103; NA = 0.3). All images were saved as 16-bit Tiff images.

2.14 Image Analyses

Detailed below are the types of image analyses employed within this thesis.

2.14.1 Semi-Quantitative Signal Intensity Normalization and Analyses

Semi-quantitative immunofluorescent imaging was employed to compare the levels of H3K79me2 between interphase and mitotic cells and identify the role DOT1L depletion/inhibition plays in modulating mitotic levels of H3K79me2 (Chapter 3). Two-dimensional indirect immunofluorescent imaging was employed to acquire a minimum of 20 interphase and 20 mitotic cells (prophase, prometaphase, and metaphase) for control and experimental conditions. All images were collected with identical exposure times and semi-quantitative imaging analyses were used to reveal changes in the global abundance of a particular fluorescently labeled epitope. Images were imported into ImageJ software (v1.48s) and mean fluorescent signal intensities were determined for both the DAPI and H3K79me2 channels on a cell-by-cell basis. To account for increases in histone content associated with DNA replication, H3K79me2 signal intensities were normalized to the corresponding DAPI intensities. Normalized H3K79me2 signal intensities were exported into Prism v6 software for statistical analyses.

2.14.2 Line Scans

Line scans were employed to demonstrate that epitopes investigate within Chapter 3 (RNF20, H2Bub1, H3K4me2 and H3K79me2) localize within the nucleus in a non-random pattern. A single representative line was placed through an entire nucleus for each epitope investigated and a fluorescence intensity profile was generated for each channel using the plot profile tools in ImageJ (v1.48s). Relative fluorescent intensity values were plotted in Prism to allow for the comparison of fluorescent intensities between channels on a pixel-by-pixel basis.

Graphs were exported as Tiff images and assembled in panels using Photoshop Creative Suite 5 (Adobe).

2.14.3 High-Content Analysis of Dual siRNA Silencing Experiments

High-content microscopy was employed to identify the number of cells remaining following dual silencing experiments (siGAPDH + siRNF20) or (siGAPDH + siPARP1) or (siRNF20 + siPARP1) (Chapter 5). Approximately 210,000 HCT116 cells or 130,000 hTERT cells were seeded into each well of a 6-well plate. Cells were incubated at 37°C for approximately 24 h prior to siRNA transfection. HCT116 and hTERT cells were transfected as detailed above (*2.6 siRNA-Based Silencing*). Approximately 24 h post-transfection, cells were detached, pelleted, resuspended in PBS and counted. Cells were diluted in pre-warmed complete media to a concentration of 4,000 cells/200 µl. Approximately 200 µl (~4,000 cells) was dispensed into each well of a 96-well optically clear plastic bottom plate (Nunc, ThermoScientific) and cells were incubated at 37°C for 72 h. Following incubation, cells were fixed in 4% formaldehyde for 15 min. Fixative was removed and nuclei were counterstained with 200 µl of Hoechst 33342 (300 ng/mL) (Appendix A) (Sigma) at 4°C overnight. Images were acquired using a Cytation 3 high-content imager (BioTek) and Gen5 software. Nine central and non-overlapping images were acquired per well, and the total number of nuclei in each well was determined by automated nuclei counting software (Gen5). All data were imported into Excel and cell numbers were normalized to a siGAPDH control. Relative cell numbers (%) were imported into Prism v6.0 (GraphPad) for statistical analysis.

2.14.4 High-Content Analysis of RNF20-silenced Cells Remaining Following Olaparib or BMN673 Treatment

High-content microscopy was employed to identify the number of siGAPDH or siRNF20 cells remaining following Olaparib or BMN673 treatment (Chapter 5). Approximately 210,000 HCT116 cells or 130,000 hTERT cells were seeded into each well of a 6-well plate. Cells were incubated at 37°C for approximately 24 h prior to siRNA transfection. HCT116 and hTERT cells were transfected as detailed above (*2.6 siRNA-Based Silencing*). Approximately 24 h post-transfection, siGAPDH and siRNF20 cells were detached, pelleted, resuspended in PBS and counted. Cells were diluted in pre-warmed complete media to a concentration of 4,000 cells/200 µl. Approximately 200 µl (~4,000 cells) was dispensed into each well of a 96-well optically clear plastic bottom plate (Nunc, ThermoScientific) and cells were incubated at 37°C overnight. The following day, a 5-fold serial dilution of Olaparib (Appendix A) (Cayman Chemicals, Ann Arbor, MI) or BMN673 (Appendix A) (Cayman Chemicals) was prepared such that 9 unique concentrations could be dispensed in sextuplet (i.e. 6-wells) across the 96-well plate. For Olaparib, final concentrations ranged from 500 µM to 256 pM. For BMN673, concentrations ranged from 100 µM to 31 pM. Cells were incubated in the presence of BMN673, Olaparib, or DMSO vehicle control for 72 h and fixed in 4% formaldehyde for 15 min. Following fixation, fixative was removed and nuclei were counterstained with 200 µl of Hoechst 33342 (300 ng/mL) (Appendix A) (Sigma) at 4°C overnight. Images were acquired using a Cytation 3 high-content imager (BioTek) and Gen5 software. Nine central and non-overlapping images were acquired per well, and the total number of nuclei in each well was determined by automated nuclei counting software (Gen5). All data were imported into Excel and cell numbers were normalized to DMSO drug vehicle controls. Relative cell numbers were imported into Prism v6.0 (GraphPad), standard

dose response curves were generated, and the SF_{50} (surviving fraction; drug concentration at which 50% of the cells remained) was identified for Olaparib and BMN673. Drug concentrations that produced the greatest reduction in siRNF20 cells and not siGAPDH cells were identified as 800 nM Olaparib and 6.4 nM BMN673 for HCT116 and 32 nM Olaparib and 1.28 nM BMN673 for hTERT. These working concentrations were employed throughout the remainder of our study.

2.14.5 High-Content Analysis of γH2AX and Activated-Caspase 3 Levels Following BMN673 Treatment.

High-content, semi-quantitative imaging microscopy was employed to evaluate increases in γH2AX and activated-caspase 3 signal intensities following BMN673 treatment (Chapter 5). RNF20-silenced cells (siRNF20 or shRNF20) or controls (siGAPDH or shGAPDH) were seeded into a 96-well optical plates and treated with 6.4 nM BMN673 for 48 h prior to 4% formaldehyde fixation for 15 min. Following fixation, cells were immunofluorescently labeled using the protocol detailed above with the exception that cells were directly labeled within 96-well plates and a volume of 60 μl of antibody solution was employed. Images were acquired using a Cytation 3 high-content imager (BioTek) and analyzed with Gen5 software. All images were collected with identical exposure times and thus changes in signal intensity reflected changes in the levels of γH2AX and activated-caspase 3. Nine central and non-overlapping images were acquired per well, and the mean γH2AX or activated-caspase 3 signal intensity was calculated for each well. All data were imported into Prism v6.0 (GraphPad) for statistical analysis.

2.15 Colony Formation Assays

A soft agar, colony-forming assay was performed to evaluate prolonged exposure of BMN673 to shGAPDH and shRNF20 cells (Chapter 5). Approximately 5,000 shGAPDH or shRNF20 cells/well were embedded in a 6-well plate containing low melt agar plus media. All conditions were performed in triplicate. Cells were permitted to grow for 3 days to establish colonies prior to the addition of BMN673 or DMSO. Fresh media containing BMN673 or DMSO were replaced every 2- to 3-days for a 14 day period. Following treatment, cells were fixed with 4% formaldehyde for 5 min. Remaining colonies were amenable to fluorescent imaging as pGIPZ shRNA plasmids also contain a GFP-expression cassette. Low magnification images were acquired using a MyECL imager equipped with a fluorescent filter cube and a 16-bit, 4.2 megapixel camera. Exposure times were optimized to produce zero pixel saturation and maximum dynamic range. Black and white images were exported into ImageJ and inverted for analyses. Image intensity thresholds were applied to identify colonies within the wells. Threshold values of 172 (lower threshold level) to 255 (upper threshold level) were used for all images. The analyze particles function was employed to identify the number and sizes of colonies remaining in each well. All data were imported into Prism, normalized to the DMSO-treated control, and Student's *t*-tests were performed to identify statistically differences in mean colony numbers and sizes between treatments.

2.16 Image Preparation and Presentation

Following image acquisition, two- or three-dimensional images were saved as Tiff files and exported to Imaris (Bitplane, V8.1.2). To ensure accurate scale bar measurements, the voxel dimensions of the image was adjusted to match the pixel dimensions of the camera. For

reference, voxel dimensions were 0.120 μm × 0.120 μm × 0.2 μm and 0.16125 μm × 0.16125 μm × 0.2 μm for the 40× and 63× objectives, respectively. For ease of viewing, brightness and contrast were adjusted for individual channels, and individual channels were exported as black and white Tiff images. When multiple channels were displayed on a single image (Merge), individual channels were pseudocolored red, green or blue. Figures were assembled and annotated in Photoshop Creative Suite 5 (Adobe).

2.16.1 Image Deconvolution

Image deconvolution was performed on 3D images in order to re-assign the out of focus light and increase image resolution (Chapters 3). Image deconvolution was performed using a maximum-likelihood expectation deconvolution in AutoQuant X3 (Media Cybernetics), using a constrained iterative algorithm and theoretical point spread functions for 460-nm (DAPI), 505-nm (Alexa Fluor 488), and 565-nm (Cy3) emission wavelengths. Deconvolved images were imported into Imaris (Bitplane) and brightness and contrasted were adjusted on displayed images (identically for compared image sets).

2.17 Statistical Approaches and Analyses

Brief descriptions of the statistical methods employed within this thesis are included below. All statistical tests were performed in Prism statistical software (GraphPad). For reference purposes, *p*-values of <0.05 are considered statistically significant.

2.17.1 Analysis of Variance (ANOVA) and Tukey-Kramer Post-tests

Analysis of variance (ANOVA) was employed throughout this thesis where three or more means are compared. ANOVA analyzes variation within a group and between groups to ultimately provide a statistical test of whether or not the means of two or more groups are equal.

Following ANOVA testing, Tukey-Kramer post-tests are performed. Tukey-Kramer Post-tests are employed throughout this thesis where all means are systematically compared to identify all pair-wise statistical combinations.

2.17.2 Student's *t*-tests

Student's *t*-tests are employed throughout this thesis to identify statistically significant differences between two means that are assumed to follow a Gaussian distribution and exhibit equal variance within each group.

2.17.3 The Multiplicative Model

The multiplicative model is employed in Chapter 5 to evaluate if dual silencing (siRNF20 + siPARP1) results in a greater reduction in cell numbers than what is predicted by multiplying the relative percentage of cells remaining from each of the individual control conditions (siGAPDH + siRNF20) × (siGAPDH + siPARP1). A greater reduction in siRNF20 + siPARP1 cells numbers indicates a greater than additive effect and suggests a SL interaction.

Chapter 3

MITOTIC ACCUMULATION OF DI-METHYLATED LYSINE 79 OF HISTONE H3 IS IMPORTANT FOR MAINTAINING GENOME INTEGRITY DURING MITOSIS IN HUMAN CELLS.

3.1 Abstract

The loss of genome stability is an early event that drives the development and progression of virtually all tumor types. Recent studies have revealed that certain histone post-translational modifications exhibit dynamic and global increases in abundance that coincide with mitosis and exhibit essential roles in maintaining genomic stability. Histone H2B ubiquitination at lysine 120 (H2Bub1) is regulated by RNF20, an E3 ubiquitin ligase that is altered in many tumor types. Through an evolutionarily conserved trans-histone pathway, H2Bub1 has been shown to modulate subsequent downstream di-methylation events at lysines 4 (H3K4me2) and 79 (H3K79me2) of histone H3. Although the role that RNF20 plays in tumorigenesis has garnered much attention, the downstream components of the trans-histone pathway, H3K4me2 and H3K79me2, and their potential contributions to genome stability remain largely overlooked. In this study, we employ single-cell imaging, and biochemical approaches to investigate the spatial and temporal patterning of RNF20, H2Bub1, H3K4me2 and H3K79me2 throughout the cell cycle, with a particular focus on mitosis. We show that H2Bub1, H3K4me2 and H3K79me2 exhibit distinct temporal progression patterns throughout the cell cycle. Most notably, we demonstrate that H3K79me2 is a highly dynamic histone PTM that reaches maximal abundance during mitosis in an H2Bub1-independent manner. Using RNAi and chemical genetic approaches, we identify DOT1L as a histone methyltransferase required for the mitotic-associated increases in H3K79me2. We also demonstrate that the loss of mitotic H3K79me2 levels correlates with increases in chromosome numbers and increases in mitotic defects. Collectively, these data suggest that H3K79me2 dynamics during mitosis are normally required to maintain genome stability and further implicate the loss of H3K79me2 during mitosis as a pathogenic event that contributes to the development and progression of tumors.

3.2 Introduction

Genome instability is a driver in the tumorigenic process and is observed in virtually all tumor types[186]. Genome instability is associated with highly aggressive tumors, the acquisition of multi-drug resistance, and consequently, poor patient prognosis[166,187,188]. Despite these associations, very little is known about the aberrant molecular origins that cause genome instability. Thus, studies aimed at identifying and characterizing the molecular events that contribute to genome instability will shed novel insight into the tumorigenic process.

Over the past few decades, a wealth of studies has correlated aberrant patterning of histone PTMs with the development and progression of cancer. Histones are the primary compaction units of DNA and are the substrates for numerous PTMs including acetylation, phosphorylation, methylation and ubiquitination. Histone PTMs have classically been examined in the context of gene expression and regulation, and typically at the single gene or single nucleosome resolution. However, recent evidence is emerging that shows the global abundance of certain histone PTMs are highly dynamic and maximal during mitosis, when transcription rates are extremely low[189]. Included amongst these dynamic PTMs are H3S10ph (histone H3 phosphorylation at serine 10)[70,190], H3K9me3 (histone H3 tri-methylation at lysine 9)[191,192] and H4K20me (histone H4 mono-methylation at lysine 20)[72]. The mis-regulation of these PTMs have functional implications in chromosome biology and is known to impact mitotic fidelity through a variety of pathways including chromosome condensation[193], chromosome segregation [191], and kinetochore structure[194]. Thus, disrupting the normal mitotic dynamics of certain histone PTMs may be a contributing factor in tumorigenesis. Indeed, many of the genes encoding the corresponding regulating enzymes (e.g. *AURKB*, *SUV39H1*, *SETD8*, etc.) are somatically altered in numerous tumor types, including lung, breast and colon cancers[195] suggesting that aberrant

expression and/or function of theses enzymes may be causally linked to cancer[196]. Thus, characterizing the cell cycle dynamics of mitotic-associated histone PTMs and identifying the enzymes that regulate these dynamic PTMs, will provide insight into the etiological origins of genome instability and tumorigenesis.

RNF20 is an evolutionarily conserved E3 ubiquitin ligase that regulates the abundance of H2Bub1 (histone H2B mono-ubiquitinated at lysine 120)[76]. *RNF20* is somatically mutated in a number of tumor types (Table 3.S1), and aberrant H2Bub1 levels are associated with genome instability[78]. However, the biological consequences of aberrant RNF20 expression are not limited to H2Bub1, as an evolutionarily conserved trans-histone pathway exists where H2Bub1 is an essential upstream prerequisite for subsequent di-methylation events that occur on histone H3 at lysines 4 (H3K4me2) and 79 (H3K79me2)[108,110,133,197]. Given the hierarchal position of RNF20 and H2Bub1 within the trans-histone pathway, the impact aberrant levels of H3K4me2 and H3K79me2 have on genomic instability is poorly understood. Accordingly, characterizing the global abundance of these histone PTMs throughout the cell cycle, and evaluating their roles in genome stability will provide new insight into the mechanisms required to maintain genome stability.

In this study, we characterize the spatial and temporal dynamics of key components in a trans-histone pathway (RNF20, H2Bub1, H3K4me2 and H3K79me2) throughout the cell cycle. Using imaging microscopy and biochemical approaches, we show that RNF20 and H2Bub1 are highly dynamic. In interphase, RNF20 is spatially confined within the nucleus and corresponding global levels of H2Bub1 are maximal. However, as cells enter mitosis, RNF20 relocates from the compacting chromosomes into the cytoplasm, and H2Bub1 levels are rapidly lost such that they are no longer detectable within metaphase chromosomes. We also characterize distinct cell cycle

kinetics for H3K4me2 and H3K79me2 that are independent of H2Bub1 during mitosis. While the global abundance of H3K4me2 remains relatively constant throughout the cell cycle, H3K79me2 levels are highly dynamic but opposite to those of H2Bub1. Surprisingly, H3K79me2 attains maximal abundance during mitosis, suggesting it may have a functional role in mitotic chromosome biology and genome stability. In support of this possibility, we identified DOT1L as a mitotic-specific H3K79me2 histone methyltransferase. Using RNAi and chemical-based approaches we show that the loss of mitotic H3K79me2 is associated with genome instability that manifested as increases in aberrant chromosome numbers. Collectively, these data indicate there is a functional uncoupling of the trans-histone pathway specifically during mitosis. They further show that mis-regulation of mitotic increases in H3K79me2 is associated with genome instability, and supports the possibility that aberrant regulation of mitotic H3K79me2 levels may be a pathogenic event that contributes to tumorigenesis.

3.3 Results

3.3.1 RNF20 is Rapidly Redistributed into the Cytoplasm During Mitosis

We first determined whether RNF20 exhibits a distinct localization pattern throughout the cell cycle that may impact the temporal progression patterns of H2Bub1, H3K4me2 and H3K79me2. Using an established single-cell immunofluorescent approach[198], a validated anti-RNF20 antibody (Figure 3.S1), and asynchronous HCT116 cells, we show that RNF20 exhibits a dynamic localization pattern. In interphase cells, RNF20 is spatially confined to the nucleus where it is presents as hundreds of immunofluorescent foci that are visually depleted from nucleoli (Figure 3.1). Line scans of interphase nuclei reveal that RNF20 localization is non-random (Figure 3.S2). RNF20 is enriched with euchromatin as visually defined by less intensely stained DAPI regions, and is depleted from heterochromatin as defined by intensely stained DAPI regions. As cells enter mitosis (i.e. prophase and prometaphase), RNF20 is rapidly redistributed away from the compacting chromosomes and into the cytoplasm (Figure 3.1B). However, as cells re-enter G1, RNF20 is re-incorporated and retained within the nucleus. To confirm the above results were not restricted to HCT116 cells, analogous experiments were performed in hTERTs (an immortalized fibroblast cell line) with very similar findings (Figure 3.S3). Finally, to determine whether changes in RNF20 expression levels accompany changes in localization Western blots were performed that show RNF20 levels are relatively consistent between mitotically enriched (Figure 3.S4) and asynchronous (predominantly interphase) populations (Figure 3.1C).

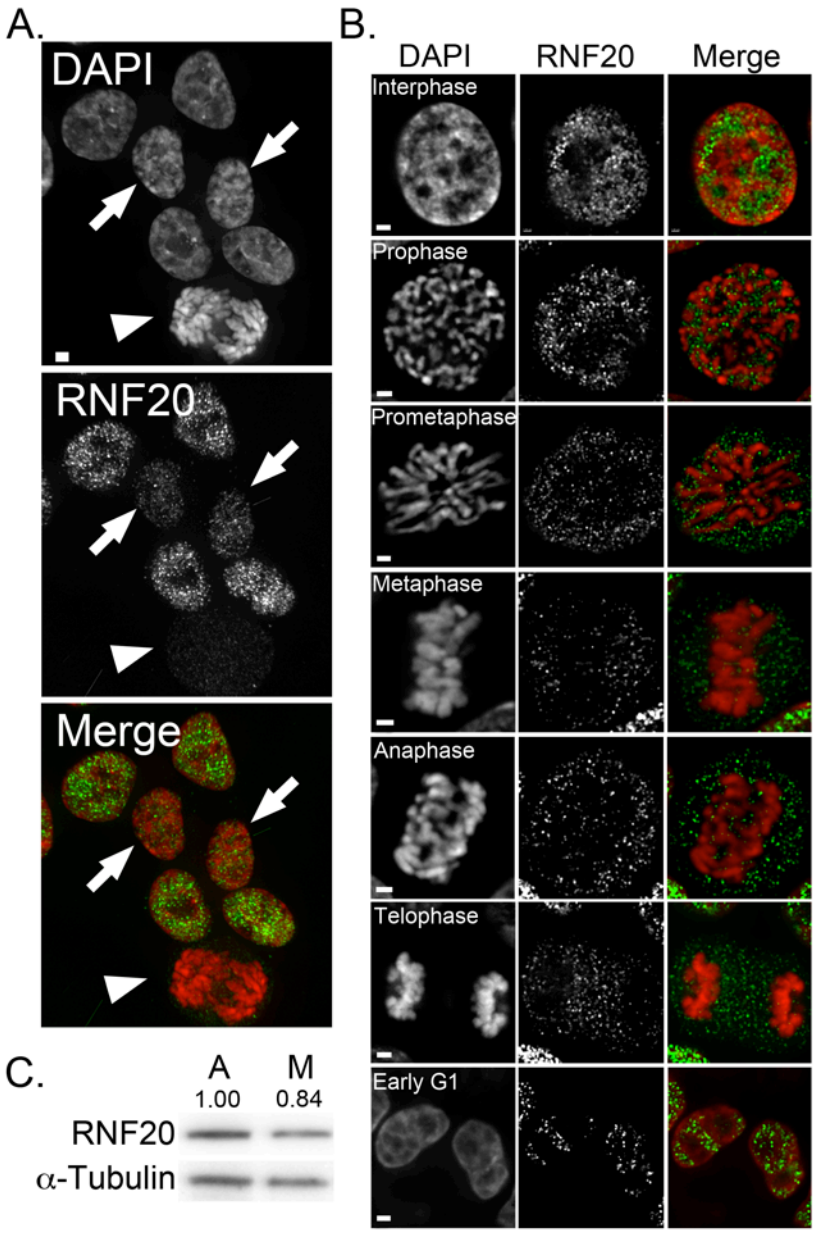

Figure 3.1: RNF20 is Spatially Relocalized from Interphase Chromatin in Mitotic Cells
(A) Representative deconvolved image of asynchronous HCT116 cells immunofluorescently labeled with an anti-RNF20 antibody (green) and counterstained with DAPI (red). Arrowhead identifies a mitotic cell, while the arrows identify early-G1 cells. Scale bar represents 5 μm. (B) High-resolution (63×) deconvolved images depicting the temporal and spatial progression pattern of RNF20 (green) throughout various stages of the cell cycle (indicated). Note that images were acquired using an identical exposure time, and thus qualitative comparisons can be made between the various cell cycle stages. Scale bar represents 2 μm. (C) Western blot depicting similar levels for RNF20 isolated from asynchronous (A) and mitotic-enriched (M; nocodazole treated) HCT116 populations. Semi-quantitative analyses were performed and the numbers indicate the relative abundance of RNF20 levels following normalization to the respective loading control (α-tubulin).

3.3.2 The Global Abundance of H2Bub1 Decreases Rapidly During Mitosis

Having established that RNF20 exhibits a dynamic localization pattern, we now sought to determine whether H2Bub1 would also exhibit dynamic temporal patterning. However, we first confirmed the specificity of the H2Bub1 antibody using a peptide competition assay and a dot blot assay (Figure 3.S1). Using the single-cell approach employed above, we show that the global abundance of H2Bub1 is highly dynamic (Figure 3.2). In interphase cells, H2Bub1 localizes within nuclei, and forms hundreds of immunofluorescent foci that are depleted from nucleoli. Line scans revealed that the H2Bub1 foci are preferentially enriched within euchromatic regions rather than heterochromatic regions (Figure 3.S2). As cells enter mitosis there is a dramatic decrease in the abundance of H2Bub1 such that levels are below the limits of detection by metaphase. Global levels remain low throughout anaphase and telophase, and begin to rise rapidly as cells enter G1 (Figure 3.2B), which coincides with the re-incorporation of RNF20 within interphase nuclei. To confirm the above results were not restricted to the HCT116 cells, similar experiments were performed in hTERT with very similar results (Figure 3.S5).

Although the *in situ* data generated above suggest there is a dramatic loss of H2Bub1 during mitosis, epitope accessibility/occlusion may adversely impact these results, particularly in mitotic cells with extensive chromosome compaction. To address this possibility, standard biochemical approaches were employed, and denaturing Western blots were performed on histones isolated from asynchronous or mitotically enriched populations. In agreement with the imaging data, there was a striking decrease in the abundance of H2Bub1 within the mitotic population compared to the interphase (asynchronous) population (Figure 3.2C). Collectively, the above data show that the global abundance of H2Bub1 is highly dynamic and attains

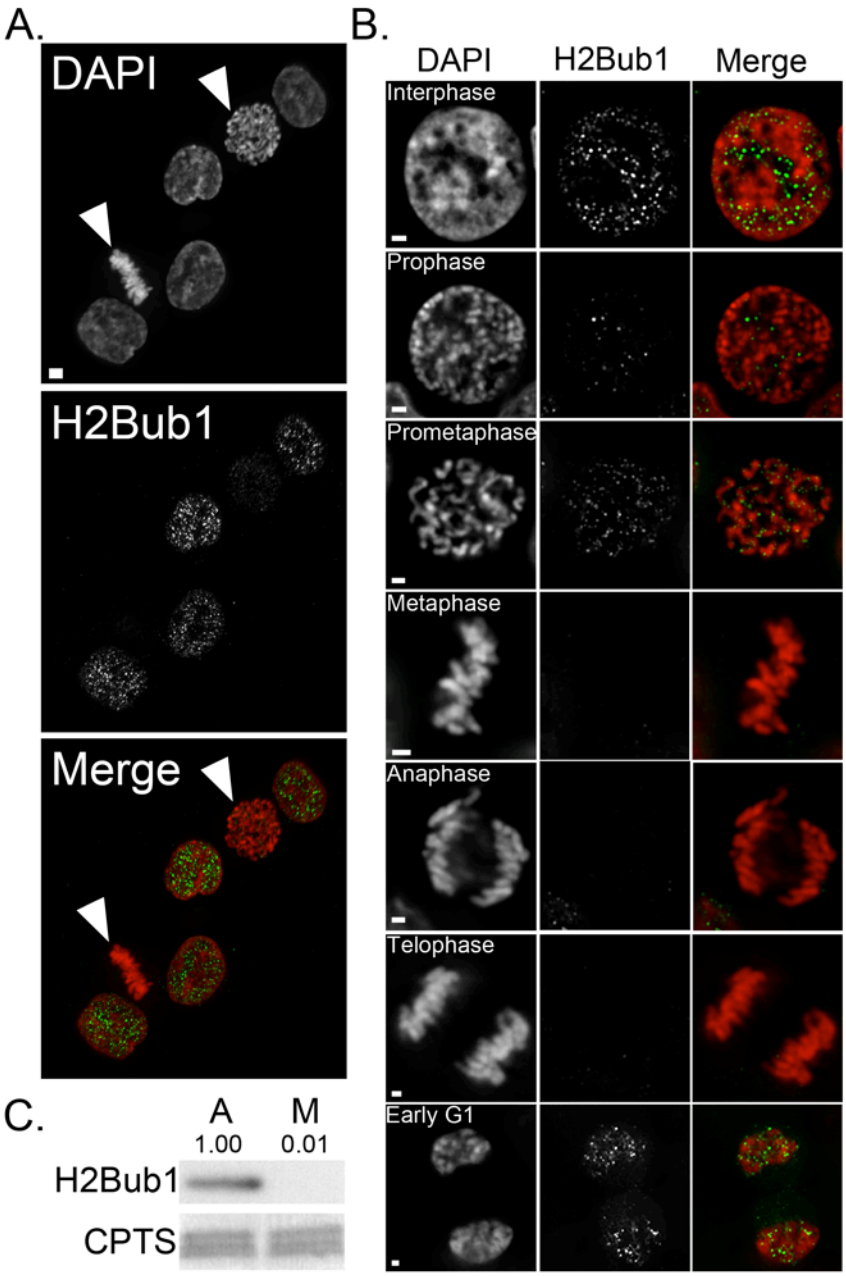

Figure 3.2: The Global Abundance of H2Bub1 Decreases Dramatically During Mitosis
(A) Representative deconvolved image of asynchronous HCT116 cells immunofluorescently labeled with an anti-H2Bub1 antibody (green) and counterstained with DAPI (red). Arrowheads identify mitotic cells. Scale bar represents 5 μm. (B) High-resolution (63×) deconvolved images depicting the temporal and spatial progression pattern of H2Bub1 (green) throughout various stages of the cell cycle (indicated). Note that images were acquired using an identical exposure time, and thus qualitative comparisons can be made between the various stages. Scale bar represents 2 μm. (C) Western blot analysis depicting the global abundance of H2Bub1 in asynchronous (A) and mitotic-enriched (M) HCT116 populations. Semi-quantitative analyses were performed and the numbers indicate the relative abundance of H2Bub1 following normalization to the respective loading control (CPTS).

maximum and minimum levels during interphase and mitosis (metaphase to telophase), respectively.

3.3.3 The Global Abundance of H3K4me2 Remains Relatively Constant Throughout the Cell Cycle

The trans-histone pathway stipulates that H2Bub1 is an essential prerequisite for subsequent H3K4me2 and H3K79me2 events. However, this pathway has only been investigated in the context of transcription and thus has been restricted to interphase cells[108,110,133,197]. We now wished to examine whether this pathway is maintained during mitosis, and determine whether the global abundance of H3K4me2 like H2Bub1, would also decrease dramatically during mitosis. Using a similar approach and a validated H3K4me2 antibody (Figure 3.S6A and B), we show that the global abundance of H3K4me2 remains relatively constant throughout the cell cycle (Figure 3.3). In interphase cells, H3K4me2 exists as hundreds of immunofluorescent foci that are highly enriched within nuclei but absent from nucleoli. Line scans revealed that H3K4me2 foci are preferentially enriched within enchromatin compared to heterochromatin (Figure 3.S2). In contrast to H2Bub1 however, the global abundance of H3K4me2 does not decrease rapidly during mitosis but rather is maintained along the length of the chromosome arms in a heterogeneous punctate pattern. hTERT cells were also evaluated and produced very similar results (Figure 3.S7). Finally, denaturing Western blots confirmed the relatively consistent levels (i.e. minimal changes) observed via indirect immunofluorescence (Figure 3.3C). Collectively, the above data show that the global abundance of H3K4me2 is relatively static throughout the cell cycle.

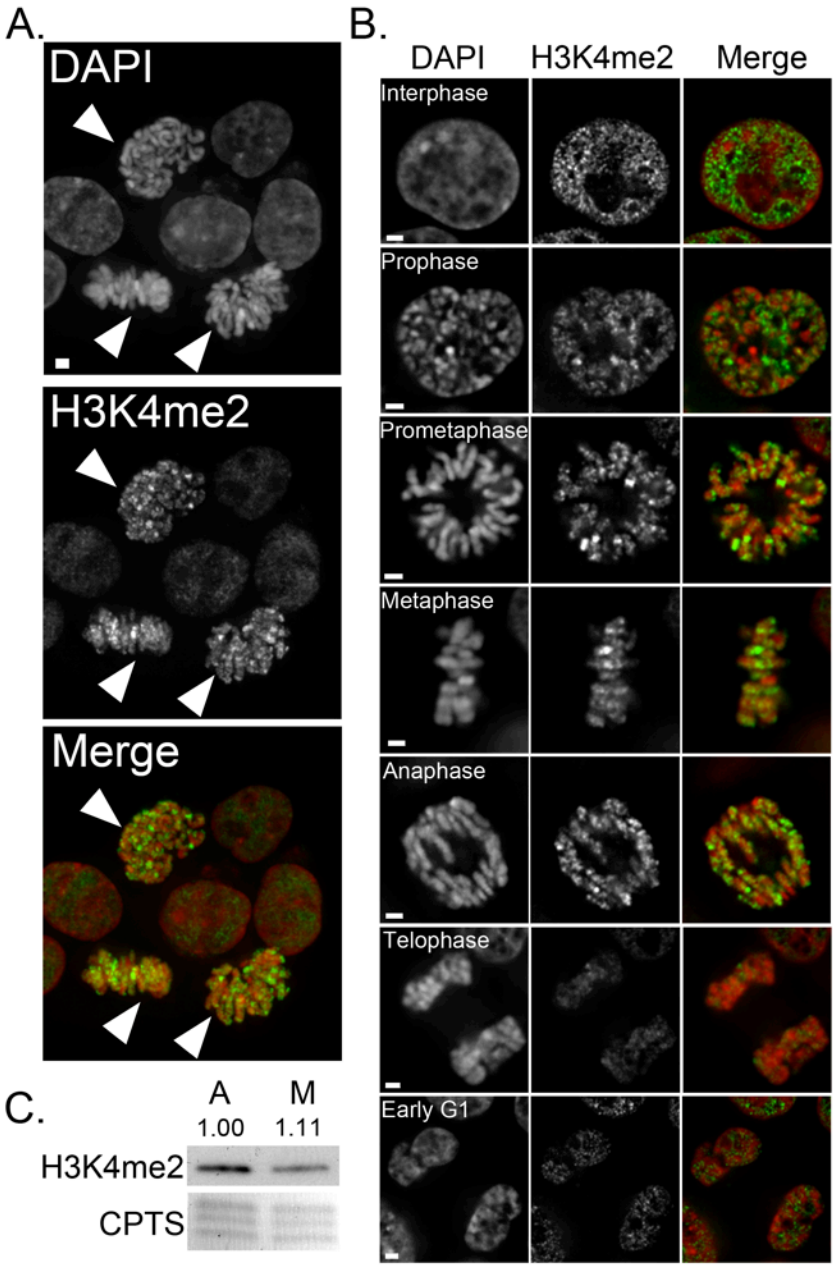

Figure 3.3: The Global Abundance of H3K4me2 Remains Relatively Constant Throughout the Cell Cycle

(A) Representative deconvolved image of asynchronous HCT116 cells immunofluorescently labeled with an anti-H3K4me2 antibody (green) and counterstained with DAPI (red). Arrowheads identify mitotic cells. Scale bar represents 5 μm. (B) High-resolution (63×) deconvolved images depicting the temporal and spatial progression pattern of H3K4me2 (green) throughout the cell cycle (indicated). Note that images were acquired using an identical exposure time, and thus qualitative comparisons can be made between the various stages. Scale bar represents 2 μm. (C) Western blot depicting similar levels of H3K4me2 in both asynchronous (A) and mitotic-enriched (M) populations. Semi-quantitative analyses were performed and the numbers indicate the relative abundance of H3K4me2 following normalization to the respective loading control (CPTS).

3.3.4 The Global Levels of H3K79me2 are Dynamic and Attain Maximal Abundance During Mitosis

Having established that the temporal dynamics of H3K4me2 are distinct from H2Bub1, we now sought to characterize the temporal and spatial patterning of H3K79me2 using a validated antibody (Figure 3.S6C and D) and similar approaches. Surprisingly, H3K79me2 levels are highly dynamic and in stark contrast to those of H2Bub1 – minimal H3K79me2 levels occurred during interphase and maximal levels of H3K79me2 occurred during mitosis (Figure 3.4). The difference in H3K79me2 signal intensities is so pronounced that interphase intensities are not readily detected when the image exposure time is optimized for the mitotic signals (Figure 3.4A; left). Nevertheless, longer exposure times clearly show H3K79me2 signals within interphase nuclei (Figure 3.4A; right) that present hundreds of immunofluorescent foci, which are enriched within nuclei. Line scans show that H3K79me2 foci are preferentially associated with euchromatic regions rather than heterochromatic regions (Figure 3.S2). Furthermore, as cells enter prophase there is an increase in H3K79me2 levels throughout the length of the chromosomes that continues to increase until maximal abundance is achieved by metaphase (Figure 3.4B). As cells enter anaphase and telophase, H3K79me2 levels rapidly decrease and return to basal levels as cells enter G1. Semi-quantitative imaging analyses of DAPI-normalized, H3K79me2 total signal intensities revealed a highly statistically significant, ~31-fold increase within mitotic cells relative to interphase cells (Figure 3.4C and Table 3.S3), while Western blots confirmed the large increase in the global levels within mitotically enriched cells (Figure 3.4D). Analogous experiments were performed in hTERT cells with very similar findings (Figure 3.S8). Thus, the above data show that the global abundance of H3K79me2 is dynamic, and unlike H2Bub1 it attains maximal levels during mitosis.

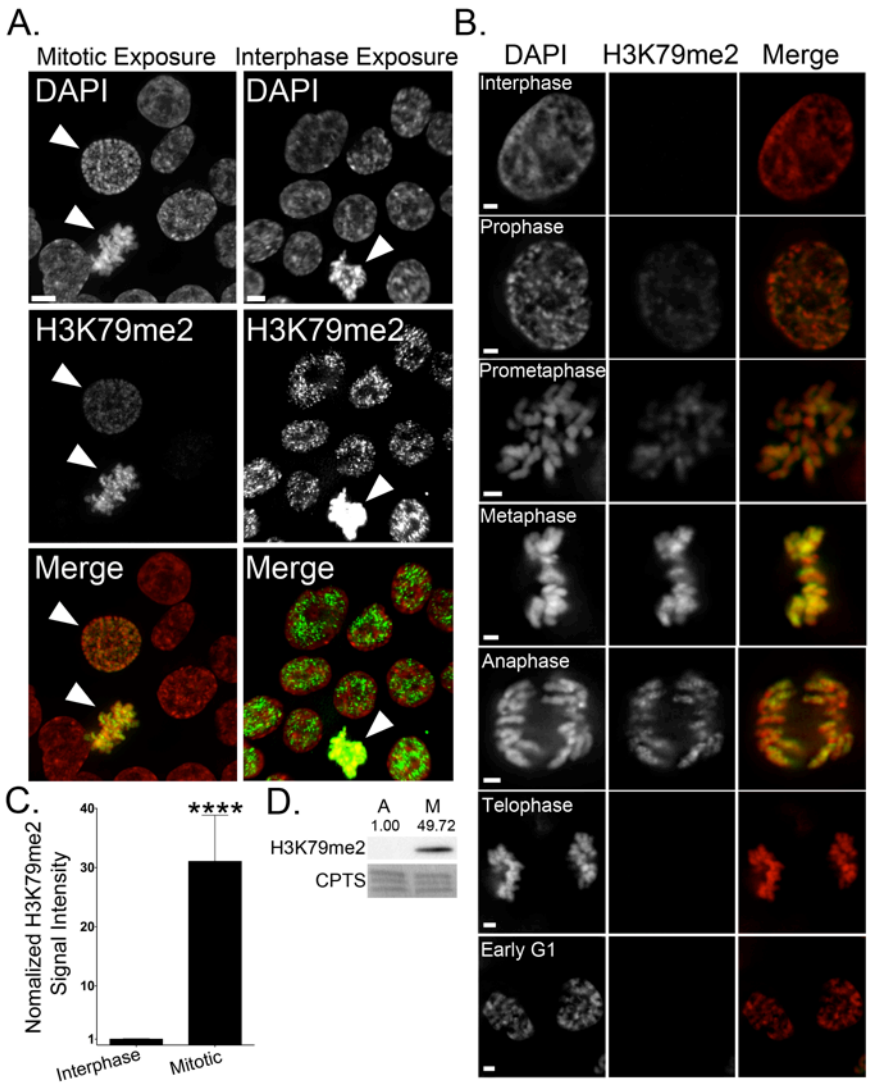

Figure 3.4: The Global Abundance of H3K79me2 Increases Dramatically during Mitosis
(A) Representative deconvolved images of HCT116 cells labeled with an anti-H3K79me2 antibody (green) and counterstained with DAPI (red). Arrowheads identify mitotic cells. Scale bars represent 5 μm. Due to the lower levels of H3K79me2 in interphase cells, two images are presented in which the exposure times were independently optimized to display the abundance of H3K79me2 either within mitotic cells (left) or interphase cells (right). Note that the mitotic cell in the right panel becomes saturated with the prolonged exposure time. (B) High-resolution (63×) deconvolved images depicting the temporal and spatial progression pattern of H3K79me2 (green) throughout the cell cycle (indicated). Scale bar represents 2 μm. (C) Bar graph depicting the statistically significant increase (p-value < 0.0001; ****) in the mean, normalized H3K79me2 signal intensity (± standard deviation) within the mitotic cells as revealed by single cell, semi-quantitative imaging microscopy from asynchronous and untreated cellular populations. (D) Western blot depicting a striking increase in the global abundance of H3K79me2 within the mitotic-enriched (M) population relative to an asynchronous (A) and predominantly interphase population. Semi-quantitative analyses were performed and the relative abundance of H3K79me2 following normalization to the respective loading control (CPTS) is shown.

3.3.5 DOT1L Expression and Function are required for the Mitosis-Specific Increases in H3K79me2

The dramatic increase in the abundance of H3K79me2 specifically during mitosis mimics that of other histone PTMs with established roles in chromosome biology and stability (e.g. H3S10ph, H3K9me2, H4K20me, etc.), and suggests that H3K79me2 may normally participate in chromosome stability. However, before examining this possibility it was necessary to identify the histone methyltransferase required for the mitotic-specific increase in H3K79me2. Currently, DOT1L is the only known H3K79me2-specific methyltransferase[133]. However, its ability to methylate H3K79 during mitosis, independent of H2Bub1 is unknown. To assess DOT1L as a candidate mitotic methyltransferase, complementary siRNA and chemical-based experiments were performed, and the impact on mitotic H3K79me2 was examined. We first evaluated the silencing efficiency of four siRNA duplexes targeting DOT1L relative to untreated and GAPDH-silenced controls within HCT116 cells (Figure 3.5A). The siDOT1L-3 duplex was deemed the most efficient, and was employed in all subsequent analyses.

To determine whether DOT1L silencing impacted H3K79me2 levels within the mitotic cells, semi-quantitative, single-cell microscopy was performed but the analyses were restricted to mitotic cells. Following silencing, a highly statistically significant decrease (~54% of control levels) in the mean DAPI-normalized H3K79me2 total signal intensity occurred relative to controls (Figure 3.5B and Table 3.S4). The large decrease in the mitotic abundance of H3K79me2 was subsequently confirmed by denaturing Western blots, where a decrease in H3K79me2 levels within the mitotically enriched population was readily detected relative to the GAPDH-silenced control (Figure 3.5C). These data show that DOT1L expression is required for normal H3K79me2 levels to occur within mitotic cells.

To determine if DOT1L function is essential for the mitotic-associated increases in H3K79me2 levels, and to address potential off-target effects associated with siRNA, similar experiments were performed using SGC0946, an established DOT1L inhibitor[199], or DMSO. Semi-quantitative microscopy was performed as above on asynchronously growing cells, and the analyses were restricted to mitotic cells. In agreement with the silencing data, DOT1L inhibition produced a statistically significant decrease (~24% of control levels) in mean DAPI-normalized H3K79me2 total signal intensity within the mitotic cells (Figure 3.5B and Table 3.S4) that was confirmed by Western blots (Figure 3.5D). It should be noted that the mitotic decrease in H3K79me2 levels was more pronounced following SGC0946-treatment than following DOT1L silencing. Although the underlying mechanism accounting for this difference is beyond the scope of the current study, it likely stems from the heterogeneous nature of siRNA-based silencing, or more likely the residual amounts of functional DOT1L remaining following silencing. In any case, the siRNA- and chemical-based data show that DOT1L expression and function are normally required to induce the dramatic increase in H3K79me2 levels specifically within mitotic cells.

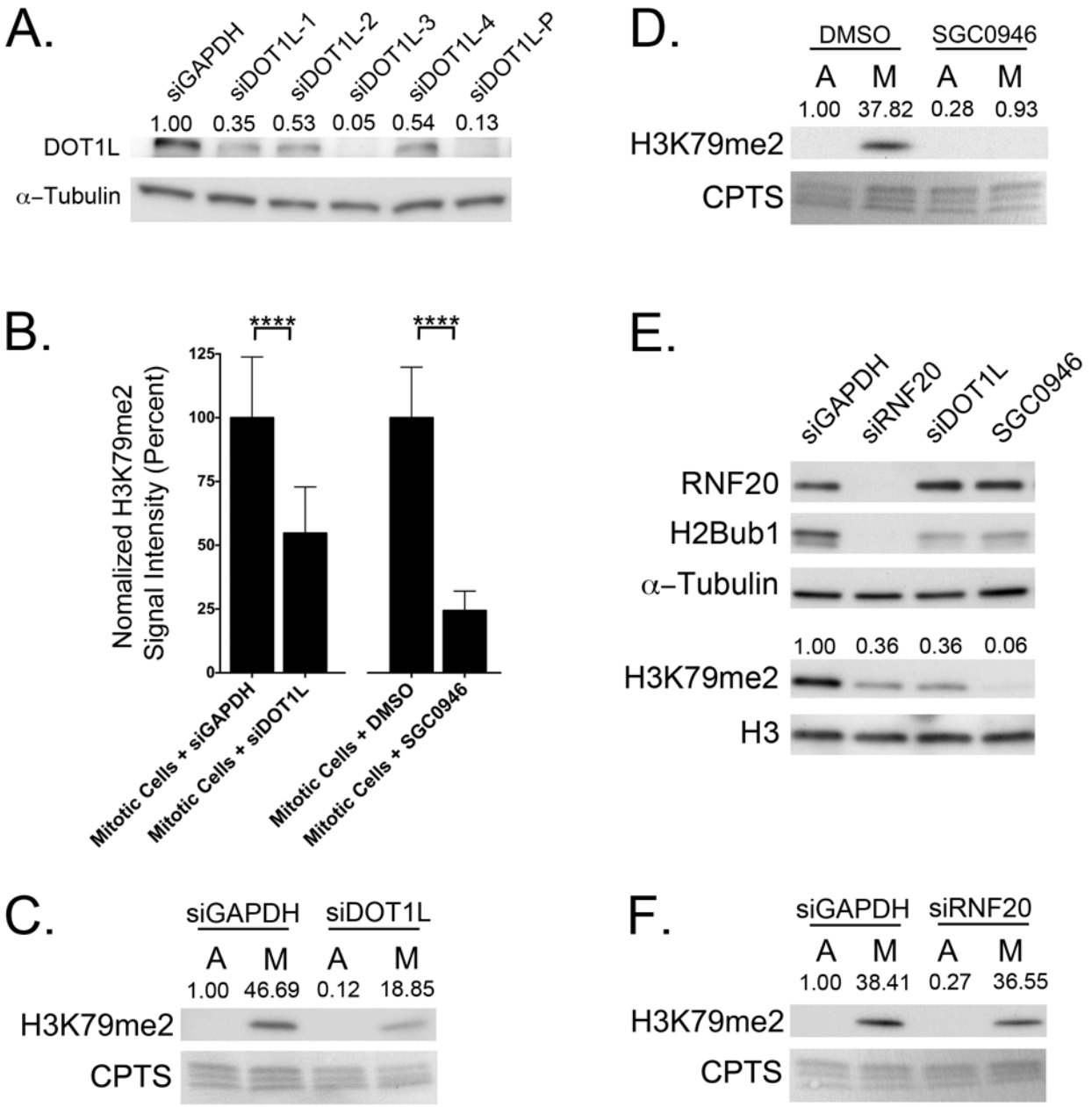

Figure 3.5: DOT1L Expression and Function are required for the Mitosis-Specific Increases in H3K79me2

(A) Western blot depicting the abundance of DOT1L following silencing with either individual (siDOT1L-1 to -4) or pooled (siDOT1L-P) siRNA duplexes relative to control (siGAPDH). Semi-quantitative analyses were performed and the relative abundance of DOT1L following normalization to the respective loading control (α-tubulin) is presented. (B) Bar graphs depicting the statistically significant (*p*-value <0.0001; ****) decreases in the mean, DAPI-normalized H3K79me2 total signal intensities in the DOT1L silenced (48 h post-transfection; left) or inhibited (2 h treatment; right) cells relative to controls. Note that only the H3K79me2 signal intensities from mitotic cells were imaged, quantified and presented. (C) Western blots showing the global abundance of H3K79me2 within asynchronous, predominantly interphase cells (A), or mitotically enriched (M) populations of control (siGAPDH) or DOT1L (siDOT1L) silenced

cells. The exposure time was optimized to display the mitotic H3K79me2 signals and not those within the asynchronous populations. Semi-quantitative analyses were performed and the relative abundance of H3K79me2 following normalization to the respective loading control (CPTS) is shown. Note the large decrease in abundance of H3K79me2 within the mitotically enriched population from the DOT1L silenced cells relative to the GAPDH silenced controls. (D) Western blot depicting a large decrease in H3K79me2 levels following SGC0946 treatment (48 h treatment) specifically within the mitotically enriched (M) population. Blots are labeled as in (C). (E) Western blots of proteins harvested from asynchronous (predominantly interphase) cells depicting the relative abundance of the indicated proteins and histone PTMs following RNF20 and DOT1L silencing, and SGC0946 treatment (48 h treatment) relative to siGAPDH controls. Semi-quantitative analyses were performed and the relative abundance of H3K79me2 following normalization to the respective H3 loading control is shown. Note that RNF20/H2Bub1 depletion is associated with a decrease in H3K79me2 within interphase cells, which supports the existence of a trans-histone pathway. (F) Western blot demonstrating that RNF20 silencing (siRNF20) does not impact the global abundance of H3K79me2 specifically within mitotic cells relative to controls (siGAPDH). Semi-quantitative analyses were performed and the relative abundance of H3K79me2 following normalization to the respective loading control (CPTS) is shown, and suggests there is an uncoupling of the trans-histone pathway within mitotic cells.

3.3.6 H2Bub1 is not a Pre-requisite for H3K79me2 During Mitosis

The observation that the global abundance of H2Bub1 and H3K79me2 are dynamic but opposite in mitosis suggests there is transient uncoupling of the trans-histone pathway during mitosis. Although our initial immunofluorescent and Western blot analyses did not detect H2Bub1 within mitotic cells, the possibility remained that extremely low levels of H2Bub1, below the limits of detection persisted within mitotic cells that could impact H3K79me2 levels. Accordingly, we sought to decrease any residual H2Bub1 within mitotic cells by silencing RNF20, and examine H3K79me2 levels. However, we first confirmed the existence of an intact trans-histone pathway within the interphase cells of our experimental system. As expected, RNF20 silencing dramatically decreased the global abundance of H2Bub1 within interphase cells (Figure 3.5E; top), and in agreement with previous studies previous studies[108,110] also decreased the global abundance of H3K79me2. Although RNF20 silencing reduced H3K79me2 to similar levels achieved following DOT1L silencing, SGC0946 treatments appeared to be the most

efficient at depleting H3K79me2 within interphase cells (Figure 3.5E; bottom). However, within mitotically enriched populations (Figure 3.5F), RNF20 silencing had very little, if any impact on the global abundance of H3K79me2, and supports the transient uncoupling of the trans-histone pathway during mitosis.

3.3.7 Loss of Mitotic-Associated H3K79me2 is Associated with Chromosome Instability

The global abundance of many histone PTMs are dynamic and exhibit mitosis-specific increases required for mitotic fidelity and genome stability[70,72,190,191]. Thus, we wished to determine whether the large increases in H3K79me2 that occur during mitosis have a similar role. HCT116 cells were purposefully selected for this analysis as they are a karyotypically stable line that has been employed extensively in chromosome instability assays[38,159,160,185]. Accordingly, we employed DOT1L silencing and inhibition (SGC0946) to decrease H3K79me2 levels during mitosis, and evaluated the impact on chromosome stability within mitotic chromosome spreads (Figure 3.6A). As predicted, there was an overall increase in the number of aberrant spreads within the silenced and inhibited populations relative to controls (Figure 3.6B). More specifically, the frequency of spreads harboring more than 45 chromosomes increased from 18% in GAPDH-silenced controls to 30% in DOT1L-silenced cells, and from 11% in DMSO-treated controls to 49% in SGC0946-treated cells, that Student's t-tests revealed to be statistically significant (Table 3.S6). Flow cytometry was also performed and confirmed that DOT1L silencing and inhibition does not adversely affect cycle progression (Figure 3.S9 and Table 3.S5). Thus, the loss of H3K79me2 in mitotic cells following DOT1L silencing or inhibition is associated with increases in chromosome numbers and the loss of genome stability.

To gain insight into the mechanism(s) underlying the increases in chromosome numbers observed above, mitotic cells were evaluated for the presence of aberrant mitotic events including chromosome congression errors, anaphase bridges and segregation defects (Figure 3.6C). Mitotic levels of H3K79me2 were depleted as above, and mitotic defects were manually scored. Overall, the loss of H3K79me2 during mitosis was associated with statistically significant increases (p-value <0.05) in aberrant mitotic events (Figure 3.6D). More specifically there was a 1.7-fold increase in the DOT1L-silenced cells (9.7%) relative to a siGAPDH-silenced control (5.6%), and a 2.5-fold increase within the SGC0946-treated cells (9.3%) relative to vehicle control (3.7%) (Table 3.S7). Thus, the loss of H3K79me2 levels within mitotic cells is associated with chromosome instability, and an increase in aberrant mitotic events, which suggest that the mitotic increases in H3K79me2 levels are required for mitotic fidelity.

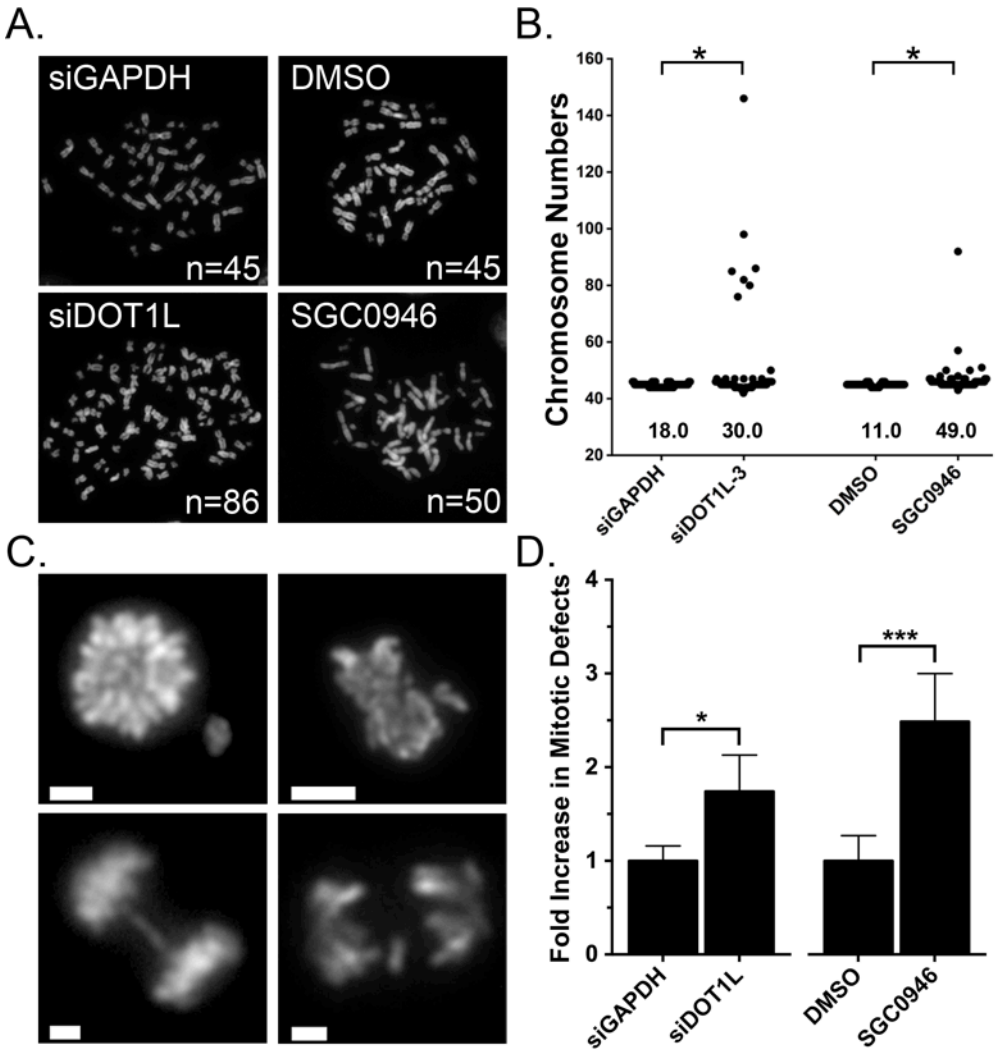

Figure 3.6: Diminished H3K79me2 Levels During Mitosis are Associated with Increases in Chromosome Numbers and Mitotic Defects

(A) Representative images of DAPI-stained mitotic chromosome spreads from control (siGAPDH or DMSO) or experimental (siDOT1L or SGC0946) conditions. The number of chromosomes contained within each spread presented is indicated at the bottom right. (B) Scatter plots depicting the total chromosome number distribution for karyotypically stable HCT116 cells treated with the indicated siRNAs or chemicals (48 h treatment). A total of 100 mitotic chromosome spreads were enumerated for each condition and the percentage of mitotic spreads with >45 chromosomes are indicated at the base of each plot. The cell populations employed and presented in Figure 3.6A and 3.6B are derived from the same populations employed for the Western blot quantification of H3K79me2 presented in Figure 3.5C and 3.5D. (C) Increases in aberrant mitotic figures are associated with global loss of H3K79me2 following DOT1L silencing and inhibition (48 h treatment). Representative images depicting the three typical aberrant mitotic events observed following the depletion of H3K79me2 within mitotic cells, which include congression errors (top quadrants), anaphase bridges (bottom left quadrant), and lagging chromosomes (bottom right quadrant). Scale bars represent 4 μm. (D) Bar graph depicting the increases in mitotic defects following DOT1L silencing and SGC0946-treatment relative to controls.

3.4 Discussion

In this study, we employ asynchronous and untreated human cell lines along with complementary single-cell microscopy and biochemical approaches to provide the first *in situ* spatial and temporal progression patterns of four key components of an established trans-histone pathway, RNF20, H2Bub1, H3K4me2, and H3K79me2. We specifically show that the global abundance of H2Bub1 is highly dynamic and reflects the spatial distribution of RNF20. H2Bub1 levels are highest in interphase, when RNF20 is spatially constrained within the nucleus, and are rapidly lost upon entry into mitosis in a manner coincident with RNF20 becoming spatially redistributed away from the chromosomes and into the cytoplasm. To our surprise, and in opposition to the established trans-histone pathway[108,133,197], the temporal progression patterns characterized for H3K4me2 and H3K79me2 were in contrast to that of H2Bub1. While H3K4me2 levels remain relatively constant throughout the cell cycle, H3K79me2 levels are highly dynamic and are minimal during interphase and maximal during mitosis. To identify the mechanism responsible for the mitotic-associated increases in H3K79me2, we employed a combination of reverse and chemical genetics and show that DOT1L expression and function are essential requirements. Although our results are most consistent with DOT1L being the mitosis-specific methyltransferase, they do not preclude the possibility that DOT1L indirectly regulates the large mitotic increases in H3K79me2 abundance through an unknown mechanism. Finally, based on similar dynamics observed for other histone PTMs (e.g. H3S10ph, H3K9me3 and H4K20me2) with established roles in chromosome biology and genome stability, we predicted that H3K79me2 would exhibit a similar role during mitosis. Using siRNA and chemical treatments, we show that the loss of H3K79me2 levels during mitosis is associated with increases in chromosome instability and aberrant mitotic events. Collectively, our data suggest

there is a transient uncoupling of the trans-histone pathway during mitosis, which is normally required to ensure mitotic fidelity and chromosome stability in human cells.

The dynamic temporal progression pattern we observe for H2Bub1 extends the observations of Wu *et al.* [200] who showed that ubiquitinated H2B, but not specifically H2Bub1 is reduced within mitotically enriched histones isolated from mouse and Chinese hamster cells. Although it is unclear why there is such a dramatic loss of H2Bub1 during mitosis, there are a number of possibilities. First, because H2Bub1 is associated with transcription[76,96], the low levels may simply reflect the transcriptionally silent status of mitotic cells[201]. Second, replication-independent nucleosome assembly may occur[202] which is a mechanism that impacts the global abundance of other histone PTMs through histone replacement. However, replication-independent nucleosome assembly is typically associated with transcription and/or DNA repair[203], and neither process occurs to a large extent within mitotic cells. It is also unlikely that this mechanism accounts for the dramatic loss of H2Bub1 along the entire length of the chromosome arms, particularly as they are compacting during mitosis and histone replacement would not be easily achieved. Finally, it is possible that the removal of ubiquitin is a normal pre-requisite for proper chromosome condensation to occur. Ubiquitin is a relatively large ~8.5kDa covalent modification that is added onto the carboxy-terminal tail (K120) of histone H2B (~13.8kDa). It is plausible that H2Bub1 represents a structural barrier to the compacting mitotic chromosomes that must be removed for proper compaction and segregation to occur. In support of this possibility, Fierz *et al.* [83] recently showed that H2Bub1 disrupts local and higher-order chromatin compaction in chemically defined nucleosomal arrays. Moreover, studies from a variety of model organisms have shown that higher-order chromosome compaction is necessary

to ensure mitotic fidelity[193,204]. In any case, the functional significance and underlying mechanism accounting for the loss of mitotic H2Bub1 warrant further investigation.

Numerous studies have characterized the inter-relationship of H2Bub1 and H3K79me2 [205]. However, since these studies focused on transcription, they are biased towards describing relationships within interphase populations. Unlike these previous studies, the current study focuses on the relationship and changes that occur within mitotic populations, when transcription rates are low[189]. Given the existence of the well-characterized trans-histone pathway, the identification of distinct temporal progression patterns for H2Bub1, H3K4me2 and H3K79me2 during mitosis are surprising. Here we show that the global abundance of H3K4me2 remains visually consistent throughout the cell cycle, and is in agreement with previous works suggesting that histone methylation is classically considered a static epigenetic mark[206,207]. Perhaps most interesting is the observation that H3K79me2 levels are highly dynamic and maximal during mitosis, which is opposite to those of H2Bub1. Our findings support those of Feng *et al.*[133] who reported an overall increase in the abundance of H3K79 methylation within mitotically enriched HeLa cells. However, they did not distinguish between the methylation subtypes (i.e. mono-, di- and tri-methylation). More recently, Kim and colleagues[208] employed Western blots to show that H3K79me2 levels are only marginally dynamic within in a lung cancer cell line. Using synchronization populations of cells, they show that H3K79me2 levels peak in S-phase, but not during mitosis as shown in the current study. Although the underlying reason for this discrepancy is unclear, it may be due to the different cell models employed, or to the fundamental differences of population-based, biochemical approaches they employed, relative to the single cell, semi-quantitative imaging microscopy employed in the current study. Furthermore, the observations and conclusions of the current study are based on experiments

conducted in two distinct cellular contexts (HCT116; transformed epithelial cells, and hTERT; immortalized fibroblast cells), and are in agreement with those gleaned from studies in model organisms including *Trypanosoma brucei*[131] and *Saccharomyces cerevisiae*[209]. Thus, our data show that H3K79me2 is highly dynamic during mitosis, and further suggests that the mitotic-associated dynamics are evolutionarily conserved in eukaryotes.

A number of studies exist that show certain histone PTMs exhibit mitosis specific increases that are essential for mitotic fidelity (reviewed in [196]). Our data show that H3K79me2 levels are dynamic, and suggest that these dynamics are essential requirements for genome stability. In support of this possibility, depleting the mitotic associated levels of H3K79me2 by DOT1L silencing or inhibition was associated with increases in chromosome numbers and aberrant mitotic events (Figure 3.6). Interestingly, *DOT1L* is somatically altered in a number of tumor types (Table 3.S1), and murine models have shown that Dot1l-deficiencies correlate with increases in DNA content[127,134]. Accordingly, DOT1L expression and function, and concomitant mitotic-increases in H3K79me2 are implicated as essential components required to maintain genome stability in human cells.

In summary, our findings show that H2Bub1, H3K4me2 and H3K79me2 exhibit unique temporal progression patterns throughout the cell cycle. Of particular interest, we show that H3K79me2 is highly dynamic during mitosis, and identify DOT1L as a mitosis-specific histone methyltransferase. We further show that H3K79me2 dynamics are normally required to preserve genome stability, which adds H3K79me2 to the emerging list of histone PTMs with similar dynamics and roles in chromosome biology and genome stability. Thus, our data coupled with DNA sequencing data from various tumor types and recent *Dot1l* animal models, strongly

suggest that altered DOT1L function, particularly during mitosis, may be a pathogenic event that drives genome instability, and contributes to tumorigenesis.

3.5 Supporting Information

3.5.1 Supporting Tables

Table 3.S1: Frequency of Somatic Gene Alterations in Cancer[195,210]

Gene	Tumor Type	n[A]	Type and Frequency of Somatic Alterations (n)			Total
			Mutation	Del[B]	Amp[C]	
RNF20	Colorectal	72	5.6% (4)	0.0% (0)	0.0% (0)	5.6% (4)
RNF20	Uterine	240	5.0% (12)	0.8% (2)	0.0% (0)	5.8% (14)
RNF20	Melanoma	121	5.0% (6)	0.0% (0)	0.0% (0)	5.0% (6)
RNF20	Lung	129	4.7% (6)	0.0% (0)	0.0% (0)	4.7% (6)
RNF20	Ovarian	316	0.9% (3)	0.6% (2)	0.3% (1)	1.8% (6)
DOT1L	Colorectal	72	11.1% (8)	0.0% (0)	0.0% (0)	11.1 (8)
DOT1L	Bladder	127	4.7% (6)	0.0% (0)	1.6% (2)	6.3% (8)
DOT1L	Melanoma	121	5.8% (7)	0.0% (0)	0.0% (0)	5.8% (7)
DOT1L	Lung	129	4.7% (6)	0.8% (1)	0.0% (0)	5.5% (7)
DOT1L	Ovarian	311	0.3% (1)	3.5% (11)	0.3% (1)	4.1% (13)

[A]Number of tumors sequenced (n)
[B]Homozygous Deletion (Del)
[C]Amplification (Amp)

Table 3.S2: Antibodies and Dilutions Employed

Antibody/Epitope	Source	Catalog No.	Species	Working Dilution[A]	
				IIF[B]	WB[C]
RNF20	Abcam	ab32629	Rabbit	1:400	1:6,000
H2Bub1	Millipore	05-1312	Mouse	1:200	1:10,000
H3K4me2	Abcam	ab32356	Rabbit	1:200	1:5,000
H3K79me2	Abcam	ab3594	Rabbit	1:400	1:15,000
H3S10ph	Abcam	ab14955	Rabbit	1:10,000	1:10,000
DOT1L	Abcam	ab180483	Mouse	n/a	1:2,000
α-Tubulin	Abcam	ab7291	Mouse	n/a	1:20,000
Rabbit IgG-Alexa Fluor 488	Molecular Probes	A-11034	Goat	1:200	n/a
Mouse IgG-Cy3	Molecular Probes	A-10521	Goat	1:200	n/a
Rabbit IgG-HRP	Jackson ImmunoResearch	111-035-006	Goat	n/a	1:15,000
Mouse IgG-HRP	Jackson ImmunoResearch	115-035-146	Goat	n/a	1:10,000

[A]not applicable (n/a)
[B]Indirect immunofluorescence (IIF)
[C]Western blot (WB)

Table 3.S3: Student *t*-test for the Mean DAPI-Normalized H3K79me2 Total Signal Intensities as Determined by Semi-Quantitative Imaging Microscopy

Cell Cycle Stage	n[A]	Mean ± Standard Deviation	*p*-value[B]	Fold Increase
Interphase	23	1.00 ± 0.02	n/a	n/a
Mitosis[C]	23	31.04 ± 1.63	<0.0001	31

[A]Number of cells analyzed (n)
[B]Based on Student's *t*-tests comparing the mean DAPI-normalized H3K79me2 total signal intensity of interphase and mitotic cells. Not applicable (n/a)
[C]limited to only those cells in prophase, prometaphase and metaphase as identified by cytological features

Table 3.S4: Student *t*-test for the Mean DAPI-Normalized H3K79me2 Total Signal Intensities Following Various Treatments as Measured by Semi-Quantitative Imaging Microscopy

Condition	n[A]	Mean ± Standard Deviation	*p*-value[A]
48 Hours Post Silencing			
Mitotic Cells + siGAPDH	23	100.00 ± 4.97	n/a
Mitotic Cells + siDOT1L	23	54.72 ± 3.78	<0.0001
2 Hours Post Treatments			
Mitotic Cells + DMSO	23	100.00 ± 4.13	n/a
Mitotic Cells + SGC0946	23	24.36 ± 1.60	<0.0001

[A]Number of cells analyzed (n)
[B]Based on Student's *t*-tests comparing the mean DAPI-normalized H3K79me2 total signal intensity of mitotic cells for either DOT1L silenced or inhibited conditions with their respective controls. Not applicable (n/a)

Table 3.S5: Cell Cycle Analyses Following Protein Silencing or Drug Treatment

Condition/Treatment	G0/G1	S-phase	G2/M
Non-treated	41.9%	35.9%	20.6%
siGAPDH	41.8%	35.9%	20.6%
siRNF20	36.3%	35.2%	26.5%
siDOT1L	39.9%	40.0%	18.8%
DMSO	35.6%	36.4%	26.3%
SGC0946	38.2%	34.4%	25.5%

Table 3.S6: Student *t*-tests Comparing Mean Chromosome Numbers Following DOT1L Silencing or Inhibition

Condition	n[A]	Mean ± Standard Deviation	*p*-value[B]
siGAPDH	100	44.80 ± 0.07	n/a
siDOT1L	100	48.38 ± 1.38	0.0102
DMSO	100	44.97 ± 0.05	n/a
SGC0946	100	46.30 ± 0.49	0.0075

[A]Number of cells analyzed (n)
[B]Not applicable (n/a)

Table 3.S7: The Loss of Mitotic H3K79me2 Levels is Associated with Increases in Aberrant Mitotic Events

Condition	Total Mitotic Cells Analyzed	Mean Frequency of Defects (%) (± Standard Deviation)	Fold Increase[A]
siGAPDH	315	5.570 ± 0.8907	n/a
siDOT1L	337	9.696 ± 2.163	1.74-fold
DMSO	306	3.742 ± 1.007	n/a
SGC0946	318	9.303 ± 1.918	2.49-fold

[A]Fold increase is calculated relative to the corresponding control. n/a; not applicable

3.5.2 Supporting Figures

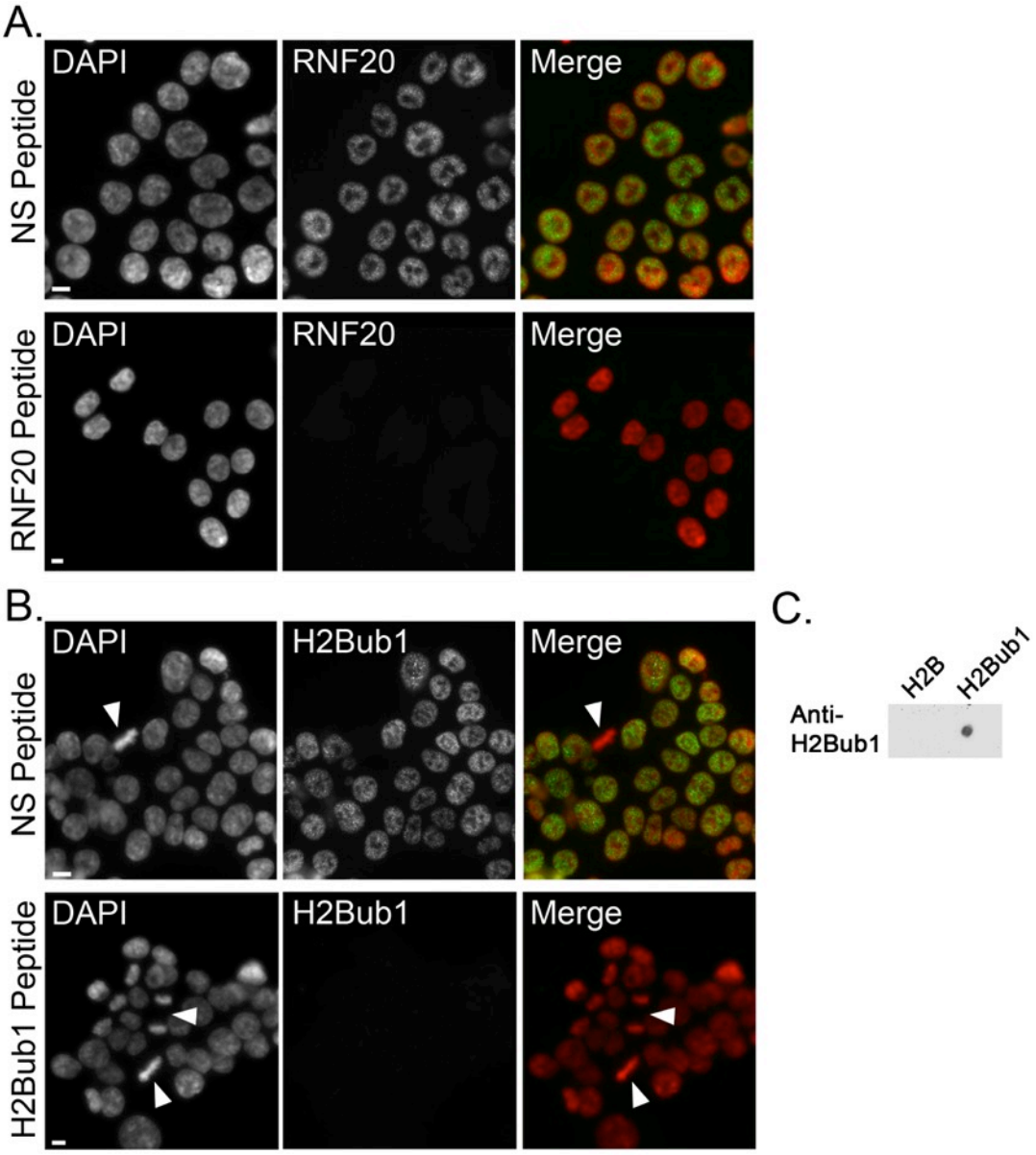

Figure 3.S1: Validation of the RNF20 and H2Bub1 Antibodies
Representative low-resolution images collected from the IIF (indirect immunofluorescent) peptide competition assays using HCT116, a non-specific peptide (NS peptide) or the RNF20-specific, immunizing peptide (A), or the H2Bub1-specific peptide (B). The epitope of interest and DAPI are pseudo-colored green and red, respectively, within the merged images. Images were acquired using identical exposure times and thus qualitative comparisons can be made between the non-specific and the corresponding specific peptide for each epitope. Arrowheads identify mitotic cells and the scale bar represents 5μm. (C) Dot blot assays demonstrating the specificity of the H2Bub1 antibody for the H2Bub1 epitope and not the unmodified control (H2B).

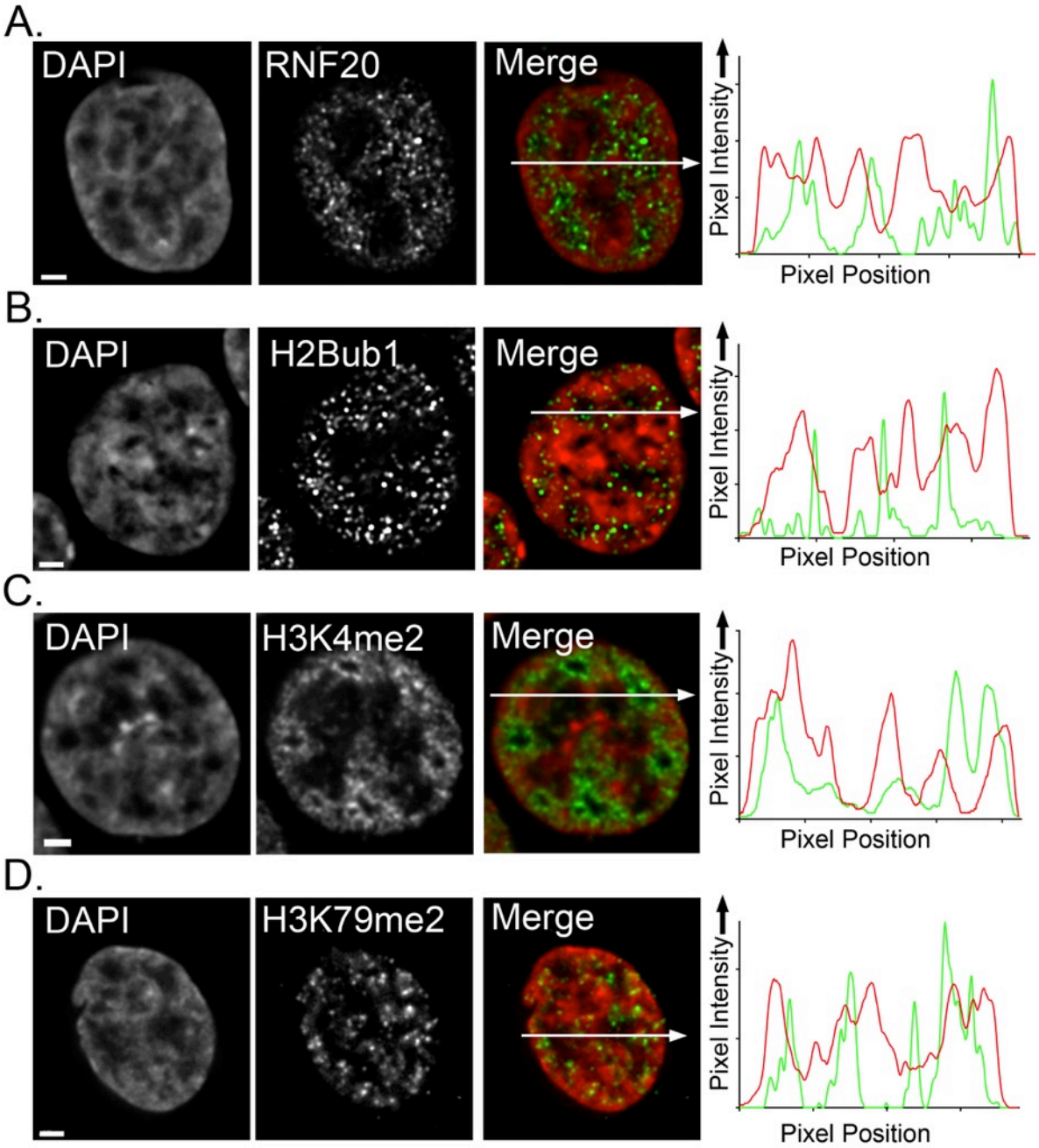

Figure 3.S2: Defining the Spatial Relationships of RNF20, H2Bub1, H3K4me2 and H3K79me2 within Interphase Chromatin

Representative high-resolution (63×) deconvolved images of interphase HCT116 cells immunofluorescently labeled for RNF20 (A), H2Bub1 (B), H3K4me2 (C), and H3K79me2 (D), and counterstained with DAPI. The epitope of interest and DAPI are pseudo-colored green and red, respectively, within the merged images. Scale bar represents 2μm. Line scans (right panels) show the spatial juxtaposition of the four specific epitopes evaluated (green) relative to DAPI (red). Lines and arrows within the Merge indicate the position and direction presented in the graph. Each epitope appears to be enriched within or adjacent to euchromatic regions (less intense DAPI stained regions), and reduced within heterochromatic regions (intense DAPI stained regions).

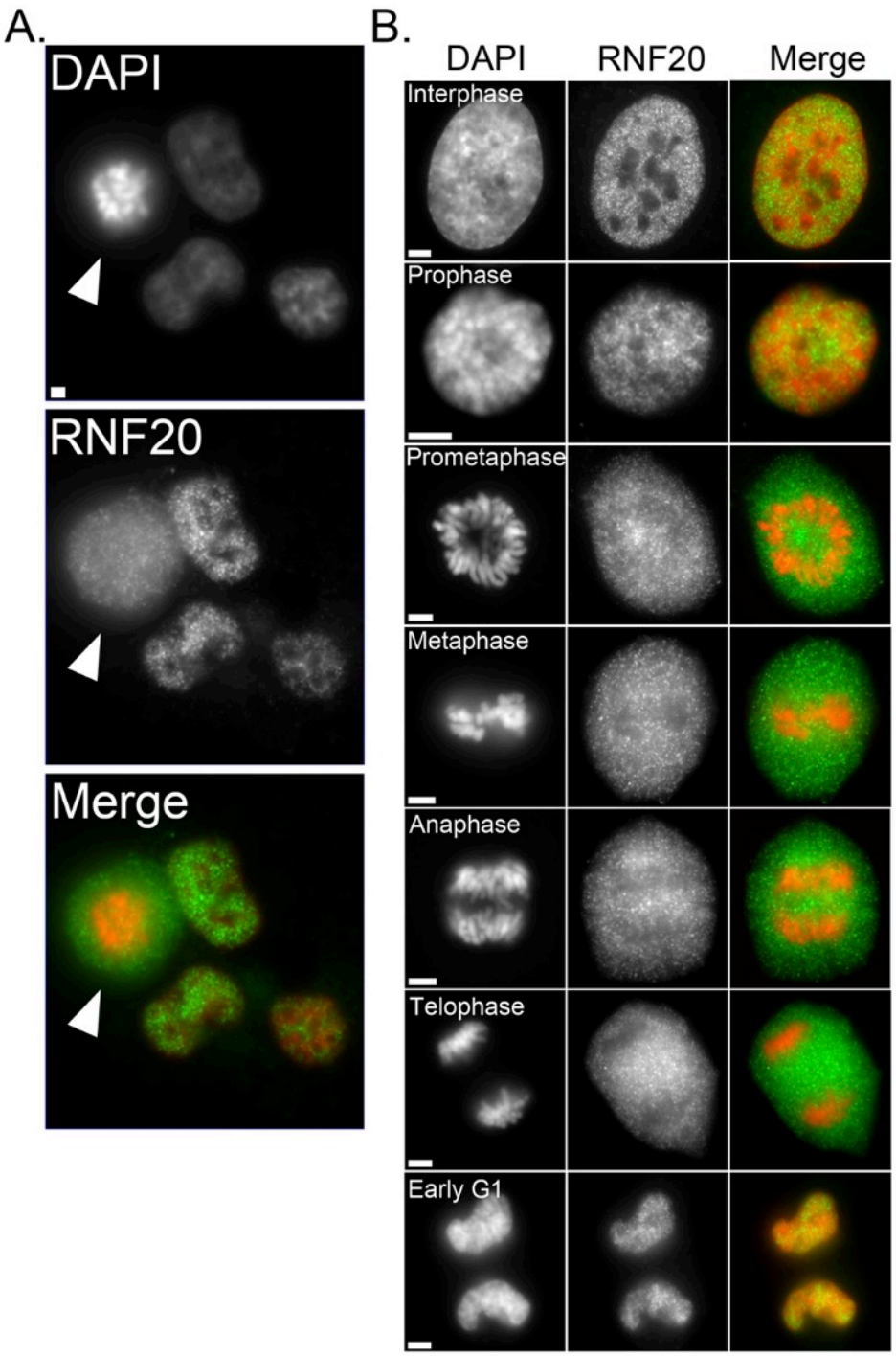

Figure 3.S3: RNF20 is Spatially Relocalized in Mitotic hTERT Cells
(A) Representative image of asynchronous hTERT cells immunofluorescently labeled with an anti-RNF20 antibody (green) and counterstained with DAPI (red). Arrowhead identifies a mitotic (prometaphase) cell, while the scale bar represents 5μm. (B) High-resolution images depicting the temporal and spatial progression pattern of RNF20 (green) throughout the various stages of the cell cycle (indicated). Note that variable exposure times were employed for each cell cycle stage so as to best capture the localization of RNF20 and thus qualitative comparisons cannot be made between stages. Scale bar represents 2μm.

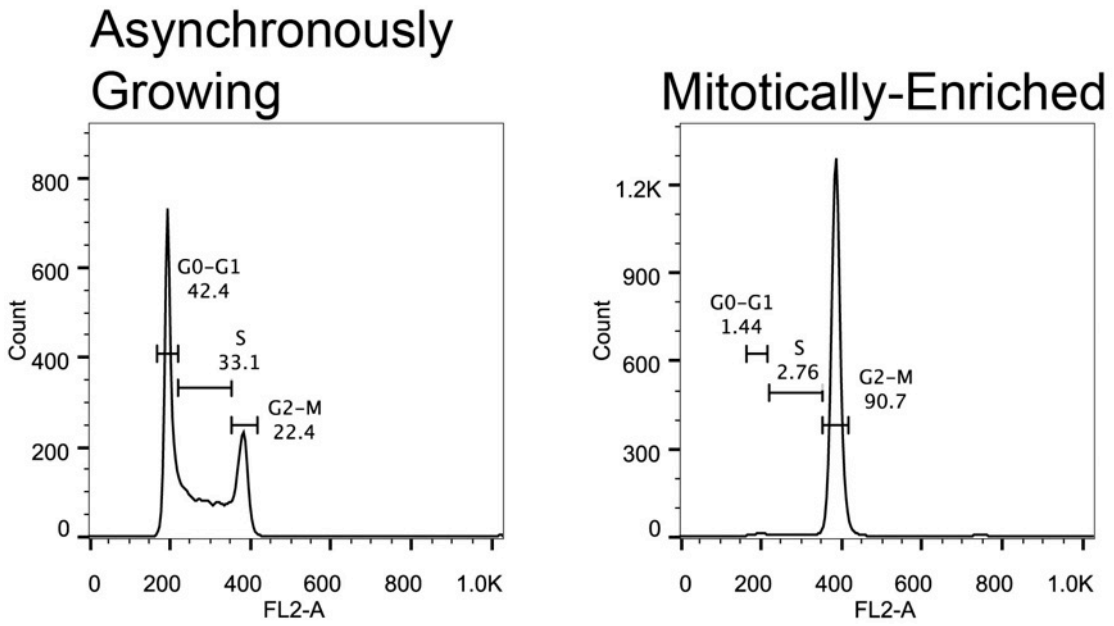

Figure 3.S4: Flow Cytometric Analyses of Asynchronous and Mitotically-enriched Populations

Cell cycle analyses of asynchronous (left) or a mitotic-enriched (nocodazole treated [right]) populations of HCT116 cells labeled with PI. Markers are included to identify the various cell cycle stages with the percentage of cells within each stage provided.

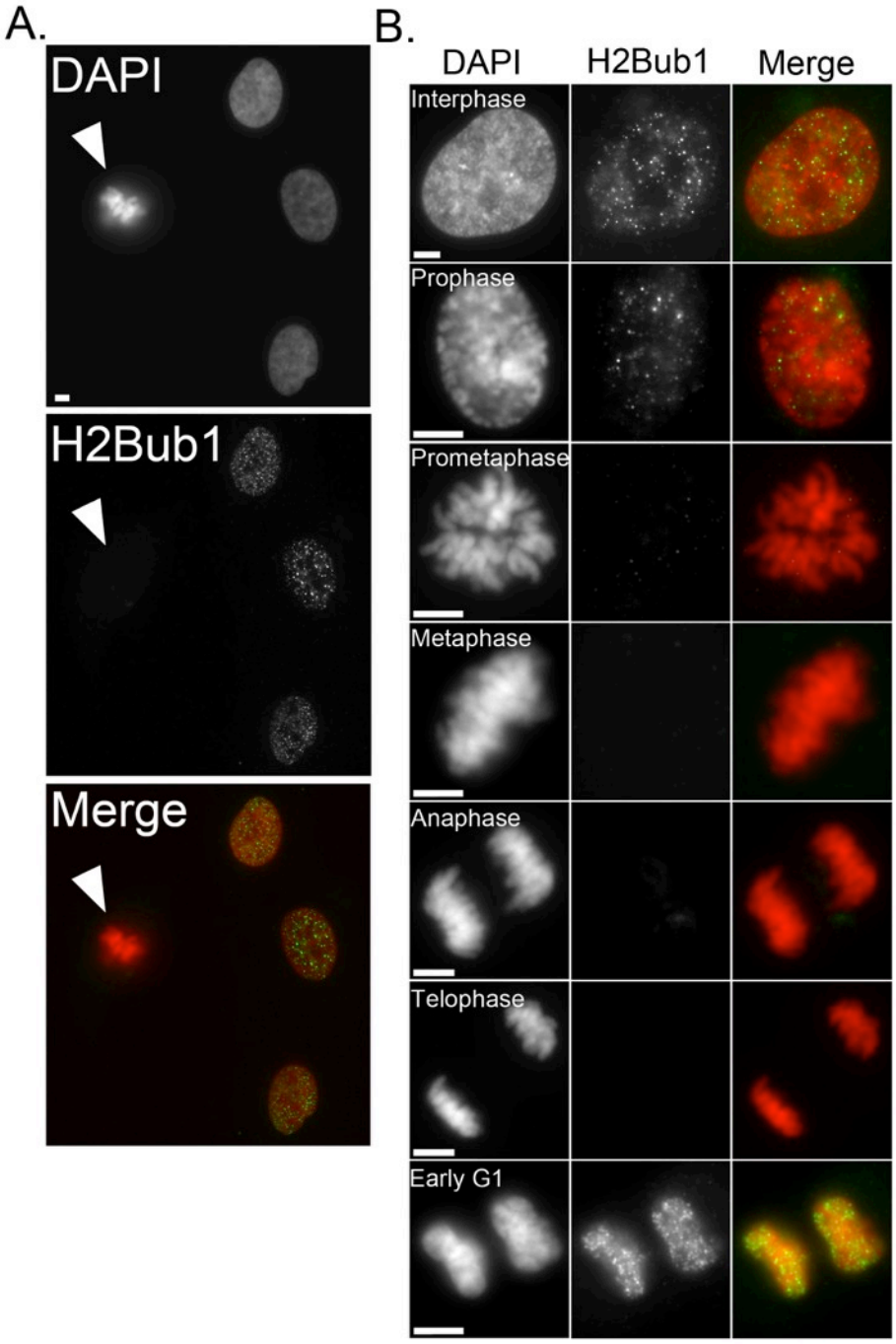

Figure 3.S5: H2Bub1 Levels Decrease Dramatically During Mitosis in hTERT Cells
(A) Representative image of asynchronous hTERT cells immunofluorescently labeled with an anti-H2Bub1 antibody (green) and counterstained with DAPI (red). Arrowhead identifies a mitotic (metaphase) cell, while the scale bar represents 5μm. (B) High-resolution images depicting the temporal and spatial progression pattern of H2Bub1 (green) throughout various stages of the cell cycle (indicated). Note that the exposure times were maintained constant for each cell cycle stage so as to show qualitative changes in abundance during mitosis relative to interphase or early G1. Scale bar represents 2μm.

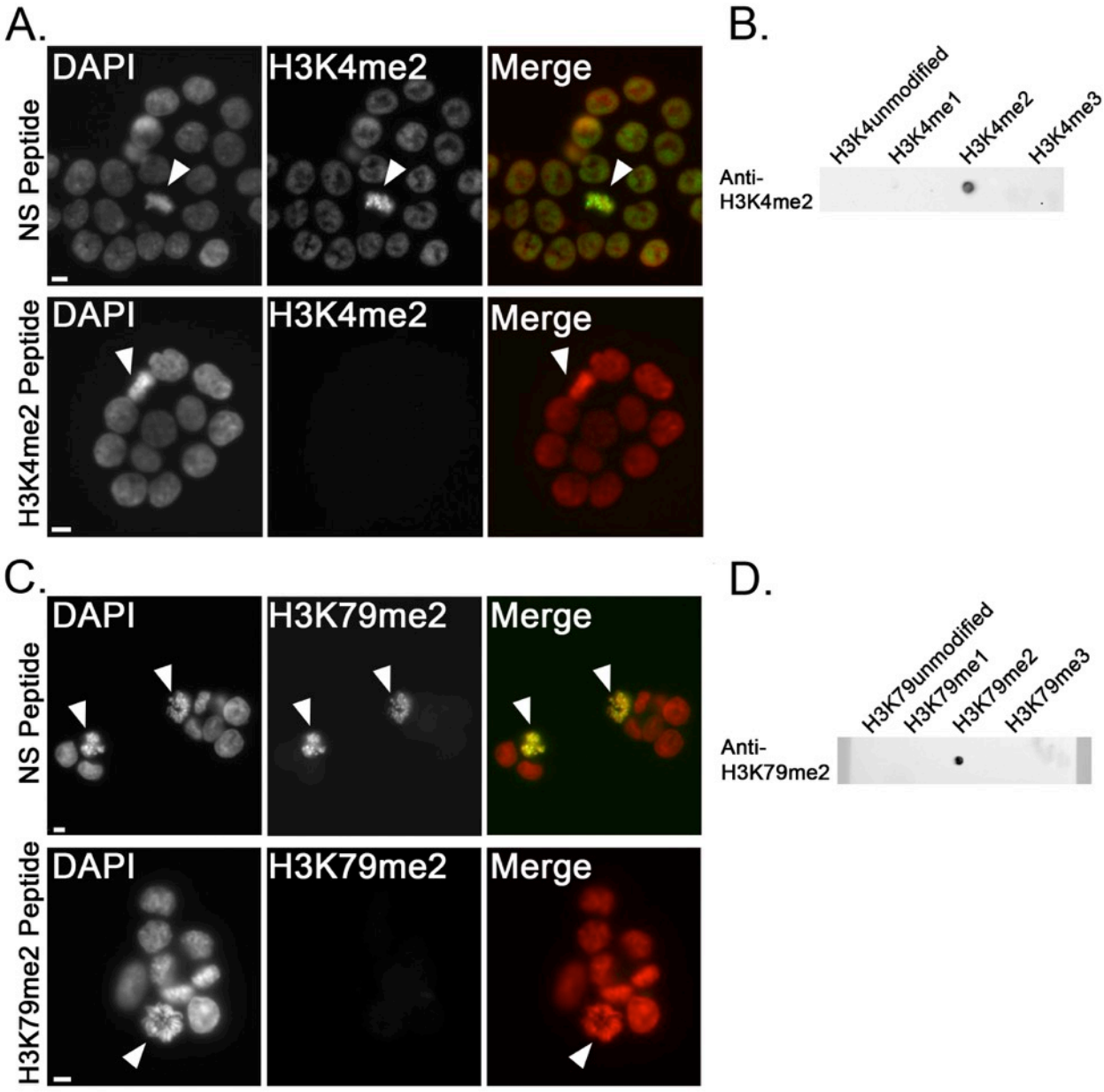

Figure 3.S6: Validation of the H3K4me2 and H3K79me2 Antibodies
Representative low-resolution images collected from the IIF peptide competition assays using a non-specific peptide (NS peptide) or the H3K4me2-specific peptide (A), or the H3K79me2-specific peptide (C). The epitope of interest and DAPI are pseudo-colored green and red, respectively, within the merged images. Images were acquired using identical exposure times and thus qualitative comparisons can be made between the non-specific and the corresponding specific peptide for each epitope. Arrowheads identify mitotic cells and the scale bars represent 5μm. Dot blot assays demonstrating the high specificity of the H3K4me2 (B) or H3K79me2 (D) antibodies for their cognate epitope, but not closely related mono- or tri-methylated species.

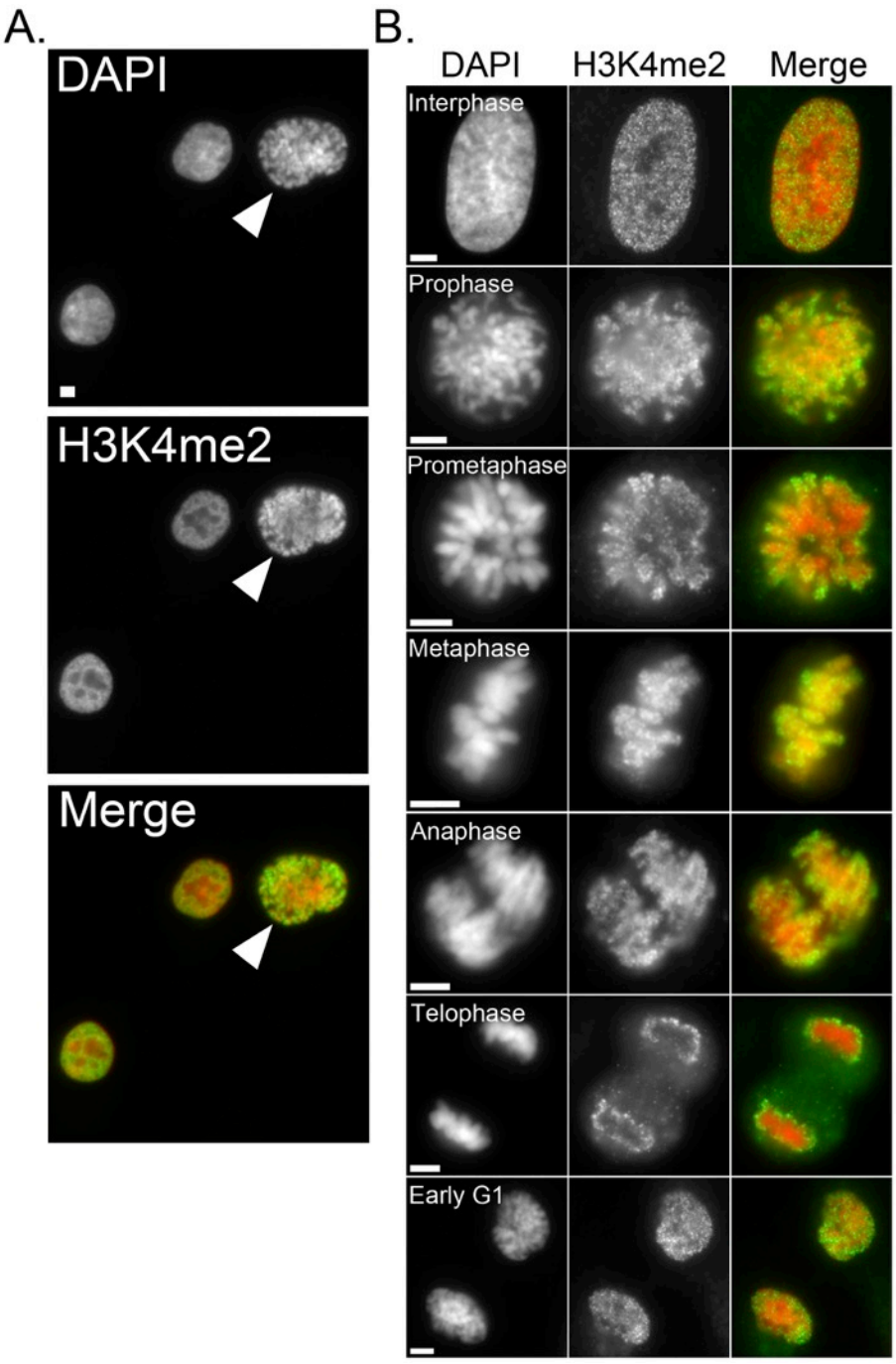

Figure 3.S7: H3K4me2 Levels in hTERT Cells are Relatively Constant Throughout the Cell Cycle

(A) Representative image of asynchronous hTERT cells immunofluorescently labeled with an anti-H3K4me2 antibody (green) and counterstained with DAPI (red). Arrowhead identifies a mitotic (prophase) cell, while the scale bar represents 5μm. (B) High-resolution images depicting the spatial and temporal progression pattern of H3K4me2 (green) throughout the cell cycle (indicated). Note that variable exposure times were employed for each cell cycle stage so as to best capture the localization of H3K4me2 and thus qualitative comparisons cannot be made between stages. Scale bar represents 2μm.

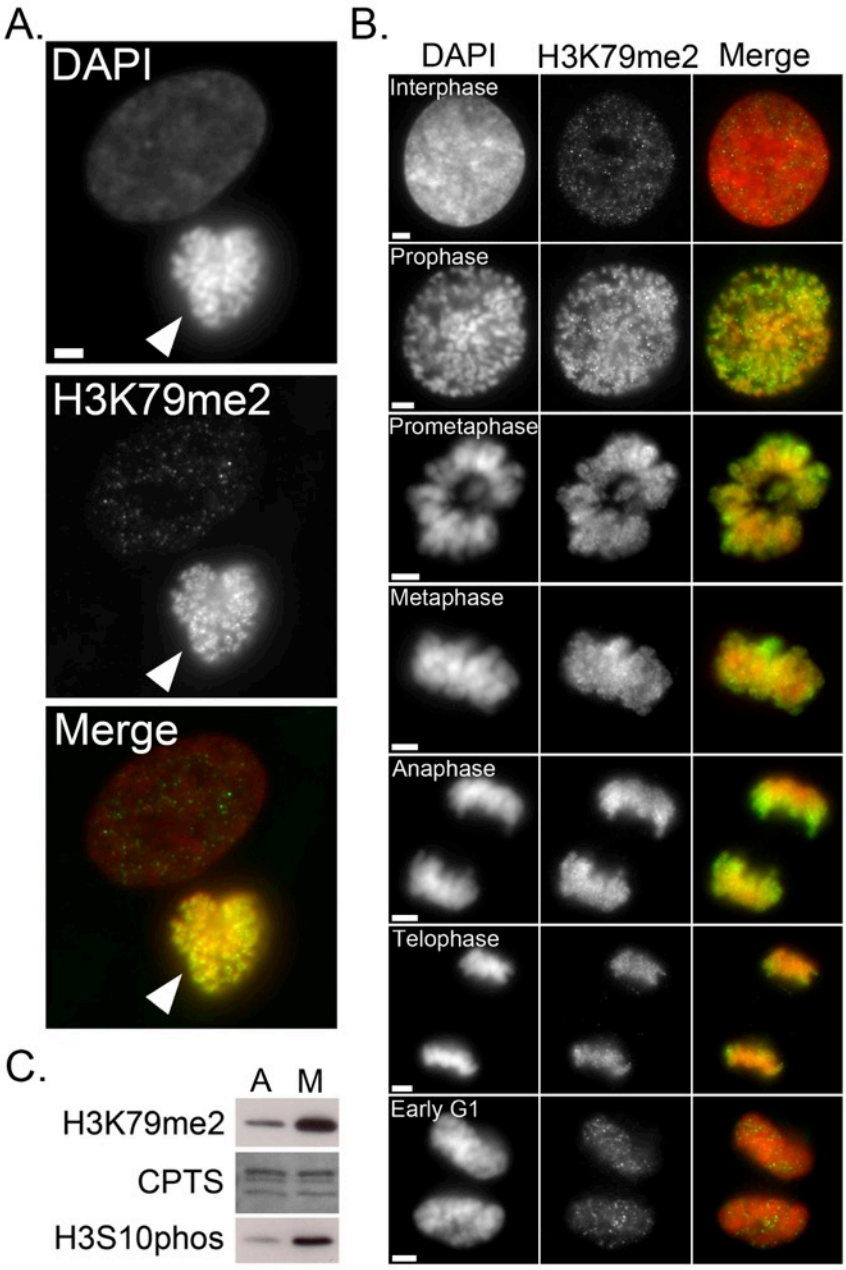

Figure 3.S8: The Global Abundance of H3K79me2 Increases Dramatically during Mitosis in hTERT Cells

(A) Representative image of asynchronous hTERT cells immunofluorescently labeled with an anti-H3K79me2 antibody (green) and counterstained with DAPI (red). Arrowhead identifies a mitotic (prometaphase) cell and the scale bar represents 5μm. (B) High-resolution images depicting the spatial and temporal progression pattern of H3K79me2 (green) throughout the cell cycle (indicated). Note that variable exposure times were employed for each cell cycle stage so as to best capture the localization of H3K79me2 and thus qualitative comparisons cannot be made between stages. Scale bar represents 2μm. (C) Western blot analysis of H3K79me2 from asynchronous (A) and mitotic-enriched (M; nocodazole treated) hTERT populations. Phosphorylation of serine 10 of histone H3 was included as a mitosis-specific marker, while CPTS serves as the loading control.

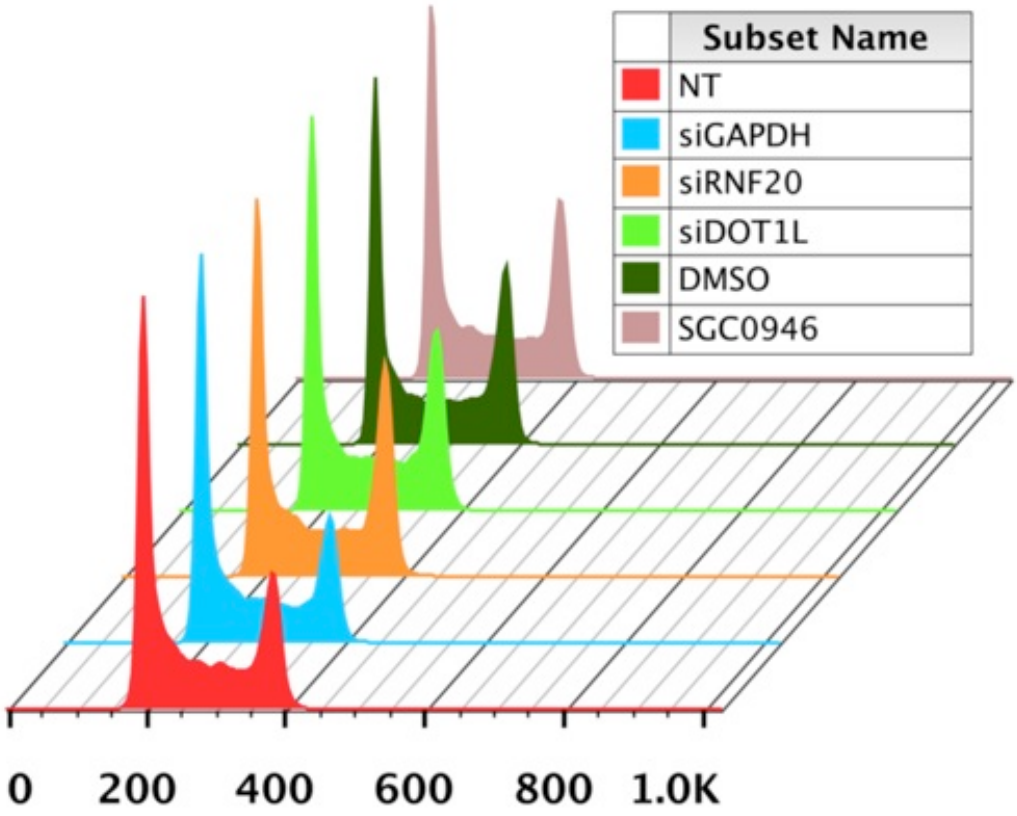

Figure 3.S9: Cell Cycle Analyses of Silenced and Drug Treated Cellular Populations
Flow cytometric analyses of DNA content profiles from asynchronously growing cells harvested from controls (Non-treated [NT] and DMSO-treated [DMSO]), protein silenced populations (siGAPDH, siRNF20 or siDOT1L) or drug treated populations (SGC0946). Percentage of cells within each stage (i.e. G0/G1, S-phase or G2/M) are presented in Table 3.S7.

Chapter 4

GENERATION AND PHENOTYPIC CHARACTERIZATION OF AN HCT116-CAS9 EXPRESSING CELL LINE

4.1 Abstract

The E3 ubiquitin ligase *RNF20* is an attractive molecule for detailed study as hypomorphic expression and/or function underlies genomic instability and occurs in a wide variety of cancer types. To date, studies characterizing the abnormal cell biology associated with hypomorphic RNF20 expression have been limited to RNA-interference approaches, which only produce transient and/or incomplete protein depletion and may not accurately model the total loss of *RNF20* predicted to occur in certain cancers. The CRISPR-Cas9 genome editing system, which enables the editing of virtually any gene by simple transfection is capable of producing complete gene inactivation and may overcome these initial limitations. The karyotype stability associated with the human colorectal cancer cell line HCT116 makes it an excellent genetic model for studying *RNF20* by CRISPR-Cas9-mediated gene inactivation. However to date, the low CRISPR-Cas9 transfection efficiency typical of HCT116 has hindered its application. Large particle transfection is a key characteristic that determines transfection efficiency and appears to be a limiting factor in certain 'hard-to-transfect' cell lines like HCT116. In this study, we increase the CRISPR-Cas9 transfection efficiency of HCT116 cells by removing the Cas9 expression cassette from the large transfection particle and stably integrating it within the genome to allow for a dramatic reduction in particle size and increase in transfection efficiency. We generate and characterize twelve HCT116-Cas9 clones that display a range of cellular phenotypes. We ultimately identify an HCT116-Cas9 clone, E08 that is highly similar to parental HCT116 cells and is capable of high efficiency CRISPR-Cas9 editing. Furthermore, in a proof-of-concept experiment, we employ E08 cells with the CRISPR-Cas9 system to produce *RNF20*- and *PPIB*-deficient HCT116 cells. Collectively, we generate a HCT116 'CRISPR-Cas9-ready' cell line that can be routinely employed in subsequent genome editing experiments.

4.2 Introduction

The putative tumor suppressor gene *RNF20* encodes a human E3 ubiquitin ligase that monoubiquitinates histone H2B on lysine residue 120[76,78,104,106,211]. RNF20 is an attractive molecule for detailed study as hypomorphic expression and/or function occur in a range of cancers. In fact, promoter hypermethylation[76], multiple somatic mutations[195,212], and altered *RNF20* expression levels[213] have been identified in various cancer types and suggest diminished or ablated *RNF20* expression underlies oncogenesis[78]. To date, investigating the biological consequences associated with reduced *RNF20* expression has been limited to traditional approaches such as RNA-interference, which only produces a transient and/or short-term reduction in protein levels and may not accurately model the total loss of *RNF20* predicted to occur in certain cancers. RNF20 is a putative human chromosome stability gene that when mutated or downregulated is predicted to elicit chromosome instability, a hallmark of cancer initiation and progression[147]. Collectively, the ability to permanently ablate *RNF20* within human cells would empower several studies including those aimed at characterizing its role in CIN. CIN, or the increase in the rate in which whole chromosomes or parts thereof are gained or loss, is an aberrant phenotype associated with a variety of cancers and is believed to be an early event in the etiology of oncogenesis[12].

Due to its inherent karyotypic stability and near diploid chromosome complement, multiple studies have employed HCT116 cells as a genetic model to provide critical insights into biological function, including human chromosome stability gene validation[159,185,214-216]. These studies often aim to genetically inactivate or diminish expression of a candidate human chromosome stability gene and evaluate the loss of karyotypic stability, often measured by changes in aneuploidy. For example, Rajagopalan *et al.*[215] employed classical homologous

recombination techniques to disrupt both alleles of *hCDC4* in HCT116 to show that *hCDC4*-deficiency caused a striking change in chromosome numbers that were not present in *hCDC4*-proficient controls. Additionally, Jallepalli *et al.*[214] employed homologous recombination techniques to inactivated both copies of *PTTG1* and validate *PTTG1* as a human chromosome stability gene. Although the above studies provided valuable information, genetic inactivation by classical gene-trapping or homologous recombination repair is time-consuming, laborious and technically challenging[217]. The recent development of highly efficient genome editing systems promise too overcome the majority of these limitations and is expected to revolutionize several studies including the identification and validation of human chromosome genes.

The prokaryotic type II Clustered Regularly Interspaced Short Palindromic Repeats (CRISPR)-Cas9 genome editing system represents a major advancement in genome engineering technologies, allowing researchers to precisely edit genomes of a wide variety of organisms with relative ease[218]. The CRISPR-Cas9 system is quickly becoming an integral tool in cancer genomics that can be employed to generate cancer-associated genomic alterations or ablate gene expression in multiple cell lines[219]. Successful CRISPR-Cas9 genome editing mandates the delivery of three essential components to target cells, a sequence-specific short 40 nucleotide (nt) non-coding small guide RNA (sgRNA), a long 4,119 nt DNA Cas9 expression cassette that encodes the DNA endonuclease, and a short 149 nt non-coding trans-activating CRISPR RNA (tracrRNA) that serves as a scaffold for all three components (Figure 4.1A). The majority of commercially available CRISPR-Cas9 editing systems employ an 'all-in-one' lipid-based transfection approach to deliver these components (Figure 4.1B, left). However, in certain 'hard-to-transfect' cell lines like HCT116, lipid-based transfection efficiency, and thus editing efficiency, is often low[220,221].

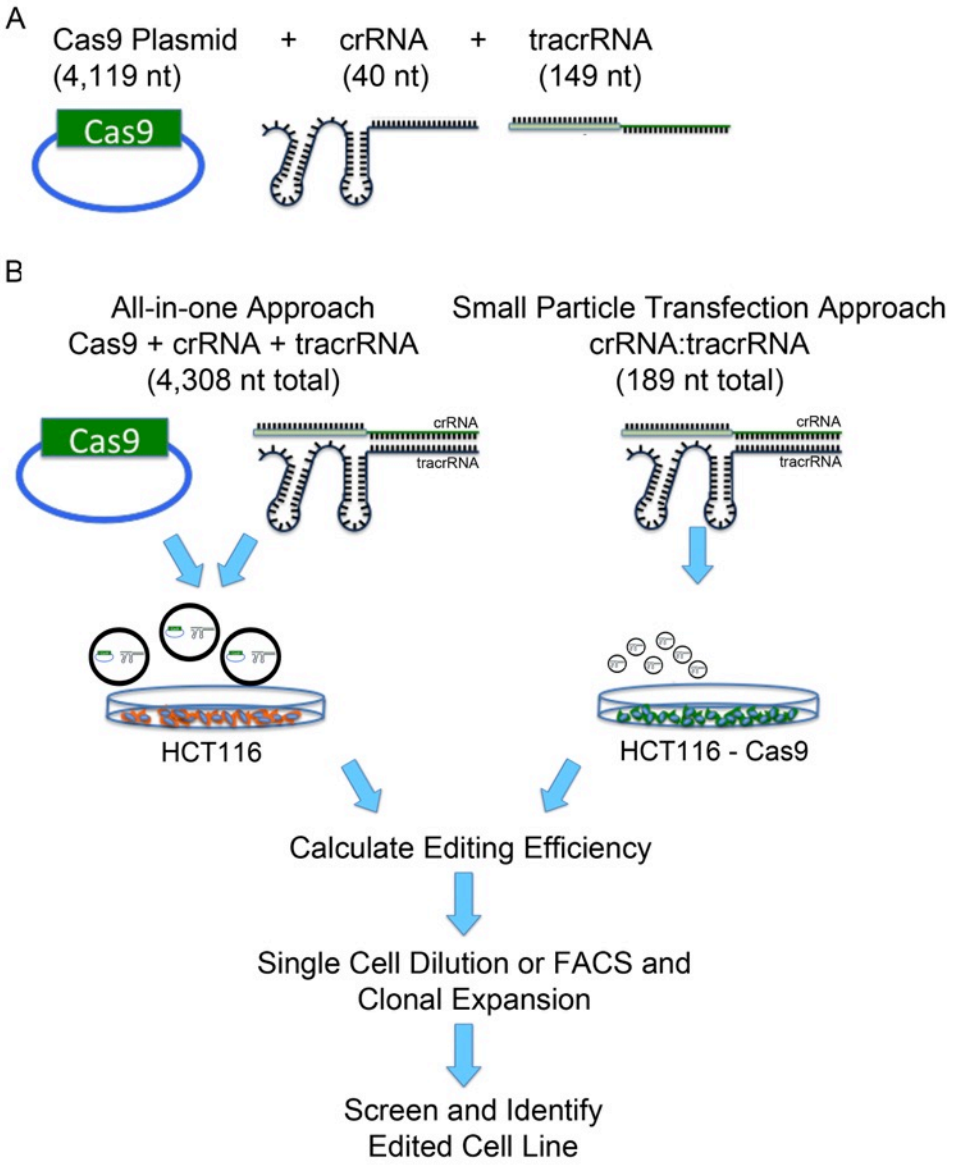

Figure 4.1: The CRISPR-Cas9 System
(**A**) Three essential components of CRISPR-Cas9. (**B**) *Left*, 'All-in-one' CRISPR-Cas9 transfection approach. All three components are delivered via large particle co-transfection. This method results in low CRISPR-Cas9 transfection efficiency when employed with the 'hard-to-transfect' HCT116 cell line. *Right*, small particle transfection approach. HCT116 cells that stably express the Cas9 endonuclease. Therefore, CRISPR-Cas9 editing only requires small particle transfection (sgRNA + tracrRNA) and is expected to increase transfection and editing efficiencies.

It is generally accepted that transfection particle size is a key characteristic that determines the successful delivery of nucleic acids into cells, and that transfection efficiency is inversely correlated with particle size[222]. To address this limitation and greatly reduce transfection particle size, the large Cas9 expression cassette is often removed from the transfection particle and stably integrated within the genome of target cell lines, where it is constitutively expressed. Consequently, once generated and characterized, these 'CRISPR-Cas9 ready' cell lines have the advantage of requiring only small particle transfection (sgRNA + tracrRNA) which is expected to increase transfection and editing efficiencies (Figure 4.1B, right).

To date, the low CRISPR-Cas9 transfection efficiency typical of HCT116 cells (<2%, unpublished observations, Guppy) has hindered the ability to efficiently produce *RNF20*-deficient cells through the CRISPR-Cas9 system[223]. HCT116 is a transformed colorectal cancer cell line with a modal number of 45 chromosomes. Furthermore, HCT116 cells have an intact DNA damage response and are thus compatible with CRISPR-Cas9-mediated homology and non-homology directed repair, making them an excellent choice for both knock-in and knock-out genome editing experiments. In addition, HCT116 exhibits microsatellite instability (*MLH1*-deficient) and not CIN, whether numerical (nCIN, changes in chromosome numbers) or structural (sCIN, changes in gross chromosome structure)[25]. Accordingly, the ability to rapidly identify and validate candidate human chromosome stability genes such as *RNF20* in HCT116 cells would allow for a greater understanding of the genetic drivers of certain cancers and thus serve as excellent models to explore potential mechanisms underlying oncogenesis, metastasis, as well as drug discovery and development.

In this study, we employ lentiviral transduction and various biochemical assays to generate and characterize twelve HCT116-Cas9 clones that display a range of cellular phenotypes. From this work, we identify an HCT116-Cas9 clone, E08 that is highly similar to parental HCT116 cells, and is capable of high efficiency CRISPR-Cas9 editing. To reduce the overall CRISPR-Cas9 transfection particle size from 4,288 base-pairs to 169 base-pairs, we stably integrate the Cas9 expression plasmid into the HCT116 genome. As predicted, the marked reduction in transfection particle size translated into a substantial increase in CRISPR-Cas9 genome editing efficiencies. Remarkably, compared to large particle 'all-in-one' HCT116 transfection, small particle transfection coupled with E08 cells showed a 9-fold increase in editing efficiency. As an initial proof-of-concept, we employ the E08 cells in combination with the CRISPR-Cas9 genome editing system and produce *RNF20*- and *PPIB*-deficient cells. Finally, we isolate and clonally expand 8 *PPIB*-deleted cells for future experiments. Collectively, we have generated and characterized a novel E08 cell line that can be efficiently employed in future CRISPR-Cas9 genome editing experiments.

4.3 Results

4.3.1 Lentiviral Cas9 Integration within the HCT116 Genome

Lentiviral transduction was employed to generate HCT116 cells that constitutively express Cas9. Briefly, HCT116 cells were seeded, allowed to attach, and transduced with commercially available pre-titred Cas9 lentiviruses (Dharmacon, VCAS10126). A multiplicity of infection of 0.10 was employed to increase the probability of a single integration event per infected cell. Transduction was performed in serum free media at 37°C for 4 h. Following transduction, pre-warmed complete media was added and cells were incubated overnight. The following day, viral-containing media was disposed of according to biosafety standards, and pre-warmed complete media was replaced. Approximately 48 h post-transduction, media was replaced with selective media (McCoy's 5A + Blasticidin). Cells were grown in selective media until distinct colonies were observed (~7 days). In order to isolate single cells for clonal expansion, colonies were dissociated by trypsinization, counted, and diluted to a concentration of approximately 96 cells per 9600 ml. Approximately 100 μl of cell solution (or approximately one cell) was dispensed into each well of a 96-well plate. Cells were grown at 37°C for 10 days. Clonal populations were identified and 12 putative HCT116-Cas9 clones were selected for initial characterization.

4.3.2 HCT116-Cas9 Clonal Populations Exhibit Heterogeneous Cas9 Expression Levels

Following lentivirus-mediated Cas9 integration, we wished to confirm and evaluate Cas9 expression in twelve HCT116-Cas9 clones. Using a Cas9 antibody (Millipore, MAC133, Anti-Cas9 Clone 7A9) and standard immunoblot detection, whole cell lysates were harvested from asynchronously dividing HCT116-Cas9 clones and analyzed (Figure 4.2A). Immunoblots revealed Cas9 expression in all HCT116-Cas9 clones that was not evident in parental HCT116 negative controls. Differences in Cas9 expression levels were observed when comparing clones. Based on immunoblots, clones E02, E06, and E08 were identified as exhibiting the highest levels of Cas9 expression. In order to empirically evaluate Cas9 expression levels, semi-quantitative indirect immunofluorescent imaging using identical exposure times was performed and mean Cas9 signal intensity was determined for each clone (Figure 4.2B to 4.2D). Subsequent analysis of variance (ANOVA) revealed statistically significant differences between HCT116-Cas9 clones (p-value < 0.0001, Table 4.S1), while Tukey multicomparison post-tests revealed statistically significant differences in mean Cas9 signal intensity between a subset of clones (Table 4.S2). Based on semi-quantitative analysis, B08, E02, and E08 were identified as having high Cas9 expression. Clones exhibiting high Cas9 expression by both immunoblotting and indirect immunofluorescence analyses (E02, E08) were prioritized as they are predicted to produce greater gene editing efficiencies. Although several HCT116-Cas9 clones met the criteria of high Cas9 expression, additional phenotyping was performed to assess morphology, growth kinetics, and karyotypic stability before pilot genome editing experiments were performed.

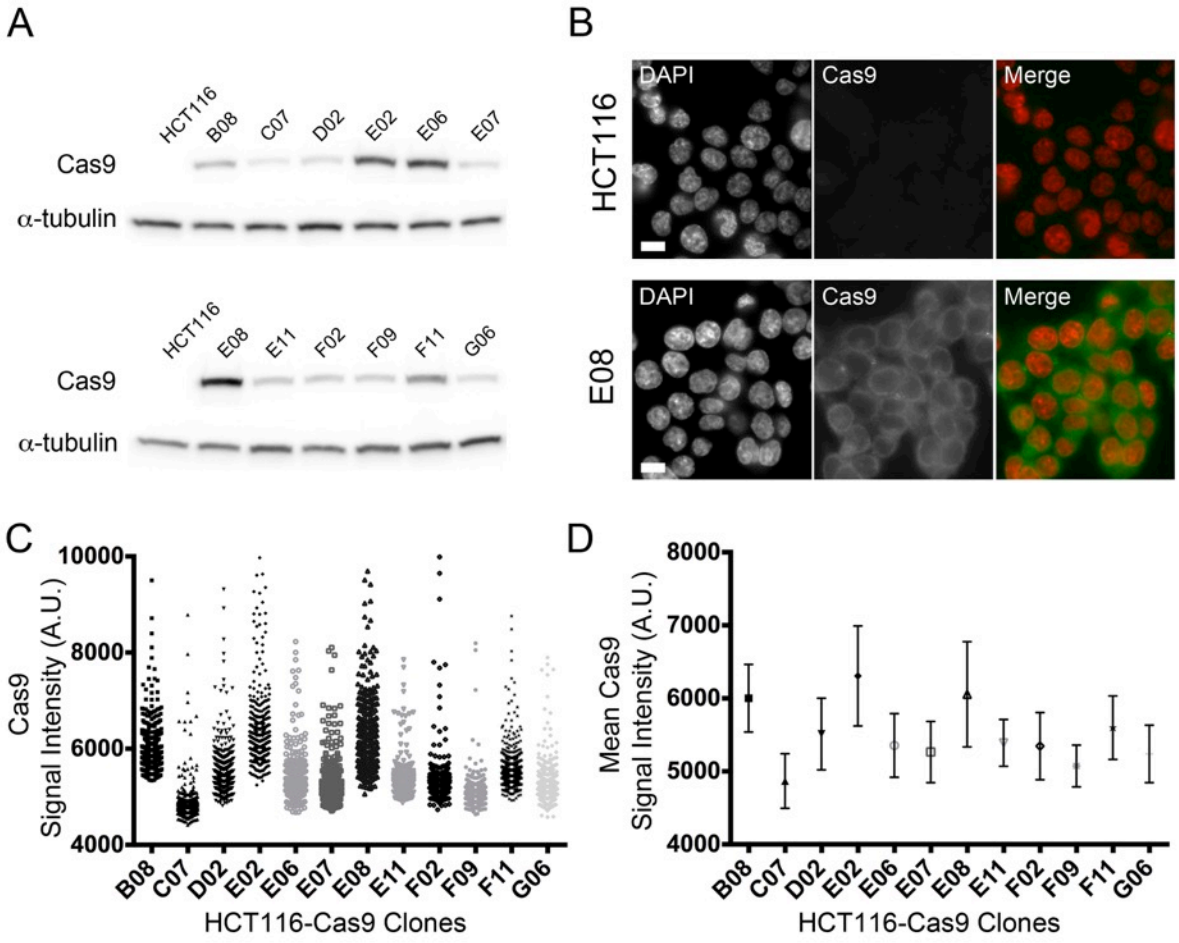

Figure 4.2: Heterogeneous Cas9 Expression levels in HCT116-Cas9 Clones
(**A**) Immunoblots depicting Cas9 expression levels in HCT116-Cas9 clones. α-tubulin serves as a loading control. (**B**) Representative indirect immunofluorescent images (40×) presenting Cas9 expression in HCT116 and clone E08. Nuclei are counterstained with DAPI. DAPI and Cas9 are pseudo-colored red and green, respectively, within the Merge. Scale bar represents 10 μm. (**C)** Scatter plots depicting mean Cas9 signal intensity on a cell-by-cell basis within HCT116-Cas9 clones. (**D)** Graph presenting the mean Cas9 signal intensity (± Standard Deviation, ± SD) on a population basis within HCT116-Cas9 clones.

4.3.3 A Subset of HCT116-Cas9 Clones Display Differences in Gross Morphology

Changes in gross cellular morphology have been shown to be a broad indicator of aberrant cellular processes[224]. Accordingly, to ensure the clones are as representative of parental HCT116 cells as possible, we sought to employ bright field microscopy to compare gross cellular morphologies between HCT116-Cas9 clones and parental cells (Figures 4.3-4.6). Surprisingly, clones D02, E06, E07, and E11 displayed unusual morphologies that were inconsistent with the parental control. Based upon visual classification, two distinct and unusual morphologies occurred. First, clones D02 (Figure 4.3) and E11 (Figure 4.5) adopted a fibroblast-like morphology that included branched and elongated cell-bodies. Second, clones E06 (Figure 4.4) and E07 (Figure 4.4) grew in unusually condensed colonies and appeared smaller in cell size when compared to the parental cell line. HCT116-Cas9 clones exhibiting abnormal gross morphologies (D02, E06, E07, E11) were excluded from subsequent characterization. Accordingly, HCT116-Cas9 clone E02 and E08, which displayed high Cas9 expression and similar cellular morphology when compared to the parental cell line, were employed for subsequent characterization.

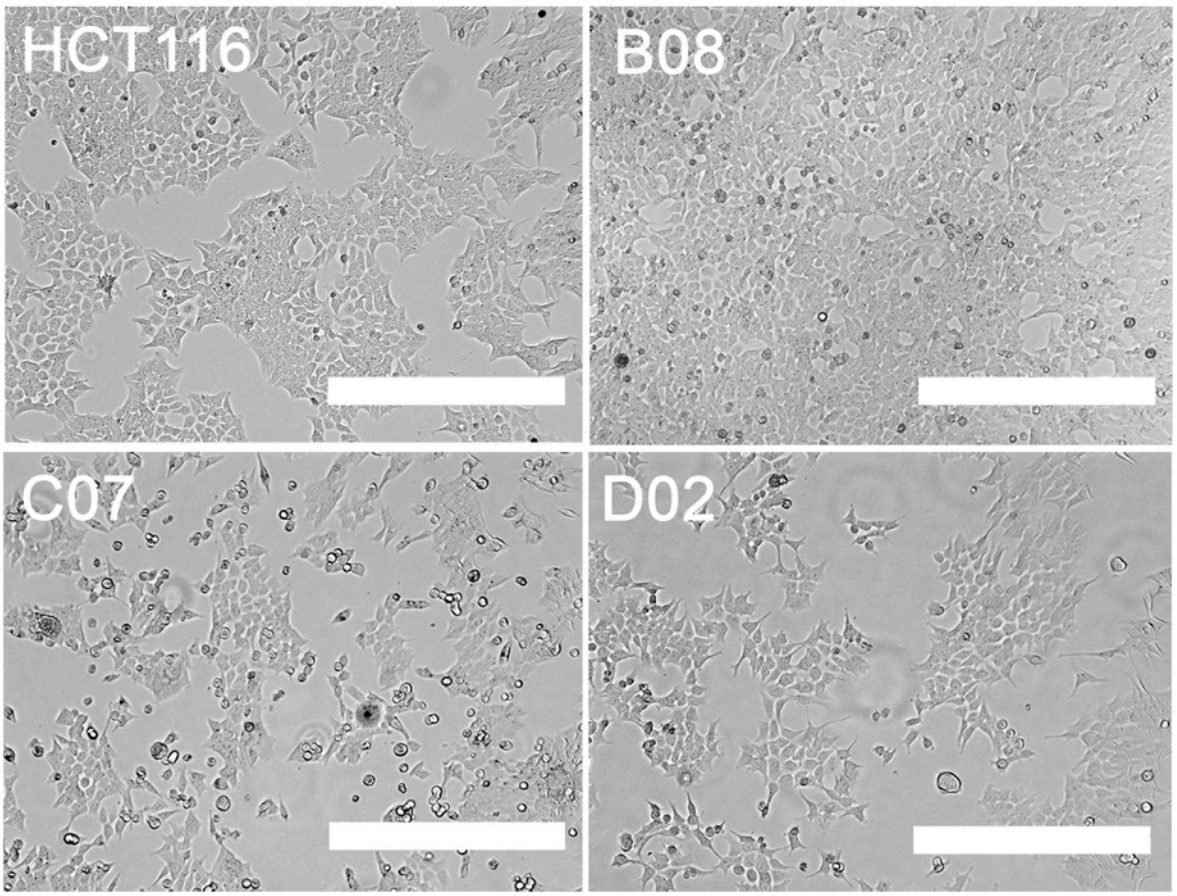

Figure 4.3: Gross Morphologies of B08, C07, and D02 Compared to HCT116
Representative low-resolution (4×) bright field micrographs presenting gross cellular morphology. Clones B08 and C07 show similar morphology as HCT116. Clone D02 shows abnormal fibroblast-like morphology. Scale bar represents 200 μm.

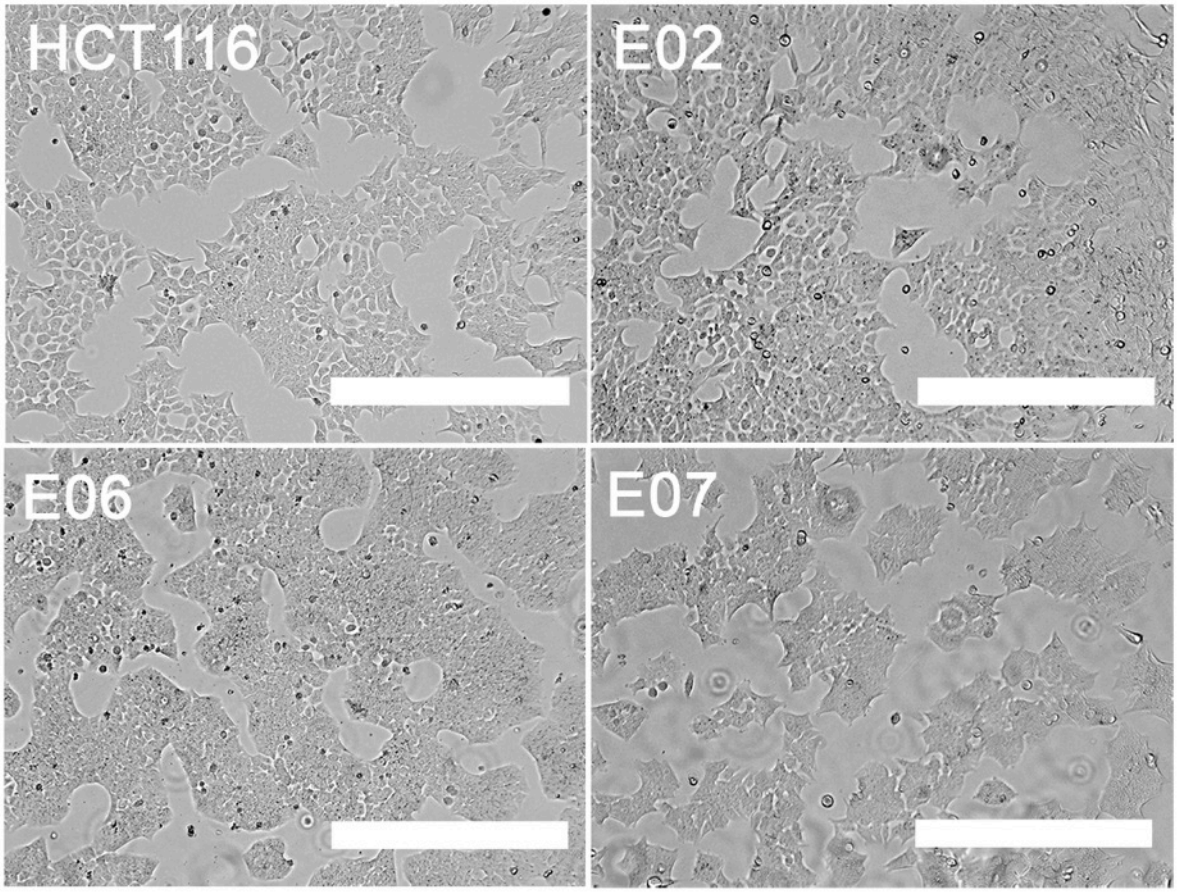

Figure 4.4: Gross Morphologies of E02, E06, and E07 Compared to HCT116
Representative low-resolution (4×) bright field micrographs presenting gross cellular morphology. Clone E02 shows similar morphology as HCT116. Clone E06 and E07 show abnormally small and tightly compacted colonies. Scale bar represents 200 μm.

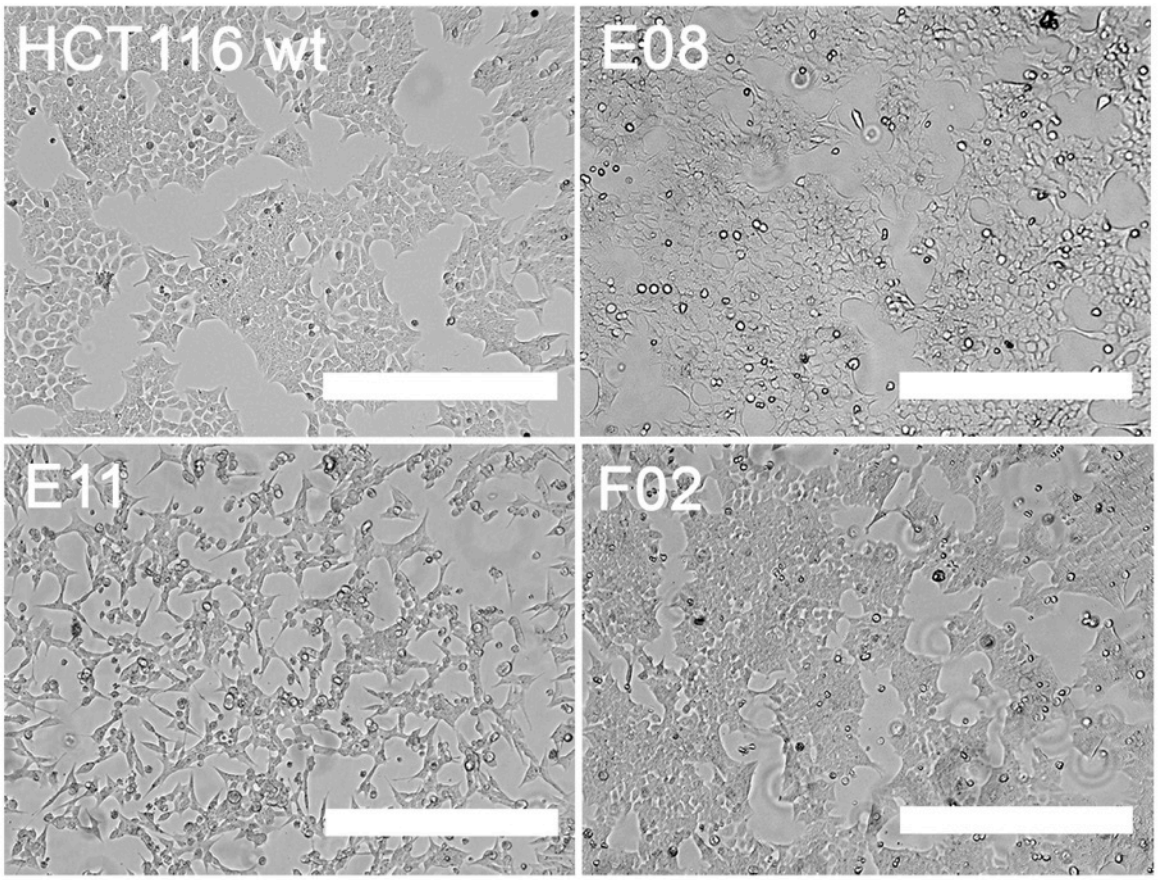

Figure 4.5: Gross Morphologies of E08, E11, and F02 Compared to HCT116
Representative low-resolution (4×) bright field micrographs presenting gross cellular morphology. Clones E08 and F02 shows similar morphology as HCT116. Clone E11 shows abnormal fibroblast-like morphology. Scale bar represents 200 μm.

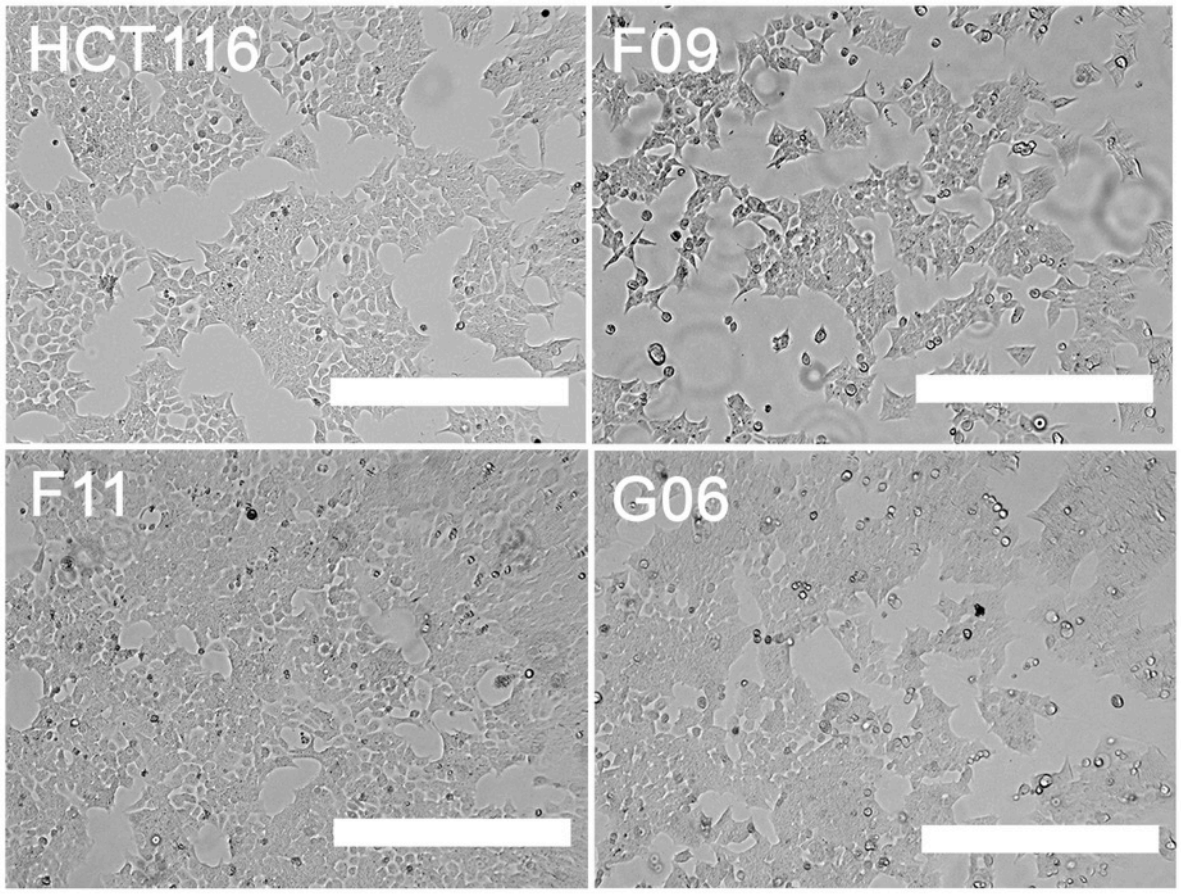

Figure 4.6: Gross Morphologies of F09, F11, and G06 Compared to HCT116
Representative low-resolution (4×) bright field micrographs presenting gross cellular morphology. Clones F09, F11, and G06 show similar morphology as HCT116. Scale bar represents 200 μm.

4.3.4 The HCT116-Cas9 E08 Clone and Controls have Similar Growth Kinetics

Real time cellular analysis was performed and the endogenous growth kinetics of E02 and E08 was compared with the parental control. Real time cellular analysis measures cell index (electrical impedance) as a metric for cell numbers to identify changes in proliferation rates and viability, the greater the number of cells making contact with the plate, the greater the cell index. Individual growth curves were generated for HCT116, E02 and E08 (Figure 4.7A) from which proliferation rates (doubling times) were determined from the linear portion of the exponential growth phase (Figure 4.7B, Table 4.S4). Mean doubling times were identified as 15.14 h, 15.90 h, and 39.06 h for HCT116, E08, and E02, respectively. Student's *t*-tests revealed a statistically significant 2.58-fold increase in doubling time within the E02 clone compared to parental controls. Notably, doubling times between E08 clones and parental controls were virtually indistinguishable and not statistically significant. (Table 4.S4). In summary, E08 possessed similar endogenous growth kinetics as HCT116 and was selected for cytogenetic characterization. The E02 cells were purposefully excluded from further analysis as real time cellular analysis revealed doubling times that were highly dissimilar from parental controls.

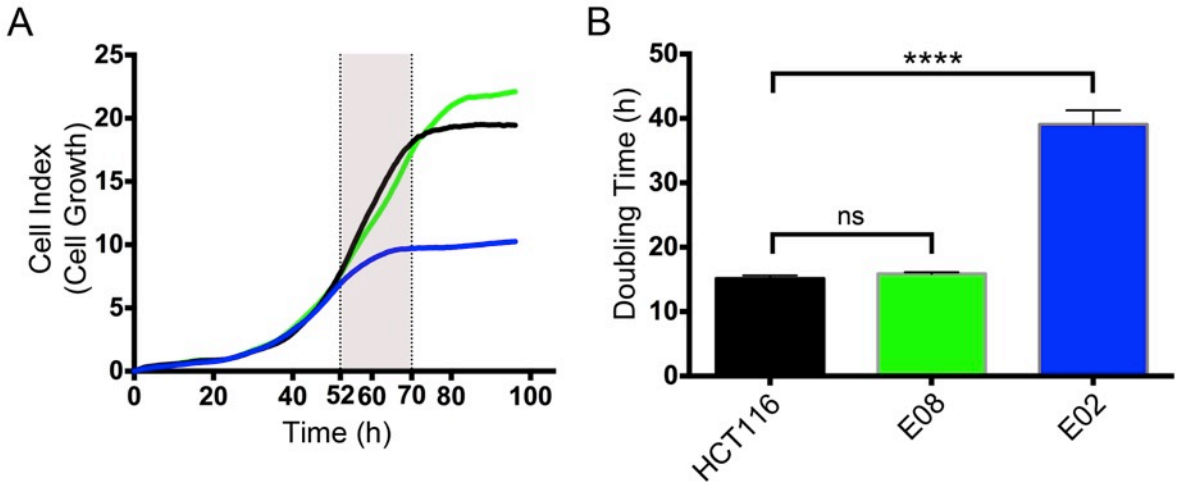

Figure 4.7: Real Time Cellular Growth Analysis of HCT116, E02, and E08
(**A**) Real-time growth curves of HCT116 (black line), E02 (blue line), and E08 (green line). The mean of a minimum of three technical replicates are presented. Growth curves show initial cell attachment (0h to 40h) and linear portion of exponential growth phase (~52 h to ~70 h, region highlighted in grey). (**B**) Graphs presenting the mean doubling time (± SD) within HCT116, E02, and E08. Student t-tests were employed to compare mean doubling times of E08 and E02 with controls (ns, not significant; ****, *p*-value < 0.0001).

4.3.5 The HCT116-Cas9 E08 Clone and Controls have Similar Karyotypes

We next wished to evaluate gross chromosomal translocations within HCT116 and E08 cells. Accordingly, spectral karyotyping was performed on 51 parental HCT116 and 52 E08 mitotic spreads. The modal karyotype identified in both HCT116 (Figure 4.8) and E08 (Figure 4.9) was 45, X,-Y, der(10) dup(10)(q24;q26), t(10;16)(q24;q24), der(16) t(8;16)(q13;p13), der(18) t(17;18)(q21;p11) and was observed at a frequency of 43/51 (84%) and 41/52 (79%), respectively. These results show that the E08 clone retains the modal parental karyotype and do not exhibit relevant changes in gross chromosomal rearrangements.

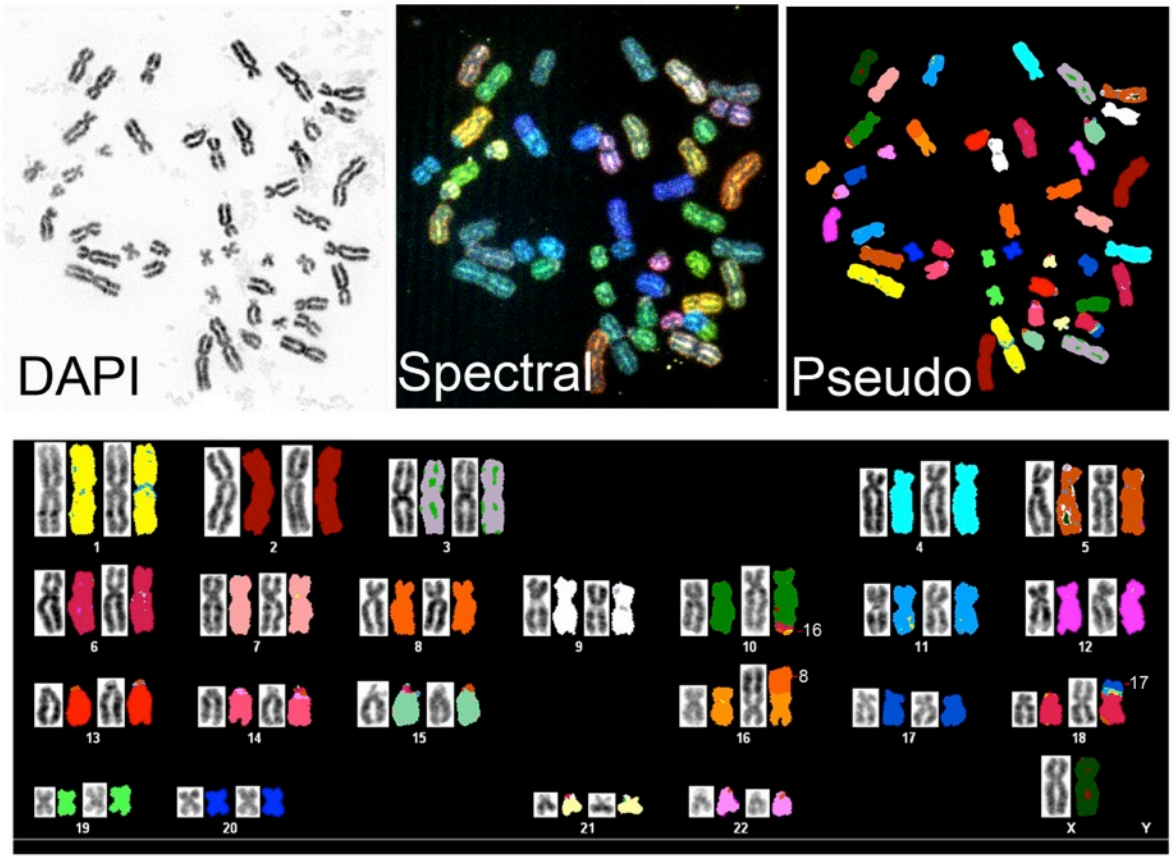

Figure 4.8: Spectral Karyotype of HCT116
(Top Left) Inverted-DAPI image of a mitotic chromosome spread. **(Top Middle)** Spectral color image. **(Top Right)** Pseudo color image based on spectral colors. **(Bottom)** Karyotyping corresponding to the mitotic chromosome spread shown. Note Y-deletion, t(10;16), t(8;16), and t(17;18), which corresponds to the modal karyotype (45).

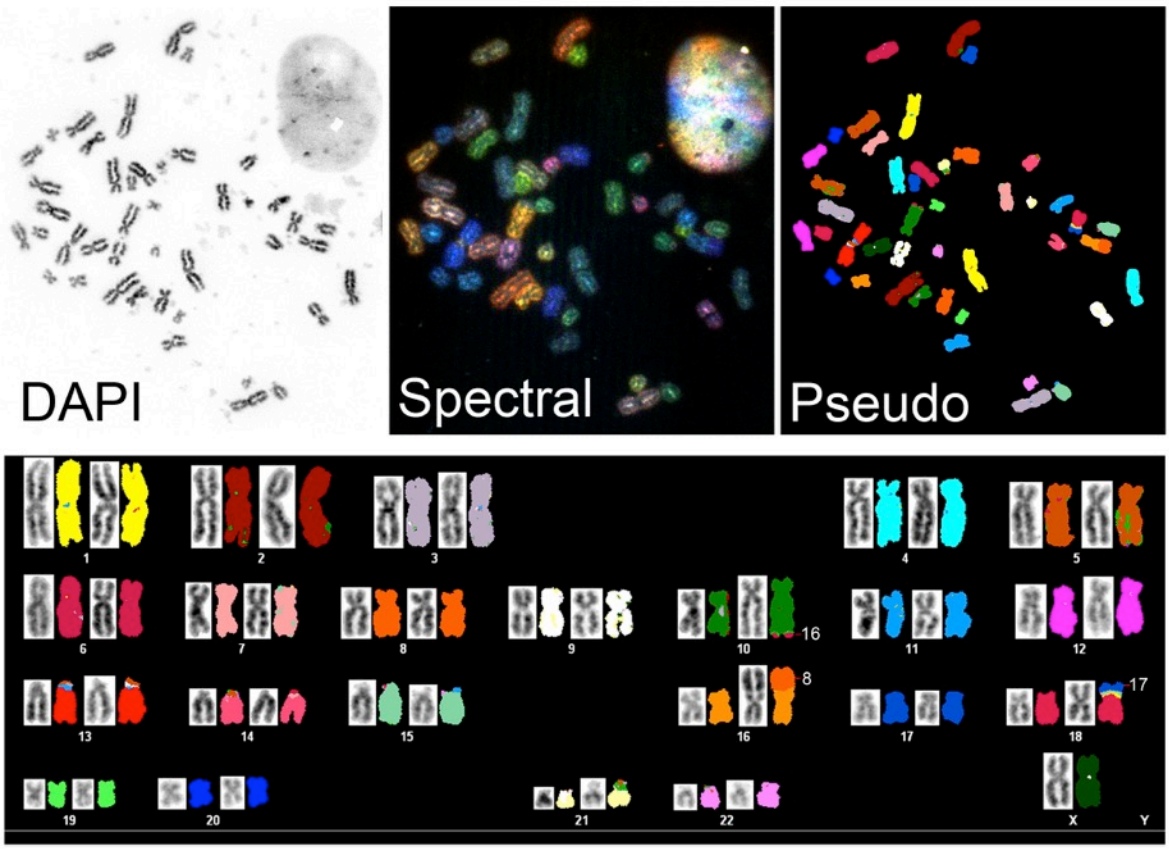

Figure 4.9: Spectral Karyotype of E08
(Top Left) Inverted-DAPI image of a mitotic chromosome spread. **(Top Middle)** Spectral color image. **(Top Right)** Pseudo color image based on spectral colors. **(Bottom)** Karyotyping corresponding to the mitotic chromosome spread shown. Note Y-deletion, t(10;16), t(8;16), and t(17;18), which corresponds to the modal parental karyotype (45).

4.3.6 CRISPR-Mediated targeting of *RNF20* and *PPIB* in HCT116-Cas9 E08 cells

As part of an initial proof-of-concept study, we employed E08 cells in a CRISPR-Cas9 editing experiment to produce both *RNF20*- and *PPIB*-deletions. *RNF20*-targeting was specifically selected because it is a putative chromosome stability gene, a current research focus, and previous efforts to generate *RNF20*-deficient cells have been unsuccessful. *PPIB*-targeting was specifically selected as it is a positive control for gene deletion identified by the manufacturer, and previous groups have demonstrated the ability to efficiently produce *PPIB*-deficient human cells[225]. *PPIB* is a non-essential peptidyl-prolyl isomerase located within the endoplasmic reticulum[226].

Briefly, using online-based CRISPR-Cas9 sgRNA design tools (http://crispr.mit.edu)[227], two sgRNA molecules, targeting exons 2 and 3 within *RNF20* were designed with the criteria of low self-complementation and low probability of off-target effects. All sgRNA and tracrRNA molecules were chemically synthesized by Dharmacon (Table 4.S5 lists all sgRNA sequences). sgRNAs were independently co-transfected with tracrRNA in E08 cells. Following transfection, targeted cells were cultured for 4 days under normal growth conditions, detached by trypsinization, transferred and grown on coverslips for 24 h, fixed, and immunofluorescently labeled with either RNF20 or PPIB antibodies (RNF20, ab32629; PPIB, ab16045). Indirect immunofluorescent imaging revealed a mixed population of both *RNF20*-proficient and *RNF20*-deficient cells that were visually apparent based on signal intensity (Figure 4.10A and 4.10C). A signal intensity of 3,860 arbitrary unites (A.U.), representing the intensity threshold separating *RNF20*-proficient (>3,860) and *RNF20*-deficient (<3,860) cells was manually identified. *RNF20*-proficient and *RNF20*-deficient cells were classified according to signal intensity and CRISPR-Cas9 editing efficiency was calculated. Semi-quantitative analysis revealed editing (*RNF20*-

deletion) efficiencies of 35 out of 294 (~11.9%, exon 2, Figure 4.10B) and 59 out of 335 (~17.6%, exon 3, Figure 4.10D) cells analyzed.

Indirect immunofluorescent imaging identified *PPIB*-proficient and *PPIB*-deficient cells that were visually apparent based on signal intensity (Figure 4.10E). An intensity threshold of 2,000 A.U., representing *PPIB*-proficient (>2,000) and *PPIB*-deficient (<2,000) cells was identified. Semi-quantitative analysis revealed editing (*PPIB*-deletion) efficiencies of 993 out of 1139 (87%) cells analyzed (Figure 4.10F). Based on high *PPIB* editing efficiencies, we sought to isolate *PPIB*-deficient cells for clonal expansion. Single cell dilutions were employed and candidate *PPIB*-deficient cells were expanded and screened by immunofluorescence imaging. Following clonal expansion and indirect immunofluorescent screening, 18 of the 25 (72%) clonal populations were identified as *PPIB*-deficient. 8 of the 18 *PPIB*-deficient clones were randomly chosen for expansion and cryogenic preservation. These initial proof-of-concept experiments demonstrate the ability to produce CRISPR-Cas9-mediated gene deletions and derive clonal cell lines from E08 cells.

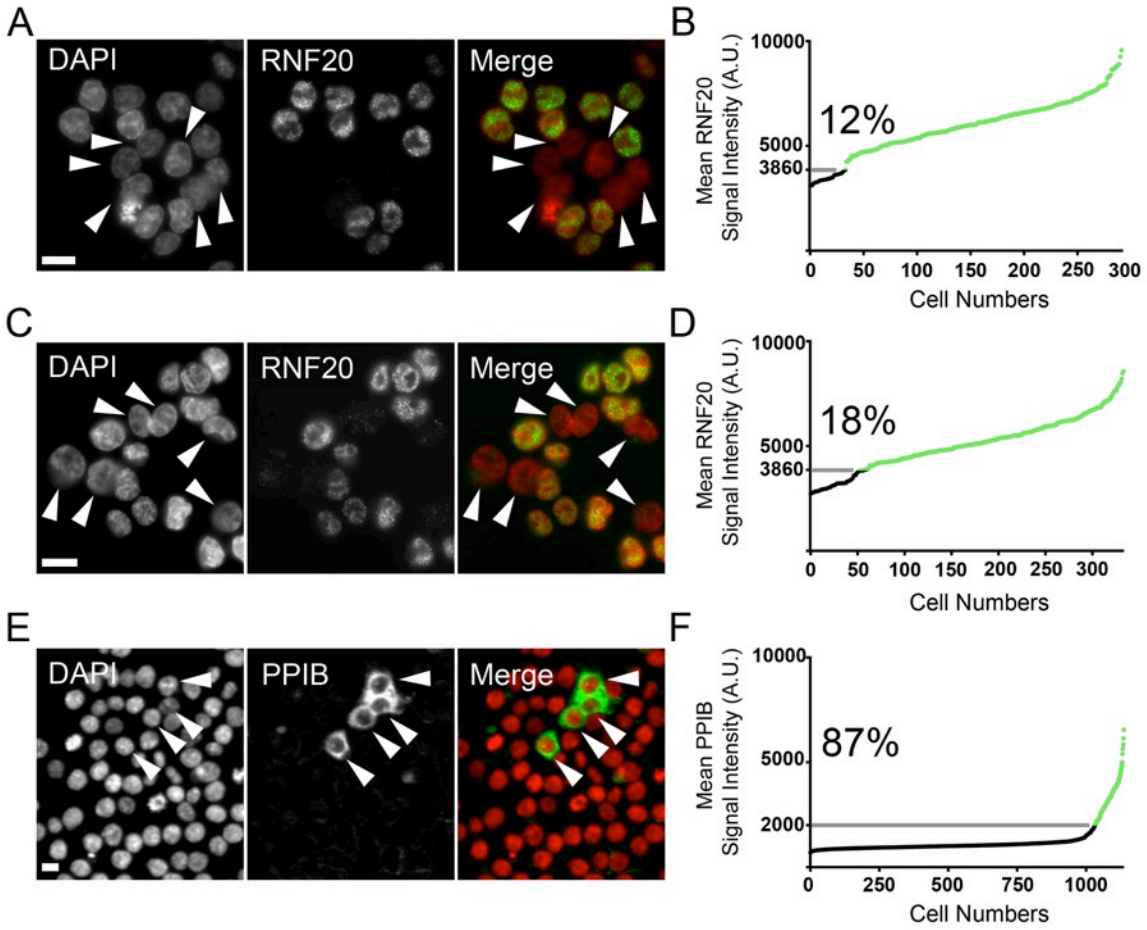

Figure 4.10: CRISPR-Mediated Deletions in E08 Cells

(**A**) Representative images (63×) depicting *RNF20* exon 2 targeted E08 cells. DAPI and RNF20 are pseudo-colored red and green, respectively. Arrowheads point to *RNF20*-deficient cells. (**B**) Scatter plot depicting RNF20 signal intensities of exon 2 targeted individual cells arranged from smallest to greatest signal intensities. Grey bar shows the intensity threshold separating *RNF20*-proficient (green dots) and *RNF20*-deficient (black dots) cells. The percentage of *RNF20*-deficient cells is indicated. (**C**) *RNF20* exon 3 targeted E08 cells. (**D**) Scatter plot showing the RNF20 signal intensities of exon 3 targeted individual cells. (**E**) *PPIB* targeted E08 cells. Arrowheads point to *PPIB*-proficient cells. (**F**) Scatter plot showing the PPIB signal intensities of individual cells. Grey bar shows the intensity threshold separating *PPIB*-proficient (green dots) and *PPIB*-deficient (black dots) cells. The percentage of *PPIB*-deficient cells is indicated. All scale bars represents 10 μm.

4.4 Discussion

In this study, we generate and characterize 12 Cas9-expressing HCT116 clones and ultimately identify E08 as a 'CRISPR-Cas9-ready' cell line capable of high efficiency editing. In a proof-of-concept study, E08 cells were transfected with independent sgRNA strands targeting *RNF20* and *PPIB* to produce *RNF20*-deficient and *PPIB*-deficient cells. Eight clonal *PPIB*-deficient cell lines were identified, expanded, and cryogenically preserved. Accordingly, we have generated and characterized a novel HCT116-Cas9 E08 cell line that exhibits high Cas9 expression, karyotypic stability, high similarity to HCT116 parental cells, and can be efficiently employed in CRISPR-Cas9 genome editing experiments.

During the generation of the Cas9 expressing cells, two distinct and unusual morphologies were observed. There are many possible explanations. First, there is the possibility that a small sub-population of HCT116 cells that display atypical gross morphologies inherently exist within the HCT116 population yet are not visually evident. Accordingly, these cells may represent normal HCT116 cells and not clones containing aberrant morphologies associated with Cas9 integration or overexpression. Second, because lentiviral transduction mandates random transgene integration, there remains the possibility of insertional mutagenesis within a gene important for maintaining normal morphology[228]. Third, although only speculative, there remains the possibility that Cas9 overexpression may cause spurious genome editing in the absence of sgRNA or tracrRNA, and aberrant off-target editing within genes important for maintaining normal morphology are being aberrantly edited. Although an interesting observation, the mechanism(s) associated with these unusual morphologies are beyond the scope of this study but are the subjects for future studies that will identify the Cas9 integration.

There are many possible explanations regarding the differences in editing efficiencies observed when targeting *RNF20* and *PPIB* in HCT116-Cas9 E08 cells. These observations are consistent with observations from others who have reported dramatic variability in editing efficiency based on sgRNA sequence[229]. Although the exact reasons for differences in sgRNA editing efficiencies are beyond the scope of this study, at least 2 possibilities exist. First, biophysical properties of the sgRNA, including overall secondary structure, structural stability, and nucleotide accessibility to target substrates, have all been shown to impact CRISPR-Cas9 editing efficiency[219]. Accordingly, low self-complementation, high-structural stability and nucleotide accessibility of the 3' end of the sgRNA sequence have all been associated with efficient sgRNA molecules[229]. Second, there may be inherent biological differences associated with loss of *RNF20*, which has been shown to play multiple roles in cellular homeostasis, versus a loss of *PPIB*, which has previously been shown to be dispensable[225]. Nevertheless, the exact mechanism(s) accounting for dramatic differences in editing efficiency between *RNF20* and *PPIB* is unknown and may warrant further investigation.

The ability to employ CRISPR-Cas9 genome editing technologies to HCT116-Cas9 E08 cells has several potential applications in the study of cancer genomics[230]. To date, a multitude of cancer-associated genomic alterations have been identified by large-scale cancer genome sequencing projects[231]. Although these projects are highly valuable in identifying genomic alterations, they lack the ability to characterize their functional implications and do not discern between passenger or driver mutations. In order to evaluate their functional significance, traditional RNA-interference (RNAi) and cDNA overexpression approaches have been employed to assess the biological impact gene-depletion/-overexpression has on phenotypes associated with oncogenesis[216,232]. Although still a valuable tool in cancer biology, RNAi is limited by

transient gene silencing and/or relatively low periods of protein depletion. Comparatively, CRISPR-Cas9 offers complete and long-term protein loss, two characteristics that may be more biologically relevant to certain cancer contexts. Although HCT116 was initially limited by low transfection efficiency, the stable integration of Cas9 in combination with small particle transfection appears to overcome these limitations. Coupling the ability to easily produce permanent genomic alterations with the karyotype stability of HCT116-Cas9 E08 cells will enable several studies aimed at validating candidate human chromosome stability genes. It can be envisioned that such studies would employ CRISPR-Cas9 editing to inactivate candidate chromosome stability genes and evaluate changes in chromosome number or structure, two hallmarks of the CIN phenotype[12,38,233].

In conclusion, we show that HCT116-Cas9 E08 cells retain the highly desirable characteristics of parental HCT116 cells. Of particular interest, we show HCT116-Cas9 E08 cells retain the modal parental karyotype and can be successfully employed with the CRISPR-Cas9 genome editing system to produce *RNF20*- and *PPIB*-deletions. Thus our data show, we have generated a novel reagent that can be routinely employed in CRISPR-Cas9 genome editing experiments. In addition, cell lines generated from this approach will serve as highly valuable models to understand the specific genomic alterations that underlie certain human diseases. Indeed, information gathered from these studies may provide the necessary biological understanding to produce the next generation of therapeutic.

This page was intentionally left blank.

4.5 Supporting Information

4.5.1 Supporting Tables

Table 4.S1: Analysis of Variance of Mean Cas9 Signal Intensity Between HCT116-Cas9 Clones

Group[A]	SS[B]	df[C]	MS[D]	F-Ratio[E]	*p*-value	Reject H_0[F]
BC	9.8×10^8	11	8.9×10^7	399.8	<0.0001	Yes
WC	1.3×10^9	5973	2.2×10^5			

[A]Defines whether or not the analysis is between clonal populations (BC) or within a clonal population (WC).
[B]SS, sum of squares.
[C]df, degrees of freedom.
[D]MS, mean square.
[E]F-ratio is calculated by MS_{BC}/MS_{WC}.
[F]The null hypothesis (H_0) is rejected if the *p*-value is < 0.05.

Table 4.S2: Tukey Multi-Comparison Tests of Mean Cas9 Signal Intensity Between HCT116-Cas9 Clones

	Statistical Significance (*p*-value)										
	B08	C07	D02	E02	E06	E07	E08	E11	F02	F09	F11	G06
B08		****	****	****	****	****	ns	****	****	****	****	****
C07			****	****	****	****	****	****	****	****	****	****
D02				****	****	****	****	**	****	****	ns	****
E02					****	****	****	****	****	****	****	****
E06						ns	****	ns	ns	****	****	**
E07							****	**	ns	****	****	ns
E08								****	****	****	****	****
E11									ns	****	****	****
F02										****	****	*
F09											****	****
F11												****
G06												

Degrees of Statistical Significance: ns, not significant; *, *p*-value < 0.05; **, *p*-value < 0.01; ****, *p*-value < 0.0001.

Table 4.S3: Summary Statistics of Mean Cas9 Expression in HCT116-Cas9 Clones

HCT116-Cas9 Clone[A]	Mean[B] ± Standard Deviation	n[C]
B08	6002 ± 463	498
C07	4869 ± 374	498
D02	5513 ± 491	491
E02	6307 ± 685*	491
E06	5355 ± 436	512
E07	5266 ± 419	494
E08	6055 ± 721*	495
E11	5390 ± 320	511
F02	5346 ± 460	498
F09	5075 ± 286	502
F11	5598 ± 435	499
G06	5239 ± 394	496

[A]HCT116-Cas9 clone identifier
[B]Mean Cas9 signal intensity, * indicates high Cas9 expressing clones identified by immunoblotting and indirect immunofluorescence analyses.
[C]Sample size, total number of cells measured.

Table 4.S4: Student's *t*-tests Comparing Doubling Times of HCT116, E08, and E02

Cell Line	n[A]	Mean[B] ± Standard Deviation	*p*-value[C]	Fold Change
wt +	3	15.14 ± 0.28		
E08	4	15.90 ± 0.21	ns	n/a
wt +	3	15.14 ± 0.28		
E02	3	39.06 ± 1.26	<0.0001	2.58

[A]Number of real time cellular analysis wells evaluated
[B]Mean doubling time was calculated using regions of exponential growth (52:09:32 to 70:09:38) with the formula: Doubling Time = [duration × log(2)] ÷ [log(Final Cell Index) - log(Initial Cell Index)].
[C]Based on Student's *t*-tests
Not applicable (n/a)
Not statistically significant (ns)

Table 4.S5: List of CRISPR-Cas9 guide strands employed

Gene Targeted	Exon Targeted	sgRNA Sequence (5' to 3')
RNF20	Exon 2	GTGGAAACAATTAAGCTAGG
RNF20	Exon 3	TATTGATTGTCAACCGATAC
PPIB	Exon 1	GGAAGTACAACGCAAGCCTC

Chapter 5

RNF20 AND *PARP1* ARE SYNTHETIC LETHAL INTERACTORS IN HUMAN CELLS

5.1 Abstract

The putative tumor suppressor gene *RNF20* encodes an essential histone H2B mono-ubiquitin ligase and has been found altered/mutated in numerous cancer types. Several studies suggest that RNF20, and by extension mono-ubiquitinated histone H2B, play important roles in the DNA homologous recombination repair response within human cells. Indeed, hypomorphic RNF20 expression and/or function have been shown to underlie several phenotypes consistent with aberrant DNA repair and genome instability, making aberrant RNF20 biology a potential driver in tumor initiation and evolution. As a result, identifying a precision medicine approach to selectively kill cancer cells harboring *RNF20*-defects could have broad clinical relevance in multiple tumor types. Many groups have demonstrated that certain cancer cells bearing defects within the homologous recombination repair pathway can be selectively killed through PARP1 inhibition. Based on this evidence, we specifically evaluated if two PARP1 inhibitors, Olaparib or BMN673, could be repurpose to selectively kill RNF20-depleted cells. Using RNA-interference to model hypomorphic RNF20 expression and/or function, we show that *PARP1*-silencing and inhibition induces preferential killing within *RNF20*-silenced cells. To characterize the underlying mechanism of cell death, we employ semi-quantitative indirect immunofluorescent imaging and show significant increases in markers of DNA damage and apoptosis. Ultimately, we show that *RNF20* and *PARP1* are synthetic lethal interactors in human cells and identify PARP1 as a candidate drug target in an *RNF20*-deficient cancer context.

5.2 Introduction

Many chemotherapies employed to fight solid tumors like colorectal cancer, are non-specific, target replicating cells, and are frequently associated with off-target effects. Consequently, there is a growing need for novel strategies to better restrict the therapeutic effect to cancer cells. It is becoming increasingly evident that certain cancer cells bearing specific defects in the HRR response can be selectively killed by a SL approach[234]. Synthetic lethality occurs when a rare combination of two or more specific mutations within a given cell leads to cell death, whereas a mutation in only one of these genes does not[235]. This rare genetic interaction can be extrapolated to a cancer context where a cancer-associated mutation can be selectively targeted by inhibiting a pair-wise SL interactor, which will ultimately result in cancer cell death. Most importantly, non-cancerous cells, which do not contain the necessary SL sensitizing mutation, remain viable[159,160,236]. Accordingly, identifying and characterizing rare human SL interactions in model cell lines is an essential preliminary step before these precision based approaches can be further studied in a preclinical setting[235].

To date, the best-characterized example of synthetic lethality is the selective killing of *BRCA1/2*-deficient cancer cells through PARP1 inhibition[179,180,237,238]. Both BRCA1 and BRCA2 play important roles in the HRR response[239]. It is generally accepted that PARP1 inhibition produces an increase in DNA damage that cannot be faithfully repaired through HRR in *BRCA1/2*-deficient cancer cells. Catastrophic DNA damage is restricted to *BRCA1/2*-deficient cells and ultimately underlies apoptosis and cell death[180]. Since this initial discovery, a myriad of PARP1 inhibitors have been developed and tested as single or combinatorial agents for their *in vitro* and *in vivo* ability to selectively kill a variety of HRR-deficient cells[240-242].

RNF20 is a putative tumor suppressor gene that plays a peripheral role in the HRR response and is altered in numerous cancers including colon, breast, lung and prostate[76,210,243]. Accordingly, identifying a novel therapeutic strategy to selectively kill cancer cells harboring *RNF20*-defects could have broad clinical relevance. *RNF20* encodes an E3 ubiquitin ligase that functions to monoubiquitinate histone H2B on lysine residue 120 (H2Bub1)[76,244]. It is generally accepted that H2Bub1 functions in HRR by remodeling local chromatin at DNA lesions to provide enhanced accessibility for HRR factors and allow for efficient repiar[106]. As expected, *RNF20*-silenced cells display several phenotypes consistent with a HRR-defect including reduced survival following radiation, delayed recruitment of key HRR components, and a direct reduction in HRR frequency[106,107]. Based on the above evidence, we hypothesized that *RNF20* and *PARP1* are human SL interactors and that RNF20-depleted cells could be selectively killed by *PARP1*-silencing or PARP1-inhibition.

In this study, we expand the potential utility of PARP1 inhibitors by identifying and validating a novel human SL interaction between *RNF20* and *PARP1* in two human cell lines. We employ RNA-interference to model human cancer cells exhibiting hypomorphic RNF20 expression and/or function in combination with two distinct PARP1 inhibitors, Olaparib and BMN673. We show that *RNF20*-silenced cells are selectively killed relative to controls, and identify increases in DNA DSBs and apoptosis as underlying mechanisms accounting for cell death. Collectively, we identify Olaparib and BMN673 as lead compounds for further pre-clinical studies designed to selectively kill cancer cells bearing hypomorphic RNF20 expression and/or function.

5.3 Results

5.3.1 *PARP1*-Silencing Induces a Significant Reduction in siRNF20 Cell Numbers

In order to evaluate *RNF20* and *PARP1* as human SL interactors, we first wished to determine whether the simultaneous (dual) silencing of *RNF20* and *PARP1* resulted in fewer cell numbers than silencing either gene simultaneously with *GAPDH* (control). To identify the most efficient silencing duplexes, we first examined four individual siRNAs for *RNF20* and *PARP1* within HCT116 cells. Using standard siRNA approaches and immunoblot detection, siRNF20-3 and siPARP1-1 were identified as the most efficient silencing duplexes and were thus employed throughout the remainder of the study (Figure 5.1A and 5.1B).

Next, dual silencing (siRNF20 + siPARP1) experiments were performed within HCT116 cells. As predicted, dual silencing of *RNF20* and *PARP1* resulted in a reproducible and statistically significant reduction in cell numbers relative to controls (siGAPDH + siRNF20 or siGAPDH + siPARP1) (Figure 5.1C, Table 5.S1). Moreover, siRNF20 + siPARP1 dual silencing resulted in a greater reduction in cell numbers than what was predicted by a multiplicative model (see materials and methods) and establishes a putative SL interaction (Figure 5.1D, Table 5.S2).

To confirm the above results were not restricted to HCT116, analogous experiments were performed in hTERT cells with very similar findings (Figure 5.S1, Table 5.S3 and 5.S4). Taken together, these data suggest *RNF20* and *PARP1* are SL interactors in two distinct human cell lines (HCT116, transformed human colon epithelium and hTERT, immortalized human fibroblasts).

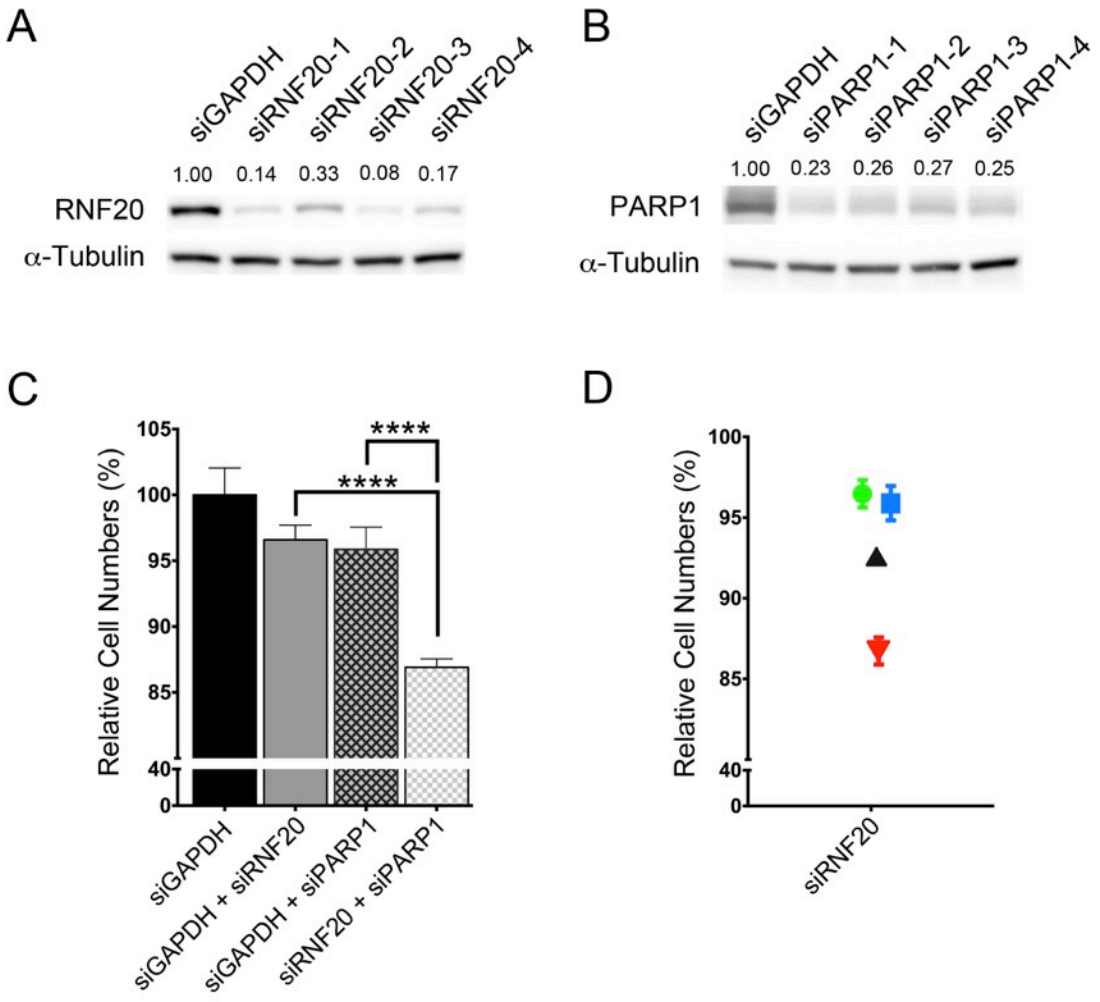

Figure 5.1: *PARP1*-Silencing Induces a Significant Reduction in siRNF20 HCT116 Cells
(**A**) Immunoblots depicting diminished RNF20 levels following silencing in HCT116 cells. Semi-quantitative analyses were performed and the relative abundance of RNF20 is presented. (**B**) Immunoblots depicting the relative abundance of PARP1 following silencing in HCT116 cells. (**C**) Bar graph depicting the mean relative number of cells remaining (± Standard Deviation [SD]) following silencing (****; *p*-value < 0.0001). (**D**) Graph depicting the SL interaction observed following dual silencing of *RNF20* and *PARP1* in HCT116 cells. Presented are the mean normalized percentages (± SD) for the controls siRNF20 + siGAPDH (green circle) or siPARP1 + siGAPDH (blue square), and the value predicted (black triangle) for siRNF20 + siPARP1 as calculated by a multiplicative model. The red triangle identifies the actual observed value for siRNF20 + siPARP1 and is lower than predicted indicating a putative SL phenotype.

5.3.2 PARP1 Inhibition Induces a Statistical Decrease in siRNF20 Cell Numbers

We next sought to employ PARP1 inhibitors to phenocopy RNAi results detailed above. However, because our approach mandates PARP1 inhibition during periods of maximum RNF20-depletion, we first characterized the temporal kinetics associated with *RNF20*-silencing (Figure 5.2A). Partial RNF20-depletion was observed 24 h post-transfection, followed by maximal depletion between the 48 h to 96 h time points, and a return to approximately base-line levels 144 h (6-days) post-transfection. Based on these results, a 72 h window (48 h to 120 h post-transfection) was identified as the optimal window in which PARP1 inhibition would likely be most effective.

We next evaluated whether siRNF20 cells would exhibit increased sensitivity to PARP1 inhibitors compared to siGAPDH controls. Standard dose response curves were generated and the SF_{50} (surviving fraction; drug concentration at which 50% of the cells remained) was determined for both Olaparib (siGAPDH = 6.84 μM; siRNF20 = 4.0 μM) and BMN673 (siGAPDH = 71.9 nM; siRNF20 = 25.8 nM) within HCT116 cells. Overall BMN673 treatments elicited a greater reduction in cell numbers compared to Olaparib. When compared to siGAPDH controls, siRNF20 cells exhibited a 1.7- and 2.8-fold increased sensitivity to Olaparib or BMN673, respectively. Drug concentrations that produced the greatest reduction in siRNF20 cells and not siGAPDH cells were identified as 800 nM Olaparib and 6.4 nM BMN673. These working concentrations were employed throughout the remainder of our study. As predicted, Olaparib and BMN673 treatment resulted in a statistically significant decrease in siRNF20 cell numbers compared to controls. (Olaparib, p-value < 0.05, Figure 5.2B Table 5.S5) (BMN673, p-value < 0.0001, Figure 5.2C, Table 5.S6). To confirm these results were not restricted to

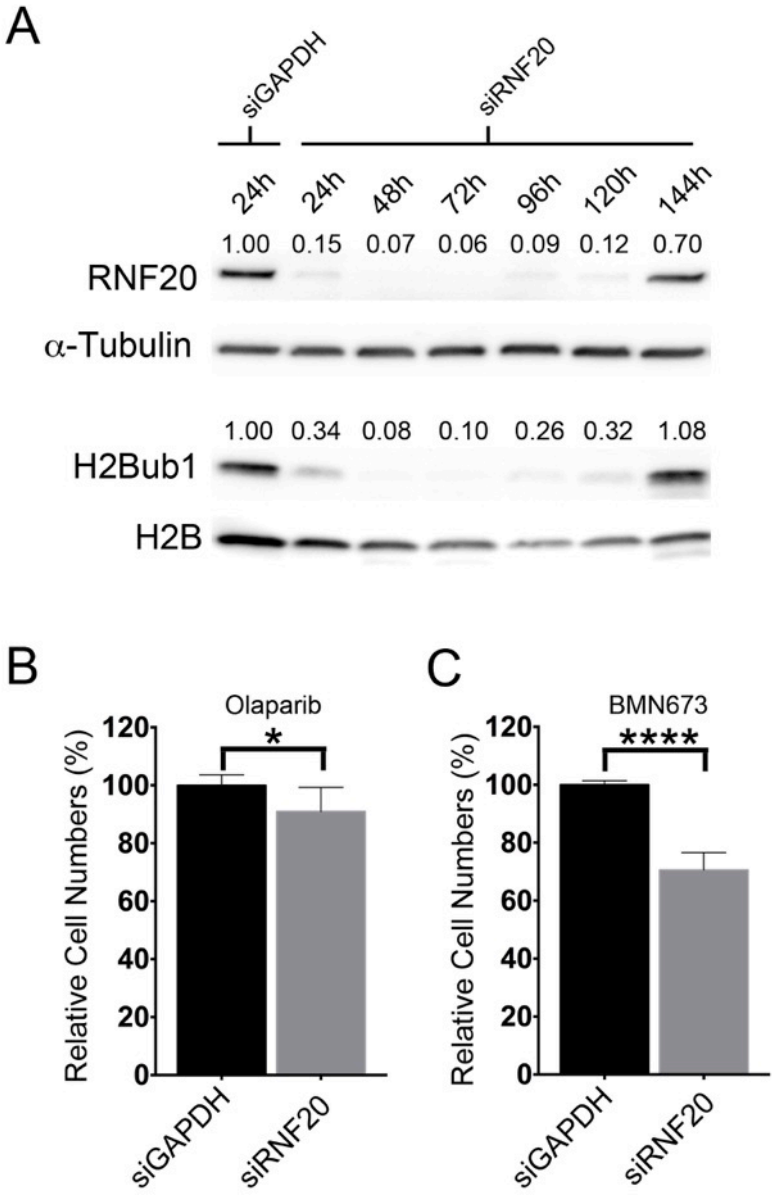

Figure 5.2: siRNF20 HCT116 Cells Exhibit Increased Sensitivity to PARP1 Inhibitors
(**A**) Immunoblots depicting the temporal dynamics of RNF20 and H2Bub1 in siRNF20 HCT116 cells. Semi-quantitative analyses were performed and the relative abundance of RNF20 and H2Bub1 are presented. H2B (unmodified) serves as a loading control. (**B**) Cells were exposed to Olaparib between 48h to 120h post-transfection. Cells were fixed and enumerated 120h post-transfection. Bar graph depicting the mean percentages of cells remaining (± SD) following Olaparib treatment. Data are presented relative to siGAPDH (*; p-value < 0.05). (**C**) Cells were exposed to BMN673 between 48h to 120h post-transfection. Cells were fixed and enumerated 120h post-transfection. Bar graph depicting the mean percentages of cells remaining following BMN673 treatment. Data are presented relative to siGAPDH (****; p-value < 0.0001).

HCT116 cells, analogous experiments were performed in hTERT with highly similar results (Figure 5.S2) (Olaparib, p-value < 0.05, Figure 5.S2B, Table 5.S7) (BMN673, p-value < 0.001, Figure 5.S2C, Table 5.S8). Collectively, these data indicate that PARP1 inhibition by either Olaparib of BMN673 phenocopies *PARP1*-silencing and further supports *RNF20* and *PARP1* as human SL interactors.

5.3.3 PARP1 Inhibition Selectively Kills shRNF20 Cells

To further validate the putative *RNF20 PARP1* SL interaction and develop novel reagents amenable to long-term studies (e.g. colony formation assay), we generated stable HCT116 shRNF20 and shGAPDH cells (detailed in Materials and Methods). Immunoblots confirmed *RNF20*-silencing in HCT116-shRNA cells (Figure 5.3A and 5.3B). As expected, shRNA-silencing phenocopied siRNA-silencing and resulted in a statistical decrease in cell numbers following PARP1 inhibition (Olaparib, p-value <0.05, Figure 5.3C, Table 5.S9) (BMN673, p-value <0.0001, Figure 5.3D, Table 5.S10). Consistent with siRNA experiments detailed above, BMN673 treatments produced a greater reduction in cell numbers compared to Olaparib and was therefore employed throughout the remainder of our study. Collectively, the above complementary siRNA and shRNA results further validate the *RNF20 PARP1* SL interaction.

To confirm the above results were not restricted to cells grown in 2D monolayers, colony formation assays were performed in soft agar. BMN673 treatment resulted in a statistical decrease in shRNF20 colony numbers (p-value < 0.05, Figure 5.3E, Table 5.S11) and size (p-value < 0.05, Figure 5.3F, Table 5.S12) relative to shGAPDH controls. The above data suggest long-term BMN673 treatment underlies a significant reduction in shRNF20 HCT116 cells and further validates the *RNF20 PARP1* SL interaction.

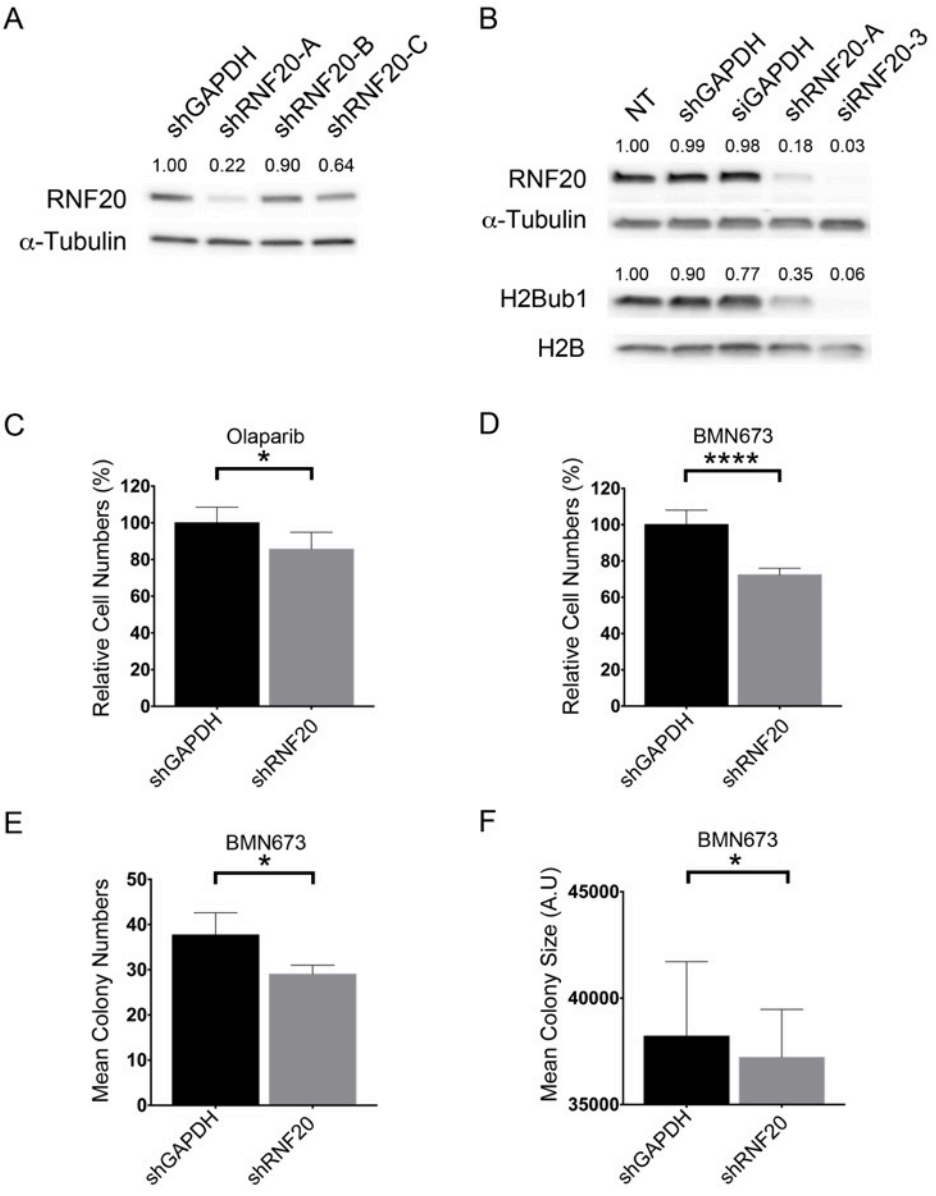

Figure 5.3: PARP1 Inhibition Induces a Significant Reduction in shRNF20 HCT116 Cells (**A**) Immunoblot depicting RNF20 levels in three unique shRNF20 HCT116 populations. The relative abundance of RNF20 is presented. (**B**) Immunoblot depicting RNF20 and H2Bub1 levels following various RNAi approaches. (**C**) Bar graph depicting the mean percentage of shRNF20 cells remaining (± SD) following Olaparib treatment (*; p-value < 0.05). (**D**) Bar graph depicting the mean percentage of shRNF20 cells remaining (± SD) following BMN673 treatment (****; p-value < 0.0001). (**E**) Bar graph depicting the mean number of shRNF20 colonies remaining (± SD) following 14 day treatment with BMN673. (**F**) Bar graph depicting the mean colony size of shRNF20 cells (± SD) following 14 day treatment with BMN673.

5.3.4 BMN673 Treatment Induces Cellular Cytotoxicity in *RNF20*-Silenced Cells

Although the above data suggest diminished cell numbers may be due to cellular cytotoxicity, it is equally plausible that cell cycle arrest or decreased proliferation rates could account for reduced cell numbers. To distinguish between these possibilities, real time cellular analysis (RTCA) was employed to evaluate changes in cell numbers following BMN673 treatment. RTCA employs electrical impedance to measure cell index (cell numbers) and is ideally suited to identify treatment related changes in cell proliferation and viability.

We first wished to confirm cell proliferation rates were not affected by RNF20 status or the addition of DMSO. Growth curves generated from siGAPDH and siRNF20 cells treated with DMSO were virtually indistinguishable (Figure 5.4A). Having established that proliferation rates were independent of RNF20 status, we wished to evaluate changes in proliferation following BMN673 addition (Figure 5.4B). Briefly, siGAPDH or siRNF20 cells were seeded onto RTCA plates and grown for 24 h. The following day, BMN673 or DMSO was added and cells were monitored for 72 h in real time. Individual growth curves were generated from siGAPDH and siRNF20 cells treated with BMN673. When comparing growth curves, siRNF20 cells exhibited a growth curve profile indicative of a cytotoxic effect (proliferation defect followed by a rapid decline in cell index). Using analogous experiments, these results were confirmed in HCT116-shRNA cells (Figure 5.4C and 5.4D). Collectively, these data indicate that BMN673 induces selective cytotoxicity in both siRNF20 HCT116 and shRNF20 HCT116 cells.

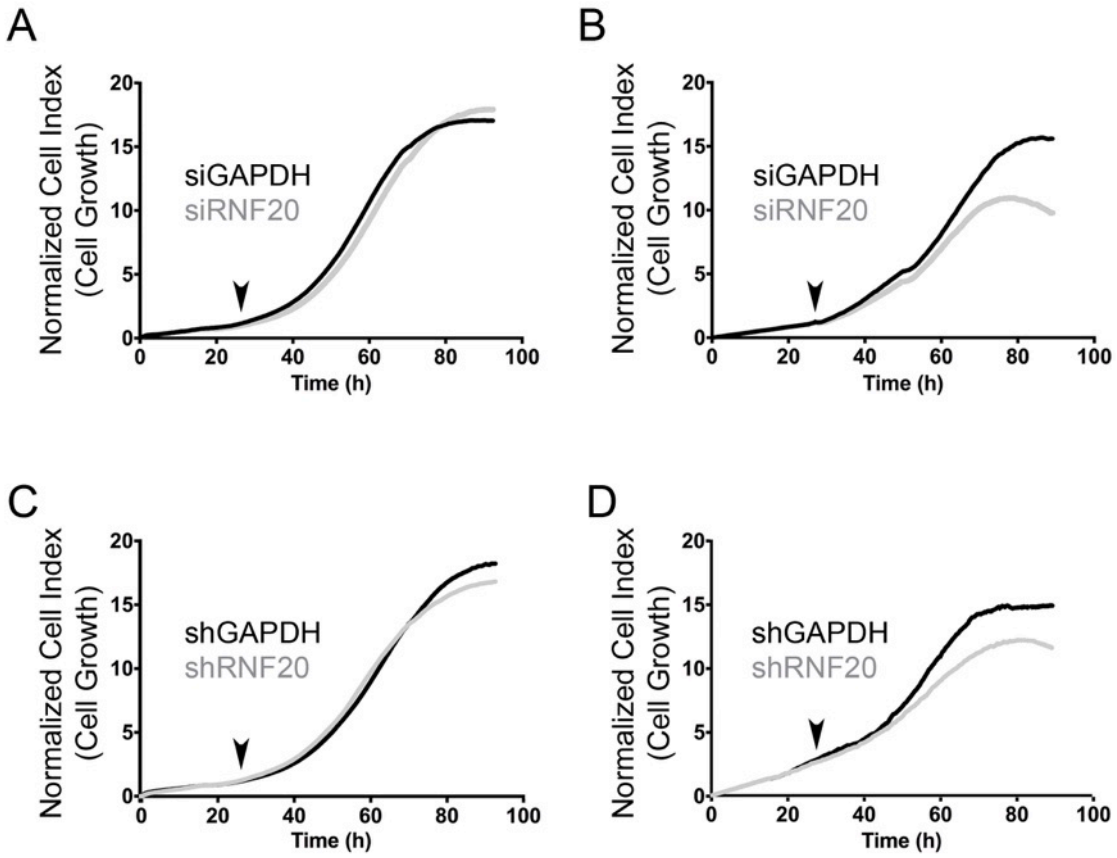

Figure 5.4: BMN673 Treatment Induces Cytotoxicity in siRNF20 Cells
(**A**) Real-time growth curves of siGAPDH and siRNF20 HCT116 cells treated with DMSO. (**B**) Real-time growth curves of siGAPDH and siRNF20 HCT116 cells treated with BMN673. (**C**) Real-time growth curves of shGAPDH and shRNF20 HCT116 cells treated with DMSO. (**D**) Real-time growth curves of shGAPDH and shRNF20 HCT116 cells treated with BMN673.
All treatments were initiated 24h post-seeding (arrow).

5.3.5 BMN673 Treatment Induces DNA Damage in HCT116 siRNF20 and shRNF20 Cells

Having established BMN673 treatment preferentially induces cytotoxicity within *RNF20*-silenced cells, we next sought to identify the underlying mechanism of cell death. PARP1 inhibition has been previously shown to cause increases in DNA DSBs and was therefore considered as a potential mechanism of cell death[180]. Accordingly, we wished to empirically assess the abundance of DNA DSBs in BMN673-treated *RNF20*-silenced cells. *RNF20*-silenced cells were treated with either DMSO or BMN673 as above, fixed, and immunofluorescently labeled with an established surrogate marker of DNA DSBs, γ-H2AX. Semi-quantitative indirect immunofluorescent imaging was performed and mean γ-H2AX signal intensity was calculated. Analysis of variance (ANOVA) was performed and Tukey multi-comparison post-tests revealed statistically significant differences in mean γ-H2AX signal intensity between a subset of treatments (Table 5.S13 and 5.S14). Specifically in all DMSO-treated cells, mean γ-H2AX signal intensities were highly similar and not statistically significant, indicating RNF20-status alone does not cause an increase in DNA DSBs. However, when examining BMN673-treated cells, visually evident (Figure 5.5A) and statistically significant (Figure 5.5B) increases in mean γ-H2AX signal intensities were observed in *RNF20*-silenced cells compared to *GAPDH*-silenced controls. Specifically, shRNF20 and siRNF20 cells displayed a 1.68-fold and 1.99-fold increase in mean γ-H2AX signal intensity, respectively. Collectively, these data show that BMN673 treatment increases mean γ-H2AX signal intensity in *RNF20*-silenced cells and thus increases in DNA DSBs may underlie cytotoxicity.

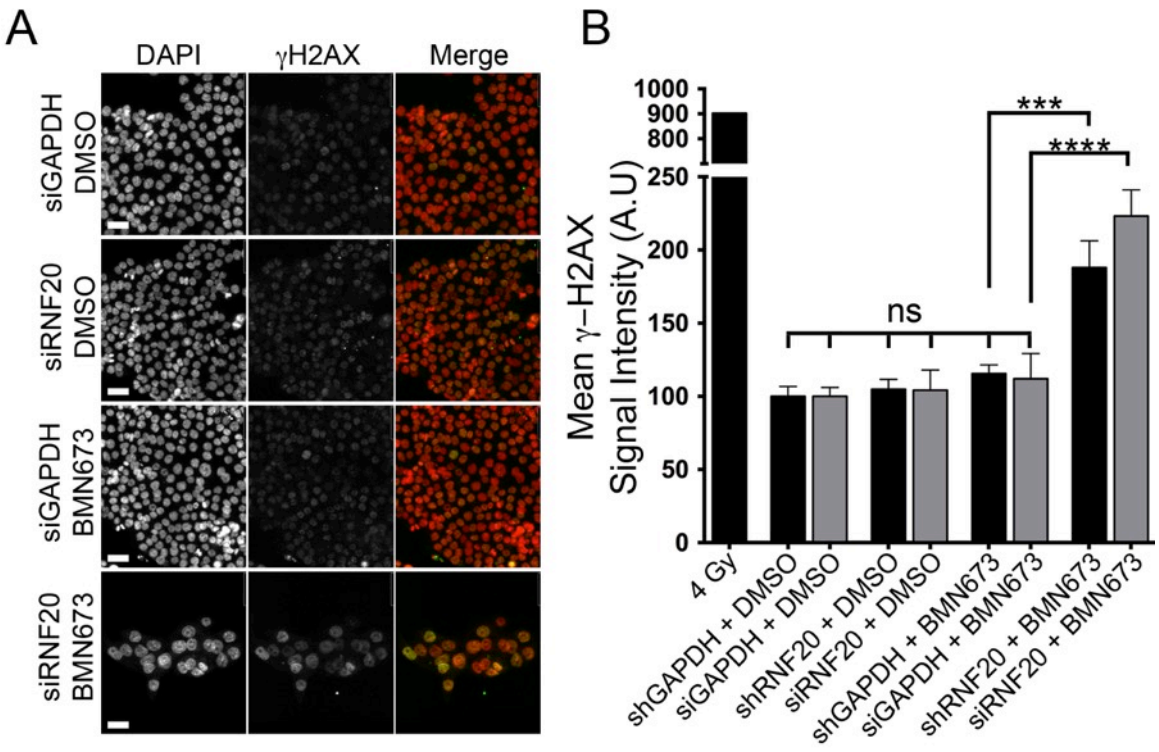

Figure 5.5: BMN673 Treatment Induces DNA Damage in HCT116 siRNF20 and shRNF20 Cells

(**A**) Representative low-resolution (10×) images presenting the qualitative differences in γ-H2AX signal intensities. DAPI and γ-H2AX are pseudo-colored red and green respectively within the merged images. Cells were imaged 48 h following BMN673 treatment. Images were acquired using identical exposure times to allow for quantitative analyses. Scale bar represents 20 μm. (**B**) Bar graph presenting the mean γ-H2AX signal intensities (± SD). 4 Gy ionizing radiation is a positive control for DNA DSBs. All data are presented relative to their respective controls (shGAPDH + DMSO) or (siGAPDH + DMSO). (ns, not significant; ***, *p*-value < 0.001; ****, *p*-value < 0.0001).

5.3.6 BMN673 Treatment Induces Apoptosis in HCT116 siRNF20 and shRNF20 Cells

Although the above data support the accumulation of DNA DSBs within *RNF20*-silenced cells, they do not address the underlying mechanism of death. We therefore sought to evaluate if BMN673 treatment induced apoptosis within *RNF20*-silenced cells. Accordingly, cells were treated as above and immunofluorescently labeled with cleaved Caspase-3, a key indicator of apoptosis. Visually evident increases in cleaved Caspase-3 signal intensity were observed in *RNF20*-silenced cells following BMN673 treatment (Figure 5.6A). ANOVA was performed and Tukey multi-comparison post-tests revealed statistically significant differences in mean cleaved Caspase-3 signal intensity between a subset of treatments (Figure 5.6B, Table 5.S15 and 5.S16). Collectively, these data show that BMN673 treatment selectively increases mean cleaved Caspase-3 signal intensity within *RNF20*-silenced cells and strongly suggests apoptotic cell death.

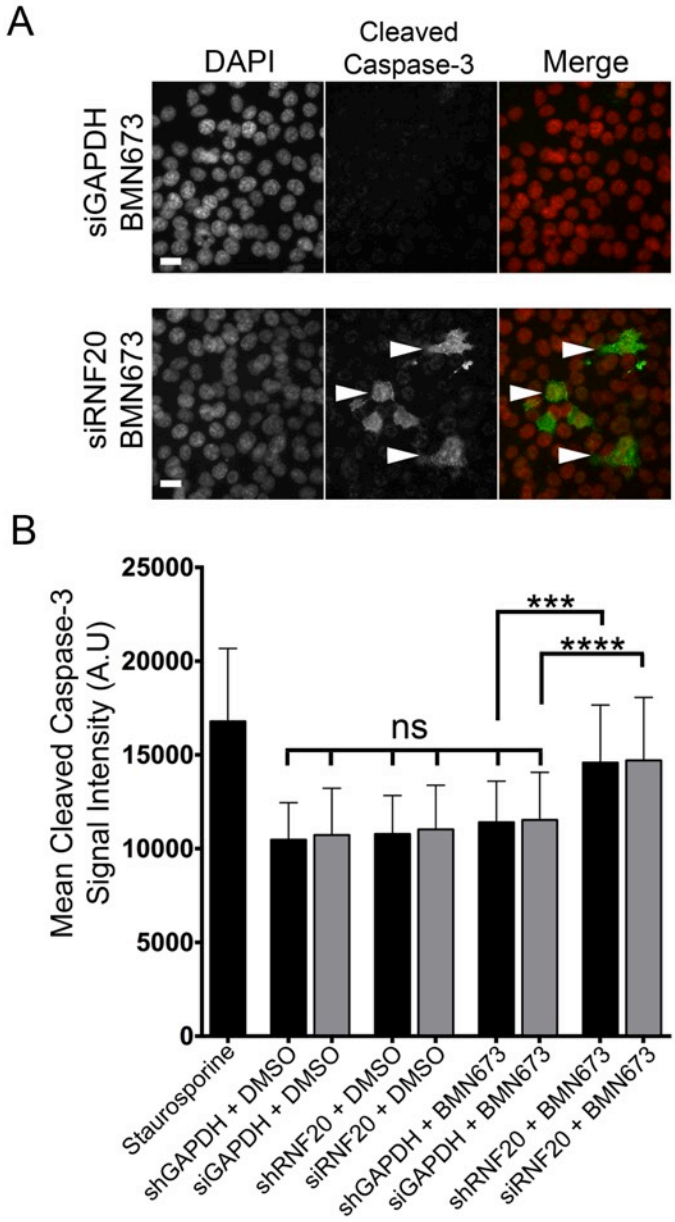

Figure 5.6: BMN673 Treatment Induces Apoptosis in HCT116 siRNF20 and shRNF20 Cells

(**A**) Representative low-resolution (20×) images presenting the qualitative differences in cleaved Caspase-3 signal intensities. DAPI and cleaved Caspase-3 are pseudo-colored red and green respectively, within the merged images. Images were acquired using identical exposure times to allow for quantitative analyses. Scale bar is 10 μm. (**B**) Bar graph presenting the mean cleaved Caspase-3 signal intensities (± SD). Staurosporine is a positive control for apoptosis. (ns, not significant; ***, p-value < 0.001; ****, p-value < 0.0001).

5.3.7 PARP1 Expression is required for Maximum BMN673-Dependent Cytotoxicity in HCT116 siRNF20 Cells

Previous groups have reported the requirement of *PARP1* expression to enhance PARP1 inhibitor related cytotoxicity in HRR-deficient cells[245-247]. Using our established siRNA approach, we performed dual silencing experiments in combination with BMN673 treatment to establish if PARP1-depletion attenuated BMN673-dependent cytotoxicity. Indeed, PARP1-depletion partially rescued siRNF20 cells from BMN673-related cytotoxicity (Figure 5.7). Specifically when treated with BMN673, the simultaneous depletion of RNF20 and PARP1 (siRNF20 + siPARP1) resulted in a statistically significant 1.14 increase in cell numbers compared to siGAPDH + siRNF20 cells (*p*-value <0.0001, Figure 5.7, Table 5.S17). These results show the requirement of *PARP1* expression for maximum BMN673-dependent cytotoxicity in siRNF20 cells.

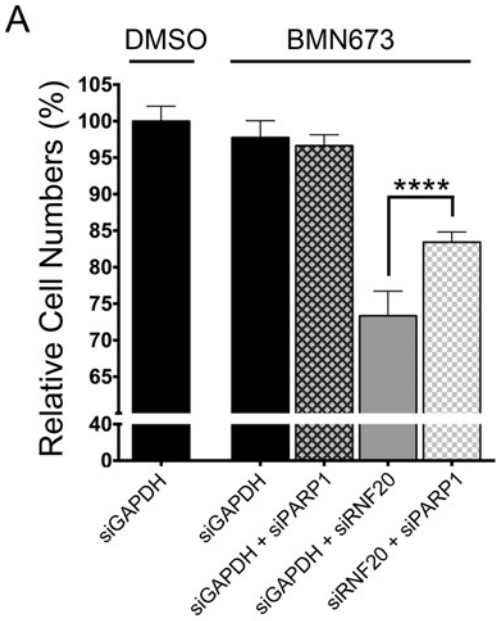

Figure 5.7: *PARP1* Expression is Required for Maximum BMN673-Dependent Cytotoxicity in siRNF20 Cells
(**A**) Graph showing the percentage of siRNA-silenced HCT116 cells remaining (± SD) following BMN673 treatment. Data are presented relative to siGAPDH DMSO (****; *p*-value < 0.0001).

5.4 Discussion

In this study, we employ RNAi in combination with Olaparib and BMN673, to identify and validate an *RNF20 PARP1* SL interaction in human cells. We specifically show that dual silencing of *RNF20* and *PARP1* causes a statistically significant decrease in cell numbers relative to controls. In addition, we show that Olaparib or BMN673 selectively kills siRNF20 cells. Using surrogate markers for DNA DSBs and apoptosis, we show that catastrophic increases in DNA damage and apoptosis are putative mechanisms underlying BMN673-dependent cell death. Furthermore, we show that *PARP1* expression is required for enhanced BMN673-dependent cell death and that PARP1-depletion partially rescues siRNF20 cells. Collectively, our data identify a novel human *RNF20 PARP1* SL interaction and Olaparib/BMN673 as lead compounds to selectively kill cancer cells exhibiting hypomorphic RNF20 expression and/or function.

There are several proposed mechanisms that describe the SL effect of PARP1 inhibition in HRR-deficient cells[242]. The classical view is that PARP1 inhibition underlies increases in DNA single strand breaks, which are converted to DNA DSBs through replication fork "drop-off" events during DNA synthesis[180]. As a result, cell death ensues from the catastrophic accumulation of DNA DSBs that are restricted to HRR-deficient cells. The cytotoxic effect is restricted to HRR-deficient cells because HRR-proficient cells, which represent normal tissues, maintain the ability to accomplish high-fidelity DNA DSB repair. In agreement with this model, we observed increases in DNA DSBs that were restricted to *RNF20*-silenced cells, suggesting that RNF20 plays an important role in HRR repair and thus hypomorphic expression and/or function underlies a HRR defect. Indeed several studies demonstrate the important role RNF20 plays in the HRR response[106,107]. Importantly, statistical increases in DNA DSBs were not observed in *RNF20*-proficient (*GAPDH*-silenced) cells following BMN673 treatment. When

extrapolating these observations to a cancer context, it is predicted that BMN673 would produce minimal genotoxicity in normal tissues, and therefore be associated with fewer treatment related side effects such as secondary cancers. This prediction is further substantiated by clinical trials confirming the high tolerability of PARP1 inhibitors[183,237,248].

An emerging model detailing the cytotoxic mechanism associated with PARP1 inhibition is a process known as "PARP1 trapping" [245-247,249]. In this model, PARP1 inhibition prevents PARP1 auto-ADP-ribosylation, which is a critical final step in displacing PARP1 from DNA lesions to allow access to accessory repair factors to complete DSB repair. For mechanisms not yet fully elucidated, PARP1 inhibitors that causes "PARP1 trapping", are more cytotoxic that PARP1 depletion[246]. In agreement with a "PARP1 trapping" model, we consistently observed a greater cytotoxic effect through PARP1-inhibition than PARP1-depletion. Furthermore, we show that *PARP1* expression is required for enhanced BMN673-depending cytotoxicity, which further supports the notion that BMN673 underlies PARP1-DNA trapping and enhanced cytotoxicity.

Although our results are consistent with both models above, we cannot discount other possible *RNF20 PARP1* SL mechanisms. For example, RNF20 has been shown to play a role in transcriptional regulation[76,100,104,244]. Using microarray analysis, Shema *et al.*[76,104] demonstrated that *RNF20*-silencing causes both an increase and decrease in the expression of a subset of HeLa genes. Accordingly, there remains the possibility that changes in gene expression patterns conferred by *RNF20*-silencing may be responsible for producing an indirect SL interaction with PARP1. Nevertheless, because by definition synthetic lethality represents *genetic* interactions, *RNF20* and *PARP1* are indeed *bona fide* human SL interactors and the exact SL molecular mechanism remains inconclusive.

HCT116 cells were ideally suited for this study as they are a near diploid, karyotypically stable human colorectal cancer cell line that has been extensively employed in similar SL studies[159,160,250]. hTERT cells which are a near diploid, karyotypically stable immortalized human fibroblast cell lines were also employed to show the conservation of the *RNF20 PARP1* SL interaction across cell types. Consequently, it is predicted that the *RNF20 PARP1* SL interaction may be conserved in several other clinically relevant cancer types including lung, breast, and prostate. However, there remains the possibility that additional genetic modifiers found within other cell types, may modulate the SL phenotype to either enhance or suppress cell death. Accordingly, additional pre-clinical experiments in other cell types must be performed to better understand the clinical potential of PARP1 as a novel therapeutic target in *RNF20*-deficient cancers. Compared to Olaparib, BMN673 consistently produced enhanced cytotoxicity. These observations were consistent with other studies that identified BMN673 as a more potent PARP1 inhibitor[249,251]. Based on the above information, additional PARP1 inhibitors should be evaluated in an *RNF20*-deficient context as subtle differences in their molecular mechanism may either enhance or suppress cell death.

Additional experiments could be performed in mouse models to evaluate the ability of BMN673 to selectively kill RNF20-depleted cells. For example, shGAPDH- and shRNF20-expressing HCT116 cells could be subcutaneously injected into the left and right flanks of athymic nude mice, respectively. Tumor growth could be monitored over time to evaluate the *in vivo* killing efficacy of BMN673. In conclusion, we have identified a *bona fide RNF20 PARP1* SL interaction in human cells and have presented data that suggests PARP1 inhibitors could be repurposed to selectively kill *RNF20*-deficient cancer cells.

5.5 Supporting Information
5.5.1 Supporting Tables

Table 5.S1: Student *t*-tests Comparing Mean Relative HCT116 Cell Numbers - siRNA

siRNA	n[A]	Mean[B] ± Standard Deviation	*p*-value[C]	Fold Change
siGAPDH + siRNF20	6	96.59 ± 0.451		
siRNF20 + siPARP1	6	86.90 ± 0.265	<0.0001	0.90
siGAPDH + siPARP1	6	95.87 ± 0.687		
siRNF20 + siPARP1	6	86.90 ± 0.265	<0.0001	0.90

[A]Number of wells enumerated (n)
[B]All Means are normalized to siGAPDH (%)
[C]Based on Student's *t*-test

Table 5.S2: HCT116 Multiplicative Model of SL Interaction Between *RNF20* and *PARP1*

siRNA	n[A]	Mean[B] ± Standard Deviation	Expected[C]	Difference[D]
siGAPDH	6	100.00 ± 2.045	n/a	n/a
siGAPDH + siRNF20	6	96.59 ± 1.105	n/a	n/a
siGAPDH + siPARP1	6	95.87 ± 1.684	n/a	n/a
siRNF20 + siPARP1	6	86.90 ± 0.650	92.60	5.7

[A]Number of wells enumerated (n)
[B]All Means are normalized to siGAPDH (%)
[C]Calculated by multiplying the Means of (siGAPDH + siRNF20) × (siGAPDH + siPARP1)
[D]Calculated as (Expected) - [Mean of (siRNF20 + siPARP1)]
Not applicable (n/a)

Table 5.S3: Student *t*-tests Comparing Mean Relative hTERT Cell Numbers - siRNA

siRNA	n[A]	Mean[B] ± Standard Deviation	*p*-value[C]	Fold Change
siGAPDH + siRNF20	6	95.67 ± 1.506		
siRNF20 + siPARP1	6	89.50 ± 2.074	0.0002	0.94
siGAPDH + siPARP1	6	94.67 ± 2.066		
siRNF20 + siPARP1	6	89.50 ± 2.074	0.0015	0.95

[A]Number of wells enumerated (n)
[B]All Means are normalized to siGAPDH (%)
[C]Based on Student's *t*-test

Table 5.S4: hTERT Multiplicative Model of SL Interaction Between RNF20 and PARP1

siRNA	n[A]	Mean[B] ± Standard Deviation	Expected[C]	Difference[D]
siGAPDH	6	100.00 ± 2.639	n/a	n/a
siGAPDH + siRNF20	6	95.67 ± 1.506	n/a	n/a
siGAPDH + siPARP1	6	94.67 ± 2.066	n/a	n/a
siRNF20 + siPARP1	6	89.50 ± 2.074	90.57	1.07

[A]Number of wells enumerated (n)
[B]All Means are normalized to siGAPDH (%)
[C]Calculated by multiplying the Means of (siGAPDH + siRNF20) × (siGAPDH + siPARP1)
[D]Calculated as (Expected) - [Mean of (siRNF20 + siPARP1)]
Not applicable (n/a)

Table 5.S5: Student *t*-tests Comparing Mean Relative HCT116 Cell Numbers - siRNA, Olaparib

siRNA	n[A]	Mean ± Standard Deviation	*p*-value[B]
siGAPDH	6	100.00 ± 1.473	n/a
siRNF20	6	90.97 ± 3.389	0.0347

[A]Number of wells enumerated (n)
[B]Based on Student's *t*-tests
Not applicable (n/a)

Table 5.S6: Student *t*-tests Comparing Mean Relative HCT116 Cell Numbers - siRNA, BMN673

siRNA	n[A]	Mean ± Standard Deviation	*p*-value[B]
siGAPDH	6	100.00 ± 0.7022	n/a
siRNF20	6	70.59 ± 3.007	<0.0001

[A]Number of wells enumerated (n)
[B]Based on Student's *t*-tests
Not applicable (n/a)

Table 5.S7: Student *t*-tests Comparing Mean Relative hTERT Cell Numbers - siRNA, Olaparib

siRNA	n[A]	Mean ± Standard Deviation	*p*-value[B]
siGAPDH	6	100.00 ± 4.852	n/a
siRNF20	6	85.86 ± 2.475	0.0267

[A]Number of wells enumerated (n)
[B]Based on Student's *t*-tests
Not applicable (n/a)

Table 5.S8: Student *t*-tests Comparing Mean Relative hTERT Cell Numbers - siRNA, BMN673

siRNA	n[A]	Mean ± Standard Deviation	*p*-value[B]
siGAPDH	6	100.00 ± 2.151	n/a
siRNF20	6	85.73 ± 1.713	0.0004

[A]Number of wells enumerated (n)
[B]Based on Student's *t*-tests
Not applicable (n/a)

Table 5.S9: Student *t*-tests Comparing Mean Relative HCT116 Cell Numbers - shRNA, Olaparib

shRNA	n[A]	Mean ± Standard Deviation	*p*-value[B]
shGAPDH	6	100.00 ± 3.480	n/a
shRNF20	6	85.61 ± 3.785	0.0188

[A]Number of wells enumerated (n)
[B]Based on Student's *t*-tests
Not applicable (n/a)

Table 5.S10: Student *t*-tests Comparing Mean Relative HCT116 Cell Numbers - shRNA, BMN673

shRNA	n[A]	Mean ± Standard Deviation	*p*-value[B]
shGAPDH	6	100.00 ± 3.285	n/a
shRNF20	6	72.36 ± 1.471	<0.0001

[A]Number of wells enumerated (n)
[B]Based on Student's *t*-tests
Not applicable (n/a)

Table 5.S11: Student *t*-tests Comparing HCT116-shRNA Colony Numbers - BMN673

shRNA	n[A]	Mean ± Standard Deviation	*p*-value[B]
shGAPDH	3	37.67 ± 2.848	n/a
shRNF20	3	29.00 ± 1.155	0.048

[A]Number of wells enumerated (n)
[B]Based on Student's *t*-tests
Not applicable (n/a)

Table 5.S12: Student *t*-tests Comparing HCT116-shRNA Colony Size - BMN673

shRNA	n[A]	Mean ± Standard Deviation	*p*-value[B]
shGAPDH	3	38,213 ± 329	n/a
shRNF20	3	37,211 ± 242	0.0213

[A]Number of wells enumerated (n)
[B]Based on Student's *t*-tests
Not applicable (n/a)

Table 5.S13: Analysis of Variance of the Mean γ-H2AX Total Signal Intensities as Determined by Semi-Quantitative Immunofluorescent Imaging Microscopy

Group[A]	SS[B]	df[C]	MS[D]	F-Ratio[E]	*P* value	Reject H_0[F]
BG	1.7×10^6	8	2.1×10^5	954	<0.0001	Yes
WG	3.8×10^3	18	219			

[A]Defines whether or not the analysis is between groups/treatments (BG) or within the group/treatments (WG)
[B]SS, sum of squares.
[C]df, degrees of freedom.
[D]MS, means square.
[E]F-Ratio is calculated by MS_{BG}/MS_{WG}
[F]The null hypothesis (H_0) is rejected if the P value is <0.05.

Table 5.S14: Mean γ-H2AX Total Signal Intensities as Determined by Semi-Quantitative Immunofluorescent Imaging Microscopy

Treatment	n[A]	Mean ± Standard Deviation	*p*-value[B]	Fold Increase
shGAPDH + BMN673	468	115.00 ± 6.04	n/a	n/a
shRNF20 + BMN673	344	187.90 ± 18.40	<0.001	1.63
siGAPDH + BMN673	329	112.00 ± 17.19	n/a	n/a
siRNF20 + BMN673	437	223.10 ± 17.99	<0.0001	1.99

[A]Number of cells analysed (n)
[B]Based on Tukey multicomparison post-tests.
Not applicable (n/a)

Table 5.S15: Analysis of Variance of the mean Cleaved Caspase-3 Total Signal Intensities as Determined by Semi-Quantitative Immunofluorescent Imaging Microscopy

Group[A]	SS[B]	df[C]	MS[D]	F-Ratio[E]	*P* value	Reject H_0[F]
BG	7.4×10^9	8	9.3×10^8	142	<0.0001	Yes
WG	1.3×10^{10}	1958	6.7×10^6			

[A]Defines whether or not the analysis is between groups/treatments (BG) or within the group/treatments (WG)
[B]SS, sum of squares.
[C]df, degrees of freedom.
[D]MS, means square.
[E]F-Ratio is calculated by MS_{BG}/MS_{WG}
[F]The null hypothesis (H_0) is rejected if the P value is <0.05.

Table 5.S16: Mean Cleaved Caspase-3 Total Signal Intensities as Determined by Semi-Quantitative Immunofluorescent Imaging Microscopy

Treatment	n[A]	Mean ± Standard Deviation	*p*-value[B]	Fold Increase
shGAPDH + BMN673	239	11,400 ± 2200	n/a	n/a
shRNF20 + BMN673	108	14,446 ± 3535	<0.0001	1.27
siGAPDH + BMN673	204	11,529± 2540	n/a	n/a
siRNF20 + BMN673	87	14,701 ± 3363	<0.0001	1.28

[A]Number of cells analysed (n)
[B]Based on Tukey multicomparison post-tests.
Not applicable (n/a)

Table 5.S17: Student *t*-tests Comparing Mean Relative HCT116 Cell Numbers Following PARP1-depletion, siRNA, BMN673

siRNA	n[A]	Mean[B] ± Standard Deviation	*p*-value[C]	Fold Change
siGAPDH + siPARP1	6	96.63 ± 0.61		
siGAPDH + siRNF20	6	73.35 ± 1.38	<0.0001	0.76
siGAPDH + siRNF20	6	73.35 ± 1.38		
siRNF20 + siPARP1	6	83.43 ± 0.57	<0.0001	1.14

[A]Number of wells enumerated (n)
[B]All Means are normalized to siGAPDH (%)
[C]Based on Student's *t*-test

5.5.2 Supporting Figures

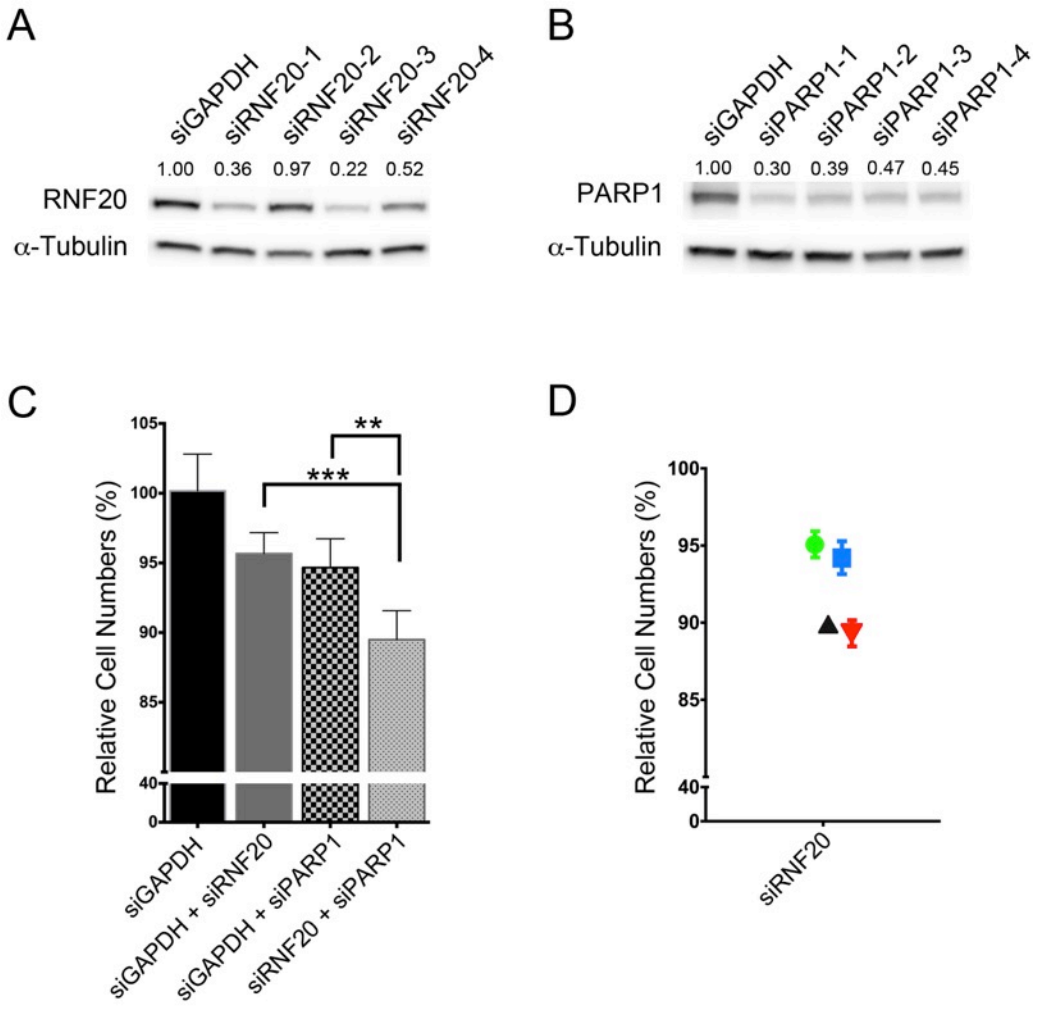

Fig. 5.S1. PARP1-Silencing Induces a Significant Reduction in siRNF20 hTERT Cells
(**A**) Immunoblots depicting diminished RNF20 levels following silencing in hTERT cells. Semi-quantitative analyses were performed and the relative abundance of RNF20 is presented. (**B**) Immunoblots depicting the relative abundance of PARP1 following silencing in hTERT cells. (**C**) Bar graph depicting the mean relative number of cells remaining (± SD) following silencing (***; p-value < 0.001) (**; p-value < 0.01). (**D**) Graph depicting the SL interaction observed following dual silencing of RNF20 and PARP1 in hTERT cells. Presented are the mean normalized percentages (± SD) for the controls siRNF20 + siGAPDH (green circle) and siPARP1 + siGAPDH (blue square), and the value predicted (black triangle) for siRNF20 + siPARP1 as calculated using a multiplicative model. The red triangle identifies the actual observed value for siRNF20 + siPARP1 and is lower than predicted indicating a SL phenotype.

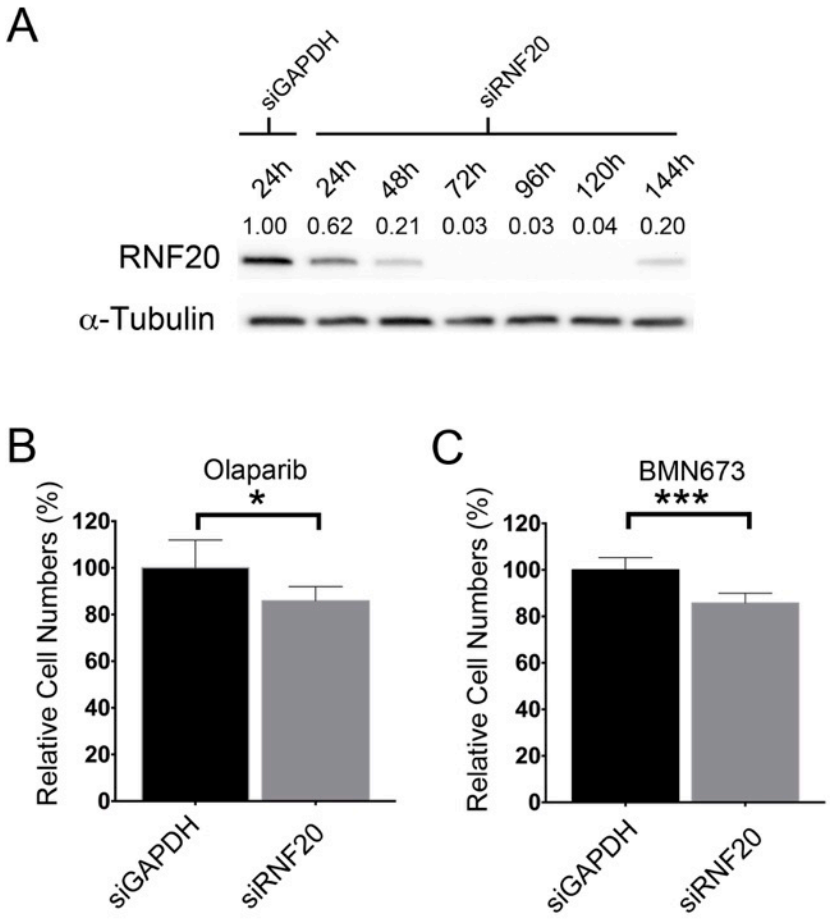

Figure 5.S2: siRNF20 hTERT Cells Exhibit Increased Sensitivity to PARP1 Inhibitors
(**A**) Immunoblots depicting the temporal dynamics of RNF20 in siRNF20 hTERT cells. Semi-quantitative analyses were performed and the relative abundance of RNF20 is presented. (**B**) Bar graph depicting the mean percentages of cells remaining (± SD) following Olaparib treatment. Data are presented relative to siGAPDH (*; p-value < 0.05). (**C**) Bar graph depicting the mean percentages of cells remaining following BMN673 treatment. Data are presented relative to siGAPDH (***; p-value < 0.001).

DISCUSSION

6.0 Discussion and Conclusions

The results detailed in the preceding chapters focus on three complementary themes; 1) characterizing the normal and aberrant biology associated with RNF20, DOT1L, and the components of the H2Bub1 trans-histone pathway (H3K4me2, H3K79me2), 2) generating and characterizing an HCT116 Cas9 expressing cell line to ultimately produce either *RNF20*- or *PPIB*-deficient cells, and, 3) employing SL strategies to selectively kill RNF20-depleted cells through PARP1-depletion or inhibition.

Chapter 3 details the cell cycle associated dynamics of the major components of the H2Bub1 trans-histone pathway. This chapter documents the previously unknown human global spatial and temporal dynamics for RNF20, H2Bub1, H3K4me2, and H3K79me2 throughout the cell cycle with a particular focus on mitosis. We found that RNF20 exhibited a dynamic pattern, dissociating from chromatin during the early stages of mitosis and re-associating with chromatin during early G1. As expected, H2Bub1 showed similar dynamics and was visually absent during mitosis and reestablished during early G1. H3K4me2 levels remained visually static throughout the cell cycle. Most interestingly, H3K79me2 exhibited a dynamic progression pattern that increased dramatically during mitosis and was unexpectedly uncoupled from H2Bub1. DOT1L was identified as the mitotic H3K79me2 KMT. Additional experiments showed that mitotic levels of H3K79me2 were important for maintaining mitotic fidelity in human cells. Taken together, we identified H3K79me2 and DOT1L as important components required to maintain genome stability during mitosis that when altered, induce CIN and are suspected to underlie oncogenesis.

Chapter 4 employed the CRISPR-Cas9 genome editing system to initiate work to develop *RNF20*- and *PPIB*-deficient cells. This chapter focused on the essential preliminary characterization steps required to validate a stable HCT116 Cas9-expressing clonal cell line including Cas9 expression, cell morphology, growth kinetics, karyotype stability, and genome editing capabilities. Out of the initial 12 candidate HCT116-Cas9 clones, we identified HCT116-Cas9 E08 cells as possessing highly similar properties compared to the parental HCT116 cells. Importantly, we converted the parental HCT116 cell line, which was initially limited by low editing efficiency, into a 'CRISPR-ready' cell line capable of high efficiency editing. In an initial proof-of-principle experiment, HCT116-Cas9 E08 cells were employed to generate *RNF20*- and *PPIB*-deficient cells.

Chapter 5 identified a novel human SL interaction between *RNF20* and *PARP1*. We employed several complementary approaches to characterize and validate this SL interaction. First, we showed that dual silencing (siRNF20 plus siPARP1) elicits a significant reduction in cell numbers. Second, we demonstrated that two PARP1 inhibitors, Olaparib or BMN673, selectively reduce cell numbers following *RNF20*-silencing relative to controls. Third, it was revealed that *RNF20*-silenced cells are selectively killed following BMN673 treatment and that DNA DSBs and apoptosis appear to underlie cytotoxicity. Finally, we showed that *PARP1* expression is required for enhanced BMN673-related cytotoxicity and that PARP1-depletion partially suppresses the SL phenotype.

In summary, the research chapters contained within this thesis have characterized putative drivers in cancer (Chapter 3), generated a valuable research reagent for future CRISPR-Cas9 genome editing experiments (Chapter 4), and identified a novel therapeutic strategy to selectively kill certain cancer cells (Chapter 5). This thesis has increased our understanding of

the etiological origins of cancer and generated novel reagents and treatments strategies that after further validation and clinical trials, could be employed to reduce morbidity and mortality rates associated with cancer.

6.1 Conceptualization and Historical Progression of Research Project

The conceptualization and historical progression of the research projects within this thesis are detailed below. The search for novel human CIN genes began with a sequencing study performed by Drs. McManus, Hieter, and Vogelstein[38]. In that study, 102 human orthologs of 96 known yeast CIN genes were sequenced in 132 CRCs exhibiting CIN. That study identified 5 mutated genes in which one was *RNF20*. Accordingly, it was hypothesized that aberrant RNF20 biology may be a driver of CIN in CRC and warranted further investigation. Based on that sequencing study, we wished to evaluate aberrant RNF20 biology and its potential contribution towards CIN. However, before we could evaluate aberrant RNF20 biology, it was first necessary to characterize normal RNF20 biology within human cells. Accordingly, we initiated work by characterizing the spatial and temporal dynamics of RNF20 throughout the cell cycle. The next logical step was to evaluate the normal biology associated with H2Bub1, the histone PTM that RNF20 governs. Because of the essential role H2Bub1 plays in modulating the downstream players of the H2Bub1 trans-histone pathway, we next sought to characterize the normal biology associated with H3K4me2 and H3K79me2. Surprisingly, when characterizing H3K79me2, we observed dynamic mitotic increases in H2K79me2 abundance. Based on prior literature that links mitotic increases in histone PTMs to genome stability[70-72], we hypothesized that H3K79me2 may also play a role in maintaining genome stability. In order to test this hypothesis, we wished to selectively deplete mitotic levels of H3K79me2 and therefore performed experiments to identify

DOT1L as the mitotic H3K79 KMT. Armed with the identity of the mitotic H3K79me2 KMT, we employed RNAi and a small molecule inhibitor to deplete and inhibit DOT1L and ultimately reduce mitotic levels of H3K79me2. This approach was coupled with genome stability assays, and DOT1L and H3K79me2 were identified as components important for maintaining genome stability in human cells[73].

To further study the aberrant biology associated with *RNF20* defects, we sought to employ the CRISPR-Cas9 genome editing system to generate *RNF20*-deficient HCT116 cells. We initially employed an 'all-in-one' transfection approach to deliver the essential CRISPR-Cas9 components (Cas9 expression cassette + crRNA + tracrRNA) within HCT116 cells (data not shown). These initial editing experiments had very limited success, as 'all-in-one' approaches resulted in extremely low transfection and editing efficiencies within HCT116 cells. To increase the probability of generating *RNF20*-deficient cells, a Cas9 expression cassette was stably integrated into the HCT116 genome to allow for small particle transfection (crRNA + tracrRNA). Using this approach, the transfection particle size was reduced from 4,288 nt to 169 nt, which dramatically increased transfection and editing efficiency within these cells. Following the generation and characterization of the HCT116-Cas9 clones, E08 cells were employed to generate *RNF20*- and *PPIB*-deficient HCT116 cells. High *PPIB* editing efficiency was achieved and *PPIB*-deficient cells were isolated and clonally expanded for future use. However, attempts to isolate and clonally expand *RNF20*-deficient cells were unsuccessful.

There are several possible explanations as to why the initial efforts to isolate *RNF20*-deficient cells were unsuccessful. First, it is possible that *RNF20* represents an essential gene and thus *RNF20*-deficient cells are non viable. However, a database query of the Cancer Cell Line Encyclopedia (www.broadinstitute.org) has revealed six cancer cell lines that are reported to be

homozygously deleted for *RNF20*. Homozygous deletions were identified in ME-1 (acute myeloid leukemia), SK-CO-1 (colon carcinoma), KELLY (neuroblastoma), MOGGUVW (astrocytoma), BV-173 (B-cell leukemia), and EOL-1 (eosinophilic leukemia). This at least suggests, that under certain cellular contexts, *RNF20* expression may be dispensable[210]. In addition, several putative *RNF20*-deficient HCT116 cells were observed through lack of IIF labeling within the CRISPR-Cas9 targeted populations (Figure 4.10A and 4.10C). Furthermore, when examining targeted populations, multiple *RNF20*-deficient clonal regions were identified suggesting they may have arisen from a single *RNF20*-deficient cell that continued to proliferate. These data suggest *RNF20*-depleted cells may maintain the ability to proliferate in the absence of *RNF20.* Second, it is possible that *RNF20* inactivation may induce senescence and therefore *RNF20*-deficient cells stop proliferation. However, arguing against this possibility is evidence from Shema *et al.*[76] who demonstrated that RNF20-depletion in NIH3T3 cells caused an increase in cell proliferation both *in vitro* and *in vivo* (flank injections of nude mice). Furthermore, results obtained in Chapter 5 show that that proliferation rates in RNF20-depleted HCT116 cells were virtually indistinguishable from controls. Collectively, these results argue against the notion that *RNF20* inactivation underlies senescence. Finally and perhaps most likely, technical challenges associated with isolating a single RNF20-depleted cell from a heterogeneous population comprised largely of unedited cells may have adversely impacted our ability to isolate an *RNF20*-deficient clone. Accordingly, additional screening may be required to isolate and characterize *RNF20* edited HCT116 clone(s). Image-based cytometry performed on targeted populations identified a 16% RNF20 editing efficiency. Based on this percentage, it was estimated that 8 out of the 56 isolated clones are expected to be *RNF20*-deficient yet none were

identified. Nevertheless, the exact reason(s) *RNF20*-deficient clones could not be isolated and expanded is beyond this proof-of-principle study.

Finally, based on the knowledge that defects within genes that encode functions within the HRR pathway can be selectively killed through PARP1 inhibition, we directly predicted that the role RNF20 plays in HRR[106,107] makes *RNF20* defects amenable to SL targeting via PARP1 inhibition (Chapter 5). Using several complimentary approaches, we determined that *RNF20* and *PARP1* are SL interactors and provided important pre-clinical evidence that suggests PARP1 may be an important drug target to selectively kill cancer cells harboring *RNF20*-defects. Accordingly, the next logical step in the validation of PARP1 as a clinically relevant drug target is to perform *in vivo* mouse models and if successful, clinical trials in cohorts stratified based on *RNF20* status.

6.2 Histone PTMs and Genome Stability

Experiments performed in Chapter 3 demonstrated that the mitotic accumulation of H3K79me2 is important for maintaining genome integrity during mitosis in human cells[73]. In addition to H3K79me2, several other mitotic associated histone PTMs have been implicated in maintaining genome stability including H3S10Phos[70], H3K9me3[71], and H4K20me[72]. Furthermore, the recent identification of H3K18ac[252] as a genome stabilizing histone PTM suggests that several others remain to be identified. Identifying and characterizing the specific histone PTMs that maintain genome stability will increase our understanding of the etiological origins of cancer and may uncover novel therapeutic targets. How can additional genome stabilizing histone PTMs be identified? Given the apparent link between dynamic mitotic

changes in histone PTMs and genome stability, perhaps those that exhibit cell cycle related changes in and around mitosis should be evaluated first.

The semi-quantitative indirect immunofluorescent imaging approach employed in Chapter 3 could be easily applied to uncover novel histone PTM with mitosis-associated dynamics. Inherent within this approach, and perhaps the greatest challenge to accurately identify specific mitosis-associated histone PTMs, are the specificities of the antibodies employed for immunological detection. Several companies have developed a myriad of antibodies targeting specific histone PTMs. However, antibodies often suffer from low specificities. Antibody validation experiments such as those performed in Chapter 3 (peptide competition assays, dot blots) provide an example as to the minimal types of analyses that should be employed to ensure epitope specificity. Once validated, histone PTM-specific antibodies can be employed to characterize the unknown cell cycle dynamics of candidate genome stabilizing histone PTMs.

Once specific mitosis-associated histone PTMs have been identified, experiments can be performed to empirically evaluate genome instability following PTM perturbation. In order to selectively deplete candidate genome stabilizing histone PTMs, site-directed mutagenesis can be performed where a histone residue is mutated to an unmodifiable residue (e.g. K to R). However, the biological significance of altering highly conserved amino acids within core histones is poorly understood and may produce confounding results stemming from unexpected changes to nucleosomal structure and/or higher order chromatin compaction[253]. Furthermore, since several distinct histone PTMs can occur on identical residues (e.g. H3K9me3 and H3K9ac[71]), the biological impact stemming from site specific mutations may not accurately reflect the loss of one particular PTM, but several. There are other better-suited experimental means to selectively

modulate a particular histone PTM. First, several transgenic knockout mice have been generated to be deficient in a particular histone-modifying enzyme[254,255]. Second, RNAi, CRISPR-Cas9, or chemical inhibition could be employed to selectively deplete, inactivate, or inhibit one or several histone modifying enzyme(s) in established cell lines[73,159,185,250]. Third, overexpression of one or several residue specific histone modifying enzyme(s) could be performed to selectively modulate a particular PTM. In any case, once a particular histone PTM is experimentally modulated, multiple assays such as those detailed within Chapter 3 and 4 are available to evaluate genome stability.

In the era of "-omics", it is foreseeable that all histone PTMs and their corresponding modifiers will be identified. Once identified, a genome-wide interrogation of all possible histone modifiers and their role in genome stability could be performed. Genome-wide RNAi or CRISPR-Cas9 sgRNA libraries could be utilized to systematically deplete or inactivate individual histone modifying enzymes. Conversely, expression plasmids could be employed to overexpress specific enzymes. These approaches could be coupled with high-content assays such as those developed in our lab, which detect three different phenotypes associated with CIN[232]. The first assay employs high-content imaging and nuclear area analysis to identify large-scale chromosome content changes that are revealed by changes in nuclear area. This is possible because of the positive correlation between DNA content and nuclear area. The second assay detects chromosome 11 copy number changes on a cell-by-cell basis. Chromosome 11 copy number is identified by fluorescent proteins which bind to specific regions on chromosome 11. Two foci that represent both copies of chromosome 11 are observed in karyotypically stable cells, whereas changes in foci number typically represent copy number changes and identify

CIN. Finally, high-content imaging can be employed to detect increases in micronucleus formation, a classic hallmark of CIN.

It is predicted that the list of genome stabilizing histone-modifying enzymes identified by either RNAi or sgRNA genome-wide approaches would differ modestly based on the biological differences associated with protein depletion (RNAi) and genetic inactivation (sgRNA). It should be noted that employing both types of genome-wide libraries could yield valuable information pertaining to normal and cancer biology. RNAi approaches, which often produce incomplete protein depletion, may best model the hypomorphic expression and/or function observed in certain cancers. Conversely, complete gene inactivation conferred by sgRNA may best model non-sense mutations and loss of heterozygosity that is typical of other cancers. Information gleaned from these approaches are predicted to identify a subset of genome stabilizing histone-modifying enzymes that when altered, underlie oncogenesis. It is further expected that these approaches may also identify a subset of genome stabilizing histone PTMs. However, these results should not be over interpreted as certain histone-modifying enzymes have been shown to target more than one residue and can modify non-histone proteins as well. Furthermore, certain histone PTMs themselves can also undergo subsequent modifications (e.g., methylated arginine to citrulline)[256]. In addition, several studies including those detailed within Chapter 3 show that certain histone PTMs can influence changes in other histone PTMs through what is referred to as histone cross talk. Collectively, identifying the genome stabilizing histone-modifying enzymes and the histone PTMs they govern, may ultimately further elucidate the molecular origins of cancer so that novel therapeutic strategies can be identified, validated and employed.

6.3 SL Interactions Between HRR Genes and *PARP1*

Using a hypothesis driven approach we suspected that the role RNF20 plays in HRR renders it amenable to SL targeting via PARP1 inhibition. As predicted, we identified *RNF20* and *PARP1* as human SL interactors and demonstrated that PARP1 inhibitors could be repurposed/expanded to selectively kill RNF20-depleted cells. Chapter 5 exemplifies the idea that PARP1 inhibitors need not be restricted to their classical role in selectively killing *BRCA1/2*-deficient cancers but should be re-evaluated in the context of other HRR defects. Indeed, studies currently being performed within the McManus lab now suggest that defects within *RAD54B*, an additional HRR component, can be selectively killed by PARP1 inhibition (unpublished observations). Furthermore, several other laboratories have employed both hypothesis driven approaches and high-throughput screens to identified additional PARP1 SL interactors[257-263] including as *CDK12*[263], *PTEN*[259], *USP1*[261], *RAD51D*[258], and *RAD51C*[262]. Collectively, hypothesis driven research and novel high-throughput screens continue to identify genes that are SL with PARP1 and sensitive to PARP1 inhibitors. Given this ever-growing list of genes, efforts should now focus on curating all known *PARP1* SL interactors and determine which are most clinically relevant and confer the greatest susceptibility to PARP1 inhibition.

6.4 HRR Components as a Repository for *PARP1* SL Interactors

Several components that function within the HRR response are altered in multiple cancer types and are predicted to be SL interactors with *PARP1*[234,241]. The HRR response has evolved a complex network of proteins to "sense" DNA DSBs, "transduce" the damage signal throughout the cell, and execute error-free repair through "effector" proteins. As such, virtually any of the

components within these three HRR "layers" may contribute to oncogenesis and thus may be exploitable through PARP1 inhibition.

Several histone post-translational modifying enzymes have been implicated in the HRR response including RNF20[107,264] and RNF40[107,265]. These and other histone modifying enzymes including RNF8[266] and RNF168[267] have been shown to generate important DNA-damage dependent histone modifications surrounding the DNA break to facilitate HRR. Following DSB induction, the RNF20/RNF40 complex is phosphorylated by ATM and recruited to the DNA lesion where it catalyzes local H2B ubiquitination within nucleosomes surrounding the break. H2Bub1 has been shown to be required for the timely recruitment of the HRR repair factors RAD51 and BRCA1, presumably through the consequences conferred by chromatin decondensation[83,106,107]. Other examples of histone PTMs and the DNA damage response include the damage-dependent ubiquitination of H2A and H2AX by RNF8, which is then sustained by RNF168[267]. Much like H2Bub1, H2A ubiquitination has been shown to promote chromatin decondensation and 53BP1 recruitment[144,268]. Accordingly, defects in the histone modifying enzymes that play key roles in HRR are strong candidate *PARP1* SL interactors. In support of this possibility, Chapter 5 shows that RNF20-depleted cells are selectively killed by PARP1 inhibition. Furthermore, others have shown that RNF168-depleted cells are also susceptible to PARP1 inhibition[263]. Collectively, these studies show that certain histone modifying enzymes such as RNF20, RNF40, and RNF168 are SL interactors with *PARP1* and that several others likely exist and should be evaluated.

An approach to identify all *PARP1* SL interactors would be to identify all components within the HRR network. Not only would this identify additional *PARP1* SL interactors but it would also increase our biological understanding of the HRR network. A comprehensive list of

HRR genes may be identified by systematically interrogating the human genome by coupling genome-wide sgRNA bi-allelic deletions with a HHR reporter assay. A variation of the I-*SceI* HRR reporter assay is ideally suited for this approach[269]. Briefly, the I-*SceI* HRR reporter assay employs drug resistance as a surrogate readout for HRR repair[270]. Following an I-*SceI* targeted cut within the drug resistance gene, cells with intact HRR will recombine DNA elements such that drug resistance is restored and cells remain viable. However, in HRR-deficient cells that cannot perform high fidelity repair, drug resistance is ablated and cells are killed. When coupled with massively parallel sequencing, sgRNA molecules that become underrepresented within the population identify putative HRR components. As with all pooled screens, putative HRR genes must be validated through additional approaches. Furthermore, pooled screens should be extended to include different cell types of various genetic backgrounds to identify genetic modifiers that either enhance or suppress the HRR response.

Synthetic lethality between *PARP1* and HRR components is an attractive therapeutic approach as several clinically relevant PARP1 chemical inhibitors have been identified and could be easily tested. Because HRR plays a fundamental role in maintaining genome stability, defects within these components are highly suspected to be initiating events in oncogenesis. Presumably then, as tumors increases in size and genomic complexity, it is predicted that these initial genomic defects will be retained in subsequent tumor progeny. This is a fundamentally important feature as these targetable defects could be found in additional cancer subclones or metastatic deposits and would make them susceptible to PARP1 inhibition.

6.5 Human SL Interactions in a Cancer Context

With the global cancer burden expected to increase two-fold in the near future[1], novel highly efficient therapeutic strategies must be rapidly identified, validated and implemented. Over the past 50 years, a large number of cancer killing compounds have been identified, yet few can restrict their cytotoxic effects to cancer cells and as a result, damage healthy normal tissues alike. The narrow therapeutic windows associated with these types of classical chemotherapeutic compounds often limit the high concentrations needed to aggressively treat cancers. Even when these necessarily high drug concentrations can be achieved, they often come at the price of hematopoietic damage or damage to other systems such as the skin (Folinic Acid[271]), heart (Fluorouracil[272] or Doxorubicin[273]), or nerves (Oxaliplatin[274]). In addition, genotoxic effects associated with certain compounds can produce mutations in normal tissues and lead to treatment-related secondary malignancies[275]. Accordingly, a new generation of chemotherapeutic agents must be identified that better restrict their cytotoxic effects to cancers cells to reduce cancer morbidity and mortality rates worldwide.

Applying the concept of synthetic lethality to cancer treatment may overcome these traditional limitations and broaden the therapeutic window for new and existing compounds. Synthetic lethality is advantageous over classical approaches because cancer cells that harbor exploitable defects are selectively killed though a SL interaction with a druggable target. In fact, these exploitable defects are predicted to render cancer cells hypersensitive to a particular drug such that low concentrations can be employed to induce targeted killing. Reduced drug concentrations coupled with enhanced targeting and killing of cancer cells conferred by synthetic lethality has the added benefit of minimizing treatment related side effects to normal tissues. Evidently the ability to employ SL approaches for cancer treatments is contingent on identifying

exploitable defects contained within the cancer cell itself. As we enter the era of genomics and personalized medicine, it can be envisioned that whole genome sequencing will be performed on *ex vivo* tissues collected from biopsy, surgery, circulating tumor cells, or circulating tumor nucleic acids in order to identify the specific cancer driving mutations/alterations that could be potentially exploitable through SL mechanisms. Inherent in the successful application of SL approaches to cancer is *a priori* knowledge of validated human SL interactions. Although a SL interaction network has been identified in yeast[276], identifying rare human SL interactors presents an even greater challenge and is the current "bottleneck" of this potential treatment paradigm. Although Chapter 5 demonstrates how knowledge based approaches can be employed to identify and validate human SL interactions, the ultimate end goal is to identify the human SL interactome. Detailed below are several approaches to increase the human SL network and curate the SL interactome.

6.6 Identifying Additional Human SL Interactors

Since the original description in flies[157], SL approaches have been expanded to include studies in numerous genetically tractable model organisms including worms[277] and yeast[276]. Consequently, we and others argue that SL interactions identified in model organisms could be used to identify conserved interactions in human cells[161]. Since many essential biological processes are highly conserved throughout evolution, it is likely that many SL interactions will be evolutionarily conserved as well. Thus SL datasets generated in model organisms can be mined to identify candidate human SL interactors. For example McManus *et al.*[159,250] employed a cross-species approach to identify two human SL interactions that were first identified in budding yeast. Using RNAi-based silencing and high-content imaging, they showed that Flap

Endonuclease 1[159] (FEN1) depletion caused selective cytotoxicity within *RAD54B*-deficient colorectal cancer cell but not in *RAD54B*-proficient controls. This identified *RAD54B* and *FEN1* as SL interactors and FEN1 as a candidate drug target in *RAD54B*-deficient cancers[159]. Using similar approaches, *SOD1* was later identified as a *RAD54B* SL interactor and thus represents an additional candidate drug target in *RAD54B*-deficient cancers[250]. RAD54B is normally involved in HRR[278] and somatic mutations are found in numerous tumor types[52-54,171,279]. Accordingly, SL datasets derived from model organisms represent highly valuable repositories that will aid in the identification of additional human SL interactions. However, employing cross-species approaches to identify conserved human SL interactions has inherent biologically limitations and will not elucidate the full human SL interactome.

6.7 Genome-Wide Screens to Identify Human SL Interactors

Whole genome approaches are also being employed to uncover novel candidate drug targets by identifying SL interactors for any given cancer gene query. However, unlike the knowledge-based and cross-species approaches detailed above that limit the number of potential interactors interrogated, a whole genome approach represents an unbiased survey of all possible interactors. Consequently, whole genome approaches are expected to identify additional SL interactions beyond those identified by the above approaches. Whole genome based screens also differ from the other two approaches detailed above in two specific ways. First, the entire genome is evaluated, and the shRNA or sgRNA libraries are purposefully designed to include multiple constructs targeting unique regions of the same gene. If similar results are obtained with multiple shRNA or sgRNA molecules targeting a single gene, there is an increased likelihood that the phenotype observed is due to a *bona fide* SL interaction and not an off target effect.

Second, because genome-wide libraries are lentiviral based, a low multiplicity of infection must be employed to increase the probability that only a single gene is interrogated within any given cell. Furthermore, whole genome approaches are typically performed in a pooled manner where cells are transduced *en masse* with genome-wide libraries. These features are critical as either microarray analyses or massively paralleled DNA sequencing are ultimately performed to identify those shRNA or sgRNA constructs that become underrepresented from the population over time, which presumably occurs due to cellular cytotoxicity induced by a putative SL interaction. As with all pooled approaches, putative SL interactions require subsequent validation prior to confirming it as a novel candidate drug target. Although genome-wide shRNA libraries appear to be an excellent tool to identify the human SL interactome, there are certain technical limitations associated with shRNA approaches such as off target effects and incomplete protein depletion. Conversely, genome-wide sgRNA libraries, which have been shown to have greater specificities and a higher validation rate, appear to overcome some of these limitations and may ultimately best serve to elucidate the human SL interactome.

Several studies are now employing genome-wide CRISPR-Cas9 sgRNA lentiviral libraries to generate bi-allelic inactivation of virtually every gene within the human genome[280,281]. These studies exemplify how the CRISPR-Cas9 genome editing system could be employed to systematically interrogate genome-wide SL interactions[280]. For example, in a proof-of-concept study Wang *et al.*[280] employed a genome-wide CRISPR-Cas9 sgRNA library to identify inactivated genes that conferred 6-thioguanin (6-TG) resistance in KBM7 cells (chronic myelogenous leukemia cell line). 6-TG is normally lethal to KBM7 cells, however, it is well established that defects within the DNA mismatch repair pathway confers 6-TG resistance[282]. As predicted, cells bearing defects in several key components of the mismatch repair pathway were

found highly enriched within 6-TG treated populations, validating the ability for CRISPR-Cas9 sgRNA libraries to be employed on the genome-wide scale[280]. It is predicted a genome-wide CRISPR-Cas9 SL screen could be performed in a similar manner. Cells containing a cancer query gene could be transduced *en masse* with the genome-wide CRISPR-Cas9 sgRNA library to systematically interrogate SL interactors. Massively paralleled DNA sequencing could be performed to identify those sgRNA molecules that become underrepresented within the population, which presumably occurs due to cellular cytotoxicity induced by a putative SL interaction. As with all screens, putative SL interactions should undergo extensive validation before being characterized as *bona fide* SL interactors.

6.8 Towards a Human SL Interactome

Substantial efforts and expenditure will be required to finally identify and curate the human SL interactome. One can imagine that advanced genome editing technologies such as the CRISPR-Cas9 system will play a vital role in identifying and curating the human SL interactome. For example, it may be possible to utilize CRISPR-Cas9 to produce multiple cell lines containing a single gene inactivation for virtually every human gene in the genome (~20,000 unique cell lines). Unique cell lines could be interrogated with the genome-wide CRISPR-Cas9 sgRNA library, and candidate interactors could be identified using the approaches described above. Conceivably, these efforts would be most amenable to a high-throughput automated platform capable of generating and analyzing large amounts of data on a routine basis.

A SL interactome identified in human cells would represent a key benchmark towards the routine evaluation of SL approaches to selectively kill certain cancers. However, there are several biological caveats to consider. Some human SL interactions are predicted to be context

dependent and may only elicit SL killing of a certain cell type or under certain conditions[158-160,277]. As a result, SL interactions identified in one particular cell type containing a unique genetic background may not necessarily be conserved in another. It is currently unknown to what extent polymorphisms within the human genome will either enhance or suppress a particular SL interaction. Accordingly, SL interactomes must be identified within several diverse cell types in order to categorize the specific genetic modifiers that either enhance of suppress a particular interaction. These complexities are further compounded when considering the genetic diversity associated with cancer genomes. As such, passenger and driver mutations must also be considered as potential genetic modifiers. Adding even further complexities, are differential gene expression patterns associated with cells grown in 2D or 3D. Differences in gene dosages conferred by various cell culture formats may also prove to be modifiers of certain SL interactions. It is currently unknown to what extent SL interactions identified within these artificial systems will be conserved within a human cancer context.

6.9 Synthetic Lethality in a Precision Medicine Era

In the era of cancer genomics, identifying specific druggable SL interactions may be amenable to a precision medicine approach, which tailors treatments to individual patients. As next generation sequencing costs continue to decrease, it will one day be routine practice to perform whole genome sequencing on patient-derived tumors or biopsies. When combined with information curated within a human SL interactome, massively paralleled DNA sequencing could rapidly identify multiple SL targets within tumor clones and/or subclones. It may then be possible to identify a unique combination of compounds to selectively kill the primary tumor and/or metastatic deposits within the patient.

Although a promising concept, the clinical application of synthetic lethality is still in its infancy. Additional clinically relevant human SL interactions and selective small molecule inhibitors must be identified and validated, and research efforts must be expanded to curate the human SL interactome. Nevertheless, data gleaned from this thesis (Chapter 5) coupled with multiple pre-clinical and clinical studies strongly suggest that SL approaches to cancer may be highly effective. Thus, SL approaches may hold tremendous potential as a novel paradigm in combating cancers by selectively targeting the aberrant genetics driving cancer development and progression, while simultaneously minimizing the collateral damage to patients' healthy tissues. Taken together, SL approaches have the potential to improve the quality of life and survival of individuals diagnosed with cancer.

Chapter 7 - REFERENCES

1. Bray F, Jemal A, Grey N, Ferlay J, Forman D. Global cancer transitions according to the Human Development Index (2008-2030): a population-based study. Lancet Oncol 2012;13:790-801.
2. Smith BD, Smith GL, Hurria A, Hortobagyi GN, Buchholz TA. Future of cancer incidence in the United States: burdens upon an aging, changing nation. J Clin Oncol 2009;27:2758-65.
3. Moller B, Fekjaer H, Hakulinen T, et al. Prediction of cancer incidence in the Nordic countries up to the year 2020. Eur J Cancer Prev 2002;11 Suppl 1:S1-96.
4. Rahib L, Smith BD, Aizenberg R, Rosenzweig AB, Fleshman JM, Matrisian LM. Projecting cancer incidence and deaths to 2030: the unexpected burden of thyroid, liver, and pancreas cancers in the United States. Cancer Res 2014;74:2913-21.
5. Maddams J, Utley M, Moller H. Projections of cancer prevalence in the United Kingdom, 2010-2040. Br J Cancer 2012;107:1195-202.
6. Mariotto AB, Yabroff KR, Shao Y, Feuer EJ, Brown ML. Projections of the cost of cancer care in the United States: 2010-2020. J Natl Cancer Inst 2011;103:117-28.
7. Society CC. Canadian Cancer Statistics 2015. Canadian Cancer Society's Advisory Committee on Cancer Statistics 2015.
8. Evans WK, Wolfson MC, Flanagan WM, et al. Canadian Cancer Risk Management Model: evaluation of cancer control. Int J Technol Assess Health Care 2013;29:131-9.
9. Society CC. Canadian Cancer Statistics 2011. Canadian Cancer Society's Advisory Committee on Cancer Statistics 2011.

10. Jessup JM, Gallick GE. The biology of colorectal carcinoma. Curr Probl Cancer 1992;16:261-328.
11. Lengauer C, Kinzler KW, Vogelstein B. Genetic instability in colorectal cancers. Nature 1997;386:623-7.
12. Rajagopalan H, Nowak MA, Vogelstein B, Lengauer C. The significance of unstable chromosomes in colorectal cancer. Nat Rev Cancer 2003;3:695-701.
13. Schroeder TM. Genetically determined chromosome instability syndromes. Cytogenet Cell Genet 1982;33:119-32.
14. Huang CC, Banerjee A, Hou Y. Chromosomal instability in cell lines derived from patients with xeroderma pigmentosum. Proc Soc Exp Biol Med 1975;148:1244-8.
15. Chrzanowska KH, Gregorek H, Dembowska-Baginska B, Kalina MA, Digweed M. Nijmegen breakage syndrome (NBS). Orphanet J Rare Dis 2012;7:13.
16. Lengauer C, Kinzler KW, Vogelstein B. Genetic instabilities in human cancers. Nature 1998;396:643-9.
17. Issa JP. CpG island methylator phenotype in cancer. Nat Rev Cancer 2004;4:988-93.
18. Boyer JC, Umar A, Risinger JI, et al. Microsatellite instability, mismatch repair deficiency, and genetic defects in human cancer cell lines. Cancer Res 1995;55:6063-70.
19. Gatalica Z, Vranic S, Xiu J, Swensen J, Reddy S. High microsatellite instability (MSI-H) colorectal carcinoma: a brief review of predictive biomarkers in the era of personalized medicine. Fam Cancer 2016.
20. Geigl JB, Obenauf AC, Schwarzbraun T, Speicher MR. Defining 'chromosomal instability'. Trends Genet 2008;24:64-9.

21. Beheshti B, Park PC, Sweet JM, Trachtenberg J, Jewett MA, Squire JA. Evidence of chromosomal instability in prostate cancer determined by spectral karyotyping (SKY) and interphase fish analysis. Neoplasia 2001;3:62-9.
22. Boveri T. Concerning the origin of malignant tumours by Theodor Boveri. Translated and annotated by Henry Harris. J Cell Sci 2008;121 Suppl 1:1-84.
23. Bakhoum SF, Compton DA. Chromosomal instability and cancer: a complex relationship with therapeutic potential. J Clin Invest 2012;122:1138-43.
24. Gordon DJ, Resio B, Pellman D. Causes and consequences of aneuploidy in cancer. Nat Rev Genet 2012;13:189-203.
25. Thomas HJ. Genetic instability in colorectal cancer. Gut 1998;43:450-1.
26. Russo A, Pacchierotti F, Cimini D, et al. Genomic instability: Crossing pathways at the origin of structural and numerical chromosome changes. Environ Mol Mutagen 2015;56:563-80.
27. Gadji M, Adebayo Awe J, Rodrigues P, et al. Profiling three-dimensional nuclear telomeric architecture of myelodysplastic syndromes and acute myeloid leukemia defines patient subgroups. Clinical cancer research : an official journal of the American Association for Cancer Research 2012;18:3293-304.
28. Gadji M, Vallente R, Klewes L, et al. Nuclear remodeling as a mechanism for genomic instability in cancer. Adv Cancer Res 2011;112:77-126.
29. Gadji M, Fortin D, Tsanaclis AM, et al. Three-dimensional nuclear telomere architecture is associated with differential time to progression and overall survival in glioblastoma patients. Neoplasia 2010;12:183-91.

30. Thompson SL, Compton DA. Chromosome missegregation in human cells arises through specific types of kinetochore-microtubule attachment errors. Proc Natl Acad Sci U S A 2011;108:17974-8.
31. Bastians H. Causes of Chromosomal Instability. Recent Results Cancer Res 2015;200:95-113.
32. Thompson SL, Compton DA. Examining the link between chromosomal instability and aneuploidy in human cells. J Cell Biol 2008;180:665-72.
33. Ghadimi BM, Sackett DL, Difilippantonio MJ, et al. Centrosome amplification and instability occurs exclusively in aneuploid, but not in diploid colorectal cancer cell lines, and correlates with numerical chromosomal aberrations. Genes Chromosomes Cancer 2000;27:183-90.
34. Ganem NJ, Godinho SA, Pellman D. A mechanism linking extra centrosomes to chromosomal instability. Nature 2009;460:278-82.
35. Silkworth WT, Nardi IK, Scholl LM, Cimini D. Multipolar spindle pole coalescence is a major source of kinetochore mis-attachment and chromosome mis-segregation in cancer cells. PLoS One 2009;4:e6564.
36. Remeseiro S, Cuadrado A, Carretero M, et al. Cohesin-SA1 deficiency drives aneuploidy and tumourigenesis in mice due to impaired replication of telomeres. EMBO J 2012;31:2076-89.
37. Remeseiro S, Cuadrado A, Losada A. Cohesin in development and disease. Development 2013;140:3715-8.

38. Barber TD, McManus K, Yuen KW, et al. Chromatid cohesion defects may underlie chromosome instability in human colorectal cancers. Proc Natl Acad Sci U S A 2008;105:3443-8.
39. Sajesh BV, Lichtensztejn Z, McManus KJ. Sister chromatid cohesion defects are associated with chromosome instability in Hodgkin lymphoma cells. BMC Cancer 2013;13:391.
40. Guardavaccaro D, Frescas D, Dorrello NV, et al. Control of chromosome stability by the beta-TrCP-REST-Mad2 axis. Nature 2008;452:365-9.
41. Vukovic B, Park PC, Al-Maghrabi J, et al. Evidence of multifocality of telomere erosion in high-grade prostatic intraepithelial neoplasia (HPIN) and concurrent carcinoma. Oncogene 2003;22:1978-87.
42. Meeker AK, Hicks JL, Gabrielson E, Strauss WM, De Marzo AM, Argani P. Telomere shortening occurs in subsets of normal breast epithelium as well as in situ and invasive carcinoma. Am J Pathol 2004;164:925-35.
43. Stewenius Y, Gorunova L, Jonson T, et al. Structural and numerical chromosome changes in colon cancer develop through telomere-mediated anaphase bridges, not through mitotic multipolarity. Proc Natl Acad Sci U S A 2005;102:5541-6.
44. Knecht H, Sawan B, Lichtensztejn D, Lemieux B, Wellinger RJ, Mai S. The 3D nuclear organization of telomeres marks the transition from Hodgkin to Reed-Sternberg cells. Leukemia 2009;23:565-73.
45. Knecht H, Sawan B, Lichtensztejn Z, Lichtensztejn D, Mai S. 3D Telomere FISH defines LMP1-expressing Reed-Sternberg cells as end-stage cells with telomere-poor 'ghost' nuclei and very short telomeres. Lab Invest 2010;90:611-9.

46. Louis SF, Vermolen BJ, Garini Y, et al. c-Myc induces chromosomal rearrangements through telomere and chromosome remodeling in the interphase nucleus. Proc Natl Acad Sci U S A 2005;102:9613-8.
47. Misri S, Pandita S, Kumar R, Pandita TK. Telomeres, histone code, and DNA damage response. Cytogenet Genome Res 2008;122:297-307.
48. Lansdorp PM. Telomeres and disease. EMBO J 2009;28:2532-40.
49. Santaguida S, Amon A. Short- and long-term effects of chromosome mis-segregation and aneuploidy. Nature reviews Molecular cell biology 2015;16:473-85.
50. Knouse KA, Wu J, Whittaker CA, Amon A. Single cell sequencing reveals low levels of aneuploidy across mammalian tissues. Proc Natl Acad Sci U S A 2014;111:13409-14.
51. McConnell MJ, Lindberg MR, Brennand KJ, et al. Mosaic copy number variation in human neurons. Science (New York, NY) 2013;342:632-7.
52. Cancer Genome Atlas Research N. Comprehensive genomic characterization of squamous cell lung cancers. Nature 2012;489:519-25.
53. Cancer Genome Atlas N. Comprehensive molecular characterization of human colon and rectal cancer. Nature 2012;487:330-7.
54. Cancer Genome Atlas N. Comprehensive molecular portraits of human breast tumours. Nature 2012;490:61-70.
55. Nicholson JM, Cimini D. Cancer karyotypes: survival of the fittest. Front Oncol 2013;3:148.
56. Cimini D. Merotelic kinetochore orientation, aneuploidy, and cancer. Biochim Biophys Acta 2008;1786:32-40.
57. Thompson SL, Bakhoum SF, Compton DA. Mechanisms of chromosomal instability. Curr Biol 2010;20:R285-95.

58. Bakhoum SF, Thompson SL, Manning AL, Compton DA. Genome stability is ensured by temporal control of kinetochore-microtubule dynamics. Nat Cell Biol 2009;11:27-35.
59. Zasadil LM, Andersen KA, Yeum D, et al. Cytotoxicity of paclitaxel in breast cancer is due to chromosome missegregation on multipolar spindles. Sci Transl Med 2014;6:229ra43.
60. Cimini D, Wan X, Hirel CB, Salmon ED. Aurora kinase promotes turnover of kinetochore microtubules to reduce chromosome segregation errors. Curr Biol 2006;16:1711-8.
61. Swanton C, Tomlinson I, Downward J. Chromosomal instability, colorectal cancer and taxane resistance. Cell Cycle 2006;5:818-23.
62. O'Sullivan CC, Moon DH, Kohn EC, Lee JM. Beyond Breast and Ovarian Cancers: PARP Inhibitors for BRCA Mutation-Associated and BRCA-Like Solid Tumors. Front Oncol 2014;4:42.
63. Luger K, Mader AW, Richmond RK, Sargent DF, Richmond TJ. Crystal structure of the nucleosome core particle at 2.8 A resolution. Nature 1997;389:251-60.
64. Cohen I, Poreba E, Kamieniarz K, Schneider R. Histone modifiers in cancer: friends or foes? Genes Cancer 2011;2:631-47.
65. Martin C, Zhang Y. Mechanisms of epigenetic inheritance. Curr Opin Cell Biol 2007;19:266-72.
66. Margueron R, Trojer P, Reinberg D. The key to development: interpreting the histone code? Curr Opin Genet Dev 2005;15:163-76.
67. Horn PJ, Carruthers LM, Logie C, et al. Phosphorylation of linker histones regulates ATP-dependent chromatin remodeling enzymes. Nat Struct Biol 2002;9:263-7.
68. Williamson WD, Pinto I. Histones and genome integrity. Front Biosci (Landmark Ed) 2012;17:984-95.

69. Ruthenburg AJ, Allis CD, Wysocka J. Methylation of lysine 4 on histone H3: intricacy of writing and reading a single epigenetic mark. Molecular cell 2007;25:15-30.
70. Hendzel MJ, Wei Y, Mancini MA, et al. Mitosis-specific phosphorylation of histone H3 initiates primarily within pericentromeric heterochromatin during G2 and spreads in an ordered fashion coincident with mitotic chromosome condensation. Chromosoma 1997;106:348-60.
71. McManus KJ, Hendzel MJ. The relationship between histone H3 phosphorylation and acetylation throughout the mammalian cell cycle. Biochem Cell Biol 2006;84:640-57.
72. Houston SI, McManus KJ, Adams MM, et al. Catalytic function of the PR-Set7 histone H4 lysine 20 monomethyltransferase is essential for mitotic entry and genomic stability. The Journal of biological chemistry 2008;283:19478-88.
73. Guppy BJ, McManus KJ. Mitotic accumulation of dimethylated lysine 79 of histone H3 is important for maintaining genome integrity during mitosis in human cells. Genetics 2015;199:423-33.
74. Khan SA, Reddy D, Gupta S. Global histone post-translational modifications and cancer: Biomarkers for diagnosis, prognosis and treatment? World J Biol Chem 2015;6:333-45.
75. Leroy G, Dimaggio PA, Chan EY, et al. A quantitative atlas of histone modification signatures from human cancer cells. Epigenetics Chromatin 2013;6:20.
76. Shema E, Tirosh I, Aylon Y, et al. The histone H2B-specific ubiquitin ligase RNF20/hBRE1 acts as a putative tumor suppressor through selective regulation of gene expression. Genes Dev 2008;22:2664-76.

77. Chernikova SB, Dorth JA, Razorenova OV, Game JC, Brown JM. Deficiency in Bre1 impairs homologous recombination repair and cell cycle checkpoint response to radiation damage in mammalian cells. Radiation research 2010;174:558-65.
78. Chernikova SB, Razorenova OV, Higgins JP, et al. Deficiency in mammalian histone H2B ubiquitin ligase Bre1 (Rnf20/Rnf40) leads to replication stress and chromosomal instability. Cancer Res 2012;72:2111-9.
79. Osley MA. Regulation of histone H2A and H2B ubiquitylation. Brief Funct Genomic Proteomic 2006;5:179-89.
80. Wang H, Wang L, Erdjument-Bromage H, et al. Role of histone H2A ubiquitination in Polycomb silencing. Nature 2004;431:873-8.
81. Gatti M, Pinato S, Maspero E, Soffientini P, Polo S, Penengo L. A novel ubiquitin mark at the N-terminal tail of histone H2As targeted by RNF168 ubiquitin ligase. Cell Cycle 2012;11:2538-44.
82. Wang H, Zhai L, Xu J, et al. Histone H3 and H4 ubiquitylation by the CUL4-DDB-ROC1 ubiquitin ligase facilitates cellular response to DNA damage. Molecular cell 2006;22:383-94.
83. Fierz B, Chatterjee C, McGinty RK, Bar-Dagan M, Raleigh DP, Muir TW. Histone H2B ubiquitylation disrupts local and higher-order chromatin compaction. Nat Chem Biol 2011;7:113-9.
84. Johnsen SA. The enigmatic role of H2Bub1 in cancer. FEBS Lett 2012;586:1592-601.
85. Kim J, Guermah M, McGinty RK, et al. RAD6-Mediated transcription-coupled H2B ubiquitylation directly stimulates H3K4 methylation in human cells. Cell 2009;137:459-71.

86. Hahn MA, Dickson KA, Jackson S, Clarkson A, Gill AJ, Marsh DJ. The tumor suppressor CDC73 interacts with the ring finger proteins RNF20 and RNF40 and is required for the maintenance of histone 2B monoubiquitination. Human molecular genetics 2012;21:559-68.
87. Peng L, Bian XW, Li DK, et al. Large-scale RNA-Seq Transcriptome Analysis of 4043 Cancers and 548 Normal Tissue Controls across 12 TCGA Cancer Types. Sci Rep 2015;5:13413.
88. Sowa ME, Bennett EJ, Gygi SP, Harper JW. Defining the human deubiquitinating enzyme interaction landscape. Cell 2009;138:389-403.
89. Nicassio F, Corrado N, Vissers JH, et al. Human USP3 is a chromatin modifier required for S phase progression and genome stability. Curr Biol 2007;17:1972-7.
90. Sarkari F, Sanchez-Alcaraz T, Wang S, Holowaty MN, Sheng Y, Frappier L. EBNA1-mediated recruitment of a histone H2B deubiquitylating complex to the Epstein-Barr virus latent origin of DNA replication. PLoS Pathog 2009;5:e1000624.
91. Zhao Y, Lang G, Ito S, et al. A TFTC/STAGA module mediates histone H2A and H2B deubiquitination, coactivates nuclear receptors, and counteracts heterochromatin silencing. Molecular cell 2008;29:92-101.
92. Zhang XY, Varthi M, Sykes SM, et al. The putative cancer stem cell marker USP22 is a subunit of the human SAGA complex required for activated transcription and cell-cycle progression. Molecular cell 2008;29:102-11.
93. Zhang Y, Yao L, Zhang X, et al. Elevated expression of USP22 in correlation with poor prognosis in patients with invasive breast cancer. J Cancer Res Clin Oncol 2011;137:1245-53.

94. Liu YL, Yang YM, Xu H, Dong XS. Increased expression of ubiquitin-specific protease 22 can promote cancer progression and predict therapy failure in human colorectal cancer. J Gastroenterol Hepatol 2010;25:1800-5.
95. Davie JR, Murphy LC. Inhibition of transcription selectively reduces the level of ubiquitinated histone H2B in chromatin. Biochem Biophys Res Commun 1994;203:344-50.
96. Davie JR, Murphy LC. Level of ubiquitinated histone H2B in chromatin is coupled to ongoing transcription. Biochemistry 1990;29:4752-7.
97. Li B, Carey M, Workman JL. The role of chromatin during transcription. Cell 2007;128:707-19.
98. Lyubartsev AP, Korolev N, Fan Y, Nordenskiold L. Multiscale modelling of nucleosome core particle aggregation. J Phys Condens Matter 2015;27:064111.
99. Fonseca GJ, Cohen MJ, Nichols AC, Barrett JW, Mymryk JS. Viral retasking of hBre1/RNF20 to recruit hPaf1 for transcriptional activation. PLoS Pathog 2013;9:e1003411.
100. Shiloh Y, Shema E, Moyal L, Oren M. RNF20-RNF40: A ubiquitin-driven link between gene expression and the DNA damage response. FEBS Lett 2011;585:2795-802.
101. Belotserkovskaya R, Oh S, Bondarenko VA, Orphanides G, Studitsky VM, Reinberg D. FACT facilitates transcription-dependent nucleosome alteration. Science (New York, NY) 2003;301:1090-3.
102. Pavri R, Zhu B, Li G, et al. Histone H2B monoubiquitination functions cooperatively with FACT to regulate elongation by RNA polymerase II. Cell 2006;125:703-17.
103. Zhang F, Yu X. WAC, a functional partner of RNF20/40, regulates histone H2B ubiquitination and gene transcription. Molecular cell 2011;41:384-97.

104. Shema E, Kim J, Roeder RG, Oren M. RNF20 inhibits TFIIS-facilitated transcriptional elongation to suppress pro-oncogenic gene expression. Molecular cell 2011;42:477-88.

105. Karpiuk O, Najafova Z, Kramer F, et al. The histone H2B monoubiquitination regulatory pathway is required for differentiation of multipotent stem cells. Molecular cell 2012;46:705-13.

106. Nakamura K, Kato A, Kobayashi J, et al. Regulation of homologous recombination by RNF20-dependent H2B ubiquitination. Molecular cell 2011;41:515-28.

107. Moyal L, Lerenthal Y, Gana-Weisz M, et al. Requirement of ATM-dependent monoubiquitylation of histone H2B for timely repair of DNA double-strand breaks. Molecular cell 2011;41:529-42.

108. Sun ZW, Allis CD. Ubiquitination of histone H2B regulates H3 methylation and gene silencing in yeast. Nature 2002;418:104-8.

109. Briggs SD, Xiao T, Sun ZW, et al. Gene silencing: trans-histone regulatory pathway in chromatin. Nature 2002;418:498.

110. Ng HH, Xu RM, Zhang Y, Struhl K. Ubiquitination of histone H2B by Rad6 is required for efficient Dot1-mediated methylation of histone H3 lysine 79. The Journal of biological chemistry 2002;277:34655-7.

111. Vlaming H, van Leeuwen F. The upstreams and downstreams of H3K79 methylation by DOT1L. Chromosoma 2016.

112. Nguyen AT, Zhang Y. The diverse functions of Dot1 and H3K79 methylation. Genes Dev 2011;25:1345-58.

113. Vlaming H, van Welsem T, de Graaf EL, et al. Flexibility in crosstalk between H2B ubiquitination and H3 methylation in vivo. EMBO Rep 2014;15:1077-84.

114. Rea S, Eisenhaber F, O'Carroll D, et al. Regulation of chromatin structure by site-specific histone H3 methyltransferases. Nature 2000;406:593-9.

115. Lachner M, O'Sullivan RJ, Jenuwein T. An epigenetic road map for histone lysine methylation. J Cell Sci 2003;116:2117-24.

116. He Y, Korboukh I, Jin J, Huang J. Targeting protein lysine methylation and demethylation in cancers. Acta Biochim Biophys Sin (Shanghai) 2012;44:70-9.

117. Steward MM, Lee JS, O'Donovan A, Wyatt M, Bernstein BE, Shilatifard A. Molecular regulation of H3K4 trimethylation by ASH2L, a shared subunit of MLL complexes. Nat Struct Mol Biol 2006;13:852-4.

118. Rosenfeld JA, Wang Z, Schones DE, Zhao K, DeSalle R, Zhang MQ. Determination of enriched histone modifications in non-genic portions of the human genome. BMC Genomics 2009;10:143.

119. Barski A, Cuddapah S, Cui K, et al. High-resolution profiling of histone methylations in the human genome. Cell 2007;129:823-37.

120. Binda O. On your histone mark, SET, methylate! Epigenetics 2013;8:457-63.

121. Koch CM, Andrews RM, Flicek P, et al. The landscape of histone modifications across 1% of the human genome in five human cell lines. Genome research 2007;17:691-707.

122. Morris SA, Rao B, Garcia BA, et al. Identification of histone H3 lysine 36 acetylation as a highly conserved histone modification. The Journal of biological chemistry 2007;282:7632-40.

123. Klose RJ, Zhang Y. Regulation of histone methylation by demethylimination and demethylation. Nature reviews Molecular cell biology 2007;8:307-18.

124. Min J, Feng Q, Li Z, Zhang Y, Xu RM. Structure of the catalytic domain of human DOT1L, a non-SET domain nucleosomal histone methyltransferase. Cell 2003;112:711-23.

125. Yang L, Lin C, Jin C, et al. lncRNA-dependent mechanisms of androgen-receptor-regulated gene activation programs. Nature 2013;500:598-602.

126. Cattaneo P, Kunderfranco P, Greco C, et al. DOT1L-mediated H3K79me2 modification critically regulates gene expression during cardiomyocyte differentiation. Cell death and differentiation 2014.

127. Barry ER, Krueger W, Jakuba CM, et al. ES cell cycle progression and differentiation require the action of the histone methyltransferase Dot1L. Stem Cells 2009;27:1538-47.

128. Greer EL, Shi Y. Histone methylation: a dynamic mark in health, disease and inheritance. Nat Rev Genet 2012;13:343-57.

129. Feng Y, Yang Y, Ortega MM, et al. Early mammalian erythropoiesis requires the Dot1L methyltransferase. Blood 2010;116:4483-91.

130. van Leeuwen F, Gafken PR, Gottschling DE. Dot1p modulates silencing in yeast by methylation of the nucleosome core. Cell 2002;109:745-56.

131. Janzen CJ, Hake SB, Lowell JE, Cross GA. Selective di- or trimethylation of histone H3 lysine 76 by two DOT1 homologs is important for cell cycle regulation in Trypanosoma brucei. Molecular cell 2006;23:497-507.

132. Shanower GA, Muller M, Blanton JL, Honti V, Gyurkovics H, Schedl P. Characterization of the grappa gene, the Drosophila histone H3 lysine 79 methyltransferase. Genetics 2005;169:173-84.

133. Feng Q, Wang H, Ng HH, et al. Methylation of H3-lysine 79 is mediated by a new family of HMTases without a SET domain. Curr Biol 2002;12:1052-8.

134. Jones B, Su H, Bhat A, et al. The histone H3K79 methyltransferase Dot1L is essential for mammalian development and heterochromatin structure. PLoS Genet 2008;4:e1000190.

135. Steger DJ, Lefterova MI, Ying L, et al. DOT1L/KMT4 recruitment and H3K79 methylation are ubiquitously coupled with gene transcription in mammalian cells. Molecular and cellular biology 2008;28:2825-39.

136. Suzuki H, Takatsuka S, Akashi H, et al. Genome-wide profiling of chromatin signatures reveals epigenetic regulation of MicroRNA genes in colorectal cancer. Cancer Res 2011;71:5646-58.

137. Fu H, Maunakea AK, Martin MM, et al. Methylation of histone H3 on lysine 79 associates with a group of replication origins and helps limit DNA replication once per cell cycle. PLoS Genet 2013;9:e1003542.

138. Huff JT, Plocik AM, Guthrie C, Yamamoto KR. Reciprocal intronic and exonic histone modification regions in humans. Nat Struct Mol Biol 2010;17:1495-9.

139. Bernt KM, Armstrong SA. A role for DOT1L in MLL-rearranged leukemias. Epigenomics 2011;3:667-70.

140. Ooga M, Inoue A, Kageyama S, Akiyama T, Nagata M, Aoki F. Changes in H3K79 methylation during preimplantation development in mice. Biol Reprod 2008;78:413-24.

141. Sjoblom T, Jones S, Wood LD, et al. The consensus coding sequences of human breast and colorectal cancers. Science (New York, NY) 2006;314:268-74.

142. Norris A, Boeke JD. Silent information regulator 3: the Goldilocks of the silencing complex. Genes Dev 2010;24:115-22.

143. Sugioka-Sugiyama R, Sugiyama T. Sde2: a novel nuclear protein essential for telomeric silencing and genomic stability in Schizosaccharomyces pombe. Biochem Biophys Res Commun 2011;406:444-8.

144. Huyen Y, Zgheib O, Ditullio RA, Jr., et al. Methylated lysine 79 of histone H3 targets 53BP1 to DNA double-strand breaks. Nature 2004;432:406-11.

145. Wysocki R, Javaheri A, Allard S, Sha F, Cote J, Kron SJ. Role of Dot1-dependent histone H3 methylation in G1 and S phase DNA damage checkpoint functions of Rad9. Molecular and cellular biology 2005;25:8430-43.

146. Pavey S, Spoerri L, Haass NK, Gabrielli B. DNA repair and cell cycle checkpoint defects as drivers and therapeutic targets in melanoma. Pigment Cell Melanoma Res 2013;26:805-16.

147. Hanahan D, Weinberg RA. Hallmarks of cancer: the next generation. Cell 2011;144:646-74.

148. Ishino Y, Shinagawa H, Makino K, Amemura M, Nakata A. Nucleotide sequence of the iap gene, responsible for alkaline phosphatase isozyme conversion in Escherichia coli, and identification of the gene product. J Bacteriol 1987;169:5429-33.

149. Mojica FJ, Diez-Villasenor C, Soria E, Juez G. Biological significance of a family of regularly spaced repeats in the genomes of Archaea, Bacteria and mitochondria. Mol Microbiol 2000;36:244-6.

150. Mojica FJ, Diez-Villasenor C, Garcia-Martinez J, Soria E. Intervening sequences of regularly spaced prokaryotic repeats derive from foreign genetic elements. J Mol Evol 2005;60:174-82.

151. Barrangou R, Fremaux C, Deveau H, et al. CRISPR provides acquired resistance against viruses in prokaryotes. Science (New York, NY) 2007;315:1709-12.

152. Garneau JE, Dupuis ME, Villion M, et al. The CRISPR/Cas bacterial immune system cleaves bacteriophage and plasmid DNA. Nature 2010;468:67-71.

153. Deltcheva E, Chylinski K, Sharma CM, et al. CRISPR RNA maturation by trans-encoded small RNA and host factor RNase III. Nature 2011;471:602-7.

154. Cong L, Ran FA, Cox D, et al. Multiplex genome engineering using CRISPR/Cas systems. Science (New York, NY) 2013;339:819-23.

155. Mali P, Yang L, Esvelt KM, et al. RNA-guided human genome engineering via Cas9. Science (New York, NY) 2013;339:823-6.

156. Jinek M, Chylinski K, Fonfara I, Hauer M, Doudna JA, Charpentier E. A programmable dual-RNA-guided DNA endonuclease in adaptive bacterial immunity. Science (New York, NY) 2012;337:816-21.

157. Dobzhansky T. Genetics of natural populations; recombination and variability in populations of Drosophila pseudoobscura. Genetics 1946;31:269-90.

158. Kaelin WG, Jr. The concept of synthetic lethality in the context of anticancer therapy. Nat Rev Cancer 2005;5:689-98.

159. McManus KJ, Barrett IJ, Nouhi Y, Hieter P. Specific synthetic lethal killing of RAD54B-deficient human colorectal cancer cells by FEN1 silencing. Proc Natl Acad Sci U S A 2009;106:3276-81.

160. van Pel DM, Barrett IJ, Shimizu Y, et al. An evolutionarily conserved synthetic lethal interaction network identifies FEN1 as a broad-spectrum target for anticancer therapeutic development. PLoS Genet 2013;9:e1003254.

161. Hartwell LH, Szankasi P, Roberts CJ, Murray AW, Friend SH. Integrating genetic approaches into the discovery of anticancer drugs. Science (New York, NY) 1997;278:1064-8.

162. Kaelin WG, Jr. Choosing anticancer drug targets in the postgenomic era. J Clin Invest 1999;104:1503-6.

163. Cahill DP, Kinzler KW, Vogelstein B, Lengauer C. Genetic instability and darwinian selection in tumours. Trends Cell Biol 1999;9:M57-60.

164. Choi CM, Seo KW, Jang SJ, et al. Chromosomal instability is a risk factor for poor prognosis of adenocarcinoma of the lung: Fluorescence in situ hybridization analysis of paraffin-embedded tissue from Korean patients. Lung Cancer 2009;64:66-70.

165. Heilig CE, Loffler H, Mahlknecht U, et al. Chromosomal instability correlates with poor outcome in patients with myelodysplastic syndromes irrespectively of the cytogenetic risk group. J Cell Mol Med 2010;14:895-902.

166. Nakamura H, Saji H, Idiris A, et al. Chromosomal instability detected by fluorescence in situ hybridization in surgical specimens of non-small cell lung cancer is associated with poor survival. Clinical cancer research : an official journal of the American Association for Cancer Research 2003;9:2294-9.

167. Kinzler KW, Vogelstein B. Cancer-susceptibility genes. Gatekeepers and caretakers. Nature 1997;386:761, 3.

168. Farnebo M, Bykov VJ, Wiman KG. The p53 tumor suppressor: a master regulator of diverse cellular processes and therapeutic target in cancer. Biochem Biophys Res Commun 2010;396:85-9.

169. Chinnam M, Goodrich DW. RB1, development, and cancer. Curr Top Dev Biol 2011;94:129-69.

170. Baselga J, Swain SM. Novel anticancer targets: revisiting ERBB2 and discovering ERBB3. Nat Rev Cancer 2009;9:463-75.

171. Cancer Genome Atlas Research N. Integrated genomic analyses of ovarian carcinoma. Nature 2011;474:609-15.

172. Taylor BS, Schultz N, Hieronymus H, et al. Integrative genomic profiling of human prostate cancer. Cancer Cell 2010;18:11-22.

173. Roy R, Chun J, Powell SN. BRCA1 and BRCA2: different roles in a common pathway of genome protection. Nat Rev Cancer 2012;12:68-78.

174. Okano S, Lan L, Caldecott KW, Mori T, Yasui A. Spatial and temporal cellular responses to single-strand breaks in human cells. Molecular and cellular biology 2003;23:3974-81.

175. de Murcia G, Schreiber V, Molinete M, et al. Structure and function of poly(ADP-ribose) polymerase. Mol Cell Biochem 1994;138:15-24.

176. de Murcia G, Menissier de Murcia J. Poly(ADP-ribose) polymerase: a molecular nick-sensor. Trends Biochem Sci 1994;19:172-6.

177. Brody LC. Treating cancer by targeting a weakness. N Engl J Med 2005;353:949-50.

178. Kuzminov A. Single-strand interruptions in replicating chromosomes cause double-strand breaks. Proc Natl Acad Sci U S A 2001;98:8241-6.

179. Bryant HE, Schultz N, Thomas HD, et al. Specific killing of BRCA2-deficient tumours with inhibitors of poly(ADP-ribose) polymerase. Nature 2005;434:913-7.

180. Farmer H, McCabe N, Lord CJ, et al. Targeting the DNA repair defect in BRCA mutant cells as a therapeutic strategy. Nature 2005;434:917-21.

181. Rouleau M, Patel A, Hendzel MJ, Kaufmann SH, Poirier GG. PARP inhibition: PARP1 and beyond. Nat Rev Cancer 2010;10:293-301.

182. Papeo G, Casale E, Montagnoli A, Cirla A. PARP inhibitors in cancer therapy: an update. Expert Opin Ther Pat 2013;23:503-14.

183. Fong PC, Boss DS, Yap TA, et al. Inhibition of poly(ADP-ribose) polymerase in tumors from BRCA mutation carriers. N Engl J Med 2009;361:123-34.

184. Orlando L, Schiavone P, Fedele P, et al. Poly (ADP-ribose) polymerase (PARP): rationale, preclinical and clinical evidences of its inhibition as breast cancer treatment. Expert Opin Ther Targets 2012;16 Suppl 2:S83-9.

185. Sajesh BV, Bailey M, Lichtensztejn Z, Hieter P, McManus KJ. Synthetic lethal targeting of superoxide dismutase 1 selectively kills RAD54B-deficient colorectal cancer cells. Genetics 2013;195:757-67.

186. Michor F, Iwasa Y, Lengauer C, Nowak MA. Dynamics of colorectal cancer. Seminars in cancer biology 2005;15:484-93.

187. Lee AJ, Endesfelder D, Rowan AJ, et al. Chromosomal instability confers intrinsic multidrug resistance. Cancer Res 2011;71:1858-70.

188. Walther A, Houlston R, Tomlinson I. Association between chromosomal instability and prognosis in colorectal cancer: a meta-analysis. Gut 2008;57:941-50.

189. Taylor JH. Nucleic acid synthesis in relation to the cell division cycle. Annals of the New York Academy of Sciences 1960;90:409-21.

190. Goto H, Yasui Y, Nigg EA, Inagaki M. Aurora-B phosphorylates Histone H3 at serine28 with regard to the mitotic chromosome condensation. Genes to cells : devoted to molecular & cellular mechanisms 2002;7:11-7.

191. McManus KJ, Biron VL, Heit R, Underhill DA, Hendzel MJ. Dynamic changes in histone H3 lysine 9 methylations: identification of a mitosis-specific function for dynamic methylation in chromosome congression and segregation. The Journal of biological chemistry 2006;281:8888-97.

192. Peters AH, O'Carroll D, Scherthan H, et al. Loss of the Suv39h histone methyltransferases impairs mammalian heterochromatin and genome stability. Cell 2001;107:323-37.

193. Wei Y, Yu L, Bowen J, Gorovsky MA, Allis CD. Phosphorylation of histone H3 is required for proper chromosome condensation and segregation. Cell 1999;97:99-109.

194. Heit R, Rattner JB, Chan GK, Hendzel MJ. G2 histone methylation is required for the proper segregation of chromosomes. J Cell Sci 2009;122:2957-68.

195. Forbes SA, Bindal N, Bamford S, et al. COSMIC: mining complete cancer genomes in the Catalogue of Somatic Mutations in Cancer. Nucleic acids research 2011;39:D945-50.

196. Thompson LL, Guppy BJ, Sawchuk L, Davie JR, McManus KJ. Regulation of chromatin structure via histone post-translational modification and the link to carcinogenesis. Cancer Metastasis Rev 2013;32:363-76.

197. Dover J, Schneider J, Tawiah-Boateng MA, et al. Methylation of histone H3 by COMPASS requires ubiquitination of histone H2B by Rad6. The Journal of biological chemistry 2002;277:28368-71.

198. McManus KJ, Hendzel MJ. Using quantitative imaging microscopy to define the target substrate specificities of histone post-translational-modifying enzymes. Methods 2005;36:351-61.

199. Yu W, Chory EJ, Wernimont AK, et al. Catalytic site remodelling of the DOT1L methyltransferase by selective inhibitors. Nat Commun 2012;3:1288.

200. Wu RS, Kohn KW, Bonner WM. Metabolism of ubiquitinated histones. The Journal of biological chemistry 1981;256:5916-20.

201. Egli D, Birkhoff G, Eggan K. Mediators of reprogramming: transcription factors and transitions through mitosis. Nature reviews Molecular cell biology 2008;9:505-16.

202. Ahmad K, Henikoff S. The histone variant H3.3 marks active chromatin by replication-independent nucleosome assembly. Molecular cell 2002;9:1191-200.

203. Janicki SM, Tsukamoto T, Salghetti SE, et al. From silencing to gene expression: real-time analysis in single cells. Cell 2004;116:683-98.

204. Bui HT, Yamaoka E, Miyano T. Involvement of histone H3 (Ser10) phosphorylation in chromosome condensation without Cdc2 kinase and mitogen-activated protein kinase activation in pig oocytes. Biology of reproduction 2004;70:1843-51.

205. Chandrasekharan MB, Huang F, Sun ZW. Histone H2B ubiquitination and beyond: Regulation of nucleosome stability, chromatin dynamics and the trans-histone H3 methylation. Epigenetics 2010;5:460-8.

206. Byvoet P, Shepherd GR, Hardin JM, Noland BJ. The distribution and turnover of labeled methyl groups in histone fractions of cultured mammalian cells. Archives of biochemistry and biophysics 1972;148:558-67.

207. Duerre JA, Lee CT. In vivo methylation and turnover of rat brain histones. Journal of neurochemistry 1974;23:541-7.

208. Kim W, Kim R, Park G, Park JW, Kim JE. Deficiency of H3K79 histone methyltransferase Dot1-like protein (DOT1L) inhibits cell proliferation. The Journal of biological chemistry 2012;287:5588-99.

209. Schulze JM, Jackson J, Nakanishi S, et al. Linking cell cycle to histone modifications: SBF and H2B monoubiquitination machinery and cell-cycle regulation of H3K79 dimethylation. Molecular cell 2009;35:626-41.

210. Cerami E, Gao J, Dogrusoz U, et al. The cBio cancer genomics portal: an open platform for exploring multidimensional cancer genomics data. Cancer discovery 2012;2:401-4.

211. Chernikova SB, Brown JM. R-loops and genomic instability in Bre1 (RNF20/40)-deficient cells. Cell Cycle 2012;11:2980-4.

212. Futreal PA, Coin L, Marshall M, et al. A census of human cancer genes. Nat Rev Cancer 2004;4:177-83.

213. Varambally S, Yu J, Laxman B, et al. Integrative genomic and proteomic analysis of prostate cancer reveals signatures of metastatic progression. Cancer Cell 2005;8:393-406.

214. Jallepalli PV, Waizenegger IC, Bunz F, et al. Securin is required for chromosomal stability in human cells. Cell 2001;105:445-57.

215. Rajagopalan H, Jallepalli PV, Rago C, et al. Inactivation of hCDC4 can cause chromosomal instability. Nature 2004;428:77-81.

216. Guppy BJ, McManus KJ. Mitotic Accumulation of Di-methylated Lysine 79 of Histone H3 Is Important for Maintaining Genome Integrity During Mitosis in Human Cells. Genetics 2014.

217. Xin HB, Deng KY, Shui B, et al. Gene trap and gene inversion methods for conditional gene inactivation in the mouse. Nucleic acids research 2005;33:e14.

218. Ran FA, Hsu PD, Wright J, Agarwala V, Scott DA, Zhang F. Genome engineering using the CRISPR-Cas9 system. Nat Protoc 2013;8:2281-308.

219. Sanchez-Rivera FJ, Jacks T. Applications of the CRISPR-Cas9 system in cancer biology. Nat Rev Cancer 2015;15:387-95.

220. Maurisse R, De Semir D, Emamekhoo H, et al. Comparative transfection of DNA into primary and transformed mammalian cells from different lineages. BMC Biotechnol 2010;10:9.

221. Volcke C, Pirotton S, Grandfils C, et al. Influence of DNA condensation state on transfection efficiency in DNA/polymer complexes: an AFM and DLS comparative study. J Biotechnol 2006;125:11-21.

222. Dim N, Perepelyuk M, Gomes O, et al. Novel targeted siRNA-loaded hybrid nanoparticles: preparation, characterization and in vitro evaluation. J Nanobiotechnology 2015;13:61.

223. Yamano S, Dai J, Moursi AM. Comparison of transfection efficiency of nonviral gene transfer reagents. Mol Biotechnol 2010;46:287-300.

224. Campisi J, d'Adda di Fagagna F. Cellular senescence: when bad things happen to good cells. Nature reviews Molecular cell biology 2007;8:729-40.

225. Sanjana NE, Shalem O, Zhang F. Improved vectors and genome-wide libraries for CRISPR screening. Nat Methods 2014;11:783-4.

226. Price ER, Zydowsky LD, Jin MJ, Baker CH, McKeon FD, Walsh CT. Human cyclophilin B: a second cyclophilin gene encodes a peptidyl-prolyl isomerase with a signal sequence. Proc Natl Acad Sci U S A 1991;88:1903-7.

227. Hsu PD, Scott DA, Weinstein JA, et al. DNA targeting specificity of RNA-guided Cas9 nucleases. Nat Biotech 2013;31:827-32.

228. Ranzani M, Cesana D, Bartholomae CC, et al. Lentiviral vector-based insertional mutagenesis identifies genes associated with liver cancer. Nat Methods 2013;10:155-61.

229. Wong N, Liu W, Wang X. WU-CRISPR: characteristics of functional guide RNAs for the CRISPR/Cas9 system. Genome Biol 2015;16:218.

230. Mao Y, Zhang H, Xu N, Zhang B, Gou F, Zhu JK. Application of the CRISPR-Cas system for efficient genome engineering in plants. Mol Plant 2013;6:2008-11.

231. Vogelstein B, Papadopoulos N, Velculescu VE, Zhou S, Diaz LA, Jr., Kinzler KW. Cancer genome landscapes. Science (New York, NY) 2013;339:1546-58.

232. Thompson LL, McManus KJ. A novel multiplexed, image-based approach to detect phenotypes that underlie chromosome instability in human cells. PLoS One 2015;10:e0123200.

233. Cassidy LD, Liau SS, Venkitaraman AR. Chromosome instability and carcinogenesis: insights from murine models of human pancreatic cancer associated with BRCA2 inactivation. Mol Oncol 2014;8:161-8.

234. Peng G, Lin SY. Exploiting the homologous recombination DNA repair network for targeted cancer therapy. World J Clin Oncol 2011;2:73-9.

235. Sajesh BV, Guppy BJ, McManus KJ. Synthetic genetic targeting of genome instability in cancer. Cancers (Basel) 2013;5:739-61.

236. Hartwell LH. Integrating Genetic Approaches into the Discovery of Anticancer Drugs. Science (New York, NY) 1997;278:1064-8.

237. Audeh MW, Carmichael J, Penson RT, et al. Oral poly(ADP-ribose) polymerase inhibitor olaparib in patients with BRCA1 or BRCA2 mutations and recurrent ovarian cancer: a proof-of-concept trial. Lancet 2010;376:245-51.

238. Evers B, Drost R, Schut E, et al. Selective inhibition of BRCA2-deficient mammary tumor cell growth by AZD2281 and cisplatin. Clinical cancer research : an official journal of the American Association for Cancer Research 2008;14:3916-25.

239. Ohta T, Sato K, Wu W. The BRCA1 ubiquitin ligase and homologous recombination repair. FEBS Lett 2011;585:2836-44.

240. Michels J, Vitale I, Saparbaev M, Castedo M, Kroemer G. Predictive biomarkers for cancer therapy with PARP inhibitors. Oncogene 2013.

241. Chernikova SB, Game JC, Brown JM. Inhibiting homologous recombination for cancer therapy. Cancer biology & therapy 2012;13:61-8.

242. De Lorenzo SB, Patel AG, Hurley RM, Kaufmann SH. The Elephant and the Blind Men: Making Sense of PARP Inhibitors in Homologous Recombination Deficient Tumor Cells. Front Oncol 2013;3:228.

243. Gao J, Aksoy BA, Dogrusoz U, et al. Integrative analysis of complex cancer genomics and clinical profiles using the cBioPortal. Sci Signal 2013;6:pl1.

244. Minsky N, Shema E, Field Y, Schuster M, Segal E, Oren M. Monoubiquitinated H2B is associated with the transcribed region of highly expressed genes in human cells. Nat Cell Biol 2008;10:483-8.

245. Hopkins TA, Shi Y, Rodriguez LE, et al. Mechanistic Dissection of PARP1 Trapping and the Impact on in vivo Tolerability and Efficacy of PARP Inhibitors. Mol Cancer Res 2015.

246. Murai J, Huang SY, Das BB, et al. Trapping of PARP1 and PARP2 by Clinical PARP Inhibitors. Cancer Res 2012;72:5588-99.

247. Murai J, Zhang Y, Morris J, et al. Rationale for poly(ADP-ribose) polymerase (PARP) inhibitors in combination therapy with camptothecins or temozolomide based on PARP trapping versus catalytic inhibition. J Pharmacol Exp Ther 2014;349:408-16.

248. Fong PC, Yap TA, Boss DS, et al. Poly(ADP)-ribose polymerase inhibition: frequent durable responses in BRCA carrier ovarian cancer correlating with platinum-free interval. J Clin Oncol 2010;28:2512-9.

249. Murai J, Huang SY, Renaud A, et al. Stereospecific PARP trapping by BMN 673 and comparison with olaparib and rucaparib. Mol Cancer Ther 2014;13:433-43.

250. Sajesh BV, McManus KJ. Targeting SOD1 induces synthetic lethal killing in BLM- and CHEK2-deficient colorectal cancer cells. Oncotarget 2015;6:27907-22.

251. Shen Y, Rehman FL, Feng Y, et al. BMN 673, a novel and highly potent PARP1/2 inhibitor for the treatment of human cancers with DNA repair deficiency. Clinical cancer research : an official journal of the American Association for Cancer Research 2013;19:5003-15.

252. Tasselli L, Xi Y, Zheng W, et al. SIRT6 deacetylates H3K18ac at pericentric chromatin to prevent mitotic errors and cellular senescence. Nat Struct Mol Biol 2016.

253. Nurse NP, Jimenez-Useche I, Smith IT, Yuan C. Clipping of flexible tails of histones H3 and H4 affects the structure and dynamics of the nucleosome. Biophys J 2013;104:1081-8.

254. Zhang Y, Kwon S, Yamaguchi T, et al. Mice lacking histone deacetylase 6 have hyperacetylated tubulin but are viable and develop normally. Molecular and cellular biology 2008;28:1688-701.

255. Hait NC, Wise LE, Allegood JC, et al. Active, phosphorylated fingolimod inhibits histone deacetylases and facilitates fear extinction memory. Nat Neurosci 2014;17:971-80.

256. Wang Y, Wysocka J, Sayegh J, et al. Human PAD4 regulates histone arginine methylation levels via demethylimination. Science (New York, NY) 2004;306:279-83.

257. Turner NC, Lord CJ, Iorns E, et al. A synthetic lethal siRNA screen identifying genes mediating sensitivity to a PARP inhibitor. EMBO J 2008;27:1368-77.

258. Loveday C, Turnbull C, Ramsay E, et al. Germline mutations in RAD51D confer susceptibility to ovarian cancer. Nat Genet 2011;43:879-82.

259. Mendes-Pereira AM, Martin SA, Brough R, et al. Synthetic lethal targeting of PTEN mutant cells with PARP inhibitors. EMBO Mol Med 2009;1:315-22.

260. Lord CJ, McDonald S, Swift S, Turner NC, Ashworth A. A high-throughput RNA interference screen for DNA repair determinants of PARP inhibitor sensitivity. DNA Repair (Amst) 2008;7:2010-9.

261. Murai J, Yang K, Dejsuphong D, Hirota K, Takeda S, D'Andrea AD. The USP1/UAF1 complex promotes double-strand break repair through homologous recombination. Molecular and cellular biology 2011;31:2462-9.

262. Min A, Im SA, Yoon YK, et al. RAD51C-deficient cancer cells are highly sensitive to the PARP inhibitor olaparib. Mol Cancer Ther 2013;12:865-77.

263. Bajrami I, Frankum JR, Konde A, et al. Genome-wide profiling of genetic synthetic lethality identifies CDK12 as a novel determinant of PARP1/2 inhibitor sensitivity. Cancer Res 2014;74:287-97.

264. Matsuoka S, Ballif BA, Smogorzewska A, et al. ATM and ATR substrate analysis reveals extensive protein networks responsive to DNA damage. Science (New York, NY) 2007;316:1160-6.

265. Mu JJ, Wang Y, Luo H, et al. A proteomic analysis of ataxia telangiectasia-mutated (ATM)/ATM-Rad3-related (ATR) substrates identifies the ubiquitin-proteasome system as a regulator for DNA damage checkpoints. The Journal of biological chemistry 2007;282:17330-4.

266. Hodge CD, Ismail IH, Edwards RA, et al. RNF8 E3 Ubiquitin Ligase Stimulates Ubc13 E2 Conjugating Activity that is Essential for DNA Double-Strand Break Signaling and BRCA1 Tumor Suppressor Recruitment. The Journal of biological chemistry 2016.

267. Nakada S. Opposing roles of RNF8/RNF168 and deubiquitinating enzymes in ubiquitination-dependent DNA double-strand break response signaling and DNA-repair pathway choice. J Radiat Res 2016.

268. Botuyan MV, Lee J, Ward IM, et al. Structural basis for the methylation state-specific recognition of histone H4-K20 by 53BP1 and Crb2 in DNA repair. Cell 2006;127:1361-73.

269. Katz SS, Gimble FS, Storici F. To nick or not to nick: comparison of I-SceI single- and double-strand break-induced recombination in yeast and human cells. PLoS One 2014;9:e88840.

270. Plessis D, Sale JE. Monitoring I-SceI-induced double-strand break repair in DT40 cells. Methods in molecular biology (Clifton, NJ) 2012;920:371-7.

271. Hironaka S, Sugimoto N, Yamaguchi K, et al. S-1 plus leucovorin versus S-1 plus leucovorin and oxaliplatin versus S-1 plus cisplatin in patients with advanced gastric cancer: a randomised, multicentre, open-label, phase 2 trial. Lancet Oncol 2016;17:99-108.

272. Shanmugasundaram S, Bharathithasan R, Elangovan S. 5-fluorouracil-Induced cardiotoxicity. Indian Heart J 2002;54:86-7.

273. Chatterjee K, Zhang J, Honbo N, Karliner JS. Doxorubicin cardiomyopathy. Cardiology 2010;115:155-62.

274. Cassidy J, Misset JL. Oxaliplatin-related side effects: characteristics and management. Semin Oncol 2002;29:11-20.

275. Ng AK, Kenney LB, Gilbert ES, Travis LB. Secondary malignancies across the age spectrum. Semin Radiat Oncol 2010;20:67-78.

276. Boone C, Bussey H, Andrews BJ. Exploring genetic interactions and networks with yeast. Nat Rev Genet 2007;8:437-49.

277. Baugh LR, Wen JC, Hill AA, Slonim DK, Brown EL, Hunter CP. Synthetic lethal analysis of Caenorhabditis elegans posterior embryonic patterning genes identifies conserved genetic interactions. Genome Biol 2005;6:R45.

278. Miyagawa K, Tsuruga T, Kinomura A, et al. A role for RAD54B in homologous recombination in human cells. EMBO J 2002;21:175-80.

279. Hiramoto T, Nakanishi T, Sumiyoshi T, et al. Mutations of a novel human RAD54 homologue, RAD54B, in primary cancer. Oncogene 1999;18:3422-6.

280. Wang T, Wei JJ, Sabatini DM, Lander ES. Genetic screens in human cells using the CRISPR-Cas9 system. Science (New York, NY) 2014;343:80-4.

281. Wang T, Lander ES, Sabatini DM. Large-Scale Single Guide RNA Library Construction and Use for CRISPR-Cas9-Based Genetic Screens. Cold Spring Harb Protoc 2016;2016:pdb top086892.

282. Glaab WE, Risinger JI, Umar A, Barrett JC, Kunkel TA, Tindall KR. Resistance to 6-thioguanine in mismatch repair-deficient human cancer cell lines correlates with an increase in induced mutations at the HPRT locus. Carcinogenesis 1998;19:1931-7.

Appendix A
Solutions and Recipes

Tris HCl (1M)

Name	Amount
Tris-HCl	15.8 g
Milli-Q water	up to 100 mL total volume
Total Volume	100 mL
-titrate to pH 8.0 or 8.4 with 4 M NaOH	

NaOH (4 M)

Name	Amount
NaOH	40 g
Milli-Q water	up to 100 mL total volume
Total Volume	100 mL

75 mM KCl Hypotonic Solution

Name	Amount
KCl	558.8 mg
Milli-Q water	up to 100 mL total volume
Total Volume	100 mL

$MgCl_2$ (1 M)

Name	Amount
$MgCl_2$	20.3 g
Milli-Q water	up to 100 mL total volume
Total Volume	100 mL

Ethylenediaminetetraacetic acid (EDTA) (0.5 M) pH 8.0

Name	Amount
EDTA	186.2 g
NaOH	20.0 g
Milli-Q water	up to 1.0 L total volume
Total Volume	1.0 L
-titrate to pH 8.0 with 10N NaOH	

70% Ethanol

Name	Amount
95% Ethanol	737.0 mL
Milli-Q water	up to 1.0 L total volume
Total Volume	1.0 L

10× Phosphate Buffered Saline (PBS)

Name	Amount
NaCl	80.0 g
KCl	2.0 g
Na_2PO_4	14.4 g
KH_2PO_4	2.4 g
Milli-Q water	800 mL
Total Volume	1.0 L
-titrate to pH 7.4 with 12.1N HCL	

1× Cell Culture PBS

Name	Amount
10× PBS	100.0 mL
Milli-Q water	up to 1.0 L total volume
Total Volume	1.0 L
-filter sterilize to remove salt particles	

-autoclave individual aliquots

10× Tris Boric Acid EDTA (TBE) Buffer

Name	Amount
Tris	157.5 g
Boric Acid	27.8 g
Na_2EDTA	9.3 g
Milli-Q water	up to 1.0 L total volume
Total Volume	1.0 L

1× TBE Buffer

Name	Amount
10× TBE	100.0 mL
Milli-Q water	up to 1.0 L total volume
Total Volume	1.0 L

10× Tris Acetic Acid EDTA (TAE) Buffer pH 8.1

Name	Amount
Tris	193.6 mL
Acetic Acid	45.7 mL
Na_2EDTA	29.8 g
Milli-Q water	up to 4.0 L total volume
Total Volume	4.0 L

-titrate to pH 8.1 with glacial acetic acid

1× TAE Buffer

Name	Amount
10× TAE	100.0 mL
Milli-Q water	up to 1.0 L total volume
Total Volume	1.0 L

Microscopy Reagents

4% Paraformaldehyde (w/v)

Name	Amount
Paraformaldehyde	0.4 g
1X PBS	up to 10.0 mL total volume
Total Volume	10.0 mL

-bring to a boil with stirring in fume hood
-allow to cool prior to use

0.5% Triton X-100 PBS (v/v)

Name	Amount
Triton X-100	5.0 mL
1X PBS	up to 1 L total volume
Total Volume	1.0 L

0.1% Triton X-100 PBS (v/v)

Name	Amount
Triton X-100	1.0 mL
1X PBS	up to 1 L total volume
Total Volume	1.0 L

4', 6-Diamidino-2-phenylindole (100mM) (DAPI)

Name	Amount
DAPI	100.0 mg
1X PBS	up to 3.606 mL total volume
Total Volume	1.0 mL

-store at 4°C protected from light

Hoechst 33342 (1mg/mL)

Name	Amount
Hoechst 33342	10.0 mg
1X PBS	up to 10 mL total volume
Total Volume	1.0 mL
-store at -20°C protected from light	

Immunoblotting Reagents

25× Protease Inhibitor

Name	Amount
Roche cOmplete Protease Inhibitor Cocktail	1 Tablet
Milli-Q water	2.0 mL
Total Volume	2.0 mL
-50 μL aliquots	
-store at -20°C	
-use within 30 min of thawing	

Radioimmunoprecipitation Assay Buffer (RIPA)

Name	Amount
Tris 50mM (pH 8.0)	5.0 mL
NaCl 150mM	7.5 mL
SDS 0.1%	0.5 mL
Sodium Deoxycholate 0.5%	0.5 g
NP40 1%	1.0 mL
Milli-Q water	up to 100 mL total volume
Total Volume	100.0 mL
-store at 4°C protected from light	

Nuclei Buffer

Name	Amount
Sucrose	8.6 g
NaCl	1.16 g
1 M Tris-HCL pH 8.0	1.0 mL
1 M $MgCl_2$	0.2 mL
1 M $CaCl_2$	0.1 mL
25% (v/v) Triton X-100	4.0 mL
Milli-Q water	up to 100 mL total volume
Total Volume	100.0 mL

-store at 4°C

3× Sample Loading Buffer (B-mercaptoethanol)

Name	Amount
Glycerol	30.0 mL
B-mercaptoethanol	3.0 mL
SDS	6.0 g
Tris	2.28 g
Bromophenol Blue	1.5 mg
Milli-Q water	up to 100 mL total volume
Total Volume	100.0 mL

-titrate to pH 6.8 with HCl
-store at -20°C
-bring to room temperature before use

5× Sample Loading Buffer (1,4-Dithiothreitol, DTT)

Name	Amount
Glycerol	12.0 mL
1,4-Dithiothreitol (DTT)	1.54 g
SDS	2.0 g
Tris 2M (pH 6.8)	2.5 mL
Bromophenol Blue	1.5 mg
Milli-Q water	up to 20 mL total volume
Total Volume	20.0 mL

-store at -20°C
-bring to room temperature before use

30% Acrylamide:Bis-Acrylamide (29:1)

Name	Amount
Acrylamide	30.0 g
Bis-acrylamide	0.8 g
Milli-Q water	up to 100.0 mL total volume

Total Volume 100.0 mL
-protect from light and store at 4°C

4× Stacking Buffer (top gel)

Name	Amount
Tris	6.05 g
SDS	0.4 g
Milli-Q water	up to 100.0 mL total volume

Total Volume 100.0 mL
-titrate to pH 6.8 with HCl

4× Resolving Buffer (bottom gel)

Name	Amount
Tris	91.0 g
SDS	2.0 g
Milli-Q water	up to 500.0 mL total volume

Total Volume 500.0 mL
-titrate to pH 8.7 with HCl

10% Ammonium Persulfate (APS)

Name	Amount
Ammonium Persulfate	0.1 g
Milli-Q water	up to 1.0 mL total volume

Total Volume 1.0 mL
-store at -20°C

10× Running Buffer

Name	Amount
Tris	30.0 g
Glycine	144.0 g
SDS	10.0 g
Milli-Q water	up to 1.0 L total volume
Total Volume	1.0 L

1× Running Buffer

Name	Amount
10× Running Buffer	100.0 mL
Milli-Q water	up to 1.0 L total volume
Total Volume	1.0 L

1× Transfer Buffer

Name	Amount
10× Running Buffer	100.0 mL
Methanol	200.0 mL
Milli-Q water	up to 1.0 L total volume
Total Volume	1.0 L

10× Tris Buffered Saline (TBS)

Name	Amount
NaCl	80.0 g
KCl	2.0 g
1 M Tris pH 7.5	250.0 mL
Milli-Q water	up to 1.0 L total volume
Total Volume	1.0 L

TBS 0.1% Tween20 (TBST)

Name	Amount
10× TBS	100.0 mL
Tween-20	1.0 mL
Milli-Q water	up to 1.0 L total volume
Total Volume	1.0 L

5% Non-fat Milk (w/v)

Name	Amount
Non-fat milk	5.0 g
1× TBS	100.0 mL
Total Volume	100.0 mL

Copper phthalocyanine 3,4',4'',4'''-tetrasulfonic acid tetrasodium salt (CPTS)

Name	Amount
CPTS	50.0 mg
HCL (conc.)	1.0 mL
Milli-Q water	up to 1.0 L total volume
Total Volume	1.0 L

Cell Cycle Inhibitors

Nocodazole (15nM)

Name	Amount
Nocodazole (Sigma - M1404)	5.0 mg
Dimethyl Sulfoxide (DMSO)	1.0 mL
Total Volume -store at -20°C	1.0 mL

Thymidine (100mM)

Name	Amount
Thymidine (Sigma - T9250)	24.2 mg
Milli-Q water	1.0 mL
Total Volume -store at -20°C	1.0 mL

Flow Cytometry Reagents

Propidium Iodide (1 mg/mL)

Name	Amount
Propidium Iodide (Sigma - P4170)	1.0 mg
Milli-Q water	1.0 mL
Total Volume	1.0 mL

-protect from light and store at 4°C

RNase A (1 mg/mL)

Name	Amount
RNase A (Sigma - R5500)	1.0 mg
Milli-Q water	1.0 mL
Total Volume	1.0 mL

-store at -20°C

Cell Culture Chemical Inhibitors

SGC0946 (50 mM)

Name	Amount
SGC0946	100.0 mg
DMSO	up to 3.053 mL
Total Volume -store at -80°C	3.053 mL

Olaparib (30mM)

Name	Amount
Olaparib	100.0 mg
DMSO	up to 7.661 mL
Total Volume -store at -80°C	7.661 mL

BMN673 (Talazoparib) (30mM)

Name	Amount
BMN673	100.0 mg
DMSO	up to 8.763 mL
Total Volume -store at -80°C	8.763 mL